Consiglio Nazionale
delle Ricerche

XXVII Convegno AIPT

# ASSOCIAZIONE ITALIANA PROPRIETÀ TERMOFISICHE

*Bari, 20th September 2024*

*editors*
Laura Fedele
Umberto Berardi
Sergio Bobbo
Alessandro Bortolin
Gianluca Cadelano
Giovanni Ferrarini

**PROCEEDINGS**

XXVII Convegno AIPT

# ASSOCIAZIONE ITALIANA PROPRIETÀ TERMOFISICHE

*Bari, 20th September 2024*

*editors*

Laura Fedele

Umberto Berardi

Sergio Bobbo

Alessandro Bortolin

Gianluca Cadelano

Giovanni Ferrarini

edizioni

Consiglio Nazionale delle Ricerche

CNR | Istituto per le Tecnologie della Costruzione

Politecnico di Bari

Be TOP Lab

Sviluppo grafico a cura di Fulvia Ciurlia, Istituto di Fisica Applicata “Nello Carrara” (IFAC-CNR)
Impaginazione a cura di Patrizia Andronico, Istituto di Informatica e Telematica (IIT-CNR)


P.le Aldo Moro 7, 00185 Roma
www.edizioni.cnr.it
ISBN 978 88 8080 645 5

## Index

**Segreteria AIPT**: info@aipt-it.it

Prof. Umberto Berardi: umberto.berardi@poliba.it

2024

Bari

# XXVII AIPT

**Associazione Italiana Proprieta' Termofisiche**

**09.00 – 09.30** **Apertura dei lavori**

**09.30 – 10.30** ***Assemblea Soci AIPT***

Comunicazioni
Approvazione bilanci
Rinnovo cariche sociali
Analisi di consuntivo ECTP2023
Varie ed eventuali

**10.30 – 11.00** **Pausa caffè**

## *PREMIO ERMANNO GRINZATO (Chair Umberto Berardi)*

**11.00 – 11.20**
*Feliciano Falcone, Gianluca Coccia*
A NEW CORRELATION TO PREDICT THE VISCOSITY OF NANOFLUIDS BASED ON WATER, ETHYLENE GLYCOL, AND PROPYLENE GLYCOL
**11.20 – 11.40**
*Eleonora Baccega, Laura Vallese, Michele Bottarelli*
ENHANCEMENT OF THERMAL CONDUCTIVITY OF PARAFFIN PCM WITH METAL FOAMS
**11.40 – 12.00**
*Davide Menegazzo, Giulia Lombardo, Laura Vallese, Sergio Bobbo*
EXPERIMENTAL COMPRESSED LIQUID DENSITY MEASUREMENTS AND CORRELATION OF THE BINARY MIXTURE {N-PENTANE (R601) + TRANS-1-CHLORO-3,3,3-TRIFLUORO-1-PROPENE (R1233ZD(E))}
**12.00 – 12.20**
*Giulia Lombardo, Davide Menegazzo, Laura Vallese, Michele De Carli, Fabio Poletto, Sergio Bobbo*
EXPLORING LOW-GWP ALTERNATIVES FOR HEAT PUMPS: A DROP-IN COMPARATIVE STUDY OF R1234YF/R600A AND R134A
**12.20 – 12.40**
*Hala Salhab, Mahdi Zanjani, Ines Belmir, Alberto Lagazzo, Sergio Nardini, Francesca Zanoni, Mona Sam, Saulo Rocha Ferreira, Antonio Caggiano*
GREEN MORTARS MADE WITH TES ENHANCED RECYCLED WOOD AGGREGATES

**12.40 – 14.00** **Intervallo pranzo**

## *RELAZIONI SCIENTIFICHE (Chair Giovanni Ferrarini)*

**14.00 – 14.15**
*Nima Razmjoo, Alice Scolieri, Stefano Signorini, Manuele Gatti*
COMPARISON OF DIFFERENT CALIBRATION METHODS FOR VIBRATING TUBE DENSIMETER
**14.15 – 14.30**
*Pengyu Cheng, Sebastiano Tomassetti, Francesca Luzi, Pietro Forcellese, Tiziano Bellezze, Giovanni Di Nicola*
ANALYSIS OF SOLID-SOLID PHASE CHANGE MATERIALS FOR SOLAR THERMAL APPLICATIONS

**14.30 – 14.45**
*Paolo Bison, Giovanni Ferrarini, Stefano Rossi*
ON MEASURING THERMAL DIFFUSIVITY OF A THIN FOIL: PHOTOTHERMAL VARIATIONS
**14.45 – 15.00**
*Giampaolo D'Alessandro, Filippo de Monte, Stefano Sfarra*
OPTIMUM EXPERIMENTAL SET-UP FOR THERMAL CONDUCTIVITIES MEASUREMENT OF COMPOSITE MATERIALS
**15.00 – 15.15**
*Elena Campagnoli, Valter Giaretto*
ADAPTED LASER-FLASH METHOD FOR ESTIMATING THERMAL DIFFUSION PROPERTIES OF A POROUS MATERIAL SURROUNDED BY COMPACT LAYERS
**15.15 – 15.30**
*Francesco Anaclerio, Adriana Dammicco, Nicola Pastore, Concetta I. Gasi*
CAN BIOFILM GROWTH AFFECT THE HEAT TRANSFER BEHAVIOUR IN FRACTURED MEDIA?

**15.30 – 15.45** **Pausa caffè**

**15.45 – 16.00**
*Konstantin Samukov, Silvia Lasala*
CALCULATION OF THE THERMODYNAMIC PROPERTIES OF BINARY REACTIVE MIXTURE. AN APPLICATION TO $N_2O_4 = 2\ NO_2$
**16.00 – 16.15**
*Gianmarco Sciurti, Alberto Muscio, Umberto Berardi*
THE ROLE OF THERMOPHYSICAL PROPERTIES IN THE ENERGY RETROFIT OF BUILDINGS WITH INTERMITTENT USE
**16.15 – 16.30**
*Laura Vallese, Giulia Lombardo, Davide Menegazzo, Laura Fedele, Sergio Bobbo*
COMBINING THERMOCHEMICAL AND PHASE CHANGE MATERIALS FOR THERMAL ENERGY STORAGE: THE ECHO PROJECT
**16.30 – 16.45**
*Maria Montrone, Umberto Berardi, Maria Annunziata M. Capozzi, Antonio Cardone*
PLA/CROCONAINE BLENDED COMPOSITE MATERIALS AS HIGH NIR ABSORBERS FOR PCM LATENT HEAT STORAGE
**16.45 – 17.00**
*Amanda Aguiar, Antonio Caggiano, Romildo Toledo Filho*
IMPACT OF WOOD BIO-AGGREGATE CONTENT ON THE THERMO-PHYSICAL PROPERTIES OF BIO-BASED COMPOSITES

**17.00 – 17.15** ***Conferimento Premio "Ermanno Grinzato"***

**17.15 – 17.45** **Conclusione dei lavori**

# Premio Ermanno Grinzato

# A New Correlation to Predict the Viscosity of Nanofluids Based on Water, Ethylene Glycol, and Propylene Glycol

**Feliciano Falcone[a,]*, Gianluca Coccia[a]**

[a]*Marche Polytechnic University, Department of Industrial Engineering and Mathematical Sciences, Ancona, Italy*

**Corresponding Author:* f.falcone@pm.univpm.it

## Abstract

The optimization of energy utilization represents a crucial objective in the context of sustainable energy resources. In this context, the use of nanofluids represents a promising technological frontier for the enhancement of heat transfer performance. The accurate design of systems and the precise assessment of heat transfer and energy consumption necessitate meticulous attention to the assessment of nanofluids' thermophysical properties, such as dynamic viscosity. This research presents a new correlation for the calculation of dynamic viscosity based on six parameters: base fluid dynamic viscosity, volume fraction, temperature, base fluid critical temperature, base fluid density, base fluid critical density. The correlation is validated using a dataset of dynamic viscosity measurements for 17 nanofluids, which comprises 439 experimental data points. The nanofluids encompass those with water as the base fluid (Ag, $Al_2O_3$, $Al_2O_3$-CuO, C, CuO, ND, Fe-Si, MWCNT, ND-Ni, $TiO_2$), ethylene glycol (Ag, $Al_2O_3$, $CeO_2$, $Co_3O_4$, SiC, $TiO_2$/CuO), propylene glycol (SiC). The dataset is based on experimental measurements reported in the literature, where samples are prepared using stable methods. This study also compares the dynamic viscosity predictions of 14 existing literature equations against the proposed correlation. The results demonstrate that the newly developed correlation exhibits a significantly lower mean absolute relative deviation (9.4%) than that observed with the existing literature equations.

### *1. Introduction*

In 1995, Choi [1] introduced the term "nanofluids" to describe a novel type of fluid with superior thermophysical properties compared to base fluids or conventional suspensions of particles in liquids. Nanofluids are created by dispersing and stabilizing particles that are nanometer-sized in common heat transfer fluids, such as water, glycols, or oils. The objective is to enhance heat transfer by improving the working fluid's effectiveness [2]. Two methods exist for the creation of nanofluids, namely the single-step and two-step techniques. The one-step process entails the simultaneous creation and blending of nanoparticles within the base fluid, resulting in a more fluid-like substance with smaller particles. Nevertheless, the high cost of implementing this method on a large

scale represents a significant obstacle [3]. The "two-step" method entails the initial production of nanoparticles in the form of dry powders through physical or chemical methods, rather than their distribution in the primary fluid. Subsequently, the powders are blended in the liquid using techniques such as ultrasonication, homogenization, or magnetic stirring. One advantage of this method is that it allows to produce more nanoparticles at a reduced cost compared to the "one-step" technique. Consequently, the two-step method has emerged as the preferred approach in industrial settings. The stability of nanofluids is of paramount importance in maintaining their enhanced thermophysical properties. The attainment of stability typically necessitates the utilization of two distinct methodologies: chemical and physical techniques. Chemical methods employ surfactants and pH modification, whereas physical methods entail homogenization via ultrasound or ball milling. Currently, there is no uniform procedure available for assessing the stability of nanofluids [4]. Several studies have evaluated the stability of nanofluids visually, with a few also examining zeta potential, that is defined as the difference in electrical potential between the surface of a particle and a point in the surrounding fluid away from the particle where the electrical charge has neutralized [5]. It is typically expressed in millivolts (mV). Nanofluids with a zeta potential greater than 40-60 mV are considered stable against electrical forces.

The basic thermophysical properties of nanofluids include density, specific heat, thermal conductivity, and dynamic viscosity. While simple correlations are sufficient for approximating the first two properties, this is not the case for the thermal conductivity and dynamic viscosity of nanofluids. In consequence, a plethora of publications have emerged, comprising a multitude of theoretical and experimental analyses pertaining to the aforementioned transport properties. The dynamic viscosity of nanofluids is of critical importance in the context of thermal and heat transfer applications for several reasons. Viscosity has a direct impact on numerous operational properties of nanofluids, making it a crucial parameter to be accurately evaluated. Nanofluids with higher viscosity can enhance the dispersion of nanoparticles within the fluid, but concurrently, they can elevate flow resistance, thereby reducing the overall efficiency of heat transfer. It was demonstrated in many studies ([6], [7], [8]) that an increase in viscosity can result in a trade-off between enhanced thermal properties and reduced flow efficiency. The Reynolds number (*Re*) is a dimensionless parameter that is proportional to the ratio

of inertia forces to viscous forces. It is used to characterize the type of fluid flow, distinguishing between laminar and turbulent flow [9]. A fundamental understanding of the flow type of nanofluids is essential for comprehending the fluid dynamics within pipes, channels, and other flow geometries. In a heat exchanger, a turbulent flow is typically preferred to enhance heat transfer efficiency due to its ability to promote greater mixing and more uniform heat distribution. Furthermore, the value of *Re* is also important for predicting pressure drops in a system. Pressure drops are related to flow resistance, which varies with the flow regime. In a turbulent flow regime, pressure drops are typically greater than in a laminar flow regime. This must be considered when designing pumps and piping. From the preceding considerations, it is evident that a precise calculation of dynamic viscosity is of paramount importance for the purpose of determining the Reynolds number with minimal margin of error.

In the recent years, nanofluids were studied in a wide range of applications, including heat exchangers and solar collectors. Heat exchangers featuring microchannels or microaligned tubes have the potential to reduce energy consumption [3]. However, such technologies may currently be approaching their maximum development. Nevertheless, enhancing the performance of the operating fluid presents a promising avenue for significantly augmenting heat transfer. Numerous studies have demonstrated that the overall heat transfer coefficient of nanofluids is higher than that of the single base fluid, which explains their prevalent use in this area. In 2020, Du et al. [10] conducted a study on the thermal performance of a geothermal exchanger system using $H_2O$ + CuO as the working fluid. The results demonstrated a 39.84% increase in thermal output and a 16.75% increase in pumping energy consumption. In 2021, Gürbüz et al. [11] conducted a numerical and experimental analysis on the use of the hybrid $H_2O$ + CuO-$Al_2O_3$ nanofluid in a tube and shell exchanger. The results indicated that the nanofluid led to an increase in the heat transfer coefficient. Additionally, the viscosity was found to be marginally higher than that of the base fluid. The experimental results indicated an increase in the heat transfer coefficient of 9.5% at a concentration of 0.5% and 12% at a concentration of 1%. Another area where nanofluids have found widespread use is that of solar collectors. For example, in 2020, Hussein et al. [12] synthesized a hybrid nanofluid comprising multi-walled carbon nanotubes and covalently functionalized graphene nanopatterns (CF-GNPs) integrated with hexagonal boron nitride and dispersed in distilled water. A series

of tests conducted on the nanofluid in a flat manifold with varying flow rates (2, 3, and 4 L $min^{-1}$) demonstrated an approximate twofold increase in thermal efficiency.

The authors of the present work have identified several issues associated with investigating the dynamic viscosity of nanofluids throughout scientific literature. Most of these articles present qualitative trend graphs without numerical data. Moreover, a significant proportion of studies rely on experimental data that lack information on the preparation of nanofluids and sufficient stability tests. This study focuses on the dynamic viscosity of nanofluids. The authors developed a database of reliable experimental data to evaluate notable correlations regarding the dynamic viscosity of nanofluids. Additionally, they propose a semiempirical scaled correlation that, based on specific data, exhibits lower deviations with respect to other correlations. The primary objective is to assist engineers and scientists in selecting the most appropriate correlation for dynamic viscosity in their heat transfer models.

The paper is organized as follows. Section 2 presents the experimental database utilized for the evaluation of dynamic viscosity. Only data that could be considered reliable and convincing were included in the analysis. Section 3 presents a review of the most important correlations available in the literature. Section 4 presents the semiempirical scaled equation proposed by the authors. Section 5 presents the results of the study and offers a detailed analysis of the equations' performance across the entire database. Additionally, the specific behavior of each base fluid is examined. This section also demonstrates the way the authors' proposed correlation compares to the other correlations. The conclusions of the study are presented in Section 6.

## *2. Materials and Methods*

This section presents the thermophysical properties of the nanofluids under study, together with other relevant parameters (such as temperature and size). About dynamic viscosity, the study also provides and discusses useful information on preparation methods, the use of dispersants, stability assessment and instrumentation.

### *2.1 .Dynamic viscosity dataset of nanofluids*

The dynamic viscosity data set comprises 439 points collected for 17 nanofluids. The analysis considered three basic fluids: water ($H_2O$), ethylene glycol (EG), and propylene glycol (PG). With regard to the first base fluid ($H_2O$), there are 10 nanoparticles (3 metal

oxides, 4 metallic, 3 hybrids) available: silver (Ag), aluminum oxide ($Al_2O_3$), copper oxide (CuO), aluminum-copper oxide ($Al_2O_3$) copper oxide (CuO), carbon (C), iron-silicon (Fe-Si), multi-walled carbon nanotubes (MWCNT), nanodiamond (ND), nanodiamond-nickel (ND-Ni), and titanium dioxide ($TiO_2$).The second base fluid (EG) comprises six nanoparticles, including three metal oxides, one metal oxide, one covalent compound, and one hybrid: silver (Ag), aluminum oxide ($Al_2O_3$) cesium dioxide ($CeO_2$), cobalt trioxide ($Co_3O_4$), silicon carbide (SiC), and titanium-copper dioxide ($TiO_2$-CuO). There is only a nanofluid containing propylene glycol (PG) as the base fluid, and the nanoparticle used is silicon carbide (SiC). Table 1 presents the primary data regarding the nanofluids. As illustrated, the experimental measurements encompass a considerable range of dynamic viscosity, temperature, and nanoparticle concentration. The relationship between dynamic viscosity and temperature is illustrated in Figure 1. For liquids, viscosity tends to decrease with increasing temperature. At higher temperatures, the molecules of a liquid vibrate faster and with greater intensity. This increase in kinetic energy reduces intermolecular attraction, allowing molecules to slide more easily over each other, which in turn decreases viscosity.

The subsequent list provides further details regarding the experimental measurements, including preparation methods, stability, and accuracy, of the literature works considered in the present study.

**EG+Ag** Zadeh et al. [13] conducted a study of this nanofluid, analyzing six different volume fractions of 0.25-0.5-0.75-1-1.5-2%. To ensure adequate dispersion and stability of the nanofluid, a surfactant was added to the base fluid, which was stirred with a magnetic mixer for 30 minutes. Subsequently, the silver nanoparticles (diameter 40 nm) were added and mixing continued until the nanoparticles were completely suspended, resulting in a stable colloidal mixture. To prevent particle aggregation, each sample was subjected to ultrasonic agitation for 30 minutes.

**Table 1.** Dynamic viscosity dataset of nanofluids.

| Nanofluid | Exp. Points | $T_{min}$ (°C) | $T_{max}$ (°C) | $\mu_{min}$ (Pa s) | $\mu_{max}$ (Pa s) | $\phi_{avg}$ (%) | Ref. |
|---|---|---|---|---|---|---|---|
| EG+Ag | 21 | 25 | 55 | 0.0083 | 0.0226 | 0.50 | [13] |
| EG+$Al_2O_3$ | 73 | 10 | 50 | 0.0075 | 0.0468 | 2.63 | [14] |

| | | | | | | | |
|---|---|---|---|---|---|---|---|
| EG+$CeO_2$ | 24 | 25 | 50 | 0.0082 | 0.0195 | 0.22 | [8] |
| EG+$CO_3O_4$ | 15 | 10 | 50 | 0.0080 | 0.0448 | 3.28 | [15] |
| EG+SiC | 44 | 10 | 80 | 0.0031 | 0.0452 | 0.93 | [16][17] |
| EG+$TiO_2$-CuO | 24 | 25 | 60 | 0.0055 | 0.0241 | 0.99 | [18] |
| H20+Ag | 3 | 20 | 60 | 0.0007 | 0.0013 | 0.02 | [19] |
| H20+ $Al_2O_3$ | 54 | 5 | 65 | 0.0006 | 0.0021 | 2.25 | [20][21] [22][23] |
| $H_2O$+Al203-CuO | 4 | 50 | 80 | 0.0006 | 0.0007 | 0.02 | [24] |
| $H_2O$+C | 10 | 20 | 60 | 0.0006 | 0.0013 | 1.74 | [25] |
| $H_2O$+CuO | 95 | 5 | 50 | 0.0005 | 0.0023 | 0.92 | [26][6] |
| $H_2O$+ND | 16 | 20 | 50 | 0.0007 | 0.0011 | 0.11 | [27] |
| $H_2O$+Fe-Si | 15 | 20 | 50 | 0.0005 | 0.0010 | 0.12 | [28] |
| $H_2O$+MWCNT | 13 | 20 | 50 | 0.0006 | 0.0016 | 0.06 | [27] |
| $H_2O$+ND-Ni | 8 | 30 | 60 | 0.0005 | 0.0009 | 0.23 | [29] |
| $H_2O$+$TiO_2$ | 26 | 10 | 70 | 0.0007 | 0.0022 | 2.87 | [6] [30] [31] |
| PG+SiC | 24 | 25 | 80 | 0.0043 | 0.0456 | 0.62 | [17] |
| Total | 439 | | | | | | |

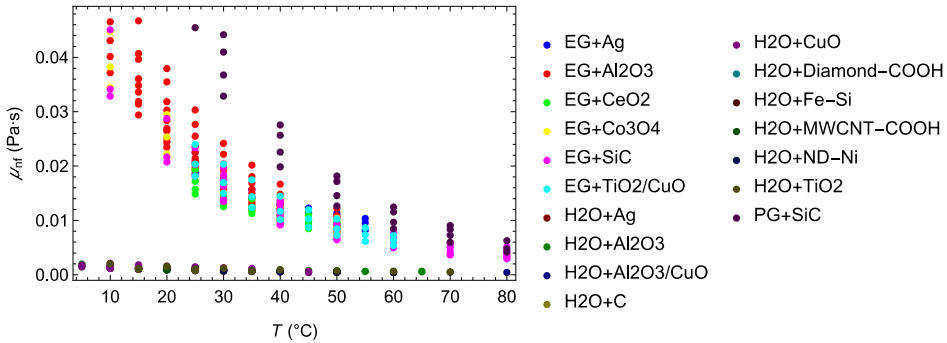


***Figure 1.*** *Experimental dynamic viscosity vs. temperature of the dataset.*

**EG+$Al_2O_3$** Gallego et al. [14] prepared the nanofluid by dispersing alumina nanoparticles (40 nm diameter) in ethylene glycol via a two-step method, yielding six distinct mixtures with volumetric concentrations of 0.5%, 1.5%, 2.1%, 3.1%, 4.8%, 6.6%, and 10%. All products were utilized without purification, and dispersants and surfactants were employed to stabilize the samples. The pH of the solution was determined to be approximately 6-7.5.

**EG+$CeO_2$** Saeedi et al. [8] investigated the dynamic viscosity of this nanofluid by considering six volume fractions, specifically 0.05%, 0.1%, 0.2%, 0.4%, 0.8%, and 1.2%. The nanofluid was prepared using a two-step technique to disperse nanoparticles with a diameter of 10–30 nm. The solution was initially subjected to magnetic stirring for a period of two hours, followed by ultrasonication for a duration of six hours, with the objective of enhancing the solution's stability. The pH of the solution was determined to be within the range of 6 to 7.5.

**EG+$Co_3O_4$** Mariano et al. [15] prepared the nanofluid via a two-step method, dispersing cobalt oxide nanoparticles (diameter 10-24 nm) in ethylene glycol to obtain five distinct mixtures with mass concentrations of 5%, 10%, 15%, 20%, and 25%, corresponding to volume concentrations of 0.9%, 2.1%, 3.1%, 4.3%, and 5.7%, respectively. The stability of the samples was enhanced through the application of ultrasonic cycles.

**EG+SiC** In the study conducted by L. Colla [16], nanofluids were provided by Nanograde LLC at concentrations of 0.1, 1, and 5% by weight. The suspensions were treated with an unidentified anionic dispersant at concentrations of 0.008, 0.08, and 0.4 wt%. The reported diameter ranged from a minimum of 10 nm to a maximum of 50 nm. The dynamic viscosity was quantified at room pressure and a temperature range spanning from 10 to 90 °C, employing the AR-G2 Rheometer.. Akilu et al. [17] prepared the nanofluid using a two-step technique, whereby silicon carbide nanoparticles with a diameter of 45-65 nm were dispersed in ethylene glycol. Viscosity was quantified using a Physica MCR 302 viscometer at volume concentrations of 0.25, 0.5, 0.75, 1%, which correspond to mass concentrations of 0.72, 1.3, 2.1, 3.0%.

**EG+$TiO_2$-CuO** In a previous study, Akilu et al. [18] developed a titanium-copper oxide ($TiO_2$-CuO) nanocomposite by employing a wet mixing protocol. The composite was characterized by scanning electron microscopy (SEM), energy dispersive X-ray spectroscopy (EDX), and X-ray powder diffraction (XRD). Next, hybrid nanofluids were prepared by dispersing the nanocomposite in ethylene glycol (EG). The zeta potential of 40 mV confirmed its stability. In the temperature range of 303.15 K to 333.15 K, dynamic viscosity was measured for volume concentrations of 0.5%, 1.0%, 1.5%, and 2.0%. The stability of the nanofluid was confirmed by measuring the zeta potential.

**$H_2O$+Ag** Bizhaem et al. [19] prepared the nanofluid by dispersing 0.2% silver by mass in water, corresponding to 0.019% by volume. The samples were then subjected to

ultrasonication to remove any aggregation of the nanoparticles. Viscosity was quantified at varying temperatures (20-40-60 °C) using the Brookfield Viscometer LVDV-II+ Pro instrument, with a measurement uncertainty of ± 5%.

**$H_2O$+$Al_2O_3$** Elcioglu et al. [20] created the nanofluid by dispersing the nanoparticles in water, resulting in 3 various volume percentages (1%, 2%, 3%); two samples were obtained for each volume percentage, one containing nanoparticle with an average diameter of 10±5 nm and the other with a diameter of 30±5nm. Ultrasonication for approximately 2 minutes was used to enhance the stability of the nanofluid. The zeta potential measurements show that the first set of samples has a zeta potential of around 49 mV, while the second set measures at 48 mV.

Nair et al. [21] created the nanofluid in water by dispersing various volume percentages ranging from 0.5% to 2.5% using a two-step method. The samples were subjected to ultrasonication for a duration of 4 hours. The zeta potential measured 35.1 mV while the pH registered at 4.3.

Coccia et al. [22] created the nanofluid by spreading various amounts of alumina in water. The obtained samples underwent ultrasonication and remained stable. Nguyen et al. [23] prepared the nanofluid with particles measuring 36 nm and 47 nm in water, achieving weight concentrations of 14-15-22%. The samples remained stable for approximately one month following their preparation. The viscometer "ViscoLab450" was used to measure viscosity with an error margin of ± 1%.

**$H_2O$+$Al_2O_3$-CuO** Zufar et al. [25] produced this blend of Al2O3 and CuO nanoparticles in water through a two-step method with a 50:50 mixing ratio, leading to a weight concentration of 0.1%. The samples were later exposed to ultrasound for a duration of 360 minutes to enhance stability. The viscosity was determined using a Brookfield LVDV Ultra rheometer with a margin of error of ± 5%.

**$H_2O$+C** Dalkilic and colleagues [24] created the nanofluid by mixing graphite nanoparticles (with an average size of 8 nm) in water, resulting in four separate mixtures with volumetric concentrations of 0.5%, 1%, 1.5%, and 2%. The nanofluids' stability was verified through the measurement of a zeta potential of 70 mV.

**$H_2O$+CuO** Nair et al. [21] created the nanofluid using the identical H20+Al2O3 method. Pastoriza-Gallego et al. [26] conducted measurements on the dynamic viscosity of the nanofluid, which had a mass concentration ranging from 1% to 5%. They acquired two

distinct sets of samples. In S1, CuO nanoparticles (with a diameter of 23-37 nm) were bought from Nanoarch; in S2, nanoparticles (with a diameter of 11 nm) were produced using the rapid precipitation technique. The method used to produce the nanofluid follows the one suggested by Zhu [32], where copper acetate and sodium hydroxide are mixed to form water, copper oxide, and sodium acetate. Once the precipitate has cooled down to room temperature, it is spun in a centrifuge, rinsed with a water and ethanol mix followed by three washes with pure ethanol, and then dried at room temperature.

**$H_2O$+ND** Alrashed et al. [27] achieved a nanofluid by blending diamond nanoparticles measuring 3-6 nm in water through a two-step process without using surfactants. After that, the samples were exposed to ultrasonication and homogenization for around 30 minutes, creating a uniform suspension that prevents particle clumping and ensures the fluid remains stable for an extended period.

**$H_2O$+Fe-Si** Huminic et al.[28] prepared the nanofluid by gradually introducing iron and silicon nanoparticles into water; they utilized an ultra176 sonic disperser (UIP 1000-hd Ultrasonic Homogenizer) along with a slender vibrating rod (for 5 minutes) to achieve uniform suspensions. The suspensions were exposed to ultrasonication for a duration of 30 minutes. In the end, three suspensions were made, each consisting of 250 ml, and containing Fe-Si nanoparticles in amounts of 2.5, 5.0, and 10 g $l^{-1}$ respectively. The three suspensions had zeta potentials of -72.2, -71.5, and -73.1 mV, respectively, as measured.

**$H_2O$+MWCNT** Alrashed et al. [27] employed a unique method to achieve four varying volume concentrations of 0.02%, 0.08%, 0.1%, and 0.2%. Following the dispersion of MWCNT nanoparticles (sized 8-15 nm) in water, a magnetic stirrer was employed to enhance the dispersion of the nanotubes; next, homogenization was carried out for around 30 minutes to enhance the dispersion of the MWCNTs in the liquid base and guarantee colloidal stability.

**$H_2O$+ND-Ni** In different research conducted by Sundar et al. [29] , the ND-Ni hybrid compound was synthesized in a similar manner as the ND-Fe3O4 compound. Hybrid nanofluids containing 0.1% and 0.3% volume concentrations of ND-Ni nanoparticles were formed by dispersing 51.57 g and 155.56 g of nanoparticles in 13 L of distilled water, respectively. Through optical analysis of the nanofluids using XRD technique, a diameter of 4.5 nm was measured.

**$H_2O$+$TiO_2$** Duangthongsuk et al. [6] created the nanofluid by distributing 21 nm diameter

titanium oxide nanoparticles in water through a two-step process. The researchers used the Bohlin rotational rheometer to measure the dynamic viscosity in their experiment. Analyses were performed on mixtures containing 0.2, 0.6, 1.0, 1.5, and 2.0% by volume, with pH levels of 7.5, 7.1, 7.0, 6.8, and 6.5. Tertsinidou et al. [30] achieved the required solutions through the two-step method. There was no dispersant added. After weighing, the liquid and solid parts were combined, and homogenization was carried out using an ultrasonic vibrator (HF-generator GM2200, Bandelin) to sonicate the mixture for approximately 1 hour to disintegrate any clumps present. The best sonication time was determined to be 1 hour as any additional time did not impact the sample's stability. Fedele et al. [31] created the nanofluid by introducing titanium oxide nanoparticles (with a diameter of 40 nm) into water through a two-step process. Mixtures containing 1-10-20-35% volumetric concentrations were tested with pH levels of 3.07, 2.34, 2.24 and 1.86 respectively. The zeta potential of all nanofluids was found to be around 55 mV.

**PG+SiC** Akilu and colleagues [17] created and analyzed the nanofluid using the identical method as EG+SiC, also examining equal mass and volume concentrations.

### *2.2. Other thermophysical properties of nanofluids*

To evaluate the correlations with dynamic viscosity, it was also necessary to collect data for the thermophysical properties of the base fluids and the nanoparticles. Table 2 presents the characteristics of the nanoparticles included in the database, with an examination of both the range of diameters ($\Delta d_{np}$) and their density ($\rho_{np}$). In particular, the diameters cited in separate articles were employed in this investigation. The density of the nanoparticles was assumed to be constant and was sourced from the DETHERM database [33]. This decision was necessary since several articles reported different density values for the same nanoparticle, which was caused by variable measurement uncertainties associated with the specific instrument utilized. Furthermore, the temperature-dependent properties considered included base fluid dynamic viscosity ($\Delta\mu_{bf}$) and base fluid density ($\Delta\rho_{bf}$).

Table **3** presents the temperature range considered, along with references to data sources, for both $\Delta\mu_{bf}$ and $\Delta\rho_{bf}$. Furthermore, the table presents the critical temperature ($T_{c,bf}$) and critical density ($\rho_{c,bf}$) of the base fluids examined in this research.

**Table 2.** Properties of nanoparticles.

| Nanoparticle | $\Delta d_{np}$ (nm) | Ref. | $\rho_{np}$ (kg·m$^{-3}$) | Ref. |
|---|---|---|---|---|
| Ag | 40-47.5 | [13] | 10500 | [34] |
| $Al_2O_3$ | 8-68 | [14] [20][21] [22] [23] | 3970 | [35] |
| $Al_2O_3$3-CuO | 10 | [24] | 5225 | [33] |
| C | 8 | [25] | 2250 | [33] |
| $CeO_2$ | 20 | [8] | 7132 | [33] |
| $CO_3O_4$ | 10-24 | [15] | 6000 | [33] |
| CuO | 21.5 | [26][6] | 6480 | [33] |
| ND | 4.5 | [27] | 3520 | [33] |
| Fe-Si | 200 | [28] | 5052 | [28] |
| MWCNT | 11.5 | [27] | 1740 | [33] |
| ND-Ni | 4.5 | [29] | 3971 | [33] |
| SiC | 55-110 | [16][17] | 3170 | [33] |
| $TiO_2$ | 5-40 | [6] [30] [31] | 4285 | [33] |
| $TiO_2$-CuO | 21.5 | [18] | 4702 | [33] |

**Table 3.** Properties of base fluids.

| Base fluid | EG | $H_2O$ | PG |
|---|---|---|---|
| $\Delta\mu_{bf}$ (Pa s) | 0.0031-0.0335 | 0.0007-0.0015 | 0.0042-0.040 |
| ($\Delta$T (°C)) | 10-80 | 5-55 | 25-80 |
| Ref. | [36] | [37] | [38] |
| $\Delta\rho_{bf}$ (kg·m$^{-3}$) | 1072-1120 | 971.7-1005.5 | 990-1033 |
| ($\Delta$T (°C)) | 10-80 | 5-55 | 25-80 |
| Ref. | [39] | [37] | [40] |
| $T_{c,bf}$ (°C) | 446.85 | 373.94 | 400.85 |
| $\rho_{c,bf}$ (kg·m$^{-3}$) | 360.0 | 400.1 | 338.96 |
| Ref. | [41] | [41] | [41] |

### *3. Correlations for dynamic viscosity*

Viscosity measures how much a fluid resists flowing between two layers that are close together. When nanoparticles are present in a fluid, they can lead to increased resistance between layers when subjected to shearing forces. This leads to an increased viscosity of the nanofluid in comparison to the original fluid. This research stands out from previous papers by specifically concentrating on the key and easy-to-use equations for nanofluid dynamic viscosity models, unlike others that have delved into the subject in depth. Table 4 displays the correlations utilized in this study, where:

- $\mu_{nf}$ is the dynamic viscosity of the nanofluid (Pa·s);
- $\mu_{bf}$ is the dynamic viscosity of the base fluid (Pa·s);
- $\phi$ is the volume concentration;
- $\phi_m$ represents the maximum volume concentration, typically ranging from 0.495 to 0.540 under quiescent conditions and reaching approximately 0.605 at high shear rates;
- $\eta$ represents the intrinsic viscosity, with a typical value of about 2.5 for monodisperse suspensions of hard spheres;
- $d$ represents the average diameter of nanoparticles (m);
- $d_f$ indicates the equivalent diameter (m) of a base fluid molecule, which can be calculated using the following equation:

$$d_f = 0.1 \left( \frac{6M}{N \cdot \pi \cdot \rho_{273K}} \right)^{-\frac{1}{3}} \quad (1)$$

where $M$ (g/mol) represents the molar mass of the base fluid, N is Avogadro's number, and $\rho_{273K}$ indicates the density of the base fluid at 273 K.

**Table 4.** Literature equations.

| *Model and Ref.* | *Correlation* | |
|---|---|---|
| Einstein [42] | $\mu_{nf}=\mu_{bf}(1+2.5\phi)$ | (2) |
| Eilers [43] | $\mu_{nf}=\mu_{bf}\left(1+\frac{1.25\phi}{1-\frac{\phi}{0.78}}\right)$ | (3) |
| De Bruijin [44] | $\mu_{nf}=\mu_{bf}(1 - 2.5\phi + 1.55\phi^2)$ | (4) |
| Vand [45] | $\mu_{nf}=\mu_{bf}(1 - \phi + 1.16\ \phi^2)^{-2.5}$ | (5) |
| Saito [46] | $\mu_{nf}=\mu_{bf}\left(1+\frac{2.5\phi}{1-\phi}\phi\right)$ | (6) |
| Brinkman [47] | $\mu_{nf}=\mu_{bf}\left(\frac{1}{(1-\phi)^{2.5}}\right)$ | (7) |
| Krieger [48] | $\mu_{nf}=\mu_{bf}\left(1-\frac{\phi}{\phi_m}\right)^{\eta\phi_m}$ | (8) |
| Thomas [49] | $\mu_{nf}=\mu_{bf}(1 + 2.5\ \phi + 10.5\ \phi^2 + 0.00273e^{1.66\phi})$ | (9) |
| Nielsen [50] | $\mu_{nf}=\mu_{bf}(1 + 1.5\phi)e^{\frac{\phi_m}{1-\phi_m}}$ | (10) |
| Lundgren [51] | $\mu_{nf}=\mu_{bf}\left(\frac{1}{1-2.5\ \phi}\right)$ | (11) |
| Batchelor [52] | $\mu_{nf}=\mu_{bf}(1 + 2.5\phi + 6.5\ \phi^2)$ | (12) |
| Maiga [53] | $\mu_{nf}=\mu_{bf}(1 + 7.3\ \phi + 123\ \phi^2)$ | (13) |
| Guo [54] | $\mu_{nf}=\mu_{bf}(1 + 2.5\ \phi + 6.5\ \phi^2)\left(1+350\frac{\phi}{d}\right)$ | (14) |
| Corcione [55] | $\mu_{nf}=\frac{\mu_{bf}}{1 - 34.87\left(\frac{d}{d_f}\right)^{-0.3}}$ | (15) |

The equations presented in Table 4 lack an explicit temperature dependence. However, both the volumetric concentration and the dynamic viscosity of the base fluid are closely related to it. The volumetric concentration of a solution is influenced by temperature due to the change in solvent volume resulting from thermal expansion or contraction.

### *4. Proposed semi-empirical correlation for dynamic viscosity*

This study introduces a semi-empirical correlation that considers the impact of temperature, nanoparticle density, volumetric concentration, and the characteristics of the base fluid on the dynamic viscosity of nanofluids. All these quantities are easily available in the literature. The correlation is as follows:

$$\mu_{nf} = \mu_{bf}\cdot\left[1+(a\cdot\phi^b)\left(\frac{T}{T_{c,bf}}\right)\left(\frac{\rho_{bf}}{\rho_{c,bf}}\right)^c\right] \quad (16)$$

where:

- $\mu_{bf}$ is the dynamic viscosity of the nanofluid (Pa·s);
- $\phi$ is the volume fraction of nanoparticles;
- $T$ is the temperature (K);
- $T_{c,bf}$ is the critical temperature of the base fluid (K);
- $\rho_{bf}$ is the density of the base fluid (kg·m$^{-3}$);
- $\rho_{c,bf}$ is the critical density of the base fluid (kg·m$^{-3}$).

In the aforementioned equation, the scaled regression coefficients are designated as "*a*," "*b*," and "*c*." Using the Random Search Method (RSM) as detailed in the referenced literature ([56],[57]), the coefficients were identified ($a$ = 0.002, $b$ = 0.613, $c$ = 7.528). This was done with the objective of minimizing the average absolute relative deviation (*AARD*) between the values calculated from the proposed equation and the data presented in Table 1. *AARD*() is defined as:

$$AARD(\mu_{nf}) = \frac{100}{N_{exp}} \sum_{i=1}^{N_{exp}} \left| \frac{\mu_{nf,exp} - \mu_{nf,calc}}{\mu_{nf,exp}} \right| \quad (17)$$

where $N_{exp}$ in the number of experimental data, while $\mu_{nf,\,exp}$ and $\mu_{nf,\,calc}$ are the experimental and calculated dynamic viscosity of nanofluids, respectively. The data regarding the properties of the base fluids and nanoparticles, as presented in Table 2 and Table3, were employed for the purpose of regression analysis.. It is important to note that the coefficients regressed for the selected nanofluids are applicable within the following ranges: 0.018 ≤ $\phi$ ≤ 5.7, 5 °C ≤ T ≤ 80 °C, 971.71 kg·m$^{-3}$ ≤ $\rho_{bf}$ ≤ 1120.23 kg·m$^{-3}$. It should be noted that by setting the volumetric concentration to zero, the dynamic viscosity of the nanofluid and that of the base fluid coincide because there are no dispersed nanoparticles.

### *5. Results and discussion*

This part offers an in-depth analysis of the outcomes achieved using various equations chosen from the existing literature (Section 3). The values of the properties utilized in this research are specified in Section 2.2. Afterwards, the outcomes achieved from the suggested scaled correlation (Section 4) are presented and compared with the equations found in the literature.

### *5.1. Results of the literature correlations*

The *AARD*($\mu_{nf}$) of the 14 chosen models were evaluated against the collected experimental data from the database in Section 2 (Table 1). The outcomes of this evaluation are displayed in Table 5, presenting the *AARD*($\mu_{nf}$) percentages from the equations for all nanofluids listed, and also illustrated in Figure 2 and Figure 3.

As demonstrated in Table 5, De Bruijin's equation (4) exhibits the least discrepancy between calculated $\mu_{nf}$ and experimental values, with an average *AARD* of 12.4%. Conversely, Lundgren's model (11) is regarded as the least robust model in the literature, with an average *AARD* of 19.7%. The models proposed by Krieger (8), Thomas (9), Nielsen (10), Batchelor (12), Maiga (13), and Corcione (15) exhibit strikingly similar characteristics, with an average *AARD* of approximately 13.5%. A comparative analysis of nanofluids with EG as the base fluid reveals that the Lundgren (11) model is the most accurate, with an average *AARD* of 14%. This model outperforms all other models, which often exceed 17%. Upon analysis of the nanofluids with $H_2O$ as the base fluid, it becomes evident that most of the reported models (Eq. (2), (3), (5), (6), (7), (8), (9), (10)) are, in fact, equivalent, with *AARD*s approximately equal to 10.5%. Batchelor's model (12) is notable for its shortcomings, exhibiting difficulties with the majority of water-based nanofluids. However, the same model (12) presents a favorable *AARD* of 13.5% with the PG+SiC nanofluid, which is significantly lower than that obtained with any other model. In addition, the comparison between the experimental and calculated data for the analyzed nanofluids is illustrated in Figure 2 and Figure 3. Figure 2 illustrates the outcomes of the literature correlations for the examined nanofluids, indicating that $\mu_{nf}$ is frequently underestimated by the literature equations, specifically the models of De Bruijin, Krieger-Dougherty, Thomas, and Batchelor (Eq. (4), (8), (9), and (12)). The equations of Maiga (13) and Guo (14) provide a different perspective, generally overestimating the dynamic viscosity. Figure 3 illustrates that while a considerable number of data points appear to align with the line of equality, indicating a satisfactory correspondence between the calculated and experimental values, several points exhibit a notable discrepancy. This indicates that for certain nanofluid combinations (EG+$Al_2O_3$, $H_2O$+$TiO_2$, EG+SiC, $H_2O$+C, etc.) the models utilized to compute viscosity may not accurately predict experimental outcomes.

**Table 5.** AARD ($\mu_{nf}$) % of the 14 literature models.

| Nanofluid | Eq. (2) | Eq. (3) | Eq. (4) | Eq. (5) | Eq. (6) | Eq. (7) | Eq. (8) | Eq. (9) | Eq. (10) | Eq. (11) | Eq. (12) | Eq. (13) | Eq. (14) | Eq. (15) |
|---|---|---|---|---|---|---|---|---|---|---|---|---|---|---|
| EG+Ag | 23.9 | 24.4 | 23.8 | 23.8 | 24.8 | 23.9 | 24.8 | 23.6 | 23.8 | 21.9 | 17.4 | 25.7 | 23.3 | 23.6 |
| EG+$Al_2O_3$ | 21.4 | 23.1 | 21.2 | 21.1 | 24.3 | 21.2 | 24.2 | 20.8 | 21.2 | 12.2 | 24.6 | 27.3 | 14.2 | 18.6 |
| EG+$CeO_2$ | 12.6 | 12.8 | 12.6 | 12.6 | 12.9 | 12.6 | 12.9 | 12.4 | 12.6 | 11.9 | 8.9 | 13.2 | 12.4 | 12.5 |
| EG+$CO_3O_4$ | 13.7 | 17.3 | 13.1 | 12.9 | 19.5 | 13.3 | 19.3 | 12.4 | 13.0 | 12.2 | 97.1 | 25.5 | 28.3 | 11.7 |
| EG+SiC | 14.9 | 15.5 | 14.9 | 14.9 | 15.9 | 14.9 | 15.9 | 14.7 | 14.9 | 12.4 | 11.3 | 17.0 | 14.2 | 14.7 |
| EG+$TiO_2$-CuO | 17.9 | 19.0 | 17.8 | 17.8 | 19.7 | 17.8 | 19.7 | 17.5 | 17.8 | 13.2 | 7.4 | 21.6 | 14.9 | 17.4 |
| All EG based nanofluids | 17.4 | 18.7 | 17.2 | 17.2 | 19.5 | 17.3 | 19.5 | 16.9 | 17.2 | 14.0 | 27.8 | 21.7 | 17.9 | 16.4 |
| $H_2O$ +Ag | 13.4 | 11.4 | 12.4 | 12.4 | 14.4 | 21.4 | 15.4 | 12.3 | 13.5 | 12.5 | 16.4 | 12.4 | 17.4 | 12.5 |
| $H_2O$ + $Al_2O_3$ | 12.2 | 13.6 | 12.1 | 12.1 | 14.6 | 12.2 | 14.5 | 11.9 | 12.1 | 10.0 | 40.3 | 17.7 | 10.5 | 11.2 |
| $H_2O$+Al2O3-CuO | 22.1 | 22.0 | 22.1 | 22.1 | 22.0 | 22.1 | 22.0 | 22.4 | 22.1 | 22.2 | 23.7 | 22.0 | 22.1 | 22.1 |
| $H_2O$+C | 12.5 | 12.7 | 12.5 | 12.5 | 12.8 | 12.5 | 12.8 | 12.5 | 12.5 | 15.8 | 158.7 | 13.8 | 15.9 | 12.5 |
| $H_2O$+CuO | 10.4 | 10.3 | 10.4 | 10.4 | 10.4 | 10.4 | 10.4 | 10.4 | 10.4 | 11.7 | 27.1 | 10.9 | 10.5 | 10.9 |
| $H_2O$+ND | 2.6 | 2.7 | 2.6 | 2.6 | 2.8 | 2.6 | 2.8 | 2.4 | 2.6 | 2.3 | 13.0 | 3.0 | 2.4 | 2.5 |
| $H_2O$+Fe-Si | 7.4 | 7.4 | 7.4 | 7.4 | 7.5 | 7.4 | 7.5 | 7.3 | 7.4 | 7.2 | 7.2 | 7.5 | 7.4 | 7.4 |
| $H_2O$+MWCNT | 6.3 | 6.4 | 6.3 | 6.3 | 6.4 | 6.3 | 6.4 | 6.3 | 6.3 | 6.2 | 6.6 | 6.4 | 6.3 | 6.3 |
| $H_2O$+ND-Ni | 12.7 | 12.6 | 12.7 | 12.7 | 12.5 | 12.7 | 12.5 | 12.8 | 12.7 | 13.1 | 49.1 | 12.3 | 13.0 | 12.8 |
| $H_2O$+$TiO_2$ | 7.3 | 7.8 | 7.2 | 7.2 | 9.1 | 7.2 | 9.0 | 7.2 | 7.2 | 17.6 | 70.6 | 12.9 | 15.1 | 9.7 |
| All $H_2O$ based nanofluids | 10.7 | 10.9 | 10.6 | 10.6 | 11.3 | 11.5 | 11.3 | 10.6 | 10.7 | 11.9 | 41.3 | 11.9 | 12.0 | 10.8 |
| PG+SiC | 18.9 | 19.6 | 18.9 | 18.9 | 20.0 | 18.9 | 20.0 | 18.7 | 18.9 | 16.5 | 13.5 | 21.1 | 18.2 | 18.6 |
| Full dataset | 14.7 | 16.9 | 12.4 | 15.5 | 13.9 | 15.2 | 13.7 | 13.5 | 13.8 | 19.7 | 13.3 | 13.8 | 15.5 | 13.9 |

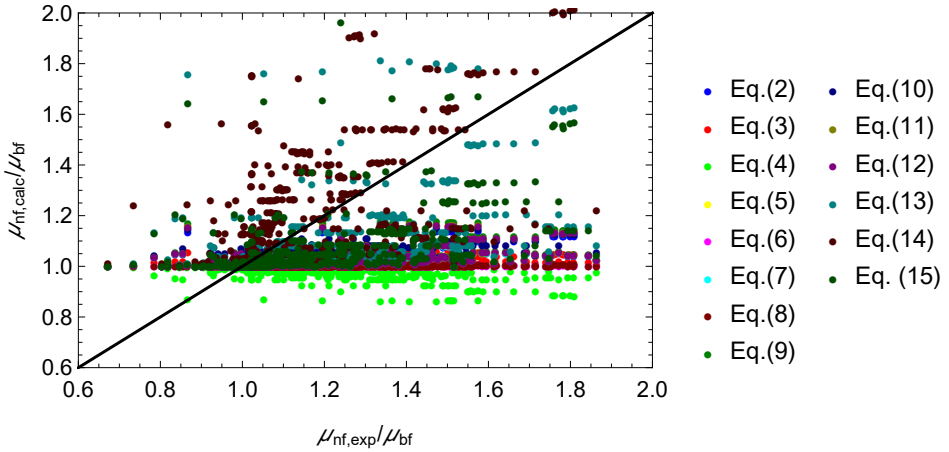


**Figure 2.** Experimental reduced dynamic viscosity compared with calculated values for all models, Eqs. (2) - (15). It should be noted that some points outside the proposed range are not displayed.

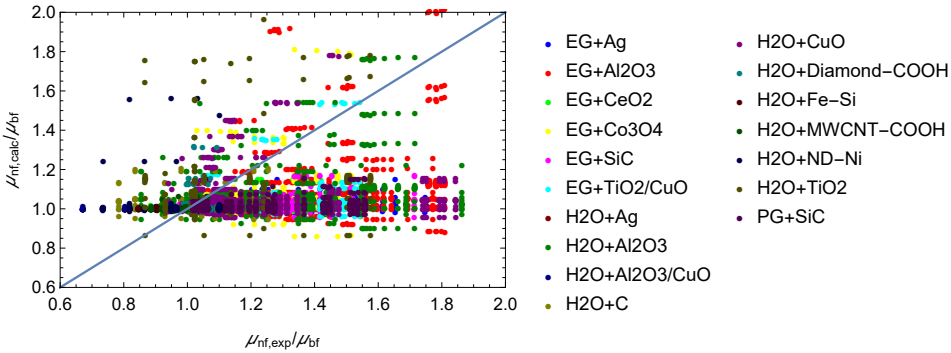


**Figure 3.** Experimental reduced dynamic viscosity compared with calculated values for all nanofluids. It should be noted that some points outside the proposed range are not displayed.

### *5.2. Results for the proposed correlation*

Figure 4 and Table 6 show the results of the proposed model for $\mu_{nf}$ (Eq. (16)). In general, a considerable number of points in Figure 4, which correspond to nanofluids such as EG+Ag, $H_2O$+CuO, and $H_2O$+ND are situated near the line of equality. This indicates that, in these instances, the calculated and experimental values are comparable. Some points, such as those identifying nanofluids such as EG+$Al_2O_3$ and EG+$Co_3O_4$, are above the equality line, indicating a slight overestimation of the calculated values. When compared

with what is shown in Figure 3, a more accurate and less dispersive representation of the correspondence between calculated and experimental values is clear.

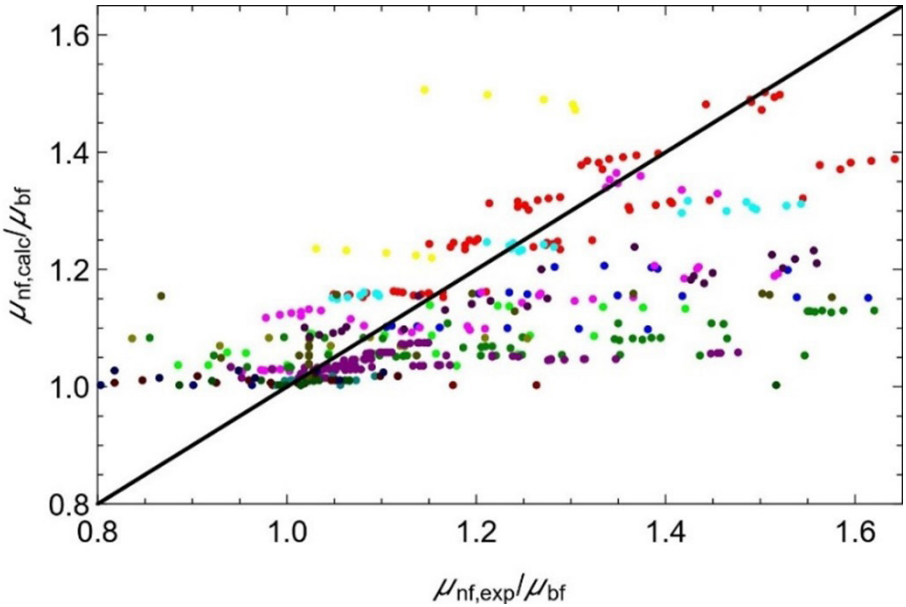


**Figure 4.** Experimental reduced dynamic viscosity vs. calculated values for the proposed semi-empirical correlation. Please refer to Figure 1, Figure 2, or Figure 3 for the legend.

The proposed semi-empirical correlation (Eq. (16)) exhibits an *AARD* of 9.4% across the entire database, which is 3% lower than the De Bruijin equation (Eq.(4)) and 5.5% lower than the average *AARD* values obtainable from all the equations selected from the literature. The overall *AARD* for EG-based nanofluids is 9.6%. In particular, the model demonstrates a high degree of accuracy in predicting the viscosity of EG+$Al_2O_3$ and EG+$TiO_2$-CuO nanofluids, with an *AARD* of 5.6 and 6.9%, respectively. In general, the model estimates the dynamic viscosity of EG-based nanofluids by reducing the *AARD* by approximately 10% with respect to the selected literature equations.

**Table 6.** AARD ($\mu_{nf}$) % of the proposed semi-empirical correlation.

| Nanofluid | Proposed Correlation (Eq.(16)) |
|---|---|
| EG+Ag | 13.3 |
| EG+$Al_2O_3$ | 5.6 |
| EG+$CeO_2$ | 9.1 |
| EG+$CO_{30}$4 | 17.0 |
| EG+SiC | 8.6 |
| EG+$TiO_2$-CuO | 6.9 |
| All EG-based nanofluids | 9.6 |
| $H_2O$+Ag | 12.3 |
| $H_2O$+$Al_2O_3$ | 10.9 |
| $H_2O$+ $Al_2O_3$-CuO | 22.6 |
| $H_2O$+C | 12.8 |
| $H_2O$+CuO | 11.3 |
| $H_2O$+ND | 2.1 |
| $H_2O$+Fe-Si | 7.1 |
| $H_2O$+MWCNT | 6.1 |
| $H_2O$+ND-Ni | 13.3 |
| $H_2O$+$TiO_2$ | 8.3 |
| All $H_2O$ -based nanofluids | 9.8 |
| PG+SiC | 10.6 |
| Full dataset | 9.4 |

In the case of $H_2O$-based nanofluids, the correlation presents an average *AARD* of 9.8%. This result is slightly lower than the *AARD* values shown by the literature equations, as shown in Table 5. In particular, the model demonstrates a high degree of accuracy in predicting the viscosity of nanofluids containing nanoparticles of ND, Fe-SiC, MWCNT, and $TiO_2$, for which it presents *AARD* values of 2.1, 7.1, 6.1, and 8.3%, respectively. The overall result is significantly influenced by the poor predictive ability of the dynamic viscosity of the H2O+$Al_2O_3$-CuO nanofluid, for which it presents an *AARD* of 22.8%. In contrast, the PG+SiC nanofluid exhibits a much lower *AARD* of 10.6%, which is a markedly superior result compared to those presented in Table 5.

### *6. Conclusions*

In this study, an experimental data set comprising 439 points was collected for 17 different nanofluids. The data points were selected with great care, based on the use of unequivocal preparation procedures, stability assessment, and the correct use of instrumentation. The study examined the dynamic viscosity of nanofluids and evaluated the *AARD* of 14 correlations in the literature and a semi-empirical correlation presented by the authors. De Bruijn's equation (Eq. (4)) exhibited the lowest discrepancies, resulting in an *AARD* of 12.4% for the proposed data set. The findings of this study illustrated that the evaluated models have elevated rejection rates, exceeding 20%, for nanofluids comprising ethylene glycol as base fluid. The mean value of the discrepancy for those with $H_2O$ as base fluid was found to be 11%. A substantial proportion of the literature models tend to overestimate the calculated viscosity values.

The authors of this article proposed instead a semi-empirical scaled equation that showed the best overall *AARD* of 9.4% for the selected dataset. Moreover, the proposed correlation demonstrated the lowest deviations for ethylene glycol, propylene glycol, and water-based nanofluids. Models in the literature, due to their simplified nature based on the Einstein model (Eq. (2)), have limited ability to accurately predict the dependence of $\mu_{nf}$ on the temperature and thermophysical properties of nanoparticles. Consequently, they can calculate $\mu_{nf}$ with low error only for limited temperature ranges, when nanoparticles are small, and when the density of the base fluid is not very high or very low.

The authors suggest that, despite its limitations, the model proposed in the present work can be used by the research community to predict the dynamic viscosity of nanofluids analyzed in their calculations, having obtained it by analyzing temperature ranges, diameters, volumetric concentrations, and extensively variable densities. The future development of this work could entail an expansion of the database, with the aim of increasing the total number of nanofluids and enhancing the model's generalizability, i.e. by considering mixtures of base fluids. Furthermore, the additional nanofluids could be employed in conjunction with larger databases and more sophisticated computing techniques that serve to minimize the *AARD*.

## Nomenclature

### Latin symbols

| | |
|---|---|
| $d_f$ | Equivalent diameter (m) expressed by Eq. (1) and used in Eq. (15) |
| $T_{c,bf}$ | Critical temperature of the base fluid, (K) in Eq. (16). |
| *AARD* | Average absolute relative deviation (%) |
| *d* | Average diameter of nanoparticles (m) |
| EDX | Energy dispersive X-ray spectroscopy |
| EG | Ethylene glycol |
| $H_2O$ | Water |
| *M* | Molar mass of the base fluid (g/mol) |
| MWCNT | Multi Wallet Carbon Nanotube |
| N | Avogadro's number ($mol^{-1}$) |
| $N_{exp}$ | Number of experimental data |
| PG | Propylene glycol |
| *Re* | Reynolds number |
| RSM | Random Search Method |
| SEM | Scanning electron microscopy |
| *T* | Temperature (°C) in Table 1 and Table 2 or (K) in Eqs.(2))-(16) |
| $T_{max}$ | Maximum Temperature (°C) |
| $T_{min}$ | Minimum Temperature (°C) |
| XRD | X-ray powder diffraction |

### Greek and composite symbols

| | |
|---|---|
| $\Delta\mu$ | Dynamic viscosity interval (Pa·s) |
| $\Delta\rho$ | Density interval ($kg \cdot m^{-3}$) |
| $\Delta$ | This symbol indicates a change in a given physical quantity |
| $\Delta d_{np}$ | Interval of average diameter of nanoparticles (m) |
| $\Delta T$ | Temperature interval (°C) in Table 3 |
| $\eta$ | Intrinsic viscosity |
| $\mu$ | Dynamic viscosity (Pa·s) |
| $\mu_{max}$ | Maximum dynamic viscosity (Pa·s) |
| $\mu_{min}$ | Minimum dynamic viscosity (Pa·s) |
| $\mu_{nf}$ | Dynamic viscosity of the nanofluid (Pa·s) |
| $\mu_{bf}$ | Dynamic viscosity of the base fluid (Pa·s) |
| $\mu_{nf,calc}$ | Calculated dynamic viscosity of nanofluids (Pa·s) |
| $\mu_{nf,exp}$ | Experimental dynamic viscosity of nanofluids (Pa·s) |
| $\rho_{273K}$ | Density of the base fluid ($kg\ m^{-3}$) at 273 K |
| $\rho_{bf}$ | Density of the base fluid ($kg \cdot m^{-3}$) |
| $\rho_{c,bf}$ | Critical density of the base fluid ($kg \cdot m^{-3}$) in Eq. (16) |
| $\phi$ | Volume concentration |
| $\phi_{avg}$ | Average volumetric concentration (%) |
| $\phi_m$ | Maximum volume concentration, Eqs. (8)) and (10) |

### *References*


[1] C. Sus, "Enhancing thermal conductivity of fluids with nanoparticles, developments and applications of non-Newtonian flows," *ASME, FED, MD, 1995*, vol. 231, pp. 99–105, 1995.

[2] S. K. Das, S. U. Choi, W. Yu, and T. Pradeep, *Nanofluids: science and technology*. John Wiley & Sons, 2007.

[3] W. Yu and H. Xie, "A review on nanofluids: preparation, stability mechanisms, and applications," *J Nanomater*, vol. 2012, pp. 1-17, 2012.

[4] N. Sezer, M. A. Atieh, and M. Koç, "A comprehensive review on synthesis, stability, thermophysical properties, and characterization of nanofluids," *Powder Technol*, vol. 344, pp. 404-431, 2019.

[5] E. Bellos, C. Tzivanidis, and D. Tsimpoukis, "Enhancing the performance of parabolic trough collectors using nanofluids and turbulators," *Renewable and Sustainable Energy Reviews*, vol. 91, pp. 358-375, 2018.

[6] W. Duangthongsuk and S. Wongwises, "Measurement of temperature-dependent thermal conductivity and viscosity of TiO2-water nanofluids," *Exp Therm Fluid Sci*, vol. 33, no. 4, pp. 706-714, 2009.

[7] W. Ajeeb, R. R. S. T. da Silva, and S. M. S. Murshed, "Experimental investigation of heat transfer performance of Al2O3 nanofluids in a compact plate heat exchanger," *Appl Therm Eng*, vol. 218, p. 119321, 2023.

[8] A. H. Saeedi, M. Akbari, and D. Toghraie, "An experimental study on rheological behavior of a nanofluid containing oxide nanoparticle and proposing a new correlation," *Physica E Low Dimens Syst Nanostruct*, vol. 99, pp. 285-293, 2018.

[9] R. Byron Bird, Warren E. Stewart, and Edwin N. Lightfoot, *Transport Phenomena, Robert Byron Bird Wiley International edition*, John Wiley & Sons., vol. Volume 1. 2006.

[10] R. Du, D. Jiang, Y. Wang, and K. W. Shah, "An experimental investigation of CuO/water nanofluid heat transfer in geothermal heat exchanger," *Energy Build*, vol. 227, p. 110402, 2020.

[11] E. Y. Gürbüz, H. \. I. Variyenli, A. Sözen, A. Khanlari, and M. Ökten, "Experimental and numerical analysis on using CuO-Al2O3/water hybrid nanofluid in a U-type tubular heat exchanger," *Int J Numer Methods Heat Fluid Flow*, vol. 31, no. 1, pp. 519-540, 2021.

[12] O. A. Hussein, K. Habib, A. S. Muhsan, R. Saidur, O. A. Alawi, and T. K. Ibrahim, "Thermal performance enhancement of a flat plate solar collector using hybrid nanofluid," *Solar Energy*, vol. 204, pp. 208-222, 2020.

[13] A. D. Zadeh and D. Toghraie, "Experimental investigation for developing a new model for the dynamic viscosity of silver/ethylene glycol nanofluid at different temperatures and solid volume fractions," *J Therm Anal Calorim*, vol. 131, no. 2, pp. 1449-1461, 2018.

[14] M. J. Pastoriza-Gallego, L. Lugo, J. L. Legido, and M. M. Piñeiro, "Thermal conductivity and viscosity measurements of ethylene glycol-based Al 2 O 3 nanofluids," *Nanoscale Res Lett*, vol. 6, pp. 1-11, 2011.

[15] A. Mariano, M. J. Pastoriza-Gallego, L. Lugo, L. Mussari, and M. M. Piñeiro, "Co3O4 ethylene glycol-based nanofluids: thermal conductivity, viscosity and high pressure density," *Int J Heat Mass Transf*, vol. 85, pp. 54-60, 2015.

[16] L. Colla, "Experimental characterization of nanofluids as heat transfer media," 2014.

[17] S. Akilu, A. T. Baheta, K. Kadirgama, E. Padmanabhan, and K. V Sharma, "Viscosity, electrical and thermal conductivities of ethylene and propylene glycol-based β-SiC nanofluids," *J Mol Liq*, vol. 284, pp. 780–792, 2019.

[18] S. Akilu, A. T. Baheta, and K. V Sharma, "Experimental measurements of thermal conductivity and viscosity of ethylene glycol-based hybrid nanofluid with TiO2-CuO/C inclusions," *J Mol Liq*, vol. 246, pp. 396-405, 2017 https://doi.org/10.1016/j.molliq.2017.09.017

[19] H. Khosravi-Bizhaem, A. Abbassi, M. R. Salimpour, and A. Zivari-Ravan, "Experimental study on heat transfer, entropy generation, and exergy destruction of Ag, MWCNT, and GO water-based nanofluids in helical tubes," *J Therm Anal Calorim*, pp. 1-24, 2022.

[20] E. B. Elcioglu, A. G. Yazicioglu, A. Turgut, and A. S. Anagun, "Experimental study and Taguchi Analysis on alumina-water nanofluid viscosity," *Appl Therm Eng*, vol. 128, pp. 973-981, 2018.

[21] V. Nair, A. D. Parekh, and P. R. Tailor, "Experimental investigation of thermophysical properties of R718 based nanofluids at low temperatures," *Heat and Mass Transfer*, vol. 55, pp. 2769-2784, 2019.

[22] G. Coccia, G. Di Nicola, L. Colla, L. Fedele, and M. Scattolini, "Adoption of nanofluids in low-enthalpy parabolic trough solar collectors: Numerical simulation of the yearly yield," *Energy Convers Manag*, vol. 118, pp. 306-319, 2016.

[23] C. T. Nguyen *et al.*, "Temperature and particle-size dependent viscosity data for water-based nanofluids–hysteresis phenomenon," *Int J Heat Fluid Flow*, vol. 28, no. 6, pp. 1492-1506, 2007.

[24] A. S. Dalkilic *et al.*, "Prediction of graphite nanofluids' dynamic viscosity by means of artificial neural networks," *International Communications in Heat and Mass Transfer*, vol. 73, pp. 33-42, 2016.

[25] M. Zufar, P. Gunnasegaran, H. M. Kumar, and K. C. Ng, "Numerical and experimental investigations of hybrid nanofluids on pulsating heat pipe performance," *Int J Heat Mass Transf*, vol. 146, p. 118887, 2020.

[26] M. J. Pastoriza-Gallego, C. Casanova, J. L. al Legido, and M. M. Piñeiro, "CuO in water nanofluid: influence of particle size and polydispersity on volumetric behaviour and viscosity," *Fluid Phase Equilib*, vol. 300, no. 1-2, pp. 188-196, 2011.

[27] A. A. A. A. Alrashed, M. S. Gharibdousti, M. Goodarzi, L. R. de Oliveira, M. R. Safaei, and E. P. Bandarra Filho, "Effects on thermophysical properties of carbon based nanofluids: experimental data, modelling using regression, ANFIS and ANN," *Int J Heat Mass Transf*, vol. 125, pp. 920-932, 2018.

[28] G. Huminic, A. Huminic, C. Fleacă, F. Dumitrache, and I. Morjan, "Experimental study on viscosity of water based Fe–Si hybrid nanofluids," *J Mol Liq*, vol. 321, p. 114938, 2021.

[29] L. S. Sundar, M. K. Singh, and A. C. M. Sousa, "Turbulent heat transfer and friction factor of nanodiamond-nickel hybrid nanofluids flow in a tube: an experimental study," *Int J Heat Mass Transf*, vol. 117, pp. 223-234, 2018.

[30] G. J. Tertsinidou *et al.*, "New measurements of the apparent thermal conductivity of nanofluids and investigation of their heat transfer capabilities," *J Chem Eng Data*, vol. 62, no. 1, pp. 491-507, 2017.

[31] L. Fedele, L. Colla, and S. Bobbo, "Viscosity and thermal conductivity measurements of water-based nanofluids containing titanium oxide nanoparticles," *International journal of refrigeration*, vol. 35, no. 5, pp. 1359-1366, 2012.

[32] J. Zhu, D. Li, H. Chen, X. Yang, L. Lu, and X. Wang, "Highly dispersed CuO nanoparticles prepared by a novel quick-precipitation method," *Mater Lett*, vol. 58, no. 26, pp. 3324-3327, 2004.

[33] U. Westhaus, T. Dröge, and R. Sass, "DETHERM®—a thermophysical property database," *Fluid Phase Equilib*, vol. 158, pp. 429-435, 1999.

[34] P. T. Yurkevich A. Komarov D., "Influence of quantity and character of filling material on thermophysical properties of composite sorbent materials for a thermocompressor," *Russ J.Appl Chem*, 1995.

[35] J. Gmehling *et al.*, "Pure compound data from DDB," *Dortmund Data Bank*, vol. 2014, 1983.

[36] C. S. Cragoe, "Aroperties of Ethylene Glycol and Its Aqueous Solutions, Report of the Cooperative Fuel Research Committee of the Coordinating," 1943.

[37] Y. A. Çengel, R. H. Turner, J. M. Cimbala, and M. Kanoglu, *Fundamentals of thermal-fluid sciences*, vol. 703. McGraw-Hill New York, 2001.

[38] S. Akilu, A. T. Baheta, K. Kadirgama, E. Padmanabhan, and K. V Sharma, "Viscosity, electrical and thermal conductivities of ethylene and propylene glycol-based β-SiC nanofluids," *J Mol Liq*, vol. 284, pp. 780-792, 2019.

[39] P. Baraldi *et al.*, "Density and Volume Properties of Ethane-1, 2-diol+ 1, 2-Dimethoxyethane+ Water Ternary Mixtures from- 10° to 80°," *J Solution Chem*, vol. 29, pp. 489-504, 2000.

[40] T. Sun and A. S. Teja, "Density, viscosity and thermal conductivity of aqueous solutions of propylene glycol, dipropylene glycol, and tripropylene glycol between 290 K and 460 K," *J Chem Eng Data*, vol. 49, no. 5, pp. 1311-1317, 2004.

[41] A. H. ASHRAE, "Fundamentals, SI ed," *American Society of Heating, Refrigerating and Air-Conditioning Engineers, Atlanta, GA*, vol. 2017, 2017.

[42] A. Einstein, "Eine neue bestimmung der molekuldimensionen," *Ann. Phys.*, vol. 34, pp. 591-592, 1911.

[43] von H. Eilers, "Die viskosität von emulsionen hochviskoser stoffe als funktion der konzentration," *Kolloid-Zeitschrift*, vol. 97, no. 3, pp. 313-321, 1941.

[44] H. De Bruijn, "The viscosity of suspensions of spherical particles.(The fundamental η-c and relations)," *Recueil des Travaux Chimiques des Pays-Bas*, vol. 61, no. 12, pp. 863-874, 1942.

[45] V. Vand, "Theory of viscosity of concentrated suspensions," *Nature*, vol. 155, no. 3934, pp. 364-365, 1945.

[46] N. Saitô, "Concentration dependence of the viscosity of high polymer solutions. I," *J Physical Soc Japan*, vol. 5, no. 1, pp. 4-8, 1950.

[47] H. C. Brinkman, "The viscosity of concentrated suspensions and solutions," *J Chem Phys*, vol. 20, no. 4, p. 571, 1952.

[48] I. M. Krieger and T. J. Dougherty, "A mechanism for non-Newtonian flow in suspensions of rigid spheres," *Transactions of the Society of Rheology*, vol. 3, no. 1, pp. 137-152, 1959.

[49] D. G. Thomas, "Transport characteristics of suspension: VIII. A note on the viscosity of Newtonian suspensions of uniform spherical particles," *J Colloid Sci*, vol. 20, no. 3, pp. 267-277, 1965.

[50] L. E. Nielsen, "Generalized equation for the elastic moduli of composite materials," *J Appl Phys*, vol. 41, no. 11, pp. 4626-4627, 1970.

[51] T. S. Lundgren, "Slow flow through stationary random beds and suspensions of spheres," *J Fluid Mech*, vol. 51, no. 2, pp. 273-299, 1972.

[52] G. K. Batchelor, "The effect of Brownian motion on the bulk stress in a suspension of spherical particles," *J Fluid Mech*, vol. 83, no. 1, pp. 97-117, 1977.

[53] S. E. B. Mäga, C. T. Nguyen, N. Galanis, and G. Roy, "Heat transfer behaviours of nanofluids in a uniformly heated tube," *Superlattices Microstruct*, vol. 35, no. 3-6, pp. 543-557, 2004.

[54] S. Guo, Z. Luo, T. Wang, J. Zhao, and K. Cen, "Viscosity of monodisperse silica nanofluids," *Bulletin of the Chinese Ceramic Society*, vol. 25, no. 5, pp. 52–55, 2006.

[55] M. Corcione, "Empirical correlating equations for predicting the effective thermal conductivity and dynamic viscosity of nanofluids," *Energy Convers Manag*, vol. 52, no. 1, pp. 789–793, 2011.

[56] G. Coccia, S. Tomassetti, and G. Di Nicola, "Thermal conductivity of nanofluids: A review of the existing correlations and a scaled semi-empirical equation," *Renewable and Sustainable Energy Reviews*, vol. 151. Elsevier Ltd, Nov. 01, 2021 https://doi.org/10.1016/j.rser.2021.111573

[57] S. Andradóttir, "An overview of simulation optimization via random search," *Handbooks in operations research and management science*, vol. 13, pp. 617-631, 2006.

# Enhancement of Thermal Conductivity of Paraffin PCM with Metal Foams

**Eleonora Baccega[a,*], Laura Vallese[b,c], Michele Bottarelli[a]**

[a] University of Ferrara, Department of Architecture, Ferrara, Italy
[b] National Research Council (CNR), Construction Technologies Institute, Padova, Italy
[c] University of Padua (UNIPD), Department of Industrial Engineering, Padova, Italy

*Corresponding author: *eleonora.baccega@unife.it*

## Abstract

Paraffin PCMs (Phase Change Materials) are widely used for thermal energy storage due to their homogeneity and stability. However, one of their main drawbacks lies in their poor thermal conductivity, usually around 0.2 W/(m·K). In the context of the Horizon Europe project "ECHO" (Efficient Compact Modular Thermal Energy Storage System), the integration of metal foams within paraffin PCM was investigated in order to increase the overall thermal conductivity, thus speeding up the melting and solidification phases. Tests were carried out in a thermostatic bath using at first pure aluminium foam. Then, considering the consistent price these materials usually have, other commercial and much cheaper foams were also tested, namely a stainless-steel foam and a brass one. As expected, pure aluminium had the best performance among the three foams. However, the behaviour of the brass foam was quite close to that of pure aluminium, which means that interesting improvements can be achieved even with low-cost materials. As regards the stainless-steel foam, barely any improvement is observed.

### *1. Introduction*

Thermal energy storage is a fundamental technology for reducing the gap between energy supply and demand, integrating renewable energy sources and contributing to the reduction of greenhouse gases emissions [1]. Latent thermal energy storage (LTES) stores heat during the phase change at constant temperature of suitable materials, called PCMs and is characterized by higher energy density compared to the more traditional systems based on sensible heat [2]. PCMs can be classified depending on their phase transition or on their chemical nature, which includes organic, inorganic and eutectic materials [1]. Organic PCMs, such as paraffin, are particularly suitable for low temperature applications, thanks to their stability, high heat capacity and good cyclability [3].

Despite their advantages, PCMs are characterized by low thermal conductivity, which increases the time required for phase change [4]. Different techniques can be used for improving heat transfer. In particular, the most used thermal conductivity enhancers

include nanoparticles, expanded graphite and metallic foams. The most promising nanoparticles are made of graphene or silver, or consist of carbon nanotubes. Among the metallic foams that have been tested in literature, the most used are made of nickel, copper, graphite and aluminium. Besides additives, other methods for enhancing thermal conductivity include encapsulation of the PCM and application of fins [4], [5], [6]. The employment of multiple phase PCM and the modification of the geometry of the heat exchanger are other techniques used for general heat transfer enhancement [4], [6].

Focusing on macro-encapsulated PCMs, heat transfer can be improved both on the PCM side, with the aforementioned methods, or on the shell side. The shell can be enhanced through high thermal conductivity materials, optimization of the geometry and increase of the heat transfer area [7].

In this study, paraffin is macro-encapsulated in vials and the behaviour of the pure PCM is compared with the one enhanced with three different metal foams. The main advantages of metal foams are their high thermal conductivity, porosity, thermal penetration capability and large surface area. Moreover, their stability, low density and large aspect ratio make them a better choice compared to nanoparticles [4], [5].

Literature studies reported in Qureshi et al. highlighted that thermal conductivity of paraffin can be enhanced by 3 to 5.8 times using nickel foam and by 15 to 47.8 times with copper foam, with higher thermal conductivity values obtained decreasing the porosity of the material. The studies pointed out also that when the layers of PCM and foam are parallel to the heat flow, thermal conductivity achieves higher values [5].

Al-Yasiri et al. collected research on the thermal conductivity enhancement of paraffin, highlighting expanded graphite and metal foams as competitive options instead of nanoparticles, which are currently the most studied technique. Research on new materials for metal foams is required [8].

Baruah et al. developed a simulation model of macro-encapsulated paraffin wax, enhanced with aluminium metal foam. Results indicated that the metal foam absorbs a higher amount of heat thanks to conduction, and that higher melting rates are reached by lowering the porosity of the foam [9]. Xiao et al. measured the thermal conductivity of copper and nickel foams impregnated with pure paraffin, achieving values from 13 to 44 times higher than pure paraffin, increasing with reducing the porosity of the metal foam [10]. El idi et al. impregnated paraffin in nickel and aluminium foams, finding an increase

in thermal conductivity of 6 and nearly 18 times for nickel and aluminium respectively, compared to pure paraffin. Changes in the structure of the nickel foam were practically irrelevant for thermal conductivity [11]. Sabrina Ferfera et al. used the finite element method to evaluate heat transfer in a heat exchanger with a composite of paraffin and metal foam. Results showed that the effective thermal conductivity increased by 28 times when a copper foam was integrated, and by 8 times with a nickel foam [12]. Wang et al. found that paraffin melting time was from 11.5% to 18.1% faster when incorporating copper foam [13]. Xu et al. built a mathematical model to compare the thermal performance of pure paraffin and paraffin enhanced with aluminium, copper and carbon steel foams. They highlighted that the effect of natural convection is decreased when adding foam to the PCM, but the thermal storage time is much faster [14].

The research here reported was carried out within the Horizon Europe project "ECHO" (Efficient Compact Modular Thermal Energy Storage Systems) [15] whose aim is the development of a novel solution for heating, cooling and hot tap water production exploiting the thermal storage capacities of both PCMs and thermochemical materials (TCMs). The core of this novel system will be a TCM reactor, whose functioning is based on the cyclic hydration and dehydration of the material, thus activating exothermic and endothermic reactions, respectively. Eutectic PCMs will be used integrated within an ice storage tank for high cooling energy demand and organic PCMs will serve as additional thermal reservoir for the TCM, as it will be used to compensate the energy for humidification with its latent heat. For the latter objective, the celerity of the phase change of the PCM plays a key role. However, despite being stable and non-corrosive, organic PCMs are usually characterized by extremely low thermal conductivities, around 0.2 W/(m·K).

This has already attracted the attention of many researchers who have tried to find possible solutions to improve the PCM thermal conductivity. In general, the addition of highly conductive aggregates proved to be a feasible solution, and this was at the basis of the research hereafter reported. An organic PCM with melting temperature of 32°C was chosen, and three different types of metal foams were tested as aggregates to enhance the thermal conductivity of the PCM.

## 2. Methodology

### 2.1. Pure PCM tests

Organic A32 PCM supplied by PCM Products [16], partner of the project, was selected for the intended application. As stated by the supplier, the PCM had a density of 845 kg/m$^3$, a thermal conductivity of 0.21 W/(m·K), a specific heat of 2200 J/(kg·K) and a latent heat capacity of 120 kJ/kg.

At first, the pure PCM encapsulated in 50 ml vials (hereafter named falcons) was cycled in a thermostatic bath where different ramps were set with the aim of monitoring its dynamic behaviour and identifying the melting and solidification ranges. The falcons, made of polyethylene, had a cylindrical shape with an inner radius of 0.014 m, a height of about 0.08 m and a thickness of 0.0005 m. The temperature was monitored by means of a T-type thermocouple (accuracy: 0.5 K), positioned at the centre of the vial. From now on, data acquired through this thermocouple immersed in the PCM will be named *REF*. Given the peak melting temperature of about 32°C and a quite wide melting range reported in the DSC provided by the supplier, two ramps of different amplitude were set in the thermostatic bath with the aim of identifying the useful phase change range and verifying the feasibility of using this PCM in the intended application.

**Table 1.** Ramp settings.

| *Ramp 1* | | *Ramp 2* | |
|---|---|---|---|
| *Time frame [min]* | *Temperature [°C]* | *Time frame [min]* | *Temperature [°C]* |
| 180 | 22 | 180 | 27 |
| 30 | 22 → 42 | 15 | 27 → 37 |
| 300 | 42 | 300 | 37 |
| 30 | 42 → 22 | 15 | 37 → 27 |

A first ramp was set between 22°C and 42°C (-10 K/+10 K) and the second one between 27°C and 37°C (-5 K/+5 K), as reported in Table 1, and the obtained data were then compared.

### 2.2. Metal foams addition

After the preliminary experimental tests that confirmed the possibility of using this PCM, the activity focused on the improvement of its performance, with particular attention paid to the thermal conductivity.

Starting from the low thermal conductivity stated by the supplier of 0.21 W/(m·K), different aggregates within the PCM were tested with the aim of investigating whether and how much the thermal conductivity could be enhanced.

Three different metal foams were used as highly conductive aggregates, which are reported in Figure 1. The first one (a, *ALU*) is an aluminium metal foam (99.7% Al) purchased by RECEMAT BV [17] with a porosity stated by the supplier of 0.95. Since the consistent price of this material risks of making the application prohibitively expensive, for the other two aggregates it was decided to try to test materials that were already available on the market and, above all, very cheap. Commercial metal foams, commonly used for dishwashing, were purchased; one made of galvanised steel (b, *STEEL*) and the other made of brass (c, *BRASS*). Inevitably, since the materials were not specifically designed for such purposes, retrieving information about the exact composition was not possible.

Other three falcons of PCM were prepared, in which each of the above-mentioned metal foams were soaked. The falcons were filled with the same volume as the one with pure PCM (*REF*), and the quantity of material for each vial is reported in Table 2. As for REF, a T-type thermocouple was positioned at the centre of the vial and an additional one was positioned at 2 cm from the bottom to verify whether the phase change was uniform. Since no relevant difference was observed, only data acquired with the thermocouples located at the centre of the falcons will be reported.

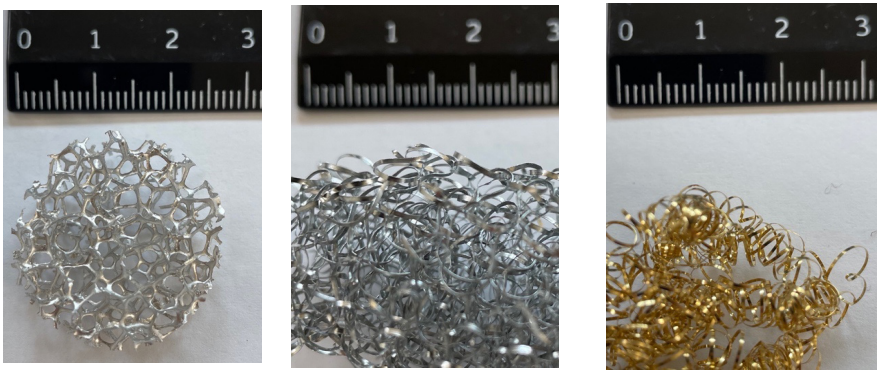


a b c

**Figure 1.** Metal foams immersed within the PCM: (a) aluminium foam (ALU), (b) galvanized steel foam (STEEL), (c) brass foam (BRASS).

**Table 2.** Quantity of material for each vial tested.

| Material | REF | ALU | STEEL | BRASS |
|---|---|---|---|---|
| A32 | 0.0389 g | 0.0378 g | 0.0377 g | 0.0377 g |
| metal foam | - | 0.0047 g | 0.0061 g | 0.0056 g |

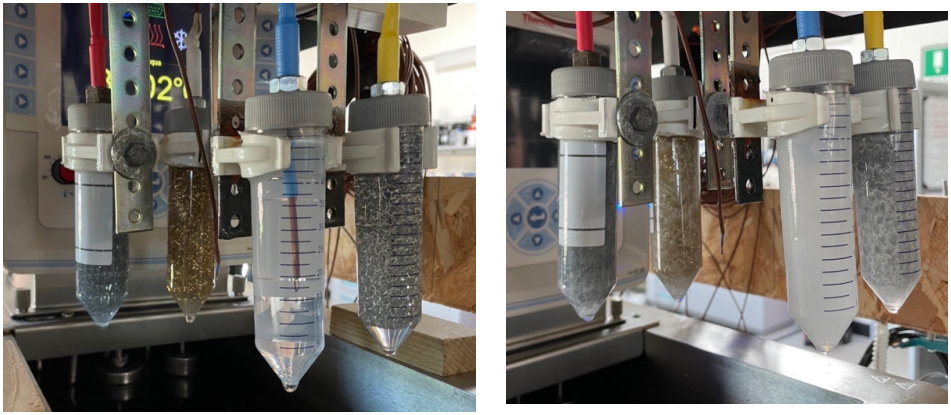

a b

**Figure 2.** Falcons during the test: (a) after a complete melting, (b) after a complete solidification. Blue sheath: pure A32 (REF), yellow sheath: A32 with aluminium foam (ALU), red sheath: A32 with galvanised steel foam (STEEL), white sheath: A32 with brass foam (BRASS).

The falcons were tested under multiple cycles in the thermostatic bath on which the above-described Ramp 2 was set and data acquired during the phase change were compared. In Figure 2 the falcons after a complete melting (a) and solidification (b) are depicted.

Based on the results obtained from the monitoring activity, an additional test was set, through which it was possible to analytically estimate the thermal conductivity of the PCM containing the metal foams.

To do so, the falcons were cooled in a refrigerator until they reached an equilibrium temperature of 15°C and were then immersed in the thermostatic bath that was set constant at 25°C. The temperature change at the centre of each vial was monitored until all of them reached the temperature of the bath. These experimental data were used to estimate the temperature at the centre of the vial, considered as if it were an infinite cylinder, through the following Eq. (1) [18]:

$$\theta_{0,\mathrm{cil}} = \frac{T_0 - T_\infty}{T_\mathrm{i} - T_\infty} = A_1 e^{-\lambda_1^2 \tau} \qquad (1)$$

where

| | |
|---|---|
| $\theta_{o,cil}$ | dimensionless temperature at the centre of the cylinder [-] |
| $T_o$ | temperature at the centre of the cylinder [°C] |
| $T_\infty$ | temperature of the fluid (water) [°C] |
| $T_i$ | initial temperature at the centre of the cylinder [°C] |

Both  and  are constants and are only functions of Biot number (Bi), that was calculated as in Eq. (2):

$$Bi = \frac{h \cdot r_0}{\lambda} \qquad (2)$$

where

| | |
|---|---|
| h | convective heat transfer coefficient [W/(m2·K)] |
| $r_o$ | radius of the cylinder [m] |
| λ | thermal conductivity [W/(m·K)] |

It should be noted that in a transient conduction problem, the characteristic length adopted in the definition of the Biot number for a long cylinder is the radius and not the volume-surface ratio.

Starting from the thermal conductivity of the pure PCM, which was assumed to be 0.21 W/(m·K) as stated by the supplier, the convective heat transfer coefficient was estimated by trial and error, and the value adopted was the one with which the best fitting between the experimental curve and the analytically calculated one was obtained. This value was then kept for the other falcons and the thermal conductivity of each of them was again estimated by trial and error, pursuing the best fitting.

Lastly, the Root Mean Square Error was calculated as in Eq. (3) to evaluate the reliability of the estimated thermal conductivities.

$$RMSE = \sqrt{\frac{\sum_{i=1}^{N} (y_i - \hat{y}_i)^2}{N}} \qquad (3)$$

where

$y_i$ actual measured value [K]

$y_{-i}$ predicted value [K]

N number of samples

## 3. Results and discussion

### 3.1. Pure PCM tests

Several cycles were carried out with the two ramps (Ramp 1, Ramp 2) in order to check the stability and repeatability of the phase change over time. Data monitored during Ramp 1 are reported in Figure 3, where the phase change is visible at around 31°C both during melting and solidification and the behaviour of the material is constant among the different cycles. Through visual inspections it was possible to confirm that at 22°C the PCM was completely in solid state and at 42°C it was completely in liquid state.

Other cycles were then carried out with Ramp 2, whose amplitude is halved compared to Ramp 1, with the main objective of investigating whether the PCM could completely melt and solidify at the temperatures set and whether there was any difference in terms of phase change with respect to Ramp 1. Data monitored during Ramp 2 are reported in Figure 4. Also in this case, the phase change is visible at around 31°C both in case of melting as well as during solidification. Moreover, as for the previous case, the behaviour of the material over time is constant,

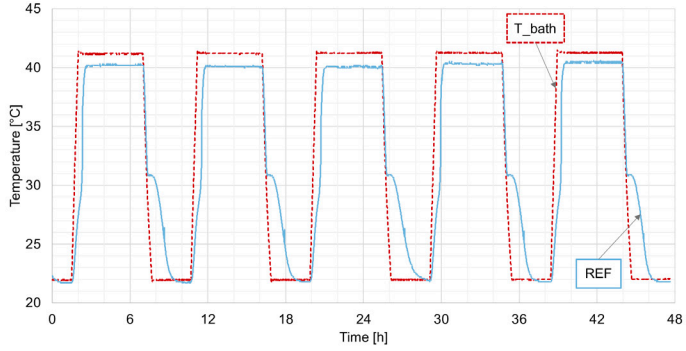


**Figure 3.** Experimental data acquired during Ramp 1.

which might mean that at the temperatures set the PCM could melt and solidify completely, which was confirmed by visual inspections carried out right before the beginning of the heating up and of the cooling down of water inside the thermostatic bath.

The phase changes occurred during the two ramps were compared and, as depicted in Figure 5, it can be observed that both melting and solidification are almost coincident, this confirming that it is sufficient to work with a temperature range of -5 K/+5 K with respect to the peak value in order to fully charge and discharge the PCM.

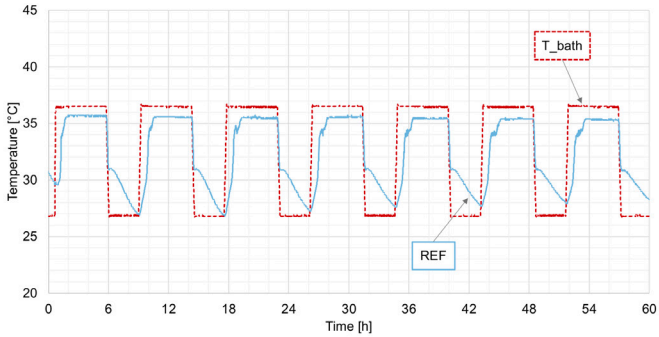


**Figure 4.** Experimental data acquired during Ramp 2.

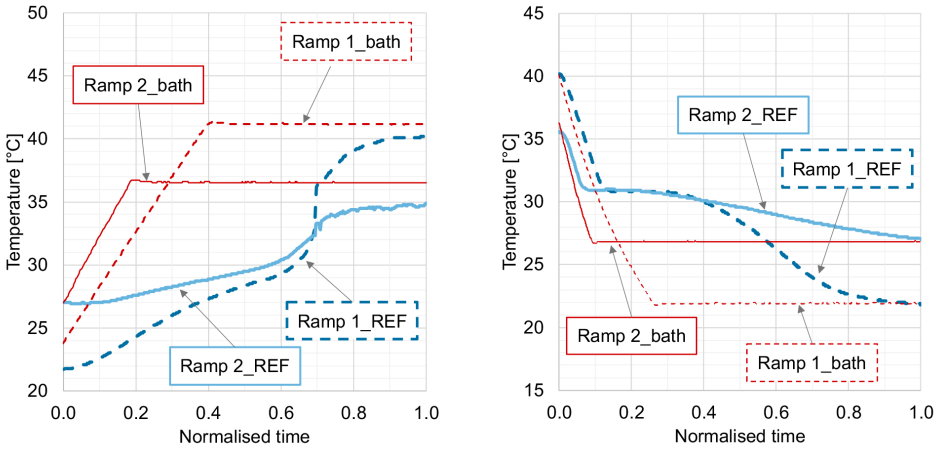


**Figure 5.** Comparison between (a) melting and (b) solidification occurring during Ramp 1 and Ramp 2.

### *3.2. Metal foams addition*

Once the falcons containing metal foams were prepared, the thermostatic bath was set with Ramp 2 and the material was cycled to investigate whether the contribution of the metal foams is visible. One complete cycle of the reference PCM and those containing metal foams is depicted in Figure 6. From the graph, the contribution of the aggregates is clearly visible. In fact, the phase change took the longest for *REF* both during melting as well as during solidification, while the one that lasted least was *ALU*, followed then by *BRASS* and, as last, by *STEEL*.

More in detail, the duration of the phase change in melting and in solidification of REF was compared to those for ALU, BRASS and STEEL and the comparison is depicted in Figure 7. As regards melting, assuming a duration of the heating phase from 27°C to 37°C for REF equal to 1, the behaviour of STEEL is quite similar to that of REF, with temperatures increasing faster but with little noticeable difference in the overall duration. As regards both BRASS and ALU the differences are more consistent, with overall shorter durations. As regards the solidification, differences are even greater: assuming a duration of the cooling phase from 37°C to 27°C for REF equal to 1, reductions of 20% for STEEL, 30% for BRASS and 40% for ALU are visible. In general, these considerations support the validity of using different metal foams to improve the thermal conductivity of PCM, but the most interesting aspect is that improvements can be obtained also with cheap commercial foams, with special regard to brass foam, whose behaviour is very close to that of aluminium.

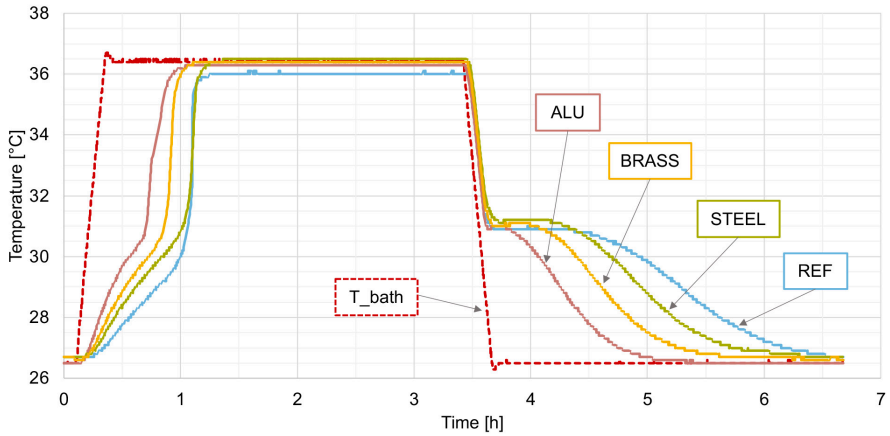


**Figure 6.** Complete melting and solidification of the pure PCM and of the PCM with metal foams.

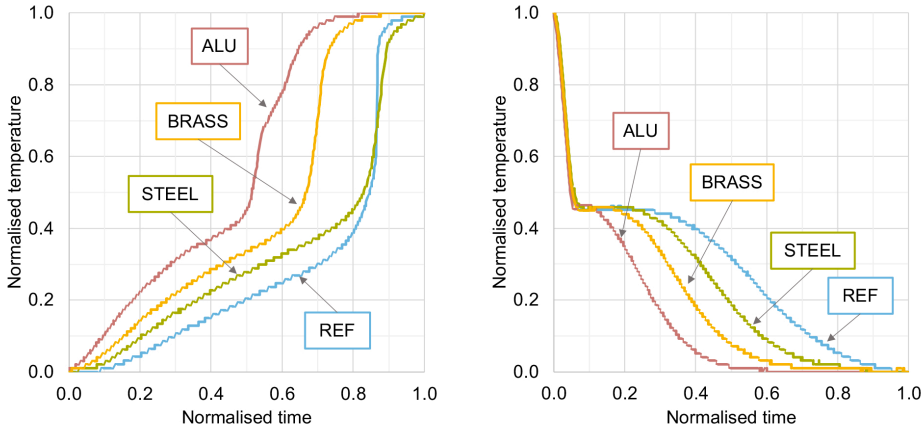


**Figure 7.** Comparison of the phase change duration during (a) melting and (b) solidification.

Based on these results, the above-mentioned additional test was carried out so that experimental data could be used to estimate the thermal conductivity of the PCM containing metal foams. As above described, the thermal conductivity of the pure PCM was assumed to be 0.21 W/(m·K) as stated by the supplier. The convective heat transfer coefficient was then estimated by trial and error and the value adopted, the one with which the best fitting between the experimental curve and the analytically calculated one was obtained, was of 40 W/(m$^2$·K). With this value the thermal conductivities of the PCM containing metal foams were again estimated by trial and error, pursuing the best fitting.

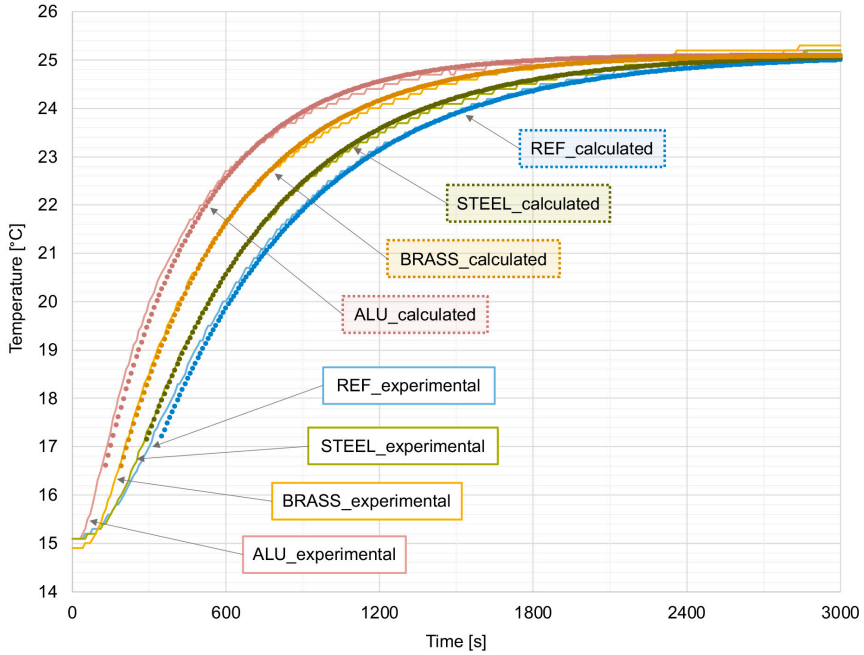


**Figure 8.** Comparison between experimental and theoretical curves.

The curves obtained are depicted in Figure 8 together with the experimental ones, while the differences over time between the two are better highlighted in Figure 9 and RMSE values are reported in Table 3. The low RMSE values, equivalent to 0.16 K for REF, 0.10 for ALU and STEEL and 0.14 for BRASS, show a good correspondence between the experimental and the theoretical values, thus supporting the reliability of the thermal conductivity values adopted, which are reported in Table 4.

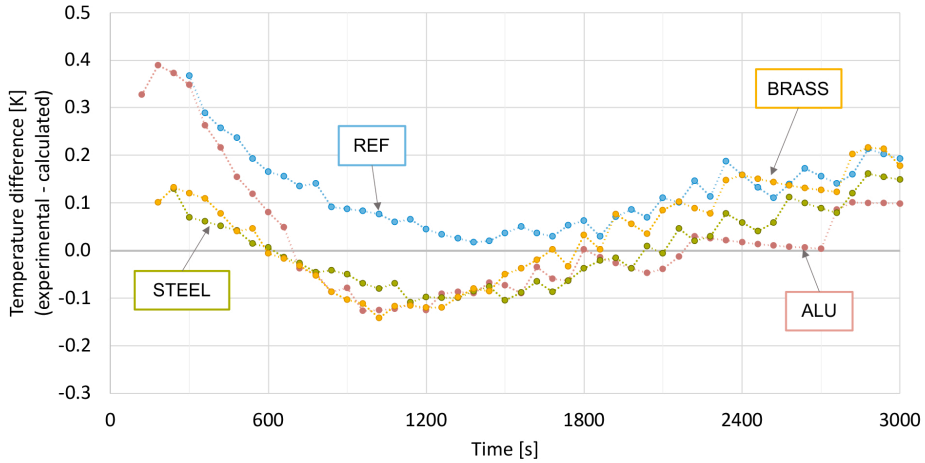


**Figure 9.** Differences between experimental and theoretical curves over time.

**Table 3.** RMSE values.

| | REF | ALU | STEEL | BRASS |
|---|---|---|---|---|
| RMSE [K] | 0.16 | 0.10 | 0.10 | 0.14 |

The addition of the galvanised steel foam (STEEL) brought an increase in the thermal conductivity from 0.21 W/(m·K) to 0.26 W/(m·K), which corresponded to an increase equivalent to 24%. The brass foam (BRASS) brought the thermal conductivity to 0.39 W/(m·K), correspondent to an increase of 86%, while with the aluminium one (ALU) the thermal conductivity increased up to 0.60 W/(m·K), with a consequent improvement of 186%. The greatest result, as predictable from the very beginning since it was the only one among the three aggregates that was a highly specific product made of almost pure material, was observed with the aluminium foam (ALU). It is worth reminding, however, that this material usually comes at a very high price. Based on the receipts of the material purchased, it was estimated that the amount of aluminium foam inside the falcon costs about 5 €, which corresponds to a price of about 128 €/kg of PCM. The second-best aggregate among those tested, namely the commercial brass foam (BRASS), brought to an almost doubled thermal conductivity with less than 0.40 € of material, with an equivalent price of less than 10€/kg of PCM. The estimated thermal conductivities

together with the indicative costs show an interesting potential of a common and cheap material such as the brass foam, opening up to future developments.

**Table 4.** Thermal conductivity estimated and relative improvement if comapred to REF.

| | REF | ALU | STEEL | BRASS |
|---|---|---|---|---|
| h [W/(m²·K)] | 40 | 40 | 40 | 40 |
| λ [W/(m·K)] | 0.21 | 0.60 | 0.26 | 0.39 |
| improvement | - | +186% | +24% | +86% |

### *4. Conclusions*

The research here reported focused on tests on paraffin PCM upgraded with three different metal foams, with the aim of increasing its low thermal conductivity. A pure aluminium foam specifically designed to increase the thermal conductivity of the material in which it is soaked was tested at the same time as other two cheap products, readily available on the market and usually employed for cleaning, one made of galvanised steel and the other one of brass. Results obtained from the experimental tests showed that in all the three configurations with metal foams the phase change occurred more rapidly than the reference case and the thermal conductivities were then estimated to be about 0.60 W/(m·K) for the aluminium foam, 0.26 W/(m·K) for the galvanised steel foam and 0.39 W/(m·K) for the brass one. The greatest improvement of the thermal conductivity of 186% with aluminium foam is accompanied, however, by a rather high price, estimated to be about 128 €/kg of PCM. On the other side the brass foam, despite showing a lower improvement of 86%, is much cheaper than the aluminium foam, with an estimated price of less than 10 €/kg of PCM. These results showed that interesting improvements can be achieved even with low-cost materials, opening up for further and deeper explorations.

### *Acknowledgments*

This work was financially supported within the ECHO project (Efficient Compact Modular Thermal Energy Storage System) funded by the European Union's Horizon Europe research and innovation programme under Grant Agreement No. 101096368.

### *References*

[1] H. Jouhara, A. Żabnieńska-Góra, N. Khordehgah, D. Ahmad, e T. Lipinski,

"Latent thermal energy storage technologies and applications: A review", Int. J. Thermofluids, vol. 5-6, p. 100039, ago. 2020 https://doi.org/10.1016/j.ijft.2020.100039

[2] I. Sarbu e C. Sebarchievici, "A Comprehensive Review of Thermal Energy Storage", Sustainability, vol. 10, fasc. 1, p. 191, gen. 2018 https://doi.org/10.3390/su10010191

[3] K. Pielichowska e K. Pielichowski, "Phase change materials for thermal energy storage", Prog. Mater. Sci., vol. 65, pp. 67-123, ago. 2014 https://doi.org/10.1016/j.pmatsci.2014.03.005

[4] B. K. Choure, T. Alam, e R. Kumar, "A review on heat transfer enhancement techniques for PCM based thermal energy storage system", J. Energy Storage, vol. 72, p. 108161, nov. 2023 https://doi.org/10.1016/j.est.2023.108161

[5] Z. A. Qureshi, H. M. Ali, e S. Khushnood, "Recent advances on thermal conductivity enhancement of phase change materials for energy storage system: A review", Int. J. Heat Mass Transf., vol. 127, pp. 838-856, dic. 2018 https://doi.org/10.1016/j.ijheatmasstransfer.2018.08.049

[6] A. NematpourKeshteli, M. Iasiello, G. Langella, e N. Bianco, "Enhancing PCMs thermal conductivity: A comparison among porous metal foams, nanoparticles and finned surfaces in triplex tube heat exchangers", Appl. Therm. Eng., vol. 212, p. 118623, lug. 2022 https://doi.org/10.1016/j.applthermaleng.2022.118623

[7] Z. Liu et al., "A review on macro-encapsulated phase change material for building envelope applications", Build. Environ., vol. 144, pp. 281-294, ott. 2018 https://doi.org/10.1016/j.buildenv.2018.08.030

[8] Q. Al-Yasiri e M. Szabó, "Paraffin As a Phase Change Material to Improve Building Performance: An Overview of Applications and Thermal Conductivity Enhancement Techniques", Renew. Energy Environ. Sustain., vol. 6, p. 38, 2021 https://doi.org/10.1051/rees/2021040

[9] J. S. Baruah, V. Athawale, P. Rath, e A. Bhattacharya, "Melting and energy storage characteristics of macro-encapsulated PCM-metal foam system", Int. J. Heat Mass Transf., vol. 182, p. 121993, gen. 2022 https://doi.org/10.1016/j.ijheatmasstransfer.2021.121993

[10] X. Xiao, P. Zhang, e M. Li, "Effective thermal conductivity of open-cell metal foams impregnated with pure paraffin for latent heat storage", Int. J. Therm. Sci., vol. 81, pp. 94-105, lug. 2014 https://doi.org/10.1016/j.ijthermalsci.2014.03.006

[11] M. M. El idi, M. Karkri, e M. Kraiem, "Preparation and effective thermal conductivity

of a Paraffin/ Metal Foam composite", J. Energy Storage, vol. 33, p. 102077, gen. 2021 https://doi.org/10.1016/j.est.2020.102077

[12] R. Sabrina Ferfera, B. Madani, e R. Serhane, "Investigation of heat transfer improvement at idealized microcellular scale for metal foam incorporated with paraffin", Int. J. Therm. Sci., vol. 156, p. 106444, ott. 2020 https://doi.org/10.1016/j.ijthermalsci.2020.106444

[13] Z. Wang et al., "Effect of enhancement in metal foam pore density on heat transfer of phase-change materials", Int. Commun. Heat Mass Transf., vol. 144, p. 106750, mag. 2023 https://doi.org/10.1016/j.icheatmasstransfer.2023.106750

[14] H. Xu, Y. Wang, e X. Han, "Analytical considerations of thermal storage and interface evolution of a PCM with/without porous media", Int. J. Numer. Methods Heat Fluid Flow, vol. 30, fasc. 1, pp. 373-400, gen. 2019 https://doi.org/10.1108/HFF-02-2019-0094

[15] https://echo-euproject.eu

[16] https://www.pcmproducts.net

[17] https://www.recemat.nl

[18] Y.A. Çengel, Termodinamica e trasmissione *del calore*, McGraw-Hill, 2009

# Experimental Compressed Liquid Density Measurements and Correlation of the Binary Mixture {n-pentane (R601) + trans-1-chloro-3,3,3-trifluoro-1-propene (R1233zd(E))}

**Davide Menegazzo[a,*], Giulia Lombardo[a,b], Laura Vallese[a,b], Sergio Bobbo[a]**

[a]*National Research Council (CNR), Construction Technologies Institute, Padova, Italy*
[b]*University of Padua (UNIPD), Department of Industrial Engineering, Padova, Italy*

**Corresponding author: menegazzo@itc.cnr.it*

## Abstract

In the context of evolving regulations such as the F-gas Regulation (EU) 2024/573 and the Kigali Amendment to the Montreal Protocol, combined to the impelling effort to mitigate climate change, the exploration of alternatives to fluorinated greenhouse gases in high temperature heat pump and power generation applications is driving the research in this field. Essential attributes sought in viable refrigerants encompass low Global Warming Potential (GWP), thermodynamic cycle efficiency, non-flammability, non-toxicity, material compatibility, and cost-effectiveness. Hydrochlorofluoroolefins (HCFOs) have emerged as promising candidates in this field, both as pure fluids and in mixtures. Recent research explored the feasibility of mixtures formed by low-pressure HCFOs and hydrocarbons (HCs) with promising results. The two classes of fluids have proven to be efficient for high temperature applications and their blend can result in non-flammable mixtures. Despite the potential of such mixtures, the lack of experimental data on their thermophysical properties is consistent.
This study presents the first experimental measurements on the {n-pentane (R601) + trans-1-chloro-3,3,3-trifluoro-1-propene (R1233zd(E))} binary system. In particular, the compressed liquid density of three mixture compositions have been measured employing a vibrating tube densimeter within the temperature range from 283.15 K to 423.15 K and at pressures ranging from 1 MPa to 12 MPa. A novel technique was applied to ensure a combined uncertainty (k=2) not greater than 0.0003 mol. fraction in the mixture composition, leading to final combined uncertainty (k=2) on the liquid density of no more than 0.15%.
Finally, a new mixture model based on the Helmholtz-energy-explicit Equation of State has been developed from such experimental data. This model accurately represents the behaviour of the binary mixture, enhancing the available understanding of its thermodynamic properties.

### *1. Introduction*

Decarbonizing energy-intensive industries is essential for attaining a carbon-neutral economy by mid-century. This transition primarily involves shifting from fossil fuel-driven processes to fully electrified solutions. Industrial high-temperature heat pumps (HTHPs) play a crucial role in this energy transition, enabling the electrification of relatively low-temperature process heat supply, such as 100-200 °C heat sink temperature. At the

same time, such heat sink temperature level may be suitable for the energy production through Organic Rankine Cycle (ORC), allowing to recover energy otherwise wasted. Comprehensive reviews about high temperature heat pumps have been carried out by Arpagaus et al. [1] and Adamson et al. [2]. Among the outcomes of such studies, the choice of the working fluid resulted to be pivotal. In the market, the most widespread working fluids for this application are hydrofluorocarbons (HFCs), such as R245fa, R245ca and R365mfc for heat sink temperatures up to 140°C, but also R134a for heat sink temperatures up to 100°C [1]. Recently, the international regulations, such as the F-gas Regulation (EU) 2024/573 [3] and the Kigali Amendment to the Kyoto Protocol [4], have been setting restrictions upon the use of high Global Warming Potential (GWP) refrigerants. Among these, HFCs are characterized by high GWP values and therefore need to be substituted. Hydrofluoroolefins (HFOs), hydrochlorofluoroolifins (HCFOs) and hydrocarbons (HCs) have been investigated as potential alternatives to HFCs. H(C)FOs are characterized by thermodynamic properties similar to the ones of HFCs and, thanks to the double carbon bond in their molecular structure, by low-GWP values. In particular, low-pressure HCFOs, such as R1224yd(Z), R1233zd(E) and R1336mzz(Z) have feasible thermodynamic properties for high temperature heat pumps and are also non-flammable. Lately, some doubts have been raised about the environmental impact of H(C)FOs, since their breakdown in the atmosphere can produce compounds like trifluoroacetic acid (TFA), hydrogen fluoride (HF), carbonyl fluoride ($COF_2$), and R23. However, the number of studies concerning this aspect is still limited, making it unclear whether their impact is significant, especially considering the quantities released into the environment [5, 6]. Furthermore, the European Commission is considering classifying HFOs and HCFOs as per- and polyfluoroalkyl substances (PFAS) due to the presence of perfluorinated methyl (-$CF_3$) or perfluorinated methylene (-$CF_2$-) groups in their structures. A decision is still pending due to the conflicting results of the few studies conducted on this issue, underscoring the need for further research [6, 7].

Among HCs, butane and isobutane are the most studied [8], but their applications are bounded by relatively low critical temperatures to supply temperatures up to 150°C. For higher supply temperatures, up to 180°C, n-pentane and isopentane have been investigated [9-10]. Other HCs, like n-hexane, isohexane and several cycling HCs have been evaluated as potential alternatives for supply temperatures up to 200°C as pure

fluids or in mixtures [10-11-12]. Spale et al. 2024 [10] carried out an explorative study on potential fluids for high temperature heat pumps focusing on supply temperatures up to 200°C. One of the outcomes of such screening was that mixing low-pressure HCFOs and HCs may lead to efficient and low-flammability solutions.

About this point, the present work is focused on the binary mixture of the HCFO trans-1-chloro-3,3,3-trifluoro-1-propene (R1233zd(E)) and the HC n-pentane (R601), which has been analyzed through the algorithm proposed by Albà et al. [13]. The calculated flammability index yields to non-flammable mixtures (class A1 [14]) for concentrations of n-pentane lower than 0.23, and mildly flammable mixtures (class A2L [14]) for concentrations of n-pentane lower than 0.47.

It is worth to notice that most of the studies concerning mixtures of HCFOs and HCs have been conducted through computer simulations of the thermodynamic cycles and the thermodynamic properties have been taken from Refprop 10.0 [15]. At the same time, the knowledge of the thermophysical properties of such mixtures is scarce, since a few experimental data are available in the literature [16].

In order to contribute to filling this gap of information, this work reports the first experimental measurements on the binary mixture of trans-1-chloro-3,3,3-trifluoro-1-propene (R1233zd(E)) and n-pentane (R601). In particular, the compressed liquid density of three different mixture compositions has been measured by means of a vibrating tube densimeter. The results have been compared to the mixing parameters available in Refprop 10.0 and a new mixture model has been developed based on the experimental data presented in this work.

## *2. Materials*

Two high purity samples have been employed in this study for R1233zd(E) and R601, supplied by Central Glass Co. Ltd. and Merck, respectively. Both the samples underwent several cycles of freezing-pumping-thawing to reduce the quantity of incondensable contaminants, employing liquid nitrogen for the freezing process. Then, both the samples have been analyzed on a Hewlett Packard 6890 gas-chromatograph (GC) to check the final purity. The GC employed a thermal conductivity detector (TCD) and a Porapak-Q column (2 m long, 1/8" diameter). After three 20 minutes runs for each sample, no impurities were detected. The sample details are reported in Table 1.

**Table 1.** Details of the measured samples (sample purity reported on mass basis).

| Substance | CAS Number | Supplier | Purity as supplied | Impurities detected after degassing |
|---|---|---|---|---|
| trans-1-chloro-3,3,3-trifluoro-1-propene (R1233zd(E)) | 102687-65-0 | Central Glass Co. Ltd. | 0.995 | No impurities detected |
| n-pentane (R601) | 109-66-0 | Merck | 0.998 | No impurities detected |

## *Experimental section*

### *2.1. Apparatus*

In this work, the experimental apparatus described by Lombardo et al. [17] was modified to allow the accurate measurement of mixtures. An Anton Paar DMA 4200M vibrating tube densimeter (VTD) is the core of the apparatus, shown in Fig. 1. Such instrument measured the oscillating period of a U-shaped tube filled with the liquid sample and converted the oscillation period in density values through a calibration function based on the measured temperature and pressure of the sample under test. The temperature was set by means of an integrated Peltier thermostat with a stability of ±0.003 K. A standard 100 Ω platinum resistance connected to a HP 3458 A multimeter was used to measure the temperature with a combined standard uncertainty (k=1) of 0.05 K. The pressure was measured by means of a Druck DPI 145 differential pressure gauge (PG), with a F.S. of 350 bar, together with an atmospheric barometer (BA), with a combined standard uncertainty (k=1) equal to 10 kPa. A syringe pump (SP) was employed to set the pressure within the circuit. The whole apparatus was monitored and controlled with a dedicated data acquisition and control system (DAC) developed in LabView. The DAC system implemented a PID control on the syringe pump with a control band of 20 kPa. The volume of the whole apparatus ranged from 15 ml to 260 ml, approximately, thanks to the syringe pump.

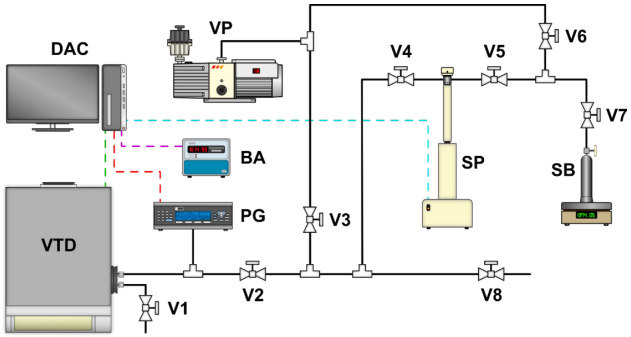


**Figure 1.** Schematic of the experimental apparatus.

### *2.2. Calibration*

The densimeter manufacturer declared an accuracy of ±0.2 kg·m$^{-3}$ for the density measurement at atmospheric pressure. In order to extend the validity range of the instrument, a calibration was performed employing water and R134a as reference fluids. The calibration was carried out along isotherms, so that the density was calculated as Eq. 1.

$$\rho = A \cdot (1 + AD_1 \cdot p + AD_2 \cdot p^2) \cdot \theta^2 - B \cdot (1 + BD_1 \cdot p + BD_2 \cdot p^2) + C \cdot \theta^4 \quad (1)$$

Where ρ is the calculated density, p is the measured pressure and θ is the measured oscillating period. A,B,C,$AD_{1,2}$,$BD_{1,2}$ are the coefficients object of calibration. As reference density values for water, the Equation of State (EoS) developed by Wagner and Pruss [18] was employed. The reported uncertainty of such EoS was equal to 0.001% in the density for pressures up to 10 MPa and temperatures up to 423 K, and generally less than 0.1% for higher temperatures and pressures. The EoS developed by Tillner-Roth and Baehr [19] was considered for R134a, with an uncertainty in the density calculation equal to 0.05%, except in the critical region. For this reason, R134a was considered in the calibration only for the temperatures below 353 K. The calibration process required also the measurement of the oscillating period under vacuum for each temperature. The calibration was carried out along eight isotherms from 283 K to 423 K, with steps of 20 K, and at pressure up to 35 MPa. For each temperature, a set of coefficients A,B,C,$AD_{1,2}$,$BD_{1,2}$

was fitted with deviations always below 0.1 kg·m$^{-3}$.

### *2.3. Procedure*

The apparatus was first evacuated for at least five hours (V1 and V8 closed, all the others were open, see Fig. 1). Then, in case of pure fluids such as for the calibration, the valves to the vacuum pump V3 and V6 were closed, and the sample was loaded directly into the apparatus through V7. Once the desired amount of sample was loaded, V5 was closed, and the measurements could start. The Peltier thermostat integrated in the densimeter set the temperature in the measuring section and the syringe pump controlled the pressure within the desired values. For each combination of measured temperature and pressure, at least three replicants have been recorded.

In case of mixtures, the loading procedure had to be modified to allow also an accurate calculation of the mixture composition. The loading procedure was the following:

1. After the evacuation process, close V4, along with V3 and V6.
2. Through V5 and V7, load the first component, n-pentane in this case, into the syringe pump cylinder, which was set to a small volume initially (around 40 ml). To facilitate the loading process, the sample bottle was heated up while the syringe pump was set to refill the cylinder.
3. Once the desired amount of sample was loaded, close V7 and heat up the tubing section up to V5 in order to have vapour in such section. Then, close V5, so that the loaded sample was isolated in the syringe pump.
4. At this point, the second sample bottle, R1233zd(E) in this case, can be connected to system. Evacuate the volume between V5 and the sample bottle through V6.
5. Repeat steps 2 and 3 for the second component, so that the mixture is isolated between V4 and V5 in syringe pump.
6. The blend is vigorously mixed by several cycles of moving the piston pump from the bottom (whole volume available) up to a high pressure (8 MPa in this case) for at least 30 minutes.
7. Finally, the syringe pump is set to keep the aforementioned high-pressure level and, consequently, V4 is opened to allow the sample in measuring cell. Opening V4 will cause a sudden pressure drop, but the pressure control through the syringe pump will restore the pressure level in a very short time limiting at minimum any eventual composition shift.
8. Once loaded, the experiment is carried out as for pure fluids.

Each sample bottle was weighted before and after the loading process on a scale with 0.01 g of accuracy. The ratio behind the described mixing process was to improve the

homogeneity of the blend by compressing the sample to a pressure in which it was certainly in the compressed liquid region and then, by flashing it to reach at least the two-phase region several times. Moreover, when loading the sample, a fixed volume of fluid (approximately 0.16 ml) was lost between V5, V6 and V7. Heating up this section while refilling the syringe pump before closing V5 (see step 3) allowed to have vapour in such section and, therefore, to have a smaller amount of mass affecting the uncertainty in the mixture composition. With the fluids involved in the present work, the amount of lost sample was lower than 5 mg, which was within the measurement uncertainty.

For the whole duration of the experiment on a single mixture, the syringe pump was set to keep a pressure of at least 0.5 MPa higher than the estimated bubble point pressure, in order to ensure that the sample was always in the compressed liquid region and to avoid any composition shifts.

In this work, three mixtures of n-pentane and R1233zd(E) have been studied and the details are reported in Table 2. It can be demonstrated that, in case of binary mixtures, the uncertainty in the mixture composition with the described loading system can be calculated as Eq. 2.

$$u(z_i) = \frac{u(m)}{m_{tot}} \sqrt{2 \cdot (1 + 2z_i^2)} \qquad (2)$$

Where $z_i$ and $u(z_i)$ are the concentration of the i-th component and its combined standard uncertainty (k=1); $m_{tot}$ is the overall sample mass loaded in the apparatus and u(m) is the uncertainty in the sample bottle weighting, which corresponds to the scale accuracy of 0.01 g.

It is worth highlighting that, once one sample was loaded, it was kept at 303 K and under pressure overnight. Thus, at the beginning of every day of measurements, one random point previously measured along the 303 K isotherm was checked before starting with the other measuring point scheduled for the same day. The deviations were no more than 0.04 $kg \cdot m^{-3}$ with respect to the measurements of the previous days, confirming the accuracy of the apparatus and that no composition shift occurred. Moreover, during the evacuation of the apparatus before and after loading each sample, the VTD oscillating period has been verified at 303 K and resulted in agreement with the calibration measurements every time.

**Table 2.** Mixture preparation details.

| $z_{R601}$ / mol. frac. | $z_{R1233zd(E)}$ / mol. frac. | Loaded sample mass / g | $u(z_{R601})$ / mol. frac.. |
|---|---|---|---|
| 0.2778 | 0.7222 | 74.86 | 0.0002 |
| 0.6308 | 0.3692 | 157.51 | 0.0001 |
| 0.8172 | 0.1828 | 66.47 | 0.0003 |

### *2.4. Uncertainty analysis*

A detailed analysis has been carried out on the experimental uncertainty, considering the influence of all the involved parameters in the final density uncertainty. The expanded uncertainty (k=2) in the density U(ρ) has been calculated as Eq. 3 for each measurement point.

$$U(\rho) = \sqrt{\left(\frac{\partial \rho}{\partial T} u(T)\right)^2_{p,z_1} + \left(\frac{\partial \rho}{\partial p} u(p)\right)^2_{T,z_1} + \left(\frac{\partial \rho}{\partial z1} u(z_1)\right)^2_{T,p} + \sigma^2(\rho) + u_0^2} \qquad (3)$$

Where ρ,T,p and $z_1$ are the measured density, temperature, pressure and concentration of the first component, respectively. u(α) denotes the combined standard uncertainty in the quantity α. σ(ρ) denotes the standard deviation in the density among the replicants of a single measurement point. $u_0$ represents the densimeter accuracy, which was fixed as equal to 0.2 kg·m$^{-3}$ considering the accuracy declared by the manufacturer and the calibration. $\left(\frac{\partial \rho}{\partial \alpha} u(\alpha)\right)_{\beta,\gamma}$ is the sensitivity factor of the density with respect to the quantity α and it has been calculated as in Eq. 4.

$$\left(\frac{\partial \rho}{\partial \alpha} u(\alpha)\right)_{\beta,\gamma} = \rho^{RP}(\alpha, \beta, \gamma) - \rho^{RP}(\alpha + u(\alpha), \beta, \gamma) \qquad (4)$$

Where α, β and γ are one among temperature, pressure and composition. The function $\rho^{RP}$ denotes the use of Refprop 10.0 [15] to calculate the density as function of temperature, pressure and composition. For this calculation, the default EoS implemented in the software was considered. Tab. 3 reports the uncertainty budget for this work in terms of average relative uncertainty along the measured isotherms. As it can be noticed, the uncertainty in the composition and the accuracy of the densimeter are the main contributors of the overall uncertainty in the density. However, also considering the maximum values, the density uncertainty did not exceed 0.05%.

**Table 3.** Average relative contributions to the overall uncertainty in the density.

| T / K | $\frac{\left(\frac{\partial \rho}{\partial T} u(T)\right)_{p,z}}{\rho}$ | $\frac{\left(\frac{\partial \rho}{\partial p} u(p)\right)_{T,z}}{\rho}$ | $\frac{\left(\frac{\partial \rho}{\partial z} u(z)\right)_{T,p}}{\rho}$ | $\frac{u_0}{\rho}$ | $\frac{\sigma(\rho)}{\rho}$ | $\frac{U(\rho)}{\rho}$ |
|---|---|---|---|---|---|---|
| 283.15 | 0.008% | 0.000% | 0.015% | 0.023% | 0.000% | 0.029% |
| 303.15 | 0.009% | 0.000% | 0.015% | 0.024% | 0.000% | 0.030% |
| 323.15 | 0.009% | 0.000% | 0.015% | 0.024% | 0.000% | 0.031% |
| 343.15 | 0.010% | 0.001% | 0.015% | 0.025% | 0.001% | 0.032% |
| 363.15 | 0.012% | 0.001% | 0.014% | 0.026% | 0.001% | 0.033% |
| 383.15 | 0.014% | 0.001% | 0.014% | 0.028% | 0.001% | 0.034% |
| 403.15 | 0.016% | 0.002% | 0.013% | 0.029% | 0.001% | 0.036% |
| 423.15 | 0.020% | 0.003% | 0.012% | 0.030% | 0.002% | 0.039% |

## *3. Results*

Table 4-6 and Fig. 2 report the experimental results obtained for the three mixture compositions of n-pentane/R1233zd(E) measured in this work, along with the corresponding uncertainties.

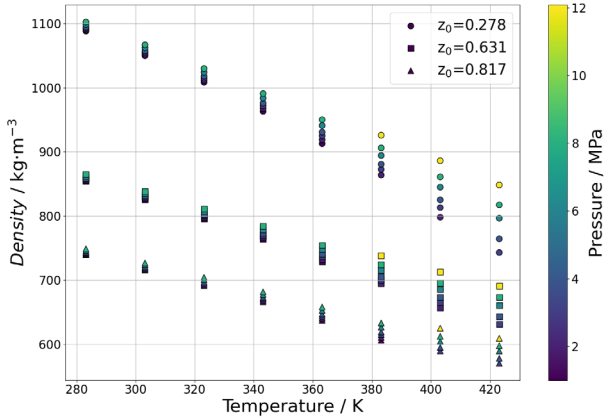


**Figure 2.** Experimental density data for the three mixture compositions of n-pentane/R1233zd(E) studied in this work. In the legend, $z_o$ refers to the molar concentration of n-pentane.

**Table 4.** Experimental density results for the mixture of n-pentane/R1233zd(E) (0.2778/0.7222 on molar basis).

| T / K | p / kPa | ρ / kg·m-3 | u(ρ) / % | T / K | p / kPa | ρ / kg·m-3 | u(ρ) / % |
|---|---|---|---|---|---|---|---|
| 283.15 | 1042.2 | 1088.50 | 0.02 | 363.15 | 1001.2 | 912.70 | 0.03 |
| 283.15 | 2021.4 | 1090.61 | 0.02 | 363.15 | 1966.0 | 918.82 | 0.03 |
| 283.15 | 3003.9 | 1092.68 | 0.02 | 363.15 | 3002.9 | 924.96 | 0.03 |
| 283.15 | 4003.2 | 1094.75 | 0.02 | 363.15 | 4014.1 | 930.58 | 0.03 |
| 283.15 | 5988.2 | 1098.75 | 0.02 | 363.15 | 6003.3 | 940.83 | 0.03 |
| 283.15 | 8017.6 | 1102.70 | 0.02 | 363.15 | 8043.9 | 950.17 | 0.03 |
| 303.15 | 1094.9 | 1049.89 | 0.02 | 383.15 | 2023.9 | 863.74 | 0.03 |
| 303.15 | 2065.4 | 1052.49 | 0.02 | 383.15 | 3039.5 | 872.51 | 0.03 |
| 303.15 | 3048.1 | 1055.05 | 0.02 | 383.15 | 4077.7 | 880.60 | 0.03 |
| 303.15 | 4030.7 | 1057.55 | 0.02 | 383.15 | 6058.8 | 894.23 | 0.03 |
| 303.15 | 5941.4 | 1062.25 | 0.02 | 383.15 | 8031.2 | 906.02 | 0.03 |
| 303.15 | 7885.1 | 1066.82 | 0.02 | 383.15 | 11891.2 | 925.73 | 0.03 |
| 323.15 | 1091.2 | 1008.47 | 0.03 | 403.15 | 2009.7 | 797.81 | 0.04 |
| 323.15 | 2020.6 | 1011.63 | 0.03 | 403.15 | 3021.5 | 812.93 | 0.04 |
| 323.15 | 2999.2 | 1014.86 | 0.03 | 403.15 | 4022.2 | 825.18 | 0.03 |
| 323.15 | 3997.9 | 1018.05 | 0.03 | 403.15 | 6008.8 | 844.88 | 0.03 |
| 323.15 | 5985.7 | 1024.11 | 0.03 | 403.15 | 8015.3 | 860.95 | 0.03 |
| 323.15 | 8019.5 | 1029.97 | 0.02 | 403.15 | 11950.3 | 886.07 | 0.03 |
| 343.15 | 1020.2 | 963.16 | 0.03 | 423.15 | 3121.5 | 742.82 | 0.05 |
| 343.15 | 2034.0 | 967.72 | 0.03 | 423.15 | 3998.1 | 764.16 | 0.04 |
| 343.15 | 3049.4 | 972.07 | 0.03 | 423.15 | 6058.9 | 796.25 | 0.04 |
| 343.15 | 4040.3 | 976.14 | 0.03 | 423.15 | 8022.0 | 817.15 | 0.03 |
| 343.15 | 6034.3 | 983.84 | 0.03 | 423.15 | 12081.7 | 848.35 | 0.03 |
| 343.15 | 8006.7 | 990.93 | 0.03 | | | | |

**Table 5.** Experimental density results for the mixture of n-pentane/R1233zd(E) (0.6308/0.3692 on molar basis).

| T / K | p / kPa | ρ / kg·m$^{-3}$ | u(ρ) / % | T / K | p / kPa | ρ / kg·m$^{-3}$ | u(ρ) / % |
|---|---|---|---|---|---|---|---|
| 283.15 | 1012.0 | 854.19 | 0.03 | 363.15 | 1091.4 | 728.37 | 0.03 |
| 283.15 | 2027.3 | 855.87 | 0.03 | 363.15 | 2084.4 | 732.71 | 0.03 |
| 283.15 | 3019.9 | 857.49 | 0.03 | 363.15 | 3073.9 | 736.79 | 0.03 |
| 283.15 | 3990.7 | 859.05 | 0.03 | 363.15 | 4062.6 | 740.64 | 0.03 |
| 283.15 | 5959.4 | 862.11 | 0.03 | 363.15 | 6038.4 | 747.79 | 0.03 |
| 283.15 | 7924.6 | 865.07 | 0.03 | 363.15 | 8007.2 | 754.25 | 0.03 |
| 303.15 | 1032.5 | 825.56 | 0.03 | 383.15 | 2071.4 | 694.63 | 0.03 |
| 303.15 | 2042.6 | 827.62 | 0.03 | 383.15 | 3041.6 | 700.28 | 0.03 |
| 303.15 | 3022.7 | 829.57 | 0.03 | 383.15 | 4028.1 | 705.58 | 0.03 |
| 303.15 | 4022.5 | 831.51 | 0.03 | 383.15 | 6093.2 | 715.61 | 0.03 |
| 303.15 | 6018.1 | 835.25 | 0.03 | 383.15 | 8046.4 | 723.85 | 0.03 |
| 303.15 | 7866.1 | 838.58 | 0.03 | 383.15 | 11987.7 | 738.12 | 0.03 |
| 323.15 | 1021.8 | 795.39 | 0.03 | 403.15 | 2073.0 | 656.45 | 0.04 |
| 323.15 | 2027.9 | 797.93 | 0.03 | 403.15 | 3068.4 | 665.12 | 0.04 |
| 323.15 | 3037.1 | 800.40 | 0.03 | 403.15 | 4062.2 | 672.60 | 0.03 |
| 323.15 | 4027.8 | 802.75 | 0.03 | 403.15 | 6046.6 | 685.18 | 0.03 |
| 323.15 | 6047.7 | 807.34 | 0.03 | 403.15 | 8029.5 | 695.59 | 0.03 |
| 323.15 | 7927.3 | 811.38 | 0.03 | 403.15 | 11984.1 | 712.43 | 0.03 |
| 343.15 | 1049.7 | 763.75 | 0.03 | 423.15 | 3042.3 | 630.74 | 0.04 |
| 343.15 | 2019.3 | 766.86 | 0.03 | 423.15 | 4017.8 | 642.82 | 0.04 |
| 343.15 | 3046.8 | 770.02 | 0.03 | 423.15 | 5980.2 | 660.19 | 0.04 |
| 343.15 | 4017.9 | 772.89 | 0.03 | 423.15 | 7939.8 | 672.80 | 0.03 |
| 343.15 | 5977.5 | 778.36 | 0.03 | 423.15 | 11859.6 | 691.03 | 0.03 |
| 343.15 | 8002.6 | 783.65 | 0.03 | | | | |

**Table 6.** Experimental density results for the mixture of n-pentane/R1233zd(E) (0.8172/0.1828 on molar basis).

| T / K | p / kPa | ρ / kg·m$^{-3}$ | u(ρ) / % | T / K | p / kPa | ρ / kg·m$^{-3}$ | u(ρ) / % |
|---|---|---|---|---|---|---|---|
| 283.15 | 1026.2 | 739.43 | 0.04 | 363.15 | 1085.4 | 637.05 | 0.04 |
| 283.15 | 2031.6 | 740.83 | 0.04 | 363.15 | 2042.6 | 640.33 | 0.04 |
| 283.15 | 3018.7 | 742.17 | 0.04 | 363.15 | 3012.6 | 643.49 | 0.04 |
| 283.15 | 4030.5 | 743.53 | 0.04 | 363.15 | 4040.9 | 646.68 | 0.04 |
| 283.15 | 6020.3 | 746.12 | 0.04 | 363.15 | 6006.8 | 652.34 | 0.04 |
| 283.15 | 7983.9 | 748.59 | 0.04 | 363.15 | 8005.5 | 657.63 | 0.04 |
| 303.15 | 1091.3 | 715.84 | 0.04 | 383.15 | 1084.6 | 605.87 | 0.04 |
| 303.15 | 2060.1 | 717.47 | 0.04 | 383.15 | 2040.6 | 610.44 | 0.04 |
| 303.15 | 3086.0 | 719.16 | 0.04 | 383.15 | 3015.8 | 614.73 | 0.04 |
| 303.15 | 4059.6 | 720.72 | 0.04 | 383.15 | 4004.6 | 618.79 | 0.04 |
| 303.15 | 6021.2 | 723.78 | 0.04 | 383.15 | 6008.4 | 626.22 | 0.04 |
| 303.15 | 7878.5 | 726.55 | 0.04 | 383.15 | 8029.6 | 632.89 | 0.04 |
| 323.15 | 1085.6 | 691.15 | 0.04 | 403.15 | 3000.1 | 589.34 | 0.04 |
| 323.15 | 2063.7 | 693.15 | 0.04 | 403.15 | 4010.3 | 594.83 | 0.04 |
| 323.15 | 3041.0 | 695.09 | 0.04 | 403.15 | 6005.5 | 604.10 | 0.04 |
| 323.15 | 4018.6 | 696.98 | 0.04 | 403.15 | 8019.3 | 611.97 | 0.04 |
| 323.15 | 5982.9 | 700.62 | 0.04 | 403.15 | 12030.7 | 624.71 | 0.04 |
| 323.15 | 8024.2 | 704.21 | 0.04 | 423.15 | 3004.3 | 570.00 | 0.05 |
| 343.15 | 1065.4 | 665.64 | 0.04 | 423.15 | 4024.5 | 577.74 | 0.04 |
| 343.15 | 2030.7 | 668.07 | 0.04 | 423.15 | 6075.7 | 589.24 | 0.04 |
| 343.15 | 3001.8 | 670.42 | 0.04 | 423.15 | 8086.1 | 597.48 | 0.04 |
| 343.15 | 4019.7 | 672.80 | 0.04 | 423.15 | 12021.9 | 608.94 | 0.04 |
| 343.15 | 5986.4 | 677.16 | 0.04 | | | | |
| 343.15 | 8057.7 | 681.47 | 0.04 | | | | |

### *4. Discussion and data correlation*

The experimental data measured in this work have been used to fit a new mixture model for n-pentane/R1233zd(E) systems. Such model was based on the Helmholtz-energy-explicit equation of state (EoS), whose detailed description can be found in several literature sources [20-21-22-23] and which is implemented in the Refprop 10.0 [15] software. For pure fluids, the model requires an empirical formulation of the Helmholtz energy as a

function of temperature and density. In case of mixtures, an explicit formulation of the Helmholtz energy is necessary for each pure fluid composing the blend, along with mixing rules to calculate the thermodynamic properties of the mixture through differentiation. It is usual to describe such model in terms of the reduced temperature τ and density δ, and to consider the reduced Helmholtz energy α(τ,δ), as shown in Eq. 5-8.

$$\alpha(\tau,\delta,\bar{z}) = \frac{a(T,\rho,\bar{z})}{RT} = \alpha^{ig} + \alpha^{r}_{cs} + \alpha^{r}_{dep} \tag{5}$$

Where a,T and ρ represent the Helmholtz energy, the temperature and the density, respectively; R is the universal gas constant; $\bar{z}$ is the vector consisting of the molar concentrations of each pure component in the mixture. The reduced Helmholtz energy is calculated as the sum of the ideal gas contribution, $\alpha^{ig}$, the corresponding states contribution (see Eq. 6), $\alpha^{r}_{cs}$, and the departure functions, $\alpha^{r}_{dep}$

$$\alpha^{r}_{cs} = \sum_{i=0}^{N_{components}} z_i \alpha^{r}_{0,i}(\tau,\delta) \tag{6}$$

$$\delta = {}^{\rho}/_{\rho_{r(\bar{z})}} \tag{7}$$

$$\tau = {}^{T_{r(z)}}/_{T} \tag{8}$$

where the subscripts r refers to the reducing parameters for temperature and density; $\alpha^{r}_{0,i}$ represents the reduced Helmholtz energy of the pure i-th component. Considering the mixing rule by Kunz and Wagner [21], the reducing parameters are calculated as in Eq. 9-1

$$T_{r,ij} = \beta_{T,ij}\gamma_{T,ij}\frac{z_i + z_j}{\beta^2_{T,ij} z_i + z_j}(T_{c,i}T_{c,j})^{1/2} \tag{9}$$

$$\frac{1}{\rho_{r,ij}} = \beta_{v,ij}\gamma_{v,ij}\frac{z_i + z_j}{\beta^2_{v,ij} z_i + z_j}\frac{1}{8}\left(\frac{1}{\rho_{c,i}{}^{1/3}} + \frac{1}{\rho_{c,j}{}^{1/3}}\right)^3 \tag{10}$$

Where the subscripts i and j refer to the i-th and j-th component of the mixture; the subscript c refers to the critical temperature or density. $\beta_T$, $\gamma_T$, $\beta_v$ and $\gamma_v$ are the four binary interaction parameters (BIPs), which should be fitted on experimental data. Although no experimental data is available in the literature, Bell and Lemmon [22] proposed a

correlation based on the molecular weight of the single pure components to estimate the binary interaction parameters. Finally, the departure function is given by Eq. 11.

$$\alpha_{dep}^{r} = \sum_{i=0}^{N_{components}} \sum_{j=i+1}^{N_{components}} z_i z_j F_{ij} \alpha_{ij}^{r}(\tau, \delta) \qquad (11)$$

Where the departure term $\alpha_{ij}^{r}$ is an arbitrary function of τ and δ. The departure function contribution is usually employed for mixtures particularly difficult to model and/or in case of a great amount of reliable data, otherwise this contribution is neglected by setting $F_{ij}$ equal to zero. This was the case of n-pentane/R1233zd(E), for which Refprop 10.0 [15] adopted the EoS by Thol et al. [24] and Mondejar et al. [25] for n-pentane and R1233zd(E), respectively, while the BIPs were estimated, and no departure function was applied. Recently, Akasaka and Lemmon [26] developed an up do date EoS for R1233zd(E), which was employed in this work in place of the EoS by Mondejàr et al. [25], also when referring to the Refprop 10.0 default model.

Fig. 3 shows the deviations of the default mixture model implemented in Refprop 10.0 [15] with respect to the experimental data measured in this work.

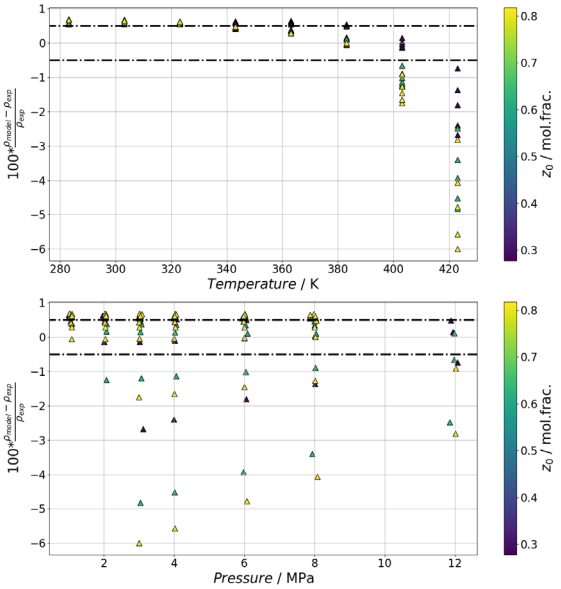


**Figure 3.** Comparison between the default Refprop 10.0 model and the experimental data measured in this work. The dashed lines refer to deviations of ±0.5%.

Remarkably, despite the BIPs were not fitted on experimental data, the absolute average deviation on the density calculation was within 0.5% for all the measured temperatures up to 383.15 K. At the same time, the absolute average deviation rapidly increased at 403.15 K and 423.15 K. Considering such results, a new model has been developed fitting the four BIPs and the departure function of Eq. 12 on the experimental data presented in this work.

$$\alpha_{ij}^{r}(\tau, \delta) = \sum_{k=1}^{2} n_k \tau^{t_k} \delta^{k} e^{-\delta^{k-1}} \qquad (12)$$

The model regression has been treated as optimization problem employing an Adaptive Search Development Particle Swarm Optimization (ASD-PSO) algorithm [27]. The employed objective function is given in Eqs . 13-14.

$$f = \sqrt{\sum_i \left( res_i \cdot \frac{T_i}{423.15} \right)^2} \qquad (13)$$

$$res = \frac{\rho_{exp} - \rho_{calc}(T,\ p,\ z)}{\rho_{exp}} \approx \frac{p_{calc}(T, \rho, z) - p_{exp}}{\rho_{exp}} \left( \frac{\partial \rho}{\partial p(T_{exp}, \rho_{exp})} \right)_T \qquad (14)$$

Where the subscripts exp and calc refer to the measured and the calculated quantities, respectively. The density deviations (Eq. 14) were calculated as in the work by Bell [23]. It is worth noting that the density deviations were multiplied by a factor $\frac{T_i}{423.15}$ in order to give priority to the high temperature data, which were more difficult to fit, and which were more interesting in the application perspective. The fitting has been carried out with dedicated codes developed in Python, employing the teqp package [23] to implement the thermodynamic model of the mixture.

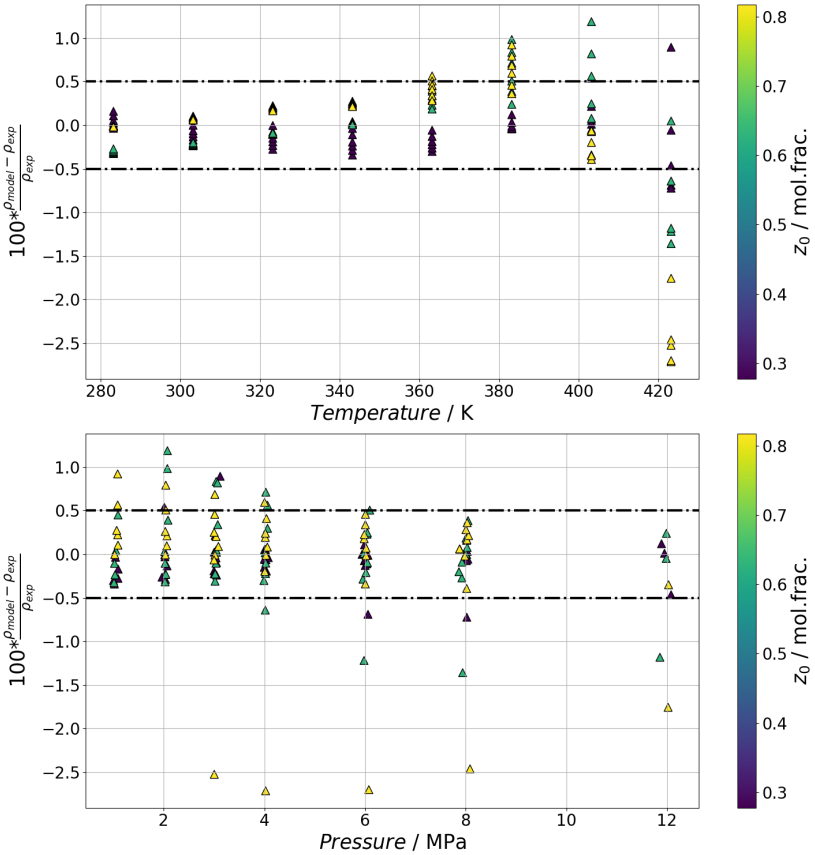


**Figure 4.** Comparison between the new mixture model developed in this work and the experimental data measured in this work.

Tab. 7 reports the Refprop 10.0 [15] default BIPs and the BIPs fitted in this work, while Tab. 8 reports the fitted parameters for the departure function. Tab. 9 compares the average density deviations obtained for the two models distinguishing for each measured temperature. As it can be noticed, the model fitted in this work reduced the deviations for all the isotherms, except for the one at 383.15 K. Overall, the relative average density deviation calculated for the default Refprop 10.0 [15] model was equal to 0.85%, while the same value was equal to 0.34% for the model fitted in this work.

**Table 7.** Comparison between the Refprop 10.0 default binary interaction parameters and the ones fitted in this work.

| | **Refprop 10.0** | **This work** |
|---|---|---|
| $\beta_T$ | 1.0 | 0.900470 |
| $\gamma_T$ | 0.9748008 | 0.949255 |
| $\beta_v$ | 1.0 | 0.945850 |
| $\gamma_v$ | 1.001555 | 0.983045 |

**Table 8.** Departure function parameters fitted in this work.

| $n_1$ | $n_2$ | $t_1$ | $t_2$ |
|---|---|---|---|
| -0.236062 | -2.300545 | 0.001657 | 1.646551 |

**Table 9.** Comparison between Refprop 10.0 and the model developed in this work in terms of average relative deviations for each measured isotherm.

| **T / K** | **283.15** | **303.15** | **323.15** | **343.15** |
|---|---|---|---|---|
| Refprop 10.0 / % | 0.602 | 0.600 | 0.589 | 0.500 |
| This work / % | 0.126 | 0.122 | 0.135 | 0.153 |
| **T / K** | **363.15** | **383.15** | **403.15** | **423.15** |
| Refprop 10.0 / % | 0.410 | 0.210 | 0.828 | 3.464 |
| This work / % | 0.311 | 0.431 | 0.318 | 1.308 |

## *5. Conclusions*

This work reports the first experimental measurements on the binary system n-pentane/ R1233zd(E). In particular, the compressed liquid density of three mixture compositions have been measured in the temperature range from 283.15 K to 423.15 K and for pressures up to 12 MPa. A vibrating tube densimeter was used for the measurements and a new charging technique has been applied, resulting in an uncertainty of no more than 0.0003 mol×mol$^{-1}$ in the mixture composition. The experimental data have been compared to

the thermodynamic model implemented in Refprop 10.0 software, but considering the up to date EoS for R1233zd(E) developed by Akasaka and Lemmon. Remarkably, the average density deviations were within 0.5% for the measured temperatures up to 383.15 K, while they increase rapidly at the higher temperatures. Overall, the average density deviation was equal to 0.85% with the Refprop 10.0 default model.

Considering this, a new mixture model has been developed based on the Helmholtz-energy-explicit formulation. The binary interaction parameters and a departure function with two exponential terms have been fitted on the experimental data presented in this work. The average density deviation of such model was equal to 0.34%.


### *Acknolowedgements*

The corresponding author (D.M.) has been financially supported by the European Union - NextGenerationEU and by the Ministry of University and Research (MUR), National Recovery and Resilience Plan (NRRP), Mission 4, Component 2, Investment 1.5, project "RAISE - Robotics and AI for Socio-economic Empowerment" (ECS00000035).


### *References*


[1] Arpagaus, C., Bless, F., Uhlmann, M., Schiffmann, J. and Bertsch, S. S. (2018), 'High temperature heat pumps: Market overview, state of the art, research status, refrigerants, and application potentials', *Energy* 152, 985--1010.

[2] Adamson, K.-M., Walmsley, T. G., Carson, J. K., Chen, Q., Schlosser, F., Kong, L. and Cleland, D. J. (2022), 'High-temperature and transcritical heat pump cycles and advancements: A review', *Renewable and Sustainable Energy Reviews* 167, 112798.

[3] 'European Commission. Regulation (EU) No 517/2014 of the European Parliament and of the Council of 16 April 2014 on fluorinated greenhouse gases and repealing Regulation (EC) No 842/2006 Text with EEA relevance'. 2014.

[4] 'United Nations Environment Programme. The Kigali Amendment to the Montreal Protocol: HFC Phase-down'. 2016.

[5] Fedele, L., Castelli, S. T., Ielpo, P., Zilio, C. and Bobbo, S. (2023), 'The environmental impact of HFOs from TEWI to PFAS. A review'. Proceedings of the International Congress of Refrigeration. Paris (France) 2023.

[6] Singh, R.R. and Papanastasiou, D.K. (2021). Comment on "Scientific Basis for Managing PFAS as a Chemical Class". Environmental Science & Technology Letters 2021 8 (2), 192-194 https://doi.org/10.1021/acs.estlett.0c00765

[7] European Commission. 'Science for Environment Policy. European Commission DG Environment News Alert Service. Science Communication Unit. The University of the West of England, Bristol'. 2023.

[8] Bamigbetan, O., Eikevik, T., Nekså, P., Bantle, M. and Schlemminger, C. (2019), 'The development of a hydrocarbon high temperature heat pump for waste heat recovery', *Energy* 173, 1141-1153.

[9] Mateu-Royo, C., Navarro-Esbrì, J., Mota-Babiloni, A., Amat-Albuixech, M. and Molés, F. (2018), 'Theoretical evaluation of different high-temperature heat pump configurations for low-grade waste heat recovery', *International Journal of Refrigeration*. 2018.

[10] Spale, J., Hoess, A., Bell, I. and Ziviani, D. (2024), 'Exploratory Study on Low-GWP Working Fluid Mixtures for Industrial High Temperature Heat Pump with 200 °C Supply Temperature', *(Under submission)*. 2024.

[11] Abedini, H., Vieren, E., Demeester, T., Beyne, W., Lecompte, S., Quoilin, S. and Arteconi, A. (2023), 'A comprehensive analysis of binary mixtures as working fluid in high temperature heat pumps', *Energy Conversion and Management* 277, 116652.

[12] Abedini, H., Tomassetti, S., Di Nicola, G., Quoilin, S. and Arteconi, A. (2023), 'Zeotropic mixtures R1234ze(Z)/acetone and R1234ze(Z)/isohexane as refrigerants in high temperature heat pumps: Influence of the accuracy in thermodynamic properties evaluations', *International Journal of Refrigeration* 152, 93-109.

[13] Albà, G.C., Alkhatib, I.I.I., Vega, L.F., and Llovell, F. (2024). Mapping the Flammability Space of Sustainable Refrigerant Mixtures through an Artificial Neural Network Based on Molecular Descriptors. *ACS Sustainable Chemistry and Engineering.*

[14] ANSI/ASHRAE 34-2019; Designation and Safety Classification of Refrigerants. ASHRAE: Peachtree Corners, GA, USA, 2019.

[15] Lemmon, E. W., Bell, I. H., Huber, M. L. and McLinden, M. O. (2018), 'NIST Standard Reference Database 23: Reference Fluid Thermodynamic and Transport Properties-REFPROP, Version 10.0, National Institute of Standards and Technology'

[16] Bell, I. H., Riccardi, D., Bazyleva, A. and McLinden, M. O. (2021), 'Survey of Data and Models for Refrigerant Mixtures Containing Halogenated Olefins', *Journal of Chemical & Engineering Data* 66(6), 2335-2354

[17] Lombardo, G., Menegazzo, D., Fedele, L., Bobbo, S. and Scattolini, M. (2023), Experimental assessment and correlation of the liquid density and and saturation pressure of trans and 2-Dichloroethene (R1130(E)). Proceedings of the International Congress on Refrigeration. Paris (France)' 2023.

[18] Wagner, W. and Prußs, A. (2002), 'The IAPWS Formulation 1995 for the Thermodynamic Properties of Ordinary Water Substance for General and Scientific Use', *Journal of Physical and Chemical Reference Data* 31(2), 387-535.

[19] Tillner-Roth, R. and Baehr, H. D. (1994), 'An International Standard Formulation for the Thermodynamic Properties of 1,1,1,2-Tetrafluoroethane (HFC-134a) for Temperatures from 170 K to 455 K and Pressures up to 70 MPa', *Journal of Physical and Chemical Reference Data* 23(5), 657-729.

[20] Span, R. (2013). '*Multiparameter Equations of State: an accurate source of thermodynamic property data*'.

[21] Kunz, O. and Wagner, W. (2012), 'The GERG-2008 Wide-Range Equation of State for Natural Gases and Other Mixtures: An Expansion of GERG-2004', *Journal of Chemical & Engineering Data* 57(11), 3032--3091.

[22] Bell, I. H. and Lemmon, E. W. (2016), 'Automatic Fitting of Binary Interaction Parameters for Multi-fluid Helmholtz-Energy-Explicit Mixture Models', *Journal of Chemical & Engineering Data* 61(11), 3752-3760.

[23] Bell, I. H., Deiters, U. K. and Leal, A. M. M. (2022), 'Implementing an Equation of State without Derivatives: teqp', *Industrial & Engineering Chemistry Research* 61(17), 6010-6027

[24] Thol, M., Uhde, T., Richter, M., Span, R. and Lemmon, E. ((to be submitted)), 'Thermodynamic Properties for Hydrocarbons. I. Fundamental Equation of State for n-pentane', *Journal of Physical and Chemical Reference Data (under submission)*.

[25] Mondejàr, M., McLinden, M. and Lemmon, E. (2015), 'Thermodynamic Properties of trans-1-Chloro-3,3,3-trifluoropropene (R1233zd(E)): Vapor Pressure, (p, ρ, T) Behavior, and Speed of Sound Measurements, and Equation of State', *Journal of Chemical and Engineering Data*.

[26] Akasaka, R. and Lemmon, E. W. (2022), 'An International Standard Formulation for trans-1-Chloro-3,3,3-trifluoroprop-1-ene [R1233zd(E)] Covering Temperatures from the Triple-Point Temperature to 450 K and Pressures up to 100 MPa', *Journal of Physical and Chemical Reference Data* 51(2), 023101.

[27] Ardizzon, G., Cavazzini, G. and Pavesi, G. (2015), 'Adaptive acceleration coefficients for a new search diversification strategy in particle swarm optimization algorithms', *Information Sciences* 299, 337-378.

# Exploring Low-Gwp Alternatives for Heat Pumps: a Drop-In Comparative Study of R1234yf/r600a and R134a

**Giulia Lombardo[a,b,*], Davide Menegazzo[a,b], Laura Vallese[a,b], Michele De Carli[b], Fabio Poletto[c], Sergio Bobbo[a]**

*a National Research Council (CNR), Construction Technologies Institute, Padova, Italy*
*b University of Padua (UNIPD), Department of Industrial Engineering, Padova, Italy*
*c Hiref S.p.A., Tribano (PD), Italy*

** Corresponding author: lombardo@itc.cnr.it*

## Abstract

The progressive phase-out of high-GWP refrigerants as mandated by the Kigali Amendment to the Montreal Protocol and the EU F-gas Regulation necessitates the exploration of sustainable alternatives within the HVAC&R industry. A recent proposal by the Council and the European Parliament aims to significantly reduce Hydrofluorocarbons (HFCs) consumption by 2050, including specific bans on high-GWP fluorinated gases in heat pumps and small air conditioning units. Heat pumps, pivotal in mitigating climate change, are expected to see a significant rise in residential applications. However, R134a, widely employed in these systems, has a high GWP of 1530, highlighting the need for more eco-friendly substitutes. Hydrofluoroolefins (HFOs) and natural fluids, particularly hydrocarbons (HCs), have emerged as promising fourth-generation refrigerants due to their negligible ozone depletion potential (ODP) and very low global warming potential (GWP). Despite the potential of these new refrigerants, an optimal replacement for R134a in heat pumps has yet to be found. In this regard, this study investigates the potential of the low-GWP HFO/HC mixture R1234yf/R600a (0.85/0.15) as a drop-in replacement for R134a in water-to-water heat pumps. The research conducts a comparative analysis between R134a and the nearly-azeotropic mixture, assessing their performance under identical heating conditions across 20 different combinations of heat sink and heat source temperatures, ranging from 35°C to 70°C and from 10°C to 20°C respectively. The R1234yf/R600a mixture exhibited a lower pressure ratio and higher mass flow rates compared to R134a. Additionally, the mixture showed favorable performance in terms of power consumption and compressor outlet temperatures, with slightly lower COP compared to the baseline fluid. These findings suggest that with proper optimization, the R1234yf/R600a mixture could be a viable and sustainable alternative to R134a in residential heat pump applications.

### *1. Introduction*

Among the sectors with a significant impact on climate change and greenhouse gas (GHG) emissions is the building sector, which accounts for 36% of the EU's total emissions and 40% of its end-use energy consumption [1]. Of this energy consumption, half is required

for space and water heating, corresponding to around 4100 Mt of $CO_2$ emissions (both direct and indirect). While gas remains the primary choice for space heating in European countries, where fossil fuels still meet over 60% of heating energy demand, the adoption of efficient and low-carbon heating technologies, particularly heat pumps, is growing steadily. Heat pumps play a crucial role in this context, providing a means to electrify heating, increase the use of renewable energy sources, and decrease reliance on imported fossil fuels [2–5]. The number of heat pumps installed in Europe, currently over 42 million (predominantly air-source heat pumps (ASHPs)), is increasing rapidly, driven by European initiatives such as the Fit-For-55 package [2] and the REPowerEU plan [6]. To facilitate the transition to heat pump-based heating systems, this technology often needs to adapt to existing emission systems, such as radiators, which are prevalent in milder climates where heat pumps could optimally serve as the primary heating technology throughout the year. However, the primary refrigerants used in heat pumps, namely R134a and R410A, are hydrofluorocarbons with high global warming potentials (GWP) of 1530 and 2256, respectively [7]. As potent contributors to climate change, their production and consumption are being phased down as prescribed by current European regulations (EU F-gas Regulation (EU) No 2024/573 [8,9]; Proposal for a Regulation of the European Parliament and of the Council on Fluorinated Greenhouse Gases [10]). This regulatory environment has led to a fourth-generation refrigerants, including natural fluids—specifically hydrocarbons (HCs)—and hydrofluoroolefins (HFOs), which possess negligible Ozone Depletion Potential (ODP) and very low GWP [11]. HCs, considered promising representatives of the fourth generation due to their low cost, availability, negligible GWP, and high energy efficiency, often face challenges related to their high flammability and regulatory constraints [12]. On the other hand, HFOs offer low GWP and null ODP, with thermophysical properties comparable to HFCs, though concerns about higher costs and long-term environmental effects have been risen recently [13], particularly concerning the production of trifluoroacetic acid (TFA) as a byproduct of their atmospheric degradation, and their similarity to perfluorinated alkylated substances (PFAS) [13]. Thus, a binary mixture of HFOs and HCs could offer a practical compromise, merging the environmental advantages and efficiency of both types while mitigating their individual challenges.

In this study, the binary mixture of 2,3,3,3-Tetrafluoroprop-1-ene (R1234yf) and isobutane (R600a) was tested in a water-to-water heat pump to evaluate its suitability as a substitute for R134a.

Among HFOs and HCs, R1234yf and R600a are the most extensively studied fluids thanks to their favourable thermophysical properties and minimal environmental impact [14]. Numerous studies have demonstrated their potential as substitutes for R134a, either as pure substances or components in blends [15–23]the application of the pure R1234yf and R1243zf are limited due to their flammability and low volumetric refrigerating capacity. The mixed refrigerants are expected to achieve excellent thermophysical performance, safety, and environmental protection. Vapor-liquid equilibrium (VLE. Additionally, research on the thermophysical properties of the mixture has been conducted: Hu et al. [24]3,3,3-tetrafluoroprop-1-ene (HFO-1234yf measured the vapor-liquid equilibrium of R1234yf/R600a at temperatures ranging from 283.15 to 323.15 K, correlating the data using a PR equation of state. Di Nicola et al. [25] presented 96 vapor density data for the binary blend, applying a fundamental Helmholtz equation of state (EoS), a PR EoS, and a truncated virial EoS to fit their data. Zhang et al. [26] gathered 101 *PVT* vapor phase datapoints for the R1234yf/R600a blend, extrapolating the blend azeotrope and developing a preliminary Helmholtz free energy equation of state for the mixture. This latter EoS has been used in this study to calculate the thermophysical properties of the mixture under working conditions.

While Zhang et al. [27] have investigated the combination of R1234yf and R600a as a replacement for R134a in automotive air conditioning, developing the vapor-liquid equilibrium (VLE) model for this mixture using the Soave-Redlich-Kwong (SRK) and Peng-Robinson (PR) equations alongside the Van der Waals (VdW) and Huron-Vidal (HV) mixing rules, this paper presents findings from experimental tests on replacing R134a with the azeotropic R1234yf/R600a (0.85/0.15) blend in a water-to-water heat pump under twenty different operating conditions, considering water user temperatures compatible with medium/high temperature emission systems. The results highlight the limits and potentialities of the binary mixture compared to R134a, providing a preliminary understanding on the implementation of this refrigerant mixture, with a focus on sustainability and energy performance.

## 2. Methods

### 2.1. Materials

As previously mentioned, R1234yf and R600a are extensively studied fluids, with a substantial body of literature available regarding their thermophysical properties [14,28] the industry of HVAC&R has faced continuous changes trying to identify environmentally friendly refrigerants for the numerous applications of the sector. However, the amount of low GWP fluids still available as potential refrigerants is limited to some natural fluids and, among synthetic chemicals, to hydrofluoroolefins (HFO. Consequently, accurate Helmholtz free energy equations of state are already available and implemented in the software REFPROP 10.0 for each of these fluids [29–31]propane, n-butane, and isobutane. Each contains 25 coefficients which were fitted to selected data for the thermal and caloric properties of the respective fluid both in the single-phase region and on the vapor–liquid phase boundary. This work provides information on the available experimental data for the thermodynamic properties of n- and isobutane, and presents all details of the new formulations. The new equations of state describe the pρT surfaces with uncertainties in density of 0.02% (coverage factor k=2 corresponding to a confidence level of about 95%. Based on these equations, Table 1 provides an overview of the fundamental properties of the two mixture components considered in this investigation, alongside their categorizations according to the ASHRAE Safety Standard 34 [32]. Specifically, Table 1 also reports key thermophysical properties of R1234yf and R600a compared to those of the baseline fluid R134a at the mean evaporating and condensing temperatures among the working conditions considered in this study: 283.15 K and 328.15 K. As shown, R1234yf has a lower molar mass and thus a lower latent heat of vaporization compared to R134a, but the addition of R600a, which has more favourable characteristics in this regard compared to R134a, can enhance the overall performance of the mixture. Both R1234yf and R600a exhibit lower liquid density compared to R134a, resulting (as demonstrated later) in a higher mass flow rate processed by the compressor. Additionally, the similar viscosity and thermal conductivity values should ensure comparable performance of heat exchangers. Finally, the higher specific heats of the fluids, particularly that of R600a, should result in a lower discharge temperature, as demonstrated by the experimental tests.

The R1234yf/R600a blend was gravimetrically prepared with a molar fraction of 0.85/0.15, corresponding to its azeotropic composition, as indicated by Zhang et al. [26]. The final expanded uncertainty (k=2) on the mixture composition was assessed to be $U_x$=0.02%. Table 2 displays the fundamental parameters of the R1234yf/R600a (0.85/0.15) blend, which can be compared to those of R134a from Table 1. While the properties of R134a are calculated using the Helmholtz equation of state implemented in REFPROP 10.0, the parameters for the mixture are calculated using the binary interaction parameters regressed by Zhang et al. [26] for the GERG-2004 equation of state developed by Kunz et al. [33] for hydrocarbons. As shown in the table, the mixture and R134a have similar normal boiling points, indicating comparable pressure curves and the suitability of R1234yf/R600a for the intended application.

**Table 1.** Environmental, safety and thermophysical properties of R1234yf, R600a and baseline fluid R134a.

| **Environmental and safety properties [7,32]** | | | | | |
|---|---|---|---|---|---|
| **Refrigerant** | | | **R1234yf** | **R600a** | **R134a** |
| **GWP** | | | 4 | 3 | 1530 |
| **ODP** | | | 0 | 0 | 0 |
| **ASHRAE Safety class** | | | A2L | A3 | A1 |
| **Thermophysical properties [29]** | | | | | |
| **Property** | **T (K)** | **State** | **R1234yf** | **R600a** | **R134a** |
| ***MM*** (kg/kmol) | — | — | 114.04 | 58.122 | 102.03 |
| ***NBP*** (K) | — | — | 243.67 | 261.401 | 247.08 |
| $T_c$ (K) | — | — | 367.85 | 407.81 | 374.21 |
| $P_c$ (MPa) | — | — | 3.38 | 3.63 | 4.06 |
| **Latent heat of vaporization** (kJ/kg) | — | — | 162.64 | 364.25 | 199.00 |
| $P_{sat}$ (MPa) | 283.15 | Liquid | 0.44 | 0.22 | 0.41 |
| | 328.15 | Vapor | 1.46 | 0.77 | 1.49 |
| **Density** ($kg/m^3$) | 283.15 | Liquid | 1144.00 | 568.92 | 1261 |
| | 328.15 | Vapor | 86.96 | 19.89 | 76.1 |

| | | | | | |
|---|---|---|---|---|---|
| **Viscosity** (mPa·s) | 283.15 | Liquid | 0.18 | 0.18 | 0.23 |
| | 328.15 | Vapor | 0.01 | 0.01 | 0.01 |
| **Thermal conductivity** (W/mK) | 283.15 | Liquid | 0.07 | 0.09 | 0.09 |
| | 328.15 | Vapor | 0.02 | 0.02 | 0.02 |
| **Specific heat** (kJ/kgK) | 283.15 | Liquid | 1.33 | 2.34 | 1.37 |
| | 328.15 | Vapor | 1.35 | 2.07 | 1.31 |

**Table 2.** Thermophysical properties of R1234yf/R600a (0.85/0.15).

| Fluid | *MM* (kg/kmol) | *NBP* (K) | $T_c$ (K) | $P_c$ (MPa) |
|---|---|---|---|---|
| R-1234yf/R-600a (0.85/0.15) | 106.65 | 242.82 | 367.83 | 3.36 |

### 2.2. Test circuit

The test circuit used for the drop-in test consists of a custom-made water-to-water heat pump, as illustrated in Figure 1. A picture of it is provided in Figure 2. This heat pump is equipped with two brazed-type plate heat exchangers (PHX) by Alfa Laval (model ACH70X), functioning as the condenser (90 plates) and evaporator (80 plates). The compressor (EC) is a fixed-speed scroll compressor, ZH125KCE-TWD by Copeland, with a displacement of 71.4 m³/h at 50 Hz, lubricated with POE RL32 oil. An oil separator (OS) is positioned at the compressor outlet to ensure that the compressor lubricant oil is returned directly to the compressor crankcase, preventing it from circulating with the refrigerant throughout the system. An electronic expansion valve (EEV), Carel E3V65, with a maximum operating pressure of 45 bar, controls both superheating and pressure ratio.

On the user and source sides, two secondary loops filled with water allow the transfer of heat from the primary refrigerant at the condenser to the end user and from the heat source to the evaporator. Centrifugal pumps (CP) on both the condenser and evaporator sides drive water within the secondary loops, with their frequencies regulated by an external voltage signal. A filter drier (DF) placed before the expansion valve absorbs any residual water and acids, preventing corrosion of the compressor's metal surfaces and ensuring that the oil and refrigerant do not decompose.

Figure 1 shows the positioning of measurement sensors (pressure, temperature, and flow rate) along the circuit. T-type thermocouples (T in Figure 1) measure the refrigerant temperatures at the inlet and outlet of the PHXs, while PT100 (T) class AA sensors are used on the water sides. Pressure transmitters (P) Keller 21Y are used for pressure measurements, with a full scale of 30 bar for those installed between the compressor and the thermostatic valve, and 10 bar for those in the low-pressure branch. Siemens MAG5100 turbine-type flowmeters (M) are used to measure the volumetric flow rates on both the condenser and evaporator sides of the water circuit, while an Endress+Hauser Promass 300 Coriolis flowmeter (M) measures the mass flow rate of the refrigerant. Finally, a digital power meter (W) by Socomec records the electrical power consumption of the compressor. The characteristics and accuracies of the measuring devices are reported in Table 3

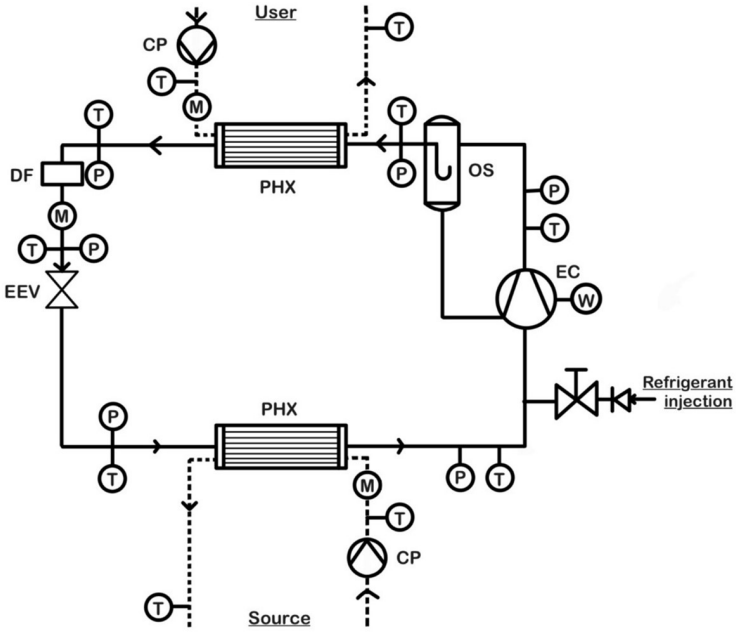


**Figure 1.** Schematic of the test circuit.

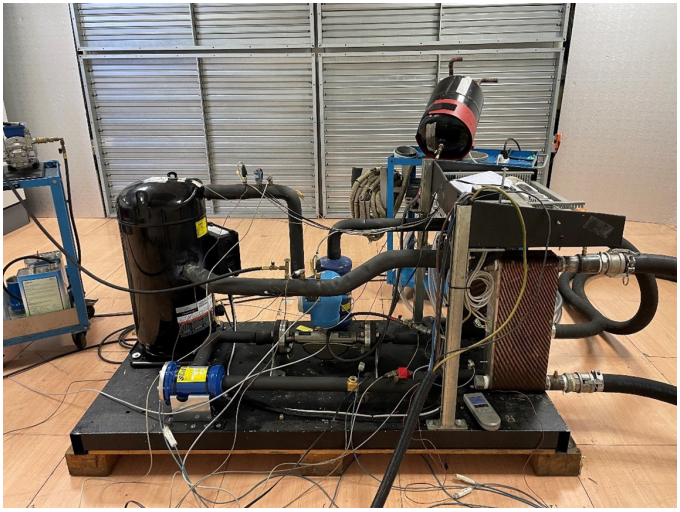

**Figure 2.** Picture of the test circuit.

T**able 3.** Accuracy of measuring devices

| Sensor | Unit | Range | Accuracy |
|---|---|---|---|
| T-type thermocouple | ◦C | −200~350 | 0.80% |
| PT100 | °C | 0~150 | 0.30% |
| Pressure transmitter (HP branch) | bar | 0~30 | 0.25% FS |
| Pressure transmitter (LP branch) | bar | 0~10 | 0.25% FS |
| Coriolis flowmeter | kg/h | 0~180 | 0.15% |
| Turbine flowmeter (user side) | $m^3/h$ | 0~30 | 0.22% |
| Turbine flowmeter (source side) | $m^3/h$ | 0~35 | 0.25% |
| Digital power meter | V | 90~520 | 0.20% |
| | A | 0~35 | 0.50% |

### *2.3. Test conditions and procedure*

To conduct the tests, the system was charged with the R1234yf/R600a blend, and the operating conditions of the heat pump were set based on water-side temperatures. A 5K temperature difference was maintained between the inlet and outlet of the PHX,

and a constant superheating (DSH) of 10 K was ensured to prevent the presence of liquid at the compressor inlet. Additionally, subcooling of 6-8 K was maintained to avoid vapor at the expansion valve inlet. Overall, tests were performed under twenty distinct conditions, derived from the combination of four different water source temperatures and five water user temperatures, as summarized in Table 4.

Once the inlet and outlet water conditions on the source and user sides were established, and a steady-state condition was achieved within the system, data acquisition commenced for all the measuring devices indicated in Figure 1. A total of 100 experimental data points were collected for each operating point, with one reading every 5 seconds. After completing the measurements with the mixture, before evacuating and flushing the system, a refrigerant sample was taken to check if different affinities for the oil of the two mixture components, the presence of impurities or contaminants in the system, or potential phase separation within the cycle might have altered the overall composition of the refrigerant. The sample, subjected to GC analysis, confirmed the initial composition of the mixture, with deviations within the uncertainty assessed for composition. This result confirmed the stability of the system and provided an initial indication of the compatibility of POE RL32 oil with the mixture.

Following this, the experimental setup was charged with R134a and operated under the same conditions to allow a comparative evaluation of the mixture's behavior relative to the pure fluid. The data collection procedure was as follows:

**Table 4.** Experimental conditions.

| **Parameter** | **Value** |
|---|---|
| Inlet water temperature at the evaporator (°C) | 10/12/15/20 |
| ΔT source (°C) | 5 |
| Outlet water temperature at the condenser (°C) | 35/45/55/65/70 |
| ΔT user (°C) | 5 |
| DSH (°C) | 10 |
| DSC (°C) | 6-8 |

For the comparative analysis of the results obtained for the binary mixture R1234yf/R600a and the baseline fluid R134a, the following performance coefficients were considered:

pressure ratio ($r_p$), coefficient of performance (COP), heat flux at the condenser ($Q_{cond}$), and volumetric heating effect (VHE). At each operating condition, these parameters were determined using the following equations:

$$r_p = \frac{p_{comp,outlet}}{p_{comp,inlet}} \quad (1)$$

$$COP_{ref} = \frac{\Delta h_{cond}}{\Delta h_{compr}} \quad (2)$$

In Equation 2, $\Delta h_{cond}$ and $\Delta h_{compr}$ represent the enthalpy change at the condenser and compressor, respectively. Enthalpy values, as well as other thermodynamic properties of fluids, were calculated using the REFPROP 10.0 [29] , based on the measured values of temperature and pressure. Specifically, for the R1234yf/R600a mixture, the KW0 model by Kunz et al. [33] was employed, incorporating the binary interaction parameters (BIPs) regressed by Zhang et al. [26].

The heat flux at the condenser Q_cond on the refrigerant side is given by:

$$Q_{cond}[\mathrm{W}] = \dot{m}_{ref}\Delta h_{cond} \quad (3)$$

Where $\dot{m}_{ref}$ is the measured refrigerant mass flow rate.

Similarly, the power exchanged at the compressor is determined by:

$$P_{compr,calc}[\mathrm{W}] = \dot{m}_{ref}\Delta h_{compr} \quad (4)$$

Finally, the volumetric heating effect (VHE) is defined as:

$$VHE\ [kJ/m^3] = \frac{Q_{cond}}{\dot{V}_{ref}} \quad (5)$$

with $\dot{V}_{ref} = \rho_{ref} * \dot{m}_{ref}$.

On the water side, heat flux at the condenser is calculated using:

$$Q_{cond,water}[\mathrm{W}] = \rho_{water}\dot{V}_{water}c_p\Delta T \quad (6)$$

where ρ is the water density, V is the volumetric flow rate measured in the user water

loop, $c_p$ is the isobaric specific heat, and ΔT is the temperature difference measured between the inlet and the outlet of the condenser. For calculating ρ and $c_p$, the mean temperature between the inlet and the outlet of the condenser was considered.

Subsequently, the coefficient of performance on the water circuit $COP_{water}$ is calculated as:

$$COP_{water} = \frac{Q_{cond,water}}{P_{compr}} \quad (7)$$

Where $P_{compr}$ is the measured electrical power absorbed at the compressor.

### *2.4. Uncertainty analysis*

An extensive uncertainty analysis (UA) was performed for each state point under each operating condition to ascertain the overall uncertainty associated with all the parameters involved in the study. The accuracies of the measuring devices listed in Table 3, regarded as standard uncertainties (k=1), were applied to all directly measured quantities, including temperatures, pressures, flow rates, and electric power. For the calculated quantities, the law of propagation, as shown in Equations 8-15, was employed. Sensitivity coefficients in the equations for R1234yf/R600a were calculated using again the mixture model developed by Zhang et al [26].

Table 5 summarizes the final maximum expanded uncertainties for the primary performance indicators across the 20 operational conditions, considering both R1234yf/R600a and R134a.

As can be seen the expanded uncertainty for the COP, $U_r$(COP), reaches 1%, while the uncertainty for the VHE $U_r$(VHE) is assessed at 1.4%. The pressure ratio exhibits the lowest uncertainty, up to 0.7%. Notably, the uncertainties on the water sides of the circuit are significantly higher than those of the refrigerant, primarily due to the greater uncertainties in temperature measurements, especially for the heat flux at the condenser, which shows expanded uncertainties up to 12%. These elevated values are attributed to the high ratio of $\frac{u(\Delta T)}{\Delta T}$, resulting from the small temperature difference ΔT=5 K, compounded by the substantially higher user water temperatures compared to those in the evaporator circuit.

$$u(r_p) = \sqrt{u(p_{in})^2 + u(p_{out})^2} \quad (8)$$

$$\frac{u(\mathrm{Q})}{\mathrm{Q}} = \sqrt{\left(\frac{u(\dot{m}_{ref})}{\dot{m}_{ref}}\right)^2 + \left(\frac{u(\Delta h)}{\Delta h}\right)^2} \quad (9)$$

$$u(\Delta h) = \sqrt{u(h_{in})^2 + u(h_{out})^2} \quad (10)$$

$$\frac{u(COP_{ref})}{COP_{ref}} = \sqrt{\left(\frac{u(\Delta h_{cond})}{\Delta h_{cond}}\right)^2 + \left(\frac{u(\Delta h_{compr})}{\Delta h_{compr}}\right)^2} \quad (11)$$

$$\frac{u(\mathrm{VHE})}{\mathrm{VHE}} = \sqrt{\left(\frac{u(\mathrm{Q}_{cond})}{\mathrm{Q}_{cond}}\right)^2 + \left(\frac{u(\dot{m}_{ref})}{\dot{m}_{ref}}\right)^2 + \left(\frac{u(\rho_{ref})}{\rho_{ref}}\right)^2} \quad (12)$$

$$\frac{u(\mathrm{Q}_{water})}{\mathrm{Q}_{water}} = \sqrt{\left(\frac{u(\dot{m}_{water})}{\dot{m}_{water}}\right)^2 + \left(\frac{u(\Delta T)}{\Delta T}\right)^2 + \left(\frac{u(c_{p,water})}{c_{p,water}}\right)^2 + \left(\frac{u(\rho_{water})}{\rho_{water}}\right)^2} \quad (13)$$

$$u(\Delta T) = \sqrt{u(T_{in})^2 + u(T_{out})^2} \quad (14)$$

$$\frac{u(COP_{water})}{COP_{water}} = \sqrt{\left(\frac{u(\mathrm{Q}_{water})}{\mathrm{Q}_{water}}\right)^2 + \left(\frac{u(P_{compr})}{P_{compr}}\right)^2} \quad (15)$$

**Table 5.** Expanded uncertainties (k=2) for the main indicators considered in this study.

| Calculated quantity | Expanded uncertainty (k=2) |
|---|---|
| $Q_{cond}$ | 1.0 % |
| $Q_{cond,\ water}$ | 12 % |
| $Q_{eva}$ | 0.9 % |
| $Q_{eva,\ water}$ | 3 % |
| $COP_{ref}$ | 2.4 % |
| $COP_{water}$ | 12 % |
| *VHE* | 1.4 % |
| $r_p$ | 0.7 % |
| $P_{compr,\ el.}$ | 1.2% |
| $P_{compr,\ calc.}$ | % |

### *3. Results*

Prior to engaging in results analysis, the reliability of the monitoring system was verified by comparing the energy fluxes exchanged on the water side ($Q_{cond,\ water}$, $Q_{eva,\ water}$) and the refrigerant side ($Q_{cond}$, $Q_{eva}$). Similarly, the measured electrical power at the compressor (Pcompr, el.) was compared with the calculated power absorbed by the compressor (Pcompr, calc), as determined by Equation 9. The percentage deviations are presented in Table 6. Regarding compressor power, a maximum difference of 6% was observed between the calculated and measured power consumption at the compressor, equivalent to 1.3 kW, occurring for R134a at the highest evaporating and condensing temperatures, which is the operating point with the highest uncertainty. The average difference was 0.8 kW for both R1234yf and R134a. Overall, the results' consistency was considered acceptable. Concerning the heat flux differences on the refrigerant and water sides for both the condenser and evaporator, the mean difference in heat flux at the condenser is nearly negligible (-0.12% for R1234yf and 0.06% for R134a), indicating high consistency between the calculated refrigerant and water values. This consistency is further supported by the small standard deviation (0.3 kW). The heat flux at the evaporator on the water side exhibits similar trends and consistency with the refrigerant side for both fluids, with deviations within 2.7%, which is lower than the declared expanded uncertainty for the parameter (3%). In conclusion, the validation results demonstrate high consistency and accuracy between the calculated and measured power consumption and heat flux values. This confirms the reliability of the performance metrics and trends observed in the analysis.

**Table 6.** Power balances at the cycle components: compressor, condenser and evaporator.

| $T_{water\_cond\_out}$ | $T_{water\_eva\_in}$ | $P_{compr}$ | | $Q_{cond}$ | | $Q_{eva}$ | |
|---|---|---|---|---|---|---|---|
| °C | °C | R134a | R1234yf/ R600a | R134a | R1234yf/ R600a | R134a | R1234yf/ R600a |
| 35 | 10 | 1.35% | 3.31% | 0.59% | -0.71% | 2.71% | 1.78% |
| 45 | 10 | 3.81% | 3.95% | -0.27% | -0.29% | 1.81% | 1.82% |
| 55 | 10 | 4.04% | 4.22% | -0.20% | -0.32% | 2.38% | 1.78% |
| 65 | 10 | 3.51% | 4.75% | 0.44% | 0.36% | 2.46% | 2.21% |

| | | | | | | | |
|---|---|---|---|---|---|---|---|
| 70 | 10 | 4.55% | 5.13% | 0.94% | 0.64% | 2.71% | 2.66% |
| 35 | 12 | 3.80% | 4.28% | -0.71% | -0.33% | 1.23% | 1.66% |
| 45 | 12 | 4.52% | 4.62% | -0.42% | 0.19% | 1.72% | 1.75% |
| 55 | 12 | 4.99% | 4.61% | -0.54% | 0.66% | 2.06% | 2.04% |
| 65 | 12 | 4.90% | 5.18% | 0.08% | 0.71% | 2.27% | 1.97% |
| 70 | 12 | 5.08% | 5.00% | 0.79% | 0.57% | 2.62% | 2.46% |
| 35 | 15 | 3.59% | 3.94% | -0.98% | -0.55% | 1.07% | 1.70% |
| 45 | 15 | 4.43% | 4.34% | -0.64% | -0.54% | 1.36% | 1.89% |
| 55 | 15 | 5.03% | 5.12% | -0.66% | -0.53% | 1.66% | 2.13% |
| 65 | 15 | 5.37% | 5.29% | -0.22% | -0.02% | 1.91% | 2.20% |
| 70 | 15 | 5.29% | 5.21% | 0.36% | 0.68% | 2.12% | 2.70% |
| 35 | 20 | 3.25% | 4.01% | -0.71% | -0.34% | 1.00% | 1.81% |
| 45 | 20 | 3.78% | 4.44% | -0.25% | -0.37% | 1.30% | 2.13% |
| 55 | 20 | 3.98% | 4.46% | -0.32% | -0.13% | 1.60% | 2.06% |
| 65 | 20 | 4.33% | 5.61% | -0.05% | 0.57% | 1.82% | 2.54% |
| 70 | 20 | 4.94% | 6.04% | 0.35% | 0.95% | 1.75% | 2.54% |

Figure 3 illustrates the relationship between the pressure ratio at the compressor ($r_p$) and the outlet temperatures at the condenser ($T_{water,cond,out}$) for various inlet temperatures at the evaporator ($T_{water,eva,in}$). As expected, the pressure ratio escalates with increasing condenser outlet temperatures for both refrigerants. The R1234yf/R600a mixture tends to exhibit a slightly lower pressure ratio compared to R134a under analogous conditions, with a mean deviation of -8%, extending to -12% at higher condensing temperatures. This suggests more favorable operating conditions and reduced compressor stress. Additionally, considering the adverse effects of a high-pressure ratio on volumetric and isentropic efficiencies, the substantial negative deviation observed with the R1234yf/R600a mixture is a positive aspect in the drop-in analysis.

However, as shown in Figure 4, the mixture requires higher mass flow rates compared to R134a across all water conditions, with no specific temperature trend. Deviations, reaching up to 20%, are due to the higher vapor density of R1234yf, as indicated in Table 1. It is known that a higher refrigerant charge can potentially increase direct emissions in case of leaks; nonetheless, given the significantly lower GWP of the mixture compared to R134a (a GWP of 3.9 is expected when weighting the GWPs of individual components by

their mass fractions within the mixture), this concern appears secondary.

In terms of power consumption, the effect of the higher mass flow rate counterbalances that of the reduced pressure ratio for the mixture, following the trend of the latter. At lower condensing temperatures, the effect of $m_{ref}$ prevails, and the mixture requires higher power at the compressor (up to 3.22%), while the difference between the two fluids decreases as the condensing temperature rises, leading to lower power requirements by up to -7.6%. Furthermore, across all considered operating conditions, the mixture required significantly lower temperatures at the compressor outlet compared to the baseline fluid (Figure 5), with notable deviations ranging from -6°C to -18°C. This phenomenon further mitigates the impact of the higher mass flow rate on compressor longevity and enhances the stability of both the refrigerant and the POE RL32 oil.

Lastly, regarding the behavior of the three crucial parameters for the energy performance of the two fluids, the trends of $Q_{cond}$ (Figure 6), COP (Figure 7), and VHE (Figure 8) are consistent with each other, showing slightly better results at lower evaporating temperatures (up to 1.03%, 2.76%, 4.29% for $COP_{ref}$, VHE, and $Q_{cond}$ respectively) and poorer performance as the condensing temperature rises (-7% for $COP_{ref}$, -16.3% for VHE, and -13% for $Q_{cond}$). Especially for VHE, these results were expected, given the lower heating capacity of R1234yf and R600a compared to R134a. However, it must be noted that this study is a drop-in analysis, with no optimization of components to adapt the cycle to the mixture characteristics to enhance its performance. Since VHE represents crucial data for selecting the compressor size under given operating conditions, results from Figure 8 highlight the need for adjustments in compressor size and characteristics, providing an initial direction for optimization efforts. Moreover, given the relatively low maximum deviation between R134a COPs of 0.3, occurring at the most challenging user temperature conditions, results suggest that, if properly optimized, the R1234yf/R600a mixture proposed here might represent a viable alternative to R134a in residential applications, particularly when sustainability is prioritized.

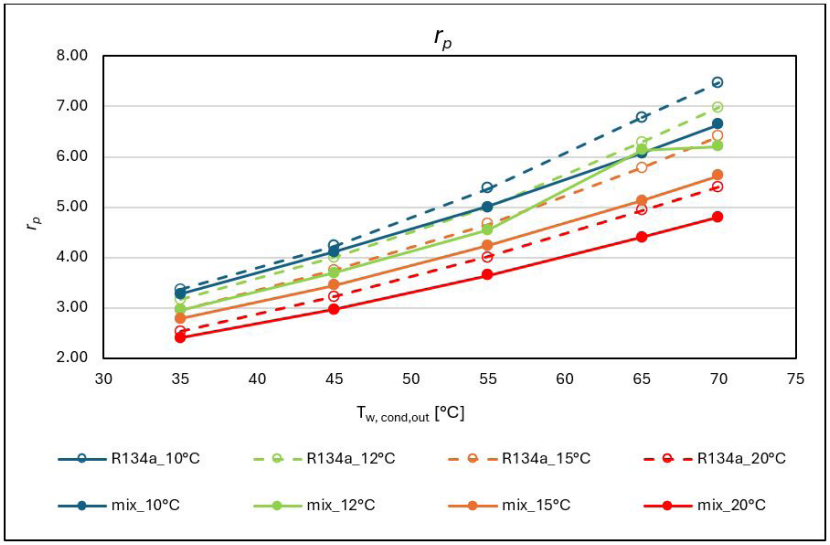


**Figure 3.** Pressure ratio as a function of condenser and evaporator water temperatures. Empty points: R134a; full points: R1234yf/R600a.

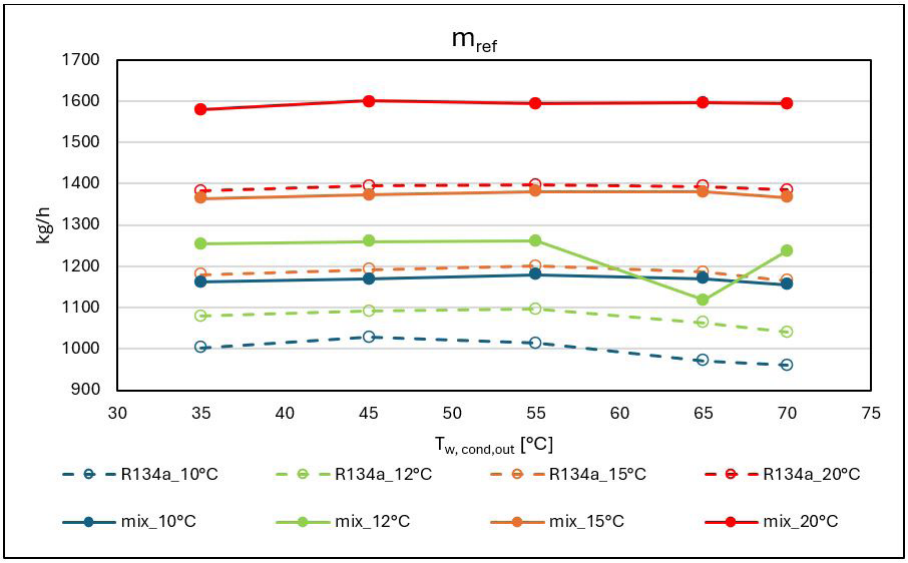


**Figure 4.** Refrigerant mass flow rate as a function of condenser and evaporator water temperatures. Empty points: R134a; full points: R1234yf/R600a.

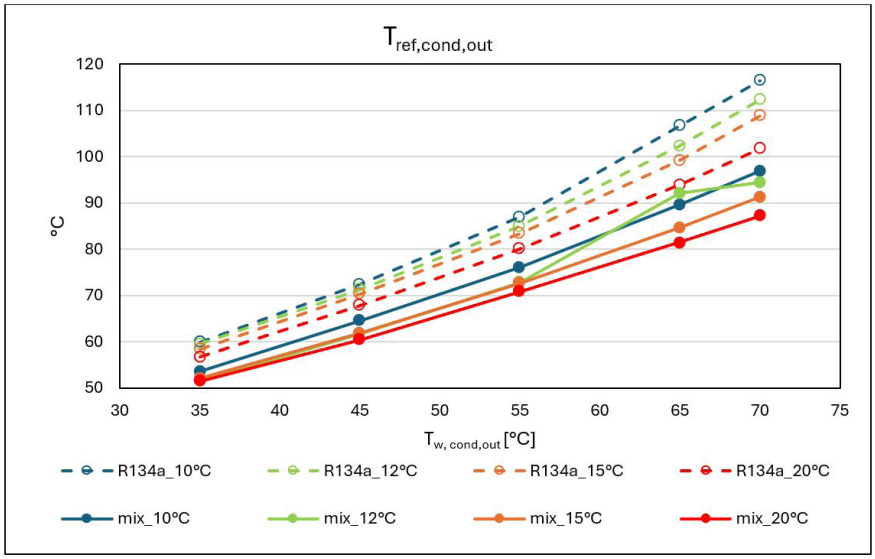


**Figure 5.** Discharge temperature as a function of condenser and evaporator water temperatures. Empty points: R134a; full points: R1234yf/R600a.

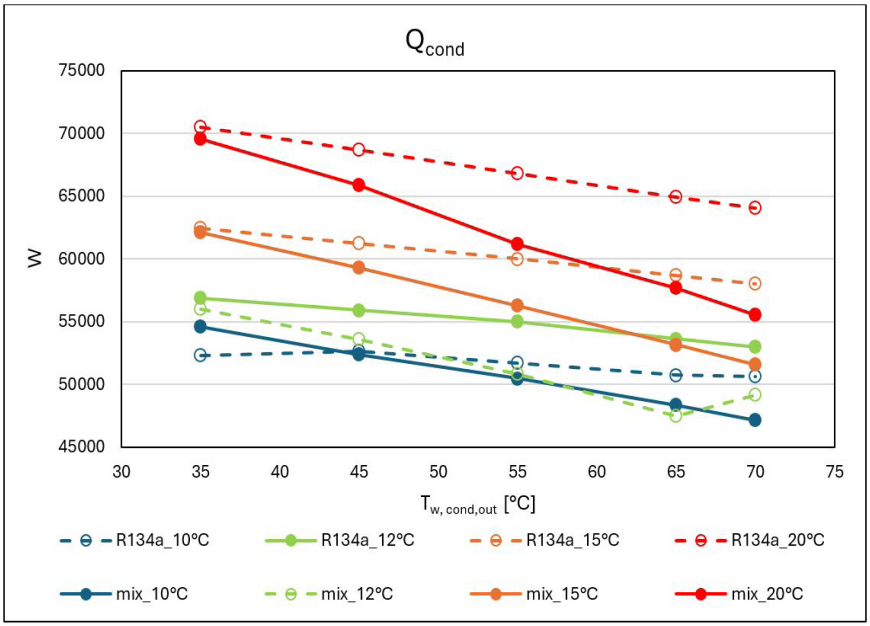


**Figure 6.** Heat flux at the condenser as a function of condenser and evaporator water temperatures. Empty points: R134a; full points: R1234yf/R600a.

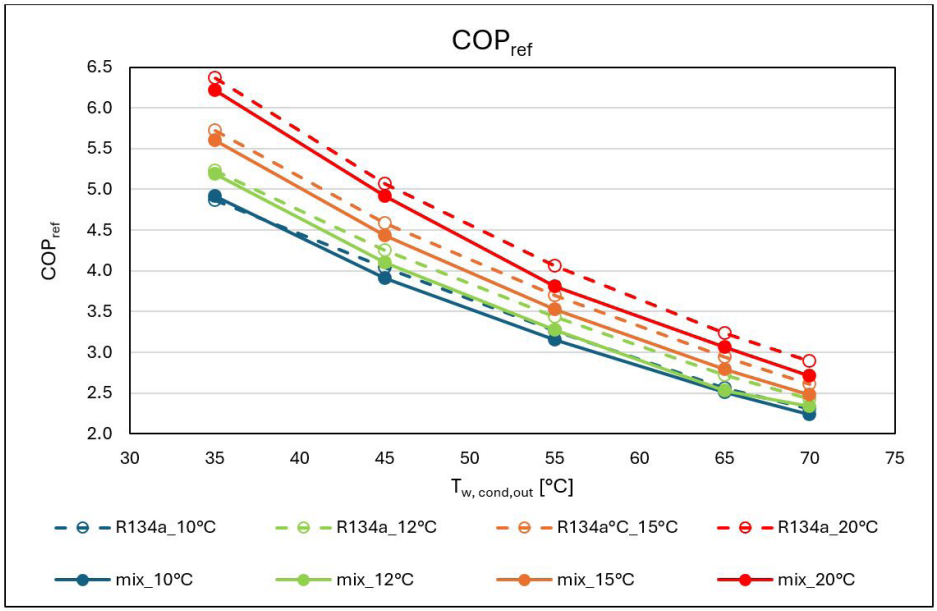


**Figure 7.** COP as a function of condenser and evaporator water temperatures. Empty points: R134a; full points: R1234yf/R600a.

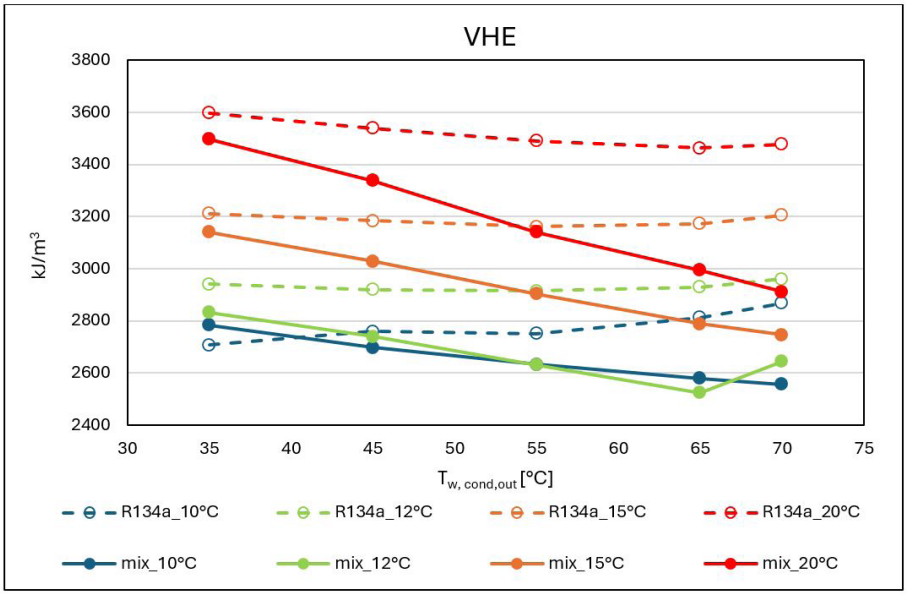


**Figure 8.** Volumetric heating effect as a function of condenser and evaporator water temperatures. Empty points: R134a; full points: R1234yf/R600a.

### *4. Conclusions*

This study investigated the performance and reliability of a custom-made water-to-water heat pump using the azeotropic binary mixture R1234yf/R600a (0.85/0.15 molar fraction) as a substitute for R134a. Given the building sector's significant contribution to greenhouse gas emissions and the regulatory phase-down of high-GWP refrigerants, this research aimed to evaluate the potential of the low-GWP refrigerant mixture. Experimental tests were conducted under twelve distinct operating conditions to compare energy fluxes, pressure ratios, and volumetric effects between the refrigerants. The reliability of the monitoring system was confirmed by validating the energy fluxes exchanged on both the water and refrigerant sides: the mean differences in heat fluxes were negligible, which supports the accuracy and consistency of the performance metrics, whereas the maximum deviation between measured and calculated values in compressor power was found to be 6%.

The R1234yf/R600a mixture demonstrated a slightly lower pressure ratio compared to R134a, which is beneficial for reducing compressor stress and improving volumetric and isentropic efficiencies. However, the mixture required higher mass flow rates due to its higher vapor density. Despite this, the significantly lower GWP of the mixture mitigates environmental concerns associated with higher refrigerant requirements, presenting a favourable trade-off in the context of environmental impact.

In terms of energy efficiency and sustainability, the mixture exhibited comparable performance to R134a, with slightly better results at lower evaporating temperatures and poorer performance at higher condensing temperatures. Given the relatively low maximum deviation in COP, the mixture shows promise as a sustainable alternative to R134a, especially when considering the potential environmental benefits. Future research should focus on optimizing the components of the heat pump system to better accommodate the specific characteristics of the R1234yf/R600a mixture. This includes refining the compressor size and design, enhancing the efficiency of heat exchangers, and further investigating the long-term stability and compatibility of the refrigerant-oil mixture.

### *References*

[1] A. Toleikyte, J. C. Roca Reina, J. volt, J. Carlsson, L. Lyons, A. Gasparella, D. Koolen, M. De Felice, D. Tarvydas, V. Czako, G. Koukoufikis, A. Kuokkanen, and S. Letout, (2023).

[2] "Fit for 55": Delivering the EU's 2030 Climate Target on the Way to Climate Neutrality. COMMUNICATION FROM THE COMMISSION TO THE EUROPEAN PARLIAMENT, THE COUNCIL, THE EUROPEAN ECONOMIC AND SOCIAL COMMITTEE AND THE COMMITTEE OF THE REGIONS EMPTY (n.d.).

[3] A. S. Gaur, D. Z. Fitiwi, and J. Curtis, Energy Res. Soc. Sci. 71, 101764 (2021).

[4] IEA, Global Heat Pump Sales Continue Double-Digit Growth (Paris, 2023).

[5] The European Green Deal. COMMUNICATION FROM THE COMMISSION TO THE EUROPEAN PARLIAMENT, THE EUROPEAN COUNCIL, THE COUNCIL, THE EUROPEAN ECONOMIC AND SOCIAL COMMITTEE AND THE COMMITTEE OF THE REGIONS. (n.d.).

[6] E. Commission and D.-G. for Communication, REPowerEU, Joint European Action for More Affordable, Secure and Sustainable Energy (Publications Office of the European Union, 2022).

[7] Climate Change 2021, The Physical Science Basis: The Working Group I Contribution to the Sixth Assessment Report of the Intergovernmental Panel on Climate Change (IPCC) (2021).

[8] European Parliament and Council of the European Union, Regulation (EU) No 517/2014 of the European Parliament and of the Council of 16 April 2014 on Fluorinated Greenhouse Gases and Repealing Regulation (EC) No 842/2006 Text with EEA Relevance (n.d.).

[9] European Parliament and Council of the Europe, Regulation (EU) 2024/573 of the European Parliament and of the Council of 7 February 2024 on Fluorinated Greenhouse Gases, Amending Directive (EU) 2019/1937 and Repealing Regulation (EU) No 517/2014 (2024).

[10] Proposal for a Regulation of the European Parliament and of the Council on Fluorinated Greenhouse Gases, Amending Directive (EU) 2019/1937 and Repealing Regulation (EU) No 517/2014. OUTCOME OF PROCEEDINGS. 19 October 2023. (2023).

[11] A. Mota-Babiloni and P. Makhnatch, Int. J. Refrig. 127, 101 (2021).

[12] B. K. Sovacool, S. Griffiths, J. Kim, and M. Bazilian, Renew. Sustain. Energy Rev. 141, 110759 (2021).

[13] L. Fedele, S. Trini Castelli, P. Ielpo, C. Zilio, and S. Bobbo, in Refrig. Sci. Technol. Proc., edited by International Institute of Refrigeration (IIR) (2023), p. Vol. 2, pp. 398–408.

[14] D. Calleja-Anta, M. Martínez-Ángeles, L. Nebot-Andres, D. Sánchez, and R. Llopis, Appl. Therm. Eng. 247, 123070 (2024).

[15] S. Peng, S. Li, Z. Yang, and Y. Duan, Int. J. Refrig. 134, 115 (2022).

[16] S. Bobbo, G. Di Nicola, C. Zilio, J. S. Brown, and L. Fedele, Int. J. Refrig. 90, 181 (2018).

[17] H. Miyamoto, M. Nishida, and T. Saito, J. Chem. Thermodyn. 158, 106456 (2021).

[18] X. Yao, L. Ding, X. Dong, Y. Zhao, X. Wang, J. Shen, and M. Gong, Int. J. Refrig. 120, 97 (2020).

[19] T. Yamada, H. Miyamoto, N. Sakoda, and Y. Higashi, Int. J. Thermophys. 41, (2020).

[20] Z. Yang, A. Valtz, C. Coquelet, J. Wu, and J. Lu, Int. J. Refrig. 120, 137 (2020).

[21] Z. Yang, X. Tang, J. Wu, and J. Lu, Fluid Phase Equilib. 498, 86 (2019).

[22] M. Kim, W. Mulroy, and D. Didion, (1994).

[23] C. Aprea, R. Mastrullo, and C. Renno, Appl. Therm. Eng. 24, 487 (2004).

[24] P. Hu, L.-X. Chen, W.-B. Zhu, L. Jia, and Z.-S. Chen, Fluid Phase Equilib. 373, 80 (2014).

[25] G. Di Nicola, L. Fedele, J. S. Brown, S. Bobbo, and G. Coccia, J. Chem. Eng. Data 62, 2496 (2017).

[26] H. Zhang, H. Li, B. Gao, Q. Zhong, W. Wu, W. Liu, X. Dong, M. Gong, and E. Luo, Int. J. Refrig. 95, 28 (2018).

[27] N. Zhang and Y. Dai, Int. J. Thermophys. 42, 152 (2021).

[28] L. Fedele, G. Lombardo, I. Greselin, D. Menegazzo, and S. Bobbo, Int. J. Thermophys. 44, 80 (2023).

[29] E. W. Lemmon, I. H. Bell, M. L. Huber, and M. O. McLinden, NIST Standard Reference Database 23: Reference Fluid Thermodynamic and Transport Properties-REFPROP, Version 10.0, National Institute of Standards and Technology (2018).

[30] M. Richter, M. O. McLinden, and E. W. Lemmon, J. Chem. Eng. Data 56, 3254 (2011).

[31] D. Bücker and W. Wagner, J. Phys. Chem. Ref. Data 35, 929 (2006).

[32] ANSI/ASHRAE Standard 34-2019, Designation and Safety Classification of Refrigerants (2019).

[33] O. Kunz, R. Klimeck, W. Wagner, and M. Jaeschke, The GERG-2004 Wide-Range Equation of State for Natural Gases and Other Mixtures (2007).

# Green Mortars Made with Tes Enhanced Recycled Wood Aggregates

**Hala Salhab[a,b], Mahdi Zanjani[a], Ines Belmir[c], Alberto Lagazzo[a], Sergio Nardini[b], Francesca Zanoni[d], Mona N. Sam[e], Saulo Rocha Ferreira[f], Antonio Caggiano[a]**

*a Università degli studi di Genova, Genova, Italy*
*b Università degli studi della Campania Luigi Vanvitelli, Caserta, Italy*
*c L'École nationale des travaux publics de l'État o ENTPE, Lyon, France*
*d Sphera Encapsulation S.r.l., Verona, Italy*
*e Independent Energy Consultant, Frankfurt at Main, Germany*
*f Federal University of Lavras, Lavras, Brasil*

## Abstract

This paper reports the results of an experimental program on sustainable cementitious mortars made of Recycled Wood Aggregates (RWAs) employed as carriers for Phase-Change Materials (PCMs). Three mortar mixtures were examined: i.e., Ordinary Portland Cement (OPC-), Wood-, and Energy-Wood (NRG-Wood)-mortar. The incorporation of PCMs into wood aggregates enhances their thermal storage capacity, making them effective for temperature regulation in buildings. The experimental campaign comprised mechanical tests that found adding NRG-Wood aggregates to mortars decreased mechanical performance, yet the NRG-Wood mortar exhibited superior flexural strength and ductility compared to the Wood mortar. Thermal evaluations showed that NRG-Wood mortar had significantly better thermal behavior due to the PCM heat absorption and release properties. Hydration tests and specific heat capacity measurements confirmed these findings, demonstrating effective energy storage and temperature regulation capabilities. Water absorption tests indicated the physical durability of the NRG-Wood mortars, revealing the porosity and permeability essential for long-term construction applications. The results highlight the potential of the tested NRG-Wood mortars in creating sustainable building materials, contributing to energy savings and environmental impact reduction.

### *1. Introduction*

Reducing climate change by mitigating global warming is closely linked to energy consumption, carbon dioxide emissions, and associated environmental hazards [1]. Given that the construction sector in Europe accounts for substantial energy consumption, with buildings responsible for approximately 40% of this demand and 36% of the EU's $CO_2$ emissions [2], there is a pressing need for innovative materials to reduce environmental impact and carbon footprint [3].

One promising solution is incorporating phase change materials (PCMs) into the open porosity of various aggregates, which enables high thermal storage density and moderate temperature fluctuations, making these objectives realistic and feasible [4]. Incorporating PCMs into cement pastes effectively reduces energy demand in modern

buildings by absorbing and releasing large amounts of thermal energy at nearly constant temperatures [5].

Several approaches have been explored in the literature: i.e., Kulkarni et al. [6] focused on enhancing the thermal properties of lightweight concrete by employing two varieties of Lightweight aggregates (LWA), perlite and aerated concrete particles (ACG), to fabricate PCM-loaded particles; Mankel et al. [7] demonstrated that recycled brick aggregates (RBAs) could also serve as effective carriers for PCMs, showing promising results in thermal energy storage with minimal acceptable strength; Guimar et al. [8] have shown that incorporating PCMs into jute fabric, used to reinforce cement matrices, allows the fabric to absorb up to 102 % of its weight in PCM, significantly enhancing its thermal storage capacity; Ahn et al. [9] have proven the effectiveness of using cellulose acetate (CA), polyether sulfone (PES), and cellulose polymers to fabricate fiber-type conductors for microencapsulated PCMs (μPCMs); Fabricio et al. [10] highlighted the potential of storing PCMs within the pores of bamboo culms, presenting a sustainable approach for temperature control. The most promising trend, however, is utilizing wood as a carrier for PCMs due to its diverse and advantageous properties, making it an ideal medium for such applications.

Wood is a complex natural composite material which can be studied through numerous levels to understand its properties. The diversity of wood species offers a large variation in wood anatomy and in properties. Therefore, the chemical composition of wood differs depending on its type, geographic localization or climatic conditions [11]. Although the precise chemical composition is to change from species, the average composition of wood material is as follows. Wood is formed by cellulose, a polymer capable of crystallizing to create strong fibers, a binder for the cellulose composed of lignin and hemicellulose, water and extractives which are the organic impurities responsible for the smell, color, size, fungus and insect of the wood [12]. Moreover, as depicted by Rowell et al. [13], wood is a three-dimensional biopolymer composite composed by an interconnected network of cellulose, hemicellulose and lignin with the presence of extractives and inorganics. Its cellular structure traps air inside which enables wood to have excellent thermal insulation properties reducing heat transfer [14].

The porosity of wood, which is related to the presence of interconnected void spaces within its structure influences its ability to absorb and desorb water affecting its

dimensional stability and durability [13]. The porous structure of wood allows it to effectively absorb and retain PCMs, enhancing its thermal performance in construction and other applications [15]. As an orthotropic material, wood has unique and independent mechanical properties in the direction of three mutually perpendicular axes related to the orientation of its fibers (parallel, radial or tangent) [16]. The layered structure of the wood cell wall is determinant concerning its strength and mechanical properties [17]. This structure allows wood to present viscoelastic properties where the mechanical behavior is time dependent and manifests itself in creep and relaxation. They are also mechano-sportive properties as demonstrated by the behavior under simultaneous load, humidity change and plastic properties which appear as permanent deformation [18]. Various characterization techniques have been used to analyze wood and its chem- structural properties such as X-ray diffraction [19] or scanning electron microscopy (SEM) [20]. These inherent properties make wood a highly adaptable and sustainable material for numerous applications.

Through the years, wood has been massively used for various applications in construction because of its sustainability, strength and availability. Historically, wood has been a fundamental building material used to construct homes, ships or monumental structures. In Europe and mediterranean tradition, timber frame construction was prevalent during the medieval period, providing robust and flexible structures that have withstood the test of time [22]. As climate change becomes a central concern, wood emerges as a promising material being a renewable resource with a lower environmental impact compared to traditional materials like steel and concrete. Consequently, the usage of wood grows in the industry in favor of buildings either alone or combined with other material [23].

In construction, wood is used in different forms. It has been promoted as a thermal insulation material that lowers energy consumption for heating and cooling [13]. Coupled with PCMs, it allows energy storage and helps regulate indoor temperature and reduce energy consumption [15]. The mechanical properties of wood enable it to be suitable for structural applications such as beam, column and trusses [24]. Combined with other materials, wood can form composites like cement composites or wood polymer composites to offer improved thermal and acoustic insulation. Torgal et al. [25] investigated wood-concrete composites and demonstrated their compressive and

flexural strength comparable to concrete, along with flexibility and enhanced energy efficiency and sustainability. Even when recycled, wood can be used as aggregates, reducing waste and the demand for virgin materials, thus contributing to sustainable building practices [26]. These features make wood a key material for sustainable development, serving future building construction needs.

In this context, the present research aims to investigate the mechanical, physical, and thermal energy storage properties of three wood-based mixtures. The primary objective is to examine the effects of adding NRG-Wood aggregates to the reference mortar and its significant role in energy savings and reducing the carbon footprint. Following this general introduction on the state-of-the-art and motivations for the research, the paper is organized as follows. Section 2 details the mixture proportioning and mix design of the bio-based composites. Section 3 and 4 presents the experimental characterization methods and results. Lastly, section 5 finalizes the work with concluding remarks and future direct lines.

## 2. *Materials*

### *2.1. Composite constituents of bio-based wood mixtures*

Mixtures considered in the present research were made by employing a cement type CEM II/B-LL 32.5 R which is a type of limestone Portland cement characterized by its high initial resistance, produced by Heidelberg Materials. Bio-based PCMs were also considered in one mortar to produce NRG-wood aggregates which are wood fibers impregnated with a phase change material (PCM), resulting in what is termed "energy wood". PCM is a key-material for clean energy frameworks. In fact, due to the endothermic phase change from solid to liquid reaction when the temperature is increasing, it can absorb heat and release it when it changes from liquid to solid when the temperature is decreasing. Moreover, to ensure optimal performance within its operational environment, the PCM melting point needs to be below the heat supply temperature and above the ambient temperature. The thermal and physical properties of the PCM used are summarized in Tab.1.

**Table 1.** Overview of thermo-physical properties of the PCMs, namely PureTemp® 25.

| Type | Tm [approx.°C] | Heat Storage Capacity [approx. In kJ/kg] | Thermal conductivity [approx. in W/m°C] | Density (liquid) [approx. in g/ml] | Specific heat (liquid) [approx. in J/g°C] |
|---|---|---|---|---|---|
| Bio-PCM | 25.2 ± 1.1 | 187 | 0.15 (liquid)<br>0.25 (solid) | 0.86 (liquid)<br>0.95 (solid) | 2.29 (liquid)<br>1.99 (solid) |

The wood aggregates considered are recycled chestnut wood and size curve is proposed in Fig.1. The results are compared with the original Fuller grain size distribution and the modified Fuller curve (with n=0.4) which coincides more with the real grain size distribution. Finally, an experimental protocol to produce NRG-wood was developed. PCM fills the pores of the wood fibers by placing a batch of wood and liquid PCM into a vacuum pump. To prevent leakage caused by the liquefaction of PCM at 25 °C, the aggregates have been encapsulated. This encapsulation is achieved by covering the fibers with a two-phase epoxy resin with hardener E45 (DEIN EPOXID HARZ), trapping the PCM. Additionally, the fibers are coated with sand powder to ensure that wood fibers of different diameters remain distinct and do not form a heap. The stages of this process are illustrated in the attached Fig.2.

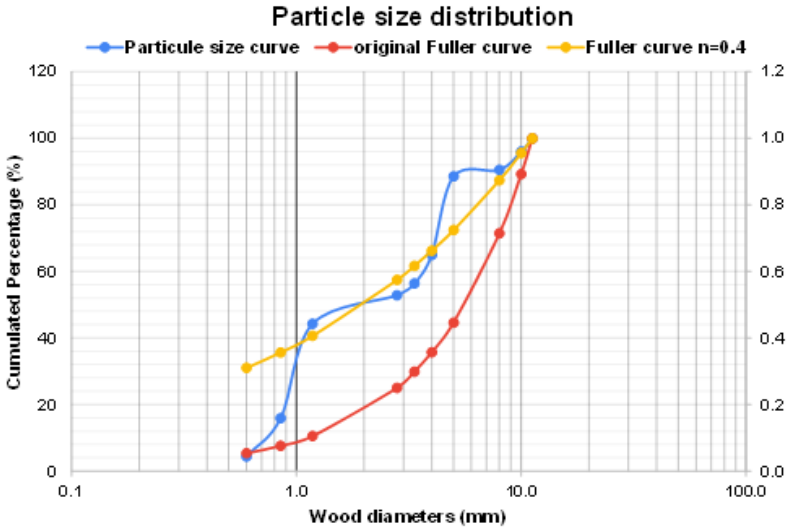


**Figure 1.** Grain size distribution of studied aggregates/particles.


(a)

(b)

(c)

(d)

**Figure 2.** NRG-Wood process (a) wood with PCM inside vacuum machine, (b) remove the excess PCM, (c) cover the fibers with epoxy resin, (d) NRG-Wood coated with sand powder.

As exposed in Tab.2 the composition of the 1597.29 gr of energy wood is 350 gr of recycled wood (21.91%), 278 gr of PCM (17.41%), 72 gr of epoxy resin (4.51%), and 897.29 gr of sand powder (56.18%).

**Table 2.** Composition of NRG-Wood aggregates.

| Weight of dry Wood (gr) | PCM absorbed (gr) | Epoxy added (gr) | Powder sand absorbed (gr) | Final weight of NRG-Wood (gr) |
|---|---|---|---|---|
| 350.00 | 278.07 | 72.00 | 897.29 | 1597.29 |
| 21.91% | 17.41% | 4.51% | 56.18% | 100.00% |

*2.2. Proposed compositions*

Three mixtures (OPC-, Wood-, and NRG-Wood-mortar) were prepared and tested in accordance with EN 196-1 (2005) [27]. For the wood mortar, a partial replacement method was used to incorporate wood into the mixture so that 40% of the sand is replaced by wood and Ca $(Cl)_2$ were added to the mixture to strengthen the overall compatibility. The wood was pre-treated by soaking it into a solution of Ca $(OH)_2$ dissolved in water for 1 hour to enhance the suitability of wood and to foster the compatibility between wood and cement.

After one day, the specimens were removed from formworks and stored underwater for 28 days. Subsequently, mechanical properties of the specimens were evaluated. For thermal testing, the specimens were dried at 50°C until they achieved a constant mass to ensure accurate temperature measurements in dry state. The mixed proportions are detailed in Tab.3.

**Table 3**. Mix design overview of the three studied composites.

| Components | Density (gr/cm³) | OPC Mortar [kg/m³] | Wood- Mortar [kg/m³] | NRG-WOOD Mortar [kg/m³] |
|---|---|---|---|---|
| Cement | 3.81 | 559.94 | 559.94 | 530.59 |
| Sand | 2.67 | 1521.04 | 940.29 | 891.00 |
| Wood | 1.00 | 0.00 | 287.18 | 0.00 |
| NRG-Wood | 1.30 | 0.00 | 0.00 | 412.99 |
| Water | 1.97 | 250.32 | 238.43 | 284.73 |
| S.P | 1.00 | 3.92 | 5.69 | 5.39 |
| Ca $(Cl)_2$ | 2.50 | 0.00 | 16.80 | 0.00 |
| W/C ratio % | - | 0.45 | 0.43 | 0.54 |

For each mortar, three prismatic specimens (40×40×160 mm³) were made for mechanical tests, two spherical specimens (diameter of 80 mm) with a thermocouple wires type K in the middle for DKK tests (see Mankel et al. [7]) and two prismatic specimens with a thermocouple wire in the middle for thermal tests.

## 3. Methods

### *3.1 Mechanical tests: compression and bending*

Mechanical tests, including both compression and bending, were conducted after 28 days of curing following the procedures outlined in EN 196-1 [18]. Prismatic specimens (40×40×160 mm³) were initially subjected to a three-points bending test, as depicted in Fig.3. a. The supports were spaced 100 mm (± 0.5 mm) apart, and the load was applied vertically at a rate of 0.2 mm/min. Both the displacement and the force exerted by the piston were recorded throughout the test until fracture occurred. Subsequently, compression tests were performed on one half of the fractured beams, adhering to the procedure specified in EN 196-1 [27] Fig.3. b.

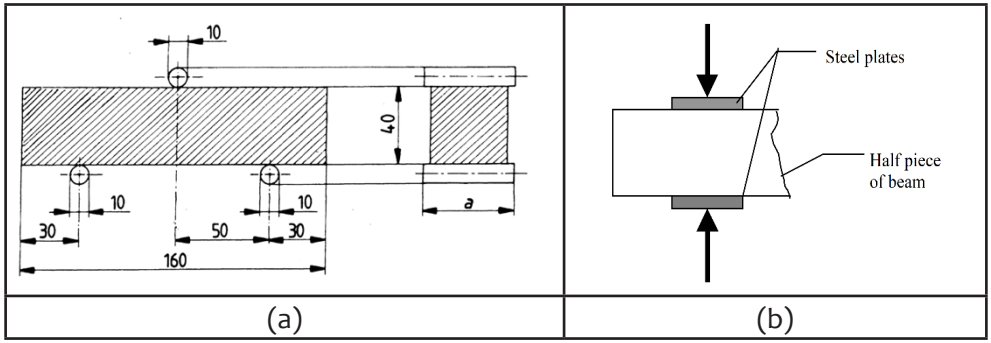


**Figure 3**. Geometry and experimental set-up of the (a) 3-point bending test and (b) compression test [27].

### *3.2 Capillarity absorption tests*

Water absorption tests were conducted to evaluate the capillary water absorption coefficients in accordance with UNE-EN (2003) and following the procedure outlined by Palomar et al. [28]. These tests are crucial to understand the durability and physical properties of mortar. By evaluating the capillary water absorption coefficient (CC), the porosity and permeability of the mortar were assessed. The bottom parts of the specimens, each with a cross-section of 40x40 mm², were submerged in water to a depth of 10 mm, while the remaining portions of the beams were covered with plastic wrap to prevent water evaporation. To ensure uniform water absorption, the bottom of

the water container was lined with gravel as shown in Fig.4. The capillary water CC was determined by weighing the specimens at specified intervals: 0,10, 20, 30, 60, 90, 120, 180, 240, and 420 minutes, as well as 24 hours after the start time of the test.

**Figure 4.** Specimens wrapped in PP plastic with the bottom part in contact with water.

### *3.3. Thermal characterization in early-age state*

A hydration test on the three mortars was performed to understand the influence of additional aggregates on the hydration process of the cement-based materials. It was monitored by measuring the temperature evolution using a thermocouple wires type K in the center of a cubic mortar sample (10×10×10 $cm^3$) under semi-adiabatic conditions during the first seven days after casting.


**Figure. 5.** Hydration process for (a). three different casted mortars, (b). the insulation thickness and the position of sensor.

Each mortar mold was insulated to prevent heat transfer by placing it in a large box (29×39×21.5 $cm^3$) lined with polyurethane foam. The insulation consisted of a thick layer (approximately 11 cm) of foam between two opposing sides of the cube mold and the box, while the other sides were insulated with a thinner layer (approximately 6.5 cm) as shown in Fig.5. a. This setup ensured minimal heat exchange with the environment, allowing accurate monitoring of the temperature changes due to the exothermic hydration reaction. The mortars were cast in molds simultaneously after being mixed separately in other containers as shown in Fig. 5.b. The entire experimental setup was maintained in a room with a constant temperature of 20 ± 1°C.

### *3.4. Thermal characterization in hardening state*

To evaluate the thermal conductivity of samples, a laboratory-developed thermal box was created, drawing inspiration from a device known as a "Hot Box" [29,10]. For this purpose, three polystyrene boxes (40×30×27 $cm^3$) were utilized.

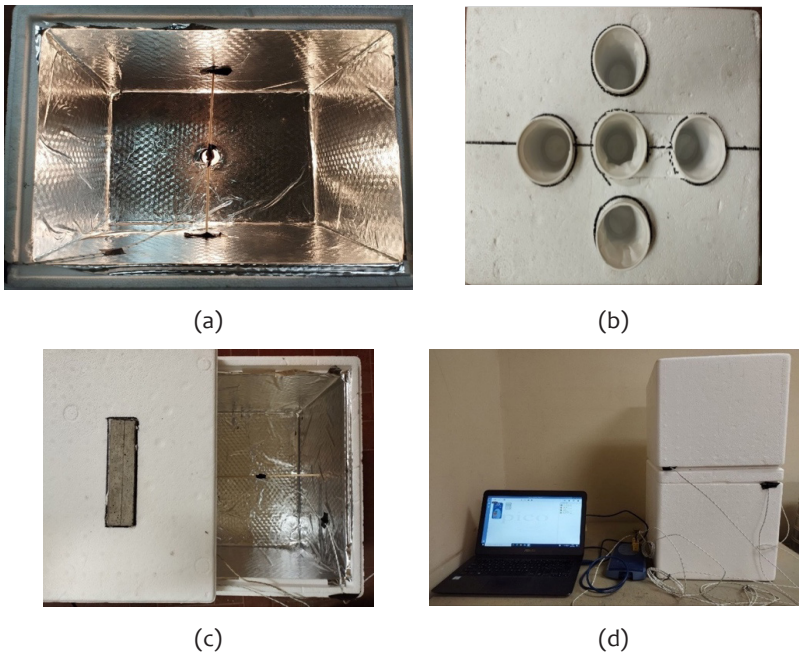


**Figure 6**. Components of Hot box (a) active chamber for heating, (b) stage for ice cooling, (c) passive chamber, (d) test procedure.

The first box, termed the "passive chamber," simulated room temperature by lining its walls with aluminum foil tape. In the second box, designated as the "active chamber" for heating, a 15 W incandescent bulb was positioned upside down at the bottom, also covered with aluminum foil tape to prevent overheating damage. The third box, also an "active chamber," simulated a cooling environment. It featured five holes at the bottom where plastic cups filled with ice cubes were placed to lower the internal temperature. Temperature inside these boxes was monitored using type K thermocouples placed centrally in each box. Additionally, one of the box lids was modified to accommodate a mortar beam with an embedded thermal sensor for conducting measurements. The objective of this experimental setup was to assess the thermal insulation properties by measuring the attenuation of heat transfer between two initially identical but isolated environments. The whole experimental material is shown in Fig. 6.

The specific heat capacity (sensible part only, $C_p$) of components and samples were analyzed using isothermal calorimetry. This technique provides precise measurements of heat flow associated with chemical or physical processes. Before measurement, the samples were dried overnight in an oven at 50°C. The measurement cell was filled with a known number of samples (1.6 - 3.4 g), while the reference cell remained empty.

The calorimetry was then sealed, and heating commenced according to the following temperature program: upon reaching the initial set point (28 °C), both cells were allowed to stabilize for 600 sec before increasing the temperature by 2°C. During the heating process, the variation in heat flow was recorded using Setsoft 2000 software. The system was maintained at a constant temperature for 7200 sec, followed by heating to the next set point (30°C) and stabilizing for another 7200 sec. These steps were repeated at regular intervals until the final heat flow peak was reached at 36°C.

The specific heat capacity [J/K×g] was measured for each component and sample. To calculate the $C_p$ value, Eq. (1) was employed [30]:

$$C_p = \frac{Q_c - Q_b}{m \cdot \Delta T} \qquad (1)$$

being $Q_c$ the total heat absorbed in the presence of a sample [J], $Q_b$ the total heat absorbed in the absence of a sample [J] and $m$ the mass of the sample placed into the measurement cell [gr]; $\Delta T$ is the temperature difference before and after the heat

capacity measurement at a certain set point, which was around 2°C.

Temperature evolution measurements for all mixtures were then conducted using specially prepared spherical samples with a diameter of approximately 80 mm. Fig. 7 shows the spheres and the positions of the thermocouples used in the experimental study. The thermocouples were positioned to measure temperature changes at the center of the samples. Each test lasted approximately 4 hours. Before testing, the samples were thoroughly dried and cooled to an initial temperature of 10°C by placing them in a climate chamber (type IVYX Scientific). Then, the testing procedure involved a heating cycle followed by a cooling cycle, with the temperature ranging from 10°C to 50°C. The procedure followed is exposed in the Fig.8.


**Figure 7.** Details of the specimen geometry and position of the thermocouples employed inside the sphere.

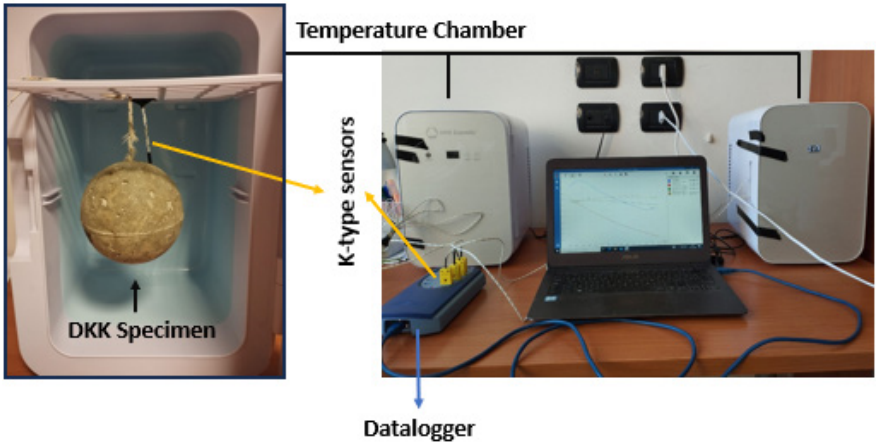


**Figure 8.** DKK test setup: (a) data acquisition equipment, (b) computer, (c-d) climatic chambers, (e) DKK sample inside the chamber

## *4. Results*

The experimental results from thermal and mechanical tests are shown in this section to understand the behavior of three mixtures: OPC mortar, Wood mortar and NRG-WOOD mortar.

### *4.1. Mechanical characterization*

Three-point bending tests were performed with the aim of characterizing the tensile strength of the considered mixtures as shown in Fig. 9. The bending strength $R_f$ [MPa] in all mixture was calculated by means of the following Eq. 2 [27]:

$$R_f = \frac{1.5 \cdot F_f \cdot l}{b^3} \qquad (2)$$

where *B* is the rib size of the cross section of the beam [mm], $F_f$ is the applied load at fracture [N], *L* is the distance between the supports [mm].

The results were obtained by considering the arithmetic mean value of the maximum force causing a crack opening for the three specimens of each mixture.

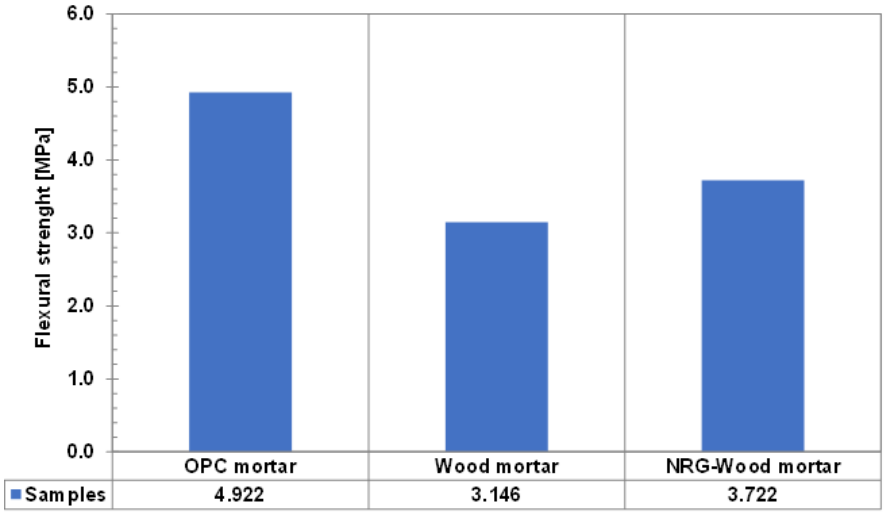


**Figure 9.** Bending strengths for three samples for each mixture.

Adding wood fibers into mortar reduced their mechanical performance and resulted in a lower bending strength as the NRG-Wood mortar. However, performances of the NRG-wood mortar equal to 3.722 MPa are better than the wood mortar 3.146 MPa because of the aggregates coating which allows a better flexural strength. Additionally, the inclusion of both NRG-wood and wood in the mortar imparts a fibrous quality to the material, resulting in greater ductility. In contrast, the behavior of OPC was brittle.

In Fig.10 the compressive strengths results $R_c$ [MPa] are shown for the considered mixtures. They were evaluated through the following Eq. 3 and elaborated following the provisions of [27]:

$$R_c = \frac{F_c}{A_c} \qquad (3)$$

where $F_c$ is the compressive load applied at fracture [N] and $A_c$ is the area of the auxiliary plates (40 × 40 mm$^2$).

The compressive strength keeps the same tendency as the bending strength so that OPC mortar has the best performance of 53.77 MPa. However, the gap between the wood

mortar at 8.21 MPa and the NRG-Wood mortar at 17.13 MPa is more pronounced. The aggregates coating significantly enhances compressive strength compared to flexural strength. Additionally, as flexural test, the NRG-Wood mortar demonstrates more ductile behavior, whereas OPC mortar is characterized by a brittle nature.

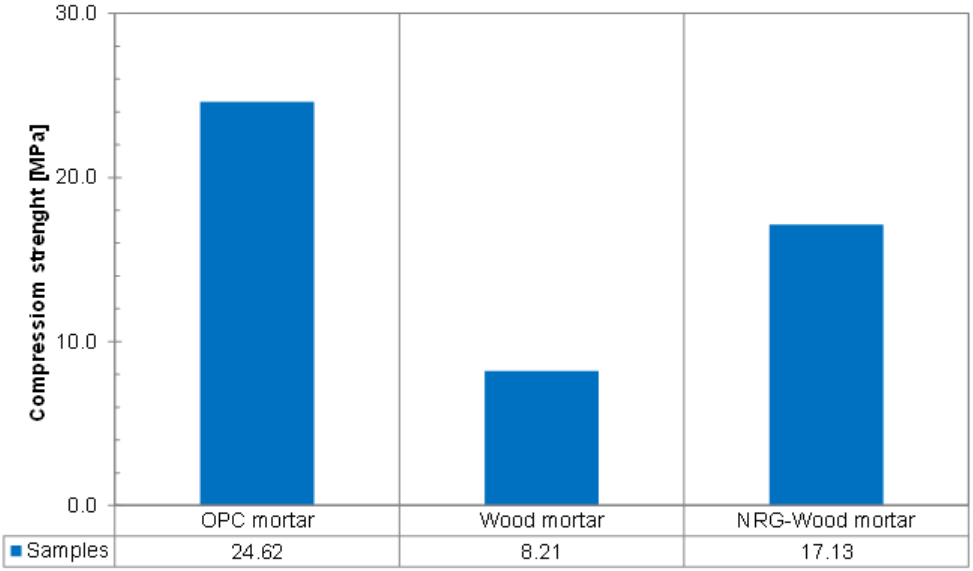


**Figure 10.** Compressive strength results of the studied composites.

The reduced flexural and compressive strength of NRG-Wood mortar is primarily due to the low strength of the PCM, which consequently affects the overall mixture.

### *4.2. Capillary water absorption characterization*

The (CC) capillary water absorption coefficient (measured in $Kg/m^2 \cdot min^{0.5}$) serves as the indicator of water absorption capacity for each material according to the following Eq.4 [31,32]:

$$CC = \frac{M_{wet} - M_{dry}}{A \cdot \sqrt{t}} \qquad (4)$$

where $M_{wet}$ is the weight of the specimen after 24 hours of saturation in [kg], $M_{dry}$ is the

weight of the dried specimen [kg], *A* is the cross-sectional area of the specimen (0.4×0.4 $cm^2$) and *t* is the time in [min].

The results for the three specimens, NRG-WOOD, Wood and OPC, are presented in the form of a bar chart in Fig.11. The NRG-WOOD sample exhibits the lowest water absorption coefficient at 0.107 $Kg/m^2 \cdot min^{0.5}$, indicating superior resistance to water uptake compared to the other samples. This characteristic could be attributed to the material's composition and structure, which likely enhances its hydrophobic properties. In contrast, the Wood sample shows the highest water absorption coefficient of 0.325 $Kg/m^2 min^{0.5}$. This result suggests that the Wood sample has a significantly higher tendency to absorb water, which might be due to its porous nature and inherent material properties. The OPC (Ordinary Portland Cement) sample has an intermediate water absorption coefficient of 0.288 $Kg/m^2 \cdot min^{0.5}$. While OPC absorbs less water than the Wood sample, it still demonstrates a higher water uptake than the NRG-WOOD sample.

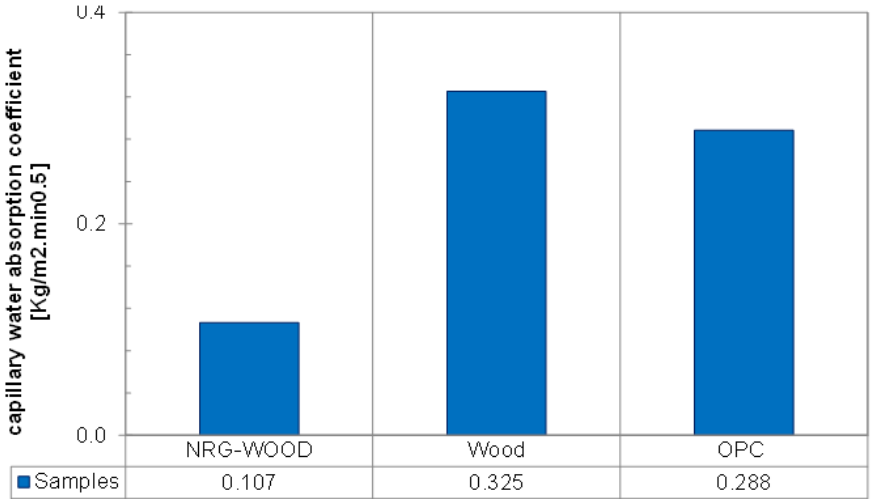


**Figure 11.** Capillary water absorption coefficient of the mixture.

### *4.3. Thermal evaluation*

The results obtained from hydration tests [33] for three mixtures highlight the effects of the mixture components and the moisture conditions of the pre-treated wood on the cement hydration reaction, including the role of NRG-Wood aggregates.

Fig.12 shows the temperature evolution in the three mixtures. The sample containing OPC mortar reached the highest peak temperature, indicating production of excess heat that could pose structural problems. Conversely, the sample with NRG-WOOD aggregates exhibited a lower peak temperature. This can be attributed to the inclusion of a phase change material, which absorbs excess energy and releases it later at a more beneficial time, thus conserving energy. The mixture containing wood showed an intermediate temperature effect over time. While its peak temperature was lower than the one of the OPC mortar, it was higher compared to the sample with NRG-Wood aggregates. This underscores the importance of this test in understanding the hydration mechanisms of each sample and their implications for the mechanical performance of cement-based materials.

The Hot Box Test was conducted to evaluate the thermal attenuation properties of different mortar beams, Wood mortar, OPC mortar, and NRG-Wood mortar, when subjected to a temperature gradient between two isolated environments.

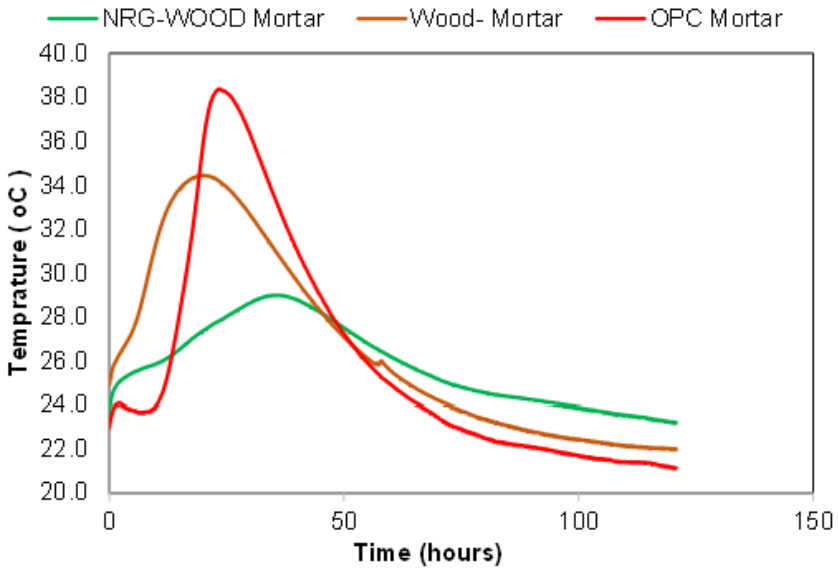


**Figure 12.** The temperature evolution of all studied mixtures during the curing time (initial 120 hours).

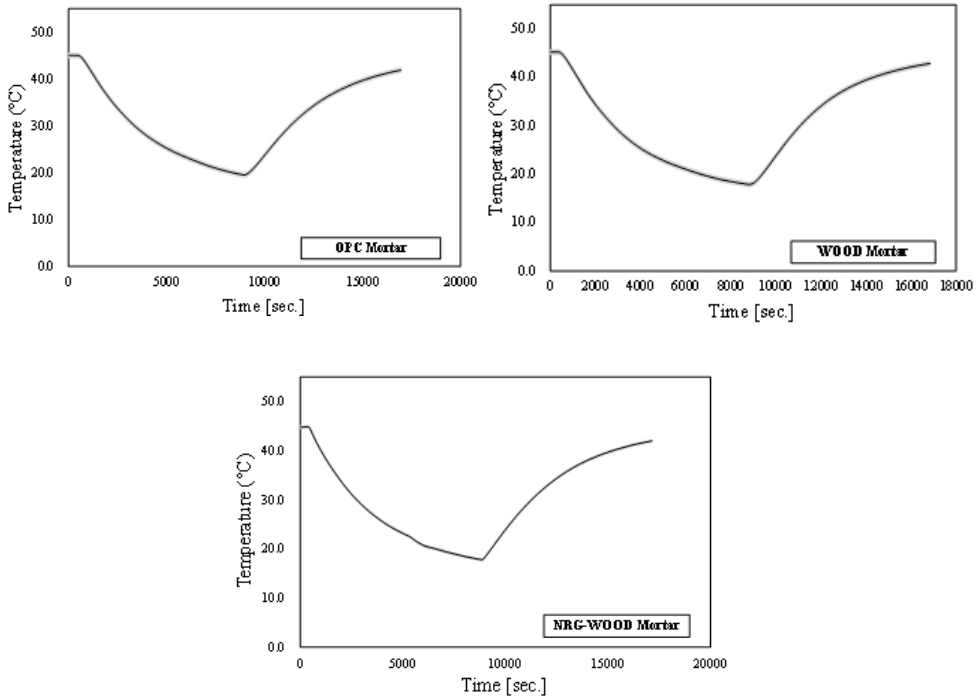


**Figure 13.** Hot box results with prismatic mortar samples (Cooling and Heating cycle).

The test proceeded through three distinct phases. Initially, the mortar beam was exposed to a heated active chamber until the temperature stabilized. This phase was followed by a period where the active chamber was replaced with a cold chamber for 2 hours and 20 min., including an additional cooling intervention with supplementary ice cubes after 1 hour and 30 min. Finally, the mortar beam was re-exposed to the heated active chamber for an equivalent duration to the cooling phase and the results of the three mixtures shown in Fig. 13.

The results of specific heat capacity ($C_p$) measurements of various components and their corresponding mortar mixes were conducted using a calorimeter over a temperature range of 28 °C to 36 °C are summarized in Fig.14 and Fig.15. Among the components, bio-PCM consistently exhibits the highest $C_p$ values, around 2 J/g×K across all temperature ranges (28-36°C). This indicates bio-PCM's superior ability to store thermal energy

compared to other components. The wood aggregates have a $C_p$ of approximately 1.4 J/g×K. This value is significantly lower than that of Bio-PCM but higher than the NRG-Wood aggregates. The inherent properties of wood contribute to its moderate thermal energy storage capacity. The $C_p$ for NRG-Wood aggregates are around 1.3 J/g×K, slightly lower than that of wood aggregates. The NRG-Wood aggregates are composed of epoxy resin and sand powder, which seem to form a shielding layer that hinders the PCM's full potential to store thermal energy.

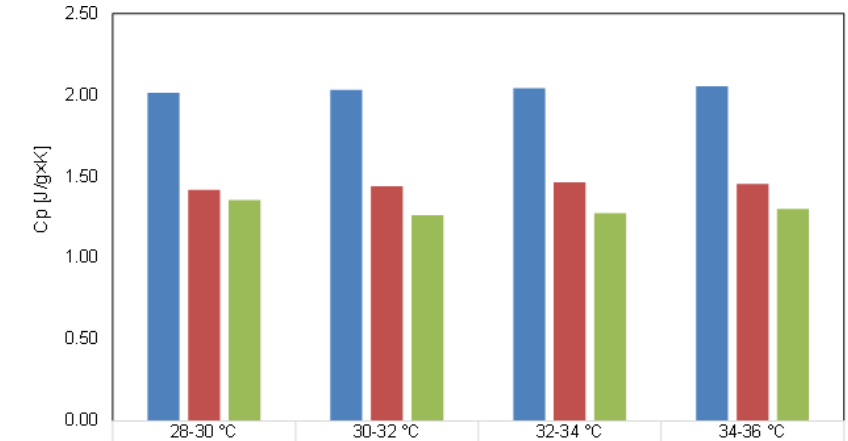


| | 28-30 °C | 30-32 °C | 32-34 °C | 34-36 °C |
|---|---|---|---|---|
| Bio-PCM | 2.01 | 2.03 | 2.04 | 2.05 |
| WOOD | 1.41 | 1.44 | 1.46 | 1.45 |
| NRG-Wood | 1.35 | 1.26 | 1.27 | 1.30 |

**Figure 14**. $C_p$ of components Bio-PCM, Wood and NRG-Wood.

In terms of the mixtures analysis, OPC mortar displays the lowest $C_p$ values, approximately 0.4 J/g×K across the measured temperature range. This indicates a limited capacity for thermal energy storage, making it less effective for applications requiring high thermal inertia. The wood mortar shows $C_p$ values close to 1 J/g×K. This is higher than OPC mortar but lower than NRG-wood mortar. The presence of wood aggregates contributes to its enhanced thermal energy storage compared to OPC mortar. NRG-wood mortar exhibits the highest $C_p$ values among the mortars, around 1.2 J/g×K. The inclusion of NRG-wood aggregates, which contain PCM, significantly enhances the thermal energy storage capacity of the mortar. The PCM present within the NRG-wood aggregates explains the superior thermal performance of this mortar mix.

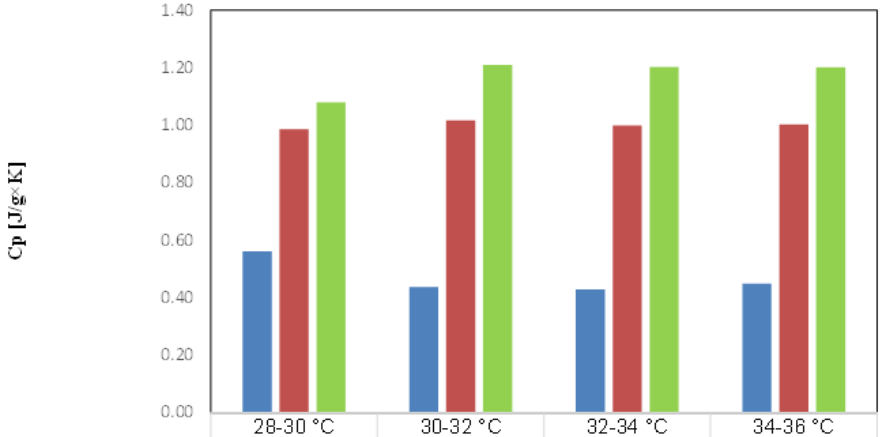


| | 28-30 °C | 30-32 °C | 32-34 °C | 34-36 °C |
|---|---|---|---|---|
| OPC mortar | 0.56 | 0.44 | 0.43 | 0.45 |
| wood mortar | 0.98 | 1.02 | 1.00 | 1.00 |
| NRG-Wood mortar | 1.08 | 1.21 | 1.20 | 1.20 |

**Figure 15.** specific heat capacity of three mixtures.

Heating and cooling DKK test analysis of NRG-Wood, Wood, and OPC mortars shows that PCM in NRG-Wood clearly enhances thermal fluctuation control and energy saving within the composites. OPC mortar heats and cools the fastest, while NRG-Wood exhibits slower temperature changes, indicating improved thermal performance and passive energy savings. The expected PCM plateau was not clearly visible, possibly due to coating thickness affecting PCM activation; however, its overall beneficial effect was evident. Due to space limitations in this manuscript, additional details and complete data will be presented in forthcoming comprehensive articles.

## *5. Conclusions*

In conclusion, this study explored the potential of NRG-Wood aggregates to enhance the sustainability and performance of cementitious mortars. The mechanical tests indicated that while the incorporation of NRG-Wood aggregates reduced overall mechanical performance compared to OPC mortar, it provided superior flexural strength and ductility compared to Wood mortar. Thermal evaluations demonstrated significantly improved thermal behavior for the NRG-Wood mortar, attributed to the phase change materials' heat absorption and release properties. Water absorption tests confirmed

the physical durability of NRG-Wood mortars, highlighting their suitability for long-term construction applications.

Future research will focus on numerical investigations to improve these composites and explore their broader applications in sustainable building practices, including advanced numerical modulizations of thermal properties and lifecycle assessments.


### *Acknowledgements*

We extend our gratitude to the European Commission for its support and funding through the Marie Skłodowska-Curie Actions scheme, under GA: 101086440: i.e. BEST (Bio-based Energy-efficient materials and Structures for Tomorrow) project, https://cordis.europa.eu/project/id/101086440/es.


### *References*


[1] Ince, C., Tayançlı, S., and Derogar, S., "Recycling waste wood in cement mortars towards the regeneration of sustainable environment," Construction and Building Materials, vol. 299, pp. 123891, 2021.

[2] Jeon, J., Lee, J. H., Seo, et al., "Application of PCM thermal energy storage system to reduce building energy consumption", Journal of thermal analysis and calorimetry, Vol.111, pp. 279-288, 2013.

[3] Guardia, C., Schicchi, D., Caggiano, A., et al., "On the capillary water absorption of cement-lime mortars containing phase change materials: Experiments and simulations," Building Simulation, vol. 13, pp. 19-31, 2020.

[4] Sharma, A., Tyagi, V.V., Chen, C.R. et al., "Review on thermal energy storage with phase change materials and applications", Renewable and Sustainable energy reviews, Vol. 13, no.2, pp. 318-345, 2009.

[5] Tyagi, V.V., Kaushik, S.C., Tyagi, S.K. et al., "Development of phase change materials based microencapsulated technology for buildings: a review", Renewable and sustainable energy reviews, Vol. 15, no.2, pp.1373-1391, 2011.

[6] P. Kulkarni and A. Muthadhi, "Improving thermal and mechanical properties of light weight aggregate concrete using inorganic phase changing material, expanded clay aggregate, alccofine1203 and manufacturing sand," Innovative Infrastructure Solutions, vol. 6, pp. 1-10, 2021.

[7] Mankel, C., Caggiano, A., and Koenders, E., "Thermal energy storage characterization of cementitious composites made with recycled brick aggregates containing PCM," Energy and Buildings, vol. 202, 2019.

[8] Guimarães, T. C., Gomes, O. d. F. M., Oliveira de Araújo, O. M., et al., "PCM-impregnated textile-reinforced cementitious composite for thermal energy storage," Textiles, vol. 3, no. 1, pp. 98-114, 2023.

[9] Y.-H. Ahn, S. J. DeWitt, S. McGuire, et al., "Incorporation of phase change materials into fibers for sustainable thermal energy storage", Industrial & Engineering Chemistry Research, vol. 60, no. 8, pp. 3374-3384, 2021.

[10] Fabricio, F., and Rocha, F. S., "Bamboo-PCM: The use of Phyllostachys aurea culms as a receptacle for thermal storage through phase change material impregnation," Proceedings of 12th World Bamboo Congress, Taiwan, Proceedings, pp. 21-30, 2024.

[11] Pettersen, Roger C. "The chemical composition of wood", The chemistry of solid wood, Vol.207, pp. 57-126, 1984.

[12] Fengel, Dietrich, and Gerd Wegener, eds. "Wood: chemistry, ultrastructure, reactions", Walter de Gruyter, 2011.

[13] Rowell, R. M. "Handbook of wood chemistry and wood composites". 2013.

[14] Sonderegger, W., Niemz, P., & Kucera, L. J., "Thermal conductivity of wood. Journal of Building Physics", Vol. 35, no. 1, pp. 9-29, 2011.

[15] Zhang, J., Fang, Z., Wang, S., et al., "Review on utilization of phase change materials in building applications". Applied Energy, Vol. 220, pp. 242-273, 2018.

[16] Ramage, M. H., Burridge, H., Busse-Wicher, C., et al., "The wood from the trees: The use of timber in construction," Renewable and Sustainable Energy Reviews, vol. 68, pp. 333-359, 2017.

[17] Kretschmann, D., "Mechanical properties of wood," in Wood Handbook: Wood as an Engineering Material, Centennial ed., General technical report FPL; GTR-190, US Dept. of Agriculture, Forest Service, Forest Products Laboratory, pp. 5.1-5.46, 2010.

[18] Hill, Callum AS. "Wood modification: chemical, thermal and other processes", 2007.

[19] Arriaga, F., Wang, X., Íñiguez-González. et al., "Mechanical properties of wood: A review", Forests, Vol. 14, no. 6, 2023.

[20] Evans, P. D., "Wood Handbook: Wood as an Engineering Material", 1999.

[21] Gustavsson, L., Pingoud, K., and Sathre, R. "Carbon dioxide balance of wood substitution: comparing concrete- and wood-framed buildings". Mitigation and Adaptation Strategies for Global Change, Vol.15, no.6, pp. 551-560, 2010.

[22] Geremia, Francesca. "Le strutture edilizie in legno nella tradizione europea e mediterranea", Ricerche di storia dell'arte, Vol 37, no. 1, pp. 93-109, 2014.

[23] Akiner, M. E., Akiner, İ., Akiner, N., et al., "Using wood as a new generation building material in the context of sustainable development". Materials Protection, Vol. 63, no.1, 68, 2020.

[24] Green, Michael, and Jim Taggart. "Tall wood buildings: Design, construction and performance". Birkhäuser, 2020.

[25] Torgal, Fernando Pacheco, and Said Jalali. "Eco-efficient construction and building materials", Springer Science & Business Media, 2011.

[26] Kögl, M., Musso, F., and Brischke, C., "Wood-concrete composites – sustainable construction materials for bridges and buildings". Construction and Building Materials, Vol. 102, pp. 242-249, 2014.

[27] EN 196-1, "Methods of Testing Cement – Part 1: Determination of Strength", 2005.

[28] Palomar, I., G. Barluenga, and J. Puentes., "Lime–cement mortars for coating with improved thermal and acoustic performance", Construction and Building Materials, Vol. 75, pp. 306-314, 2015.

[29] Eugênio, T. M. C. "Propriedades físicas, mecânicas e térmicas de argamassas de revestimento com utilização de resíduos de pneu", Universidade Federal de Lavras, 2016.

[30] Lu, X., et al., "Evolution of specific heat capacity with temperature for typical supports used for heterogeneous catalysts," Processes, vol. 8, pp. 911, 2020.

[31] Palomar, I., and G. Barluenga., "A multiscale model for pervious lime-cement mortar with perlite and cellulose fibers", Construction and Building Materials, Vol.160, pp.136-144, 2018.

[32] Caggiano, A., et al. "A mesoscale approach for modeling capillary water absorption and transport phenomena in cementitious materials." Computers & Structures, Vol. 200, pp. 1-10, 2018.

[33] Martinelli, E. et al., "A numerical recipe for modelling hydration and heat flow in hardening concrete". Cement Concrete Composites. Vol. 40, pp. 48-58, 2013.

# Articoli

# Comparison of Different Calibration Methods for Vibrating Tube Densimeter Applied to Co2-Based Mixtures

**Nima Razmjoo[a,#], Alice Scolieri[a], Stefano Signorini[b], Manuele Gatti[a]**

*a Department of Energy, Politecnico di Milano, Milan, Italy*
*b Laboratorio Energia Ambiente Piacenza (LEAP), Piacenza, Italy*

*# Corresponding Author:* nima.razmjoo@polimi.it

## Abstract

Vibrating Tube Densimeters are capable of accurately measuring fluid density across a wide temperature and pressure range if a suitable calibration fluid is selected and a calibration model with accurately fitted parameters is used. This study aims to evaluate the performance of different classes of calibration models for a vibrating tube densimeter using $CO_2$ as the calibration fluid in the temperature range between 273 to 313 K and pressure up to 20 MPa in order to conduct density measurements of CO2-based mixtures.
An optimization framework is discussed for both the physically-based calibration model and the polynomial ones with RMSE of density of 0.40 and 0.32 kg/m³ respectively, when evaluating the density of the calibration fluid. To validate the calibrated models, measurements of binary mixtures of $CO_2$ and $CH_4$, for which literature data are available, have been performed at different $CO_2$ concentrations. Results show the similar performance of the physically-based and polynomial models (with at least 6 coefficients) for the validation fluid within the temperature range of calibration and for $CO_2$ concentrations above $90\%_{mol}$.

### *1. Introduction*

Density is a thermodynamic property used in many steps during process simulations and other applications, such as flow assurance, as it forms the basis of several flowmeters [1]. In the research area, knowledge of the density of different pure and binary mixtures of fluids is crucial for the development of accurate equations of state (EOS) [2]. Various experimental setups have been investigated for laboratory-scale density measurements, including single-sinker [3], [4] and two-sinker [5], [6] densimeters, microwave re-entrant cavity resonators [7], magnetic suspension balances [8], and Vibrating Tube Densimeters (VTDs) [9]. While some of these setups work by directly measuring density-related variables, such as mass or volume, others such as VTD do not measure density directly. In this case, finding an appropriate method to correlate the measured variable (oscillation period) to the target variable (density) plays and important role in the accuracy of the generated data. This requires understanding the behavior of the experimental apparatus

and developing a calibration that accurately replicates its behavior under test conditions. The choice of calibration model can influence the new experimental data that will ultimately result from the work. Since the initial introduction of VTD in 1998 [9] calibration models have been continuously developed to reach a robust method with physically meaningful parameters, reduce structural complexity, and enhance the extrapolation behavior of the calibration model beyond the range of the calibration fluid data [10]. The models can be divided into discrete and continuous categories and different approaches can be summarized below and in Table 1:

- Discrete models
  - ◊ One calibration fluid
  - ◊ Two calibration fluids
- Continuous models (one or more calibration fluids can be used)
  - ◊ Polynomials
    - · Fully empirical
    - · Semi-empirical
  - ◊ Physically-based
    - · Forced path mechanical calibration (FPMC)
    - · May's model

Such models are based on or can be rearranged according to the simple relation as in Equation (1). The relationship between $\tau^2$ and ρ is not exactly linear and for this reason, A and B depend both on temperature and pressure, and a viscosity correction might be needed if the test fluid is very different than the calibration one. To this end, the selection of a proper calibration method is crucial to provide mixtures density measurements with satisfactory accuracy with a Vibrating Tube Densimeter, to minimize the experimental uncertainty contribution resulting from the calibration step.

$$\rho = A\tau^2 - B \quad \textbf{(1)}$$

Discrete models require the estimation of the values of A and B at each temperature and pressure. While they achieve good accuracy, their implementation requires extensive experimental effort with one or two different calibration fluids at the exact temperature and pressure of the test fluid. This implementation prevents us from understanding the behavior of the system and limits the test condition to those for which calibration fluid data are available.

Continuous models enable us to capture the trend of A and B as polynomial functions

of temperature and pressure. Hence, it is not required to measure the calibration fluid at the exact T and p. Instead, including sufficient data in the selected temperature and pressure range, which covers the extreme conditions of the test is sufficient. Further advancement of continuous models is studied by implementing the physical behavior of the densimeter in the functional form of the calibration model. This can be achieved by incorporating the vacuum behavior of the apparatus to enhance the model by capturing the behavior of the VTD which leads to the semi-empirical polynomial model. However, it is important to cover the entire range of targeted density values by utilizing one or more calibration fluids [11].

Moving in this direction led to the introduction of forced-path mechanical calibration (FPMC) and more recently, the integration of polynomial models with FPMC by May et al. [10]. By implementing such a model, the VTD can be used in extended operational ranges than the calibration one while maintaining good accuracy. Table 1 below summarizes the different calibration approaches, showing the model, calibration fluids, temperature and pressure range, phases, and their performance with respect to the reported reference data or EOS.

**Table 1.** Summary table of different calibration models reported in the literature and their performance for fitting the calibration fluid density calculated with the model to fit the reference data and/or reference EOS.

*(RD: Relative Deviation, MRD: Maximum Relative Deviation, AAD: Average Absolute Deviation, AARD: Average Absolute Relative Deviation, RMSE: Root Mean Square Error, U: Overall Uncertainty, %U: Overall Relative Uncertainty)*

| Calibration model | Reference | Calibration fluid(s) | T [K] | p [MPa] | Phase(s) | Performance* |
|---|---|---|---|---|---|---|
| Discrete | Sousa 1992 [12] | Toluene | 300 – 370 | 0 – 19 | L | %U [V]: ±1%[i] |
| | Lagourette 1992 [13] | $H_2O$ | 278 – 353 | 0.1 – 40 | V, L | %U [L]: ±0.02%[i] |
| | Sousa 2019 [14] | He, $H_2O$ | 283 – 473 | 1 – 65 | V, L, SC | %U = ±0.1%[ii] |
| | | | | | | %U = ±(0.06 to 1.4%)[iii] |
| Empirical polynomial | Ihmels 2001 [15] | $H_2O$, Butane | 273 – 623 | 0.3 – 40 | V, L, SC | RD [L] = ±0.020% to ±0.075% |
| | | | | | | MRD [V, SC] = ±0.3% |
| | | | | | | RMSE = ±0.3 kg/m³ |
| | Atilhan 2012 [16] | $N_2$, $CH_4$ | 250 – 450 | 0 – 65 | V, SC | AARD = 0.07% |
| Semi-empirical polynomial | Holcomb and Outcalt 1998 [17] | $N_2$, $H_2O$ | 273 – 423 | 0 – 14 | V, L, SC | RMSE = 0.5 kg/m³ |
| | Outcalt and McLinden 2007 [18] | Propane, Toluene | 270 – 470 | 0.5 – 50 | V, L, SC | AAD [Propane] = 0.10 kg/m³ |
| | | | | | | AAD [Toluene] = 0.12 kg/m³ |
| | Outcalt 2018 [11] | Toluene, $H_2O$ | 270 – 470 | 0.5 – 50 | L | AAD [Toluene] = 0.11 kg/m³ |
| | | | | | | AAD [Water] = 0.08 kg/m³ |
| | Sampson 2019 [19] Yang 2020 [20] | He, $H_2O$ | 283 – 382 | 5 – 91 | L, SC | AAD = 0.17 kg/m³ |
| FPMC | Bouchot and Richon 2001 [21] | $H_2O$, R-12 | 253 – 333 | 2.5 – 40 | V, L | AAD = 0.20 kg/m³ |
| Physically based by May et al. | May 2014 [10] | $H_2O$, Toluene | 273 – 448 | 0 – 135 | V, L | RMSE = 0.22 kg/m³ |
| | May 2014 [10] | He, $H_2O$, $CO_2$ | 304 – 473 | 5 – 65 | V, L, SC | RMSE = 0.35, 0.44 kg/m³ (for two different VTDs) |
| | May 2014 [10] | He, $H_2O$, Toluene | 283 – 473 | 1 – 65 | V, L, SC | RMSE = 0.09, 0.12, 0.17 kg/m³ (for three different VTDs) |
| | Gomez-Osorio 2016 [22] | Ar, $N_2$, $CH_4$ | 303 – 474 | 10 – 137 | SC | U [p<200 kg/m³] = ±0.1 kg/m³ |
| | | | | | | %U [p>200 kg/m³] = ±0.05% |
| | Sampson 2019 [19] Yang 2020 [20] | He, $H_2O$ | 283 – 382 | 5 – 91 | L, SC | AAD = 0.31 kg/m³ |
| | Jiao 2020 [23] | $CH_4$, Propane | 203 – 423 | 0 – 35 | V, L | RMSE = 1.34 kg/m³ |
| Other approaches | Lampreia 2011 [24] | $H_2O$, Toluene, Cyclohexane, Isooctane | 283 – 323 | 0.1 – 30 | L | RD = ±0.2% |

* Various indicators are used in the literature to evaluate calibration model behavior with the calibration fluid. The relevant indicator and its value are provided here to demonstrate the performance of different models. Uncertainty is reported where no other indicator was mentioned in the literature. To check the different contributions to the reported uncertainty, please check the reference literature.

[i] For HCFC 142b as the test fluid

[ii] For benzene and cyclohexane as the test fluid.

[iii] For $CO_2$ as the validation fluid.

Densimeter calibration over a wider range enhances usability and extending calibration to low densities improves accuracy in the vapor region and shall be repeated over time to account for factors like instrument aging. In this work, four models with their parameters fitting strategy and performances are compared. The empirical approach involves developing two different polynomials to analyze the significance of terms, while the physically-based model by May et al. [10] represents the latest development in physically-based models. Additionally, the classical discrete approach was implemented to provide a comprehensive view of the performance of different model categories to predict the density of CO2-based mixtures.

## 2 Methodology

### *2.1. Apparatus description and measurement methodology*

The setup used in the present work consists of a DMA 512 – HPM commercial Vibrating Tube Densimeter (VTD) manufactured by Anton Paar as described more in detail by Mantovani et al. [25]. The VTD is composed of a U-shaped vibrating tube to determine liquid and gas densities under pressures of up to 20 MPa and within a temperature range of 253.15 K to 423.15 K. Figure 1 shows a schematic of the VTD and other components of the setup, which enables us to control the temperature and pressure of the loaded sample. The sample fluid was introduced into the system directly from certified supply cylinders or a loading cell. The use of a hand pump allows us to pressurize the loading cell to 20 MPa in cases of lower source pressure, preventing phase separation and variation in the composition of the fluid introduced to the line.

The temperature of the sample line and devices was regulated using two distinct thermostatic baths, which allow temperature settings within the range of 203.15 K to 453.15 K, with a resolution of 0.1 K. The bath temperatures were monitored with a calibrated PT100 thermometer located in the silicone oil of the bath, while the built-in temperature sensor of the VTD block was used to read the exact temperature inside the VTD. The overall standard uncertainty of the cell temperature was estimated to be 0.05 K, considering temperature gradients and fluctuation. The pressure of the line was monitored using three pressure transducers, each calibrated for different ranges: 0 to 2 MPa, 2 to 10 MPa, and 10 to 20 MPa, with a relative uncertainty of 0.06% of full scale as defined by internal calibration.

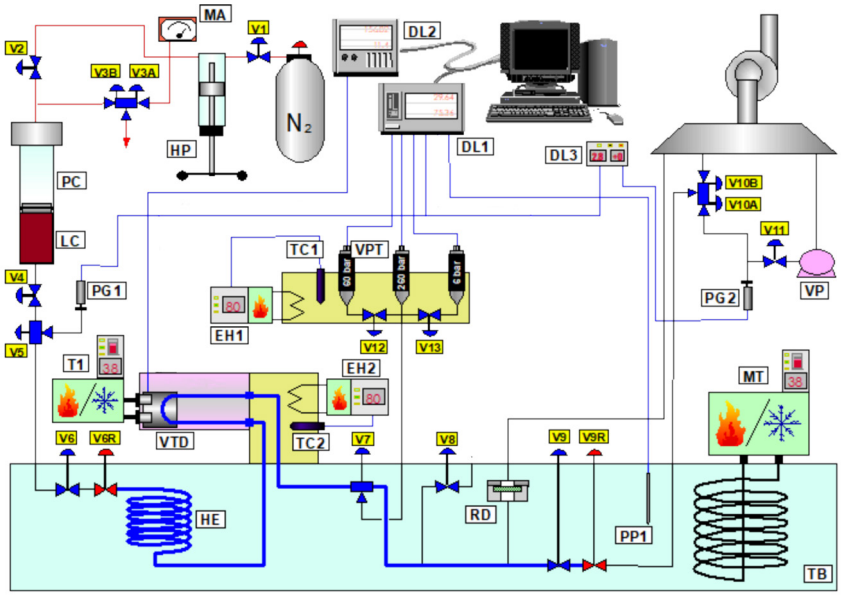


**Figure 1.** Experimental VTD apparatus schematic diagram with main components denoted as V1-13: manually controlled valves, LC: loading cell, HP: hand pump, TB: thermostatic bath, VTD: vibrating tube densimeter block and built-in temperature sensor, PT: pressure transducers, PP1: platinum probes of thermostatic bath to monitor its temperature.

Density measurement can be performed in different modes. In the first method, the pressurization or vent valve can be regulated to reach the target pressure level at the maintained temperature, without careful monitoring of the pressure change rate. In this mode, it is necessary to wait for the system until the pressure and oscillation period become stable [23]. Alternatively, the pressurization and vent valves can be regulated to maintain a slight and continuous rate of pressure change. Bouchot and Richon [9] suggested this method of data acquisition as it expands the application of VTD to estimate saturation points. They discussed maintaining a pressure change rate of ±0.05 MPa/s and regulating the temperature of the VTD to be slightly (i.e. ±0.2 K) higher or lower than the thermostatic bath, making it possible to form the first bubble or drop of liquid inside the VTD block, respectively. Several authors have reported bubble or dew point data of mixtures using this measurement method with modified methodologies [26], [27], [28], [29]. However, there is still a lack of clear methodology to estimate the saturation points with known uncertainty.

It is worth noting that maintaining such a low pressure change rate requires an experienced operator to avoid losing the sample and acquiring data over the entire isotherm. In this work, this approach was used for data acquisition of the calibration fluid (i.e., $CO_2$) as well as the test fluids. Hence, we could approach the saturation points in the phase-changing isotherms and gather more data in the supercritical region, which is of interest for future tests with the apparatus.

Before each measurement, the entire system was evacuated using a vacuum pump to prevent water condensation from the air at low temperatures and to eliminate impurities. Additionally, manual valves were installed to regulate pressure during VTD calibration and density measurements. A typical test procedure starts with introducing the sample fluid to the system by carefully regulating the valve to maintain a pressurization rate of 0.05 MPa/s. As the pressurization rate tended to decrease with increasing line pressure, the valve was regulated again to maintain the target pressurization rate. Data acquisition was performed over the entire isotherm, and the data obtained during the pressurization step was used only in the vapor region. Although this would not significantly affect the pure fluid, it is important to measure the mixture to ensure that the mixture composition does not alter inside the densimeter. The same procedure was used for depressurizing the line, starting from the highest pressure of the test (i.e., 20 MPa) and maintaining a depressurization rate of 0.05 MPa/s by regulating the vent valve. The data in the liquid region was considered from this set of experiments. In the supercritical region, data below the critical pressure of $CO_2$ was taken from the pressurization step, while data from the maximum pressure down to the critical pressure of $CO_2$ was taken from the depressurization step.

### *2.2. Calibration models and fitting strategy*

#### *Discrete*

Using two reference fluids with known densities is a classical method for converting the oscillation periods measured with the VTD to the density of the test fluid [21]. Three measurements at ideally the same temperature and pressure are necessary for such a transformation; with the test fluid and the two calibration fluids as well. Then, with linear interpolation, the density of the test fluid can be determined. The main problem with this approach is the propagation of uncertainty, as two reference fluids and their corresponding reference EOS are involved. To overcome this issue, one calibration fluid

can be used along with the oscillation period in the vacuum condition at the target temperature [12], [13] using Equation (2):

$$\rho(T,p) = \rho_{REF}(T,p) + \rho_{REF}(T,p_1) * \frac{\tau^2(T,p) - \tau^2_{REF}(T,p)}{\tau^2_{REF}(T,p_1) - \tau^2_0(T)} \quad \textbf{(2)}$$

With the formulation in Equation (2), using the reference fluid density at a reference pressure (e.g., 1 MPa) better represents the pressure dependency of the density on changes in the oscillation period [13]. The idea of using one calibration fluid is further developed through the continuous models, which not only decreases the uncertainty of the measured data but also introduces some physically meaningful parameters to the calibration equation.

*Continuous*

Continuous models present different approaches: some of them are based on the physical properties of the densimeter and its physical behavior during the oscillations (physically-based and semi-empirical), while other models do not have a physical meaning but simply use a generic function which in any case leads to an accurate result. Polynomial models calculate unknown density as a function of T, p, and τ. They are easy to develop since they do not require studying VTD vibrations, but their fit quality is only measured by error relative to the calibration fluid EOS. Complex polynomials can be overfitted by incorporating measurement errors, while simple ones can be underfitted by not capturing trends of data well. To ensure a non-biased model, each term's meaning must be analyzed in detail, and the training dataset must be broad enough to ensure generality and prevent overfitting.

Outcalt and McLinden [18] developed a polynomial model, by expanding the A and B coefficients of Equation (1) from a statistical analysis of the models previously advanced by several authors [15], [17] to better understand the significance of the terms. By introducing the vacuum period term to the polynomial model as well as two different calibration fluids, they tried to implement the thermal behavior of the tube's material in the functional form of the calibration model and expand the validity of the model over the wider density range. The proposed polynomial is represented in Equation (3), where the denominator of the A coefficient represents the squared of the vacuum period.

$$\rho_{VTD} = \frac{(A_1 + A_2T + A_3T^2 + A_4T^3 + A_5p + A_6p^2 + A_7Tp)}{(C_0 + C_1T + C_2T^2)^2}\tau^2 - (B_1 + B_2T^2 + B_3T^3 + B_4p + B_5p^2 + B_6Tp) \quad (3)$$

The same model has been recently considered by other authors [19], [20]. Yang et al. [20] recalibrated the densimeter with water and helium using Equation (3), validated with argon and propane to finally measure propylene glycol. Two models were calibrated with these data: the polynomial model and the physically-based model of May et al. [10]. The polynomial model is proven to be more accurate in the calibration phase. Sampson et al. [19] analyzed a simplified version of Equation (3) with 9 terms where the terms with the highest exponent for T and p were eliminated to achieve a simpler but still accurate compromise. The parameters were fitted with a non-linear damped least-squared method. They concluded that the simplified version represents the same accuracy as the model proposed by the manufacturer and better performance in the validation tests, while slightly less accurate than the 13-term one.

In this work, initially, the 13-term polynomial from Outcalt and McLinden [18] was analyzed. Subsequently, the significance of each term was assessed to produce a reduced polynomial model. Initially, C parameters were determined by fitting a 2$^{nd}$-order polynomial to the vacuum oscillation period at different temperatures (as reported in Figure 3). Fitting was performed via constrained non-linear optimization with MATLAB (www.mathworks.com) using fmincon with MultiStart algorithm to provide multiple starting points, ensuring a sound local minimum is obtained. Values estimated by Sampson et al. [19] for their apparatus were used as the initial guess. At each step, boundaries were adjusted ensuring no fitting coefficient was close to its defined boundary.

To understand the importance of each term of Equation (3) on the final result, a significance analysis is performed by multiplying all the coefficients by all the variables related to it (T, p or $\tau^2/\tau_0^2$) along all the operative ranges to see the variation of their values. The term with lower significance is eliminated and the polynomial is reoptimized, eventually iterating in case of problematic boundaries. If the result is similar or better than the previous one the term is eliminated definitively, otherwise other terms chosen according to the significance analysis are considered. The term that leads to the lower error is then eliminated definitively and the procedure starts again from the beginning until the polynomial is reduced to the simpler formula.

Figure 2 shows the values of the objective function (RMSE relative, RMSEr) and RMSE after re-fitting the model to each specific polynomial formulation. The objective function increased slightly after eliminating the first term and remained nearly constant from the 13-term to the 5-term polynomial while increasing significantly for simpler formulations, but the 6-term polynomial showed a lower RMSE compared to the 5-term one. For this reason, the 6-term polynomial is chosen for further comparison together with the 13-term reference formulation.

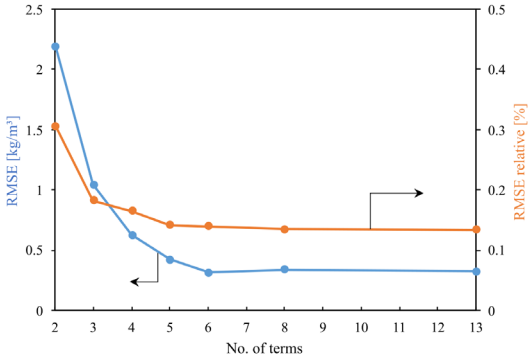


| No. of terms | A coefficients | B coefficients |
|---|---|---|
| 2 | $A_1$ | $B_1$ |
| 3 | $A_1,A_3$ | $B_1$ |
| 4 | $A_1,A_3$ | $B_1,B_2$ |
| 5 | $A_1,A_3,A_5$ | $B_1,B_2$ |
| 6 | $A_1,A_3,A_5,A_6$ | $B_1,B_2$ |
| 8 | $A_1,A_2,A_3,A_5,A_6$ | $B_1,B_2,B_5$ |
| 13 | $A_1,A_2,A_3,A_4,A_5,A_6,A_7$ | $B_1,B_2,B_3,B_4,B_5,B_8$ |

**Figure 2.** Term-by-term reduction of the polynomial model highlighting the trends of the RMSE relative (RMSEr) and RMSE values. RMSE relative is the objective function actually minimized by the optimizer.

May et al. [10] developed a physically-based calibration model as noted in Equation (4), to correlate the oscillation period of the densimeter to the fluid density, using seven parameters adjusted to the vacuum and calibration fluid oscillation periods at test conditions. The method is the extension of the framework developed by Holcomb and Outcalt [17] which is similar in several aspects to the model presented by Bouchot and Richon [21] that allows the pressure dependence of the tube's volume to be calculated from the elastic and geometrical properties of the tube.

$$\rho_{VTD} = \frac{\rho_M S_{00}}{1 + \alpha_V t + \beta_V p}\left(\left(\frac{\tau}{\tau_{00}(1 + \varepsilon_{\tau 1} t + \varepsilon_{\tau 2} t^2)}\right)^2 (1 + \beta_\tau p) - 1\right) \quad \textbf{(4)}$$

Re-writing in the conventional form of $\rho_{VTD}=A\tau^2- B$, Equation (4) results in:

$$\rho_{VTD} = \left\{\left(\frac{\rho_M}{S_{00}\tau_{00}^2}\right)\left[\frac{(1+\beta_\tau p)}{(1+\varepsilon_{\tau 1}t+\varepsilon_{\tau 2}t^2)^2(1+\alpha_V t+\beta_V p)}\right]\right\}\tau^2 - \left\{\frac{\rho_M}{S_{00}(1+\alpha_V t+\beta_V p)}\right\} \quad \textbf{(5)}$$

Three of the seven parameters of this model, namely $\tau_{00}$, $\varepsilon_{\tau 1}$, and $\varepsilon_{\tau 2}$, represent the behavior of the system in vacuum conditions as the temperature changes. The vacuum periods at different temperatures are fitted to a second-order polynomial function using linear least squares regression on the measured vacuum data as written in Equation (6):

$$\tau_{00}(t) = \tau_{00}(1+\varepsilon_{\tau 1}t+\varepsilon_{\tau 2}t^2) \quad \textbf{(6)}$$

Five different temperature levels were considered, and the oscillation period was measured twice: once at the beginning of the measurement before pressurizing the line, and then at the end of depressurization after performing the vacuum. Hence, a total of ten data points were used to calculate the vacuum parameters. Figure 3 shows the fitted polynomial on the measured vacuum periods which is reported in Table 2.

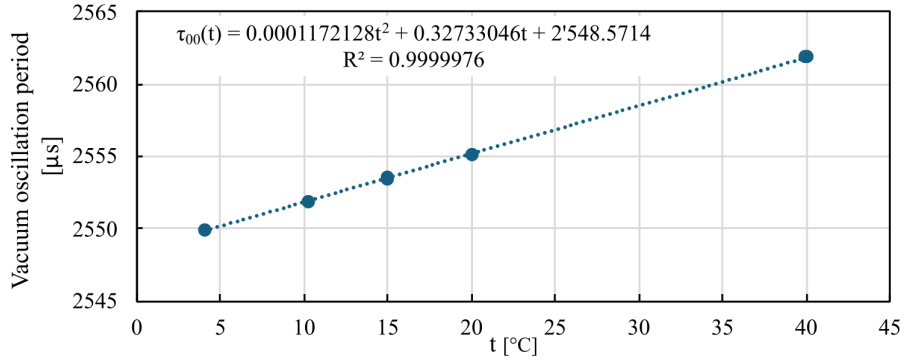


**Figure 3.** Second-order polynomial curve and equation fitted to measure vacuum periods at different temperature levels. t is the temperature in °C

**Table 2.** Measured vacuum oscillation periods at different temperature levels.

| Temperature [°C] | Oscillation period [μs] | Temperature [°C] | Oscillation period [μs] |
|---|---|---|---|
| **4.01** | **2549.890** | **14.99** | **2553.497** |
| **4.02** | **2549.894** | **20.00** | **2555.175** |
| **10.19** | **2551.911** | **20.02** | **2555.179** |
| **10.19** | **2551.915** | **39.98** | **2561.849** |
| **14.94** | **2553.483** | **40.09** | **2561.877** |

To optimize the other four parameters of the model, the oscillation period of pure $CO_2$ was measured at four temperature levels (273, 277, 293, and 313 K) up to 20 MPa. The density obtained from the measured data was compared against the multiparameter Helmholtz energy EOS for pure $CO_2$ developed by Span and Wagner [30] to optimize the objective function. The optimization procedure was performed in MATLAB by minimizing the objective function as reported in Equation (7):

$$RMSEr = \sqrt{\frac{\sum_{n=1}^{N}\left(\frac{\rho_{VTD}-\rho_{EOS}}{\rho_{EOS}}\right)^2}{N}} \quad (7)$$

The temperature parameter other than the ones estimated by correlating vacuum periods to temperature is α_V which depends on the material of the tube and its elastic behavior with temperature [23]. For this parameter, an average value of (13.62 ± 0.68) × $10^{-6}$ $K^{-1}$ is reported by May et al. [10] and is used as the initial guess in the optimization of model parameters with the small bound to let the optimizer adjust the value due to the peculiarity of our system.

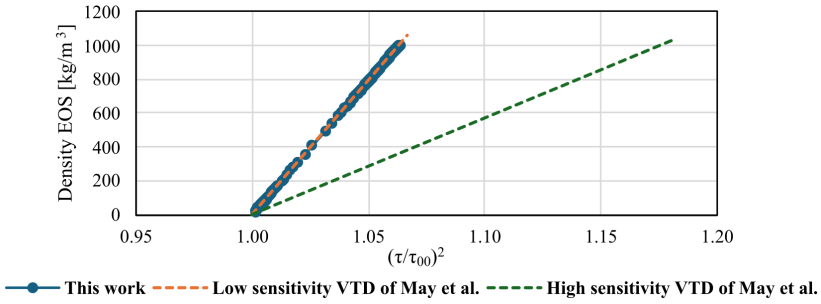


**Figure 4.** Sensitivity of the VTD reported by May et al. [10] for two different apparatuses ($S_{oo}$ of 0.552 for the low sensitivity and 1.53 for the highly sensitive VTD) and from this work.

Regarding the pressure-dependent parameters, the volume pressure-dependence parameter, $\beta_V$, describes the expansion of the tube from standard elastic theory which depends on the tube material. To estimate the pressure dependence of the spring constant, $\beta_\tau$, the variation of the tube's outer radius while the system undergoes pressurization should be estimated [10], [23]. While for estimation $\beta_V$ same approach as of $\alpha_V$ was followed, $\beta_\tau$ is optimized with more careful variations of bounds to model the behavior of the pressurized systems.

$S_{oo}$ highlights the sensitivity of the system to the measured oscillation period. Among the VTDs analyzed by May et al. [10], this value is reported in a range between 0.552 and 1.628 for different systems, indicating the lowest to highest sensitivity of the system to the oscillation period, respectively. In Figure 4, the sensitivity of the target apparatus is compared with the ones studied by May et al. [10].

## *3. Results and discussion*

### *3.1. Calibrated parameters and model performance*

The estimated parameters of the physically-based model developed in this work are reported in Table 3, along with the values reported by Jiao et al. [23] for their calibration using the same model. Comparing the values, it can be observed that the sensitivities of these two systems are similar, with the apparatus in this work being slightly more sensitive, as indicated by the relatively higher value of $S_{oo}$, as shown in Figure 4.

In Table 4, the parameters of the polynomial models are represented. As mentioned in the methodology section, careful control of the boundary of each parameter for the 13-term polynomial was considered, by expanding the selected bounds gradually to control the value of the objective function of Equation (7) and keep each estimated value far from the imposed boundary. Moving towards the 6-term polynomial, it was observed that eliminating pressure-dependent parameters from the B coefficients in Equation (3) and highest order coefficients of A coefficients as well as the first-order temperature-dependent one, leads to an objective function value of 0.14% which is slightly higher than the 13-term one, while lowering slightly the RMSE as represented in Table 5. Although the choice of the objective function plays a role, additional terms in the 13-term polynomial avoid capturing the correct trend of the calibration fluid data as the bounds of those parameters did not let the optimizer make them zero.

**Table 3.** Optimized parameters of the physically-based model for the apparatus of this work and the values reported by Jiao et al. [23].

| Parameters \ Model | | Jiao et al. [23] | This work |
|---|---|---|---|
| $S_{00}$ | [-] | 0.5527 | 0.5601 |
| $\tau_{00}$ | [μs] | 2567.961 | 2548.571 |
| $\varepsilon_{\tau 1}\cdot 10^{6}$ | [$K^{-1}$] | 126.952 | 128.437 |
| $\varepsilon_{\tau 2}\cdot 10^{8}$ | [$K^{-2}$] | 5.830 | 4.599 |
| $\alpha_V/3\cdot 10^{6}$ | [$K^{-1}$] | 13.618 | 14.969 |
| $\beta_V\cdot 10^{5}$ | [$MPa^{-1}$] | 3.627 | 6.923 |
| $\beta_\tau\cdot 10^{5}$ | [$MPa^{-1}$] | 0.201 | -0.196 |

Figure 5, reports the density values of CO2 data used during the parameter optimization for the the three models developed in this work. The uncertainty in density prediction of the Span and Wagner EOS [30] for $CO_2$ is reported to be 0.03% to 0.05% for temperatures up to 523 K and pressures up to 30 MPa. For data points above 5 MPa, most lie within the uncertainty bound of the EOS for all the calibration models, except at the supercritical temperature of 313 K, where points near the phase transition show faster density changes with pressure. Another region with higher relative deviation is the vapor region. Besides the higher relative deviation due to low density values, the VTD's accuracy in predicting density in the vapor region is also lower because of its limited sensitivity compared to more accurate apparatuses like sinker densimeters [4].

**Table 4.** Parameters of polynomial models calibrated in this work.

| Parameter \ Polynomial | | Sampson et al. [19] 13-term | This work 13-term | This work 6-term |
|---|---|---|---|---|
| $A_1$ | [$kg/m^3$] | 1.60E+04 | 1.60E+04 | 1.60E+04 |
| $A_2$ | [$kg/m^3$-K] | 1.36E-01 | 1.25E-01 | n.a. |
| $A_3$ | [$kg/m^3$-$K^2$] | -1.77E-03 | -1.71E-03 | -1.61E-03 |
| $A_4$ | [$kg/m^3$-$K^3$] | 4.77E-07 | 2.39E-07 | n.a. |
| $A_5$ | [$kg/m^3$-MPa] | -1.73E-01 | -1.66E-01 | -4.96E-02 |
| $A_6$ | [$kg/m^3$-$MPa^2$] | -4.88E-03 | -4.98E-03 | -1.74E-03 |
| $A_7$ | [$kg/m^3$-K-MPa] | -6.30E-05 | -6.63E-05 | n.a. |
| $B_1$ | [$kg/m^3$] | 1.60E+04 | 1.60E+04 | 1.60E+04 |
| $B_2$ | [$kg/m^3$-$K^2$] | -1.49E-03 | -1.47E-03 | -1.61E-03 |
| $B_3$ | [$kg/m^3$-$K^3$] | 3.69E-07 | 1.84E-07 | n.a. |
| $B_4$ | [$kg/m^3$-MPa] | -7.47E-02 | -6.75E-02 | n.a. |
| $B_5$ | [$kg/m^3$-$MPa^2$] | -5.47E-03 | -5.38E-03 | n.a. |
| $B_6$ | [$kg/m^3$-K-MPa] | -9.06E-05 | -9.01E-05 | n.a. |

The polynomial model can better capture the trend of the vapor density data due to their higher flexibility as they incorporate more adjustable terms, which is also demonstrated

by Yang et al. [20]. Looking at the residual values in Figure 5, the residuals of density are comparable for the liquid and vapor regions, while the higher deviation trend at supercritical temperature is still observable for all the models, slightly better for polynomials showing less bias in such regions.

The main uncertainty contributions to the data used in the calibration models and showed in Figure 5 include uncertainties in the measured values of temperature, pressure, oscillation period, and repeatability of vacuum period reading at different temperatures. For those contributions, which can be considered as related to the measurements only (and not due to the calibration method or to the EOS of the calibration fluid, that have to be accounted for the whole uncertainty budget after calibration is completed), the average expanded uncertainty in the vapor region (pressures below 7 MPa and $\rho<200$ kg/m³) is estimated as ±0.06 kg/m³, while the same contribution in the liquid region increases to ±0.13 kg/m³. In relative terms, in the vapor region the estimated relative uncertainty is ±0.15%, while it decreases to ±0.01% for liquid density.

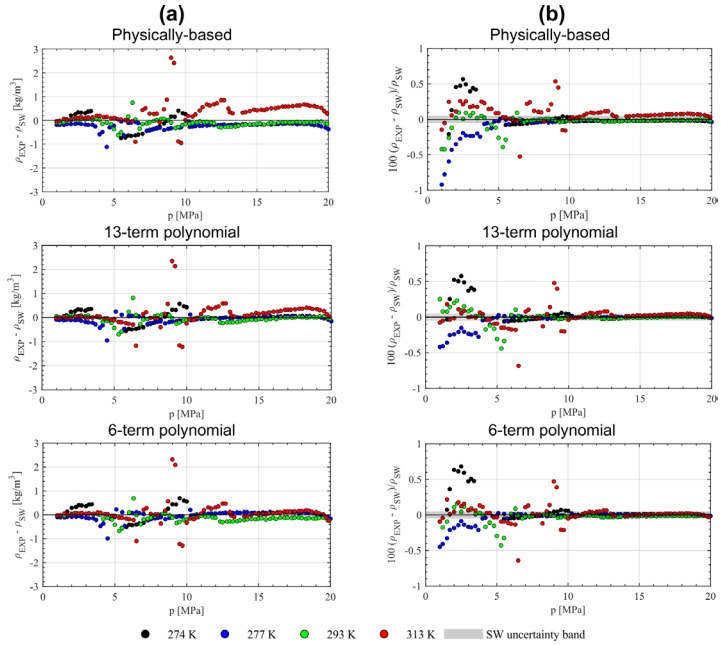


**Figure 5.** (a) Absolute Residuals in kg/m³ and (b) relative deviation of the calibration fluid density calculated with each optimized calibration model and compared with data from reference EOS for $CO_2$ (at the measured T and p).

Based on the Key Performance Indicators (KPIs) presented in Table 5, a low bias value indicates that all models effectively capture the underlying data trend, thereby avoiding underfitting. Conversely, the low RMSE within the density range of 10 to 1000 kg/m³ indicates a reasonable fitting within the whole density region. This achievement is linked to the controlled minimization of the objective function.

**Table 5.** KPIs of different calibration models studied in this work.

| KPI \ Model | | Physically based | 13-terms polynomial | 6-terms polynomial |
|---|---|---|---|---|
| **Bias** | [kg/m³] | -0.007 | 0.004 | -0.010 |
| **AvgAD** | [kg/m³] | 0.28 | 0.18 | 0.19 |
| **AvgARD** | [-] | 0.09% | 0.07% | 0.07% |
| **RMSE** | [kg/m³] | 0.40 | 0.32 | 0.32 |
| **RMSEr** | [-] | 0.16% | 0.13% | 0.14% |

### *3.2. Validation with $CO_2$-based binary mixture*

To validate the performance of the calibration models, literature data of $CO_2$+$CH_{42}$were gathered and new experimental data were generated at very similar conditions (composition, temperature and pressure). The test fluids mainly consist of $CO_2$ (90% molar or greater) with other components representing impurities in $CO_2$ transportation conditions. To perform validation tests at different temperatures and pressures, binary mixtures of $CO_2$ and $CH_4$ were gravimetrically prepared. Since it is almost impossible to replicate exactly the same temperature, pressure, and composition as of the literature data, the evaluation of data sets is performed both with the calibrated VTD models and against GERG-2008 [31], an accurate mixture model for $CO_2$+$CH_4$ with an uncertainty in density of 0.3% in the liquid [3]. Results are reported in Table 6.

The discrete model outperforms the other two models where calibration fluid data is available at the same T and p for CO2 concentration from 0.90 to 0.95 mol/mol. Continuous models show similar accuracy in the liquid phase, considering that their deviation is close to or within the average uncertainty of EOS data (i.e., ±0.3%). Is worth mentioning that the density predictions with the May's model and polynomial ones differ no more than 0.33 kg/m³ in the liquid/supercritical points and less than 0.1 kg/m³ for vapor data, confirming an agreement close to the uncertainty band for properly calibrated physically-based or polynomial models.

Generally, the data represented in this work, shows lower deviation to GERG-2008,

compared to the literature data targeted in the wide CO2 concentration range, except the supercritical region with CO2 concentration of 0.9887 at a critical temperature of CO2 of 304 K where higher uncertainty of the EOS is reported. [30], [31].

**Table 6.** Literature and experimental data of this work were used as validation and their performance against GERG-2008.

$$\%RD = (\rho_{EXP} - \rho_{GERG\text{-}2008}) / \rho_{GERG\text{-}2008}$$

| Literature data* | | | GERG-2008 | This work | | | | | | | | | | | |
|---|---|---|---|---|---|---|---|---|---|---|---|---|---|---|---|
| | | | | | | | | *Physically based* | | *13-term polynom.* | | *6-term polynomial* | | *Discrete*** | |
| Ref | Density [kg/m³] | %RD | Density [kg/m³] | $CO_2$ mol frac. | T [K] | p [MPa] | Phase | Density [kg/m³] | %RD | Density [kg/m³] | %RD | Density [kg/m³] | %RD | Density [kg/m³] | %RD |
| [32] | 76.340 | -0.25 | 75.790 | 0.9887 | 273.91 | 2.998 | V | 75.196 | -0.78 | 75.177 | -0.81 | 75.254 | -0.71 | 74.945 | -1.11 |
| | 934.540 | 0.07 | 928.497 | 0.9887 | 273.80 | 6.100 | L | 925.904 | -0.28 | 926.056 | -0.26 | 926.116 | -0.26 | 926.591 | -0.21 |
| | 961.980 | 0.11 | 955.898 | 0.9887 | 273.85 | 10.101 | L | 954.001 | -0.20 | 954.158 | -0.18 | 954.287 | -0.17 | 953.820 | -0.22 |
| | 988.490 | 0.13 | 982.366 | 0.9887 | 273.92 | 15.101 | L | 980.840 | -0.16 | 981.017 | -0.14 | 981.149 | -0.12 | 978.396 | -0.40 |
| | 1005.730 | 0.11 | 999.589 | 0.9887 | 273.97 | 19.023 | L | 998.160 | -0.14 | 998.361 | -0.12 | 998.429 | -0.12 | 990.823 | -0.88 |
| [33] | 44.753 | 0.21 | 43.819 | 0.9887 | 288.25 | 2.098 | V | 43.862 | 0.10 | 43.932 | 0.26 | 43.907 | 0.20 | 43.585 | -0.53 |
| | 873.469 | 0.01 | 895.741 | 0.9887 | 288.24 | 12.502 | L | 894.805 | -0.10 | 894.911 | -0.09 | 894.875 | -0.10 | 897.209 | 0.16 |
| [34] | 64.010 | 0.11 | 63.708 | 0.9887 | 304.24 | 3.100 | SC | 63.808 | 0.16 | 63.774 | 0.10 | 63.775 | 0.11 | 63.029 | -1.07 |
| | 122.000 | 0.53 | 120.902 | 0.9887 | 304.24 | 4.999 | SC | 121.205 | 0.25 | 121.080 | 0.15 | 121.106 | 0.17 | 118.490 | -1.99 |
| | 793.490 | 0.06 | 792.197 | 0.9887 | 304.21 | 12.600 | SC | 791.550 | -0.08 | 791.452 | -0.09 | 791.333 | -0.11 | 800.215 | 1.01 |
| | 827.200 | 0.06 | 824.644 | 0.9887 | 304.20 | 15.000 | SC | 824.318 | -0.04 | 824.223 | -0.05 | 824.080 | -0.07 | 829.392 | 0.58 |
| | 872.860 | 0.04 | 871.335 | 0.9887 | 304.20 | 20.003 | SC | 870.800 | -0.06 | 870.719 | -0.07 | 870.463 | -0.10 | 872.968 | 0.19 |
| [35] | 836.064 | 2.82 | 808.103 | 0.9554 | 288.30 | 8.999 | L | 803.852 | -0.53 | 803.928 | -0.52 | 803.885 | -0.52 | 808.688 | 0.07 |
| | 877.182 | 2.82 | 849.317 | 0.9554 | 288.29 | 12.495 | L | 844.234 | -0.60 | 844.307 | -0.59 | 844.277 | -0.59 | 846.958 | -0.28 |
| [36] | 860.380 | 1.80 | 862.066 | 0.9554 | 288.26 | 13.898 | L | 856.887 | -0.60 | 856.961 | -0.59 | 856.925 | -0.60 | 859.156 | -0.34 |
| | 883.400 | 1.92 | 884.951 | 0.9554 | 288.23 | 16.900 | L | 879.705 | -0.59 | 879.785 | -0.58 | 879.712 | -0.59 | 881.280 | -0.42 |
| [37] | 672.859 | -2.22 | 694.816 | 0.9072 | 294.17 | 10.201 | L | 693.040 | -0.26 | 693.014 | -0.26 | 692.961 | -0.27 | 697.953 | 0.45 |
| | 746.381 | -2.86 | 772.406 | 0.9072 | 294.18 | 14.803 | L | 769.186 | -0.42 | 769.153 | -0.42 | 769.074 | -0.43 | 771.109 | 0.17 |
| | 785.116 | -2.87 | 811.755 | 0.9072 | 294.17 | 18.910 | L | 809.181 | -0.32 | 809.151 | -0.32 | 808.990 | -0.34 | 810.431 | -0.16 |

* Temperature, pressure, and composition of the literature data are not exactly the same as those measured in this work. Hence, the %RD also refers to the calculation with EOS at the exact literature data conditions (temperature, pressure and composition).
** Linear interpolation was performed where calibration fluid data was not available at the exact temperature and pressure of the mixture.

## *4. Conclusions*

In this study, we evaluated the performance of various calibration models for vibrating tube densimeters using $CO_2$ as the calibration fluid. Although model results are close to the uncertainty band, semi-empirical polynomial models showed slightly better performance with an %AAD of 0.07% (RMSE = 0.32 kg/m³) in calculating the density of the calibration fluid w.r.t the reference EOS, while %AAD reached 0.09% (RMSE = 0.40 kg/m³) for the physically-based May's model. To validate the methodology and extrapolative behavior of the models, binary mixtures of $CO_2$ with $CH_4$ at different concentrations for which literature data are available were considered, covering the whole density range. With the discrete model, it was possible to stay within the ±0.3% uncertainty band of the GERG-2008 for CO2 and CH4 mixtures, where the temperature and pressure of the test fluid exist for the calibration fluid. The physically-based and polynomial models performed better than the discrete ones when the calibration fluid was not measured at the exact temperature of the test fluid and close to each other.

The findings suggest that careful calibration of the polynomial model can be as accurate as the physically-based model in the same operating conditions as the calibration fluid (i.e. when the model is applied according to an interpolation-like approach within the

same region from calibration) and within the uncertainty of the measured parameters in most density ranges up to 1000 kg/m³. A good agreement was found, both during the calibration and validation steps, between the May and 13-term or 6-term polynomial models, provided that accurate numerical fitting is performed for all models.

As a future step, the analysis should be performed under different conditions than calibration ones (e.g. different temperatures and compositions) to further corroborate the improved extrapolative robustness of the physically-based model, as it should better captures the intrinsic behavior of the VTD compared to the empirical polynomial models.

In conclusion, this study provides insight into how different calibration models behave and procedures for controlled estimation of parameters. One of the calibration models proposed in this work will be used to generate new experimental data of multicomponent $CO_2$-rich mixtures within the ENCASE project.


### *Acknowledgments*

This research has been conducted within the ENCASE project which has received funding from the European Union's Horizon Europe research and innovation programme under grant agreement No 101094664. Views and opinions expressed are however those of the author(s) only and do not necessarily reflect those of the European Union. Neither the European Union nor the granting authority can be held responsible for them.


### *Nomenclature*

***Latin symbols***

| | |
|---|---|
| $A_i, B_i, C_i$ | Polynomial coefficients [relevant units] |
| $N$ | Number of points [-] |
| $p$ | pressure [MPa] |
| $S_{00}$ | Geometric sensitivity factor of the evacuated tube at reference T [-] |
| $T$ | Temperature [K] |
| $t$ | Temperature [°C] |

***Greek and composite symbols***

| | |
|---|---|
| $\alpha_V$ | Linear temperature response coefficient of tube volume [$K^{-1}$] |
| $\beta_V$ | Pressure response coefficient of tube volume [$MPa^{-1}$] |
| $\beta_\tau$ | Pressure response coefficient of spring constant [$MPa^{-1}$] |
| $\varepsilon_{\tau 1}$ | Linear temperature response coefficient of spring constant [$K^{-1}$] |
| $\varepsilon_{\tau 2}$ | Quadratic temperature response coefficient of spring constant [$K^{-2}$] |
| $\rho$ | Density [$kg/m^3$] |
| $\rho_{VTD}$ | Density calculated by the calibration model [$kg/m^3$] |
| $\rho_{REF}$ | Reference (calibration) fluid density [$kg/m^3$] |
| $\rho_M$ | Density of tube material [$kg/m^3$] |
| $\rho_{EOS}$ | Density calculated from the equation of state [$kg/m^3$] |
| $\tau$ | Oscillation period of the VTD [μs] |
| $\tau_{00}$ | Oscillation period of evacuated tube at reference temperature [μs] |

## *References*


[1] G. Chinello et al., 'Toward standardized measurement of CO2 transfer in the CCS chain', Nexus, vol. 1, no. 2, p. 100013, Jun. 2024, doi: 10.1016/j.ynexs.2024.100013.

[2] Multiparameter equations of state an accurate source of thermodynamic property data ; with 36 tables. Berlin: Springer, 2000.

[3] M. E. Mondéjar, T. E. Fernández-Vicente, F. Haloua, and C. R. Chamorro, 'Experimental Determination of ( p , ρ, T ) Data for Three Mixtures of Carbon Dioxide with Methane for the Thermodynamic Characterization of Nonconventional Energy Gases', J. Chem. Eng. Data, vol. 57, no. 9, pp. 2581–2588, Sep. 2012, doi: 10.1021/je300665n.

[4] W. Wagner, K. Brachthuser, R. Kleinrahm, and H. W. Losch, 'A new, accurate single-sinker densitometer for temperatures from 233 to 523 K at pressures up to 30 MPa', Int J Thermophys, vol. 16, no. 2, pp. 399–411, Mar. 1995, doi: 10.1007/BF01441906.

[5] X. Yang, M. Richter, M. A. Ben Souissi, R. Kleinrahm, and R. Span, 'Vapor-Phase ( p , ρ, T, x ) Behavior and Virial Coefficients for the Binary Mixture (0.05 Argon + 0.95 Carbon Dioxide) over the Temperature Range from (273.15 to 323.15) K with Pressures up to 9 MPa', J. Chem. Eng. Data, vol. 61, no. 8, pp. 2676–2681, Aug. 2016, doi: 10.1021/acs.jced.6b00120.

[6] W. Wagner and R. Kleinrahm, 'Densimeters for very accurate density measurements of fluids over large ranges of temperature, pressure, and density', Metrologia, vol. 41, no. 2, pp. S24–S39, Apr. 2004, doi: 10.1088/0026-1394/41/2/S03.

[7] G. Tsankova, P. L. Stanwix, E. F. May, and M. Richter, 'Densities, Dielectric Permittivities, and Dew Points for (Argon + Carbon Dioxide) Mixtures Determined with a Microwave Re-entrant Cavity Resonator', J. Chem. Eng. Data, vol. 62, no. 9,

pp. 2521–2532, Sep. 2017, doi: 10.1021/acs.jced.6b01043.

[8] D. Lozano-Martín, G. U. Akubue, A. Moreau, D. Tuma, and C. R. Chamorro, 'Accurate experimental (p, ρ, T) data of the ($CO_2$ + $O_2$) binary system for the development of models for CCS processes', The Journal of Chemical Thermodynamics, vol. 150, p. 106210, Nov. 2020, doi: 10.1016/j.jct.2020.106210.

[9] C. Bouchot and D. Richon, 'Direct Pressure–Volume–Temperature and Vapor–Liquid Equilibrium Measurements with a Single Equipment Using a Vibrating Tube Densimeter up to 393 K and 40 MPa: Description of the Original Apparatus and New Data', Ind. Eng. Chem. Res., vol. 37, no. 8, pp. 3295–3304, Aug. 1998, doi: 10.1021/ie970804w.

[10] E. F. May, W. J. Tay, M. Nania, A. Aleji, S. Al-Ghafri, and J. P. Martin Trusler, 'Physical apparatus parameters and model for vibrating tube densimeters at pressures to 140 MPa and temperatures to 473 K', Review of Scientific Instruments, vol. 85, no. 9, p. 095111, Sep. 2014, doi: 10.1063/1.4894469.

[11] S. L. Outcalt, 'Calibration Fluids and Calibration Equations: How Choices May Affect the Results of Density Measurements Made with U-Tube Densimeters', J. RES. NATL. INST. STAN., vol. 123, p. 123017, Oct. 2018, doi: 10.6028/jres.123.017.

[12] A. T. Sousa, P. S. Fialho, C. A. N. De Castro, R. Tufeu, and B. Le Neindre, 'Density of HCFC 142b and of its mixture with HCFC 22', Fluid Phase Equilibria, vol. 80, pp. 213–225, Nov. 1992, doi: 10.1016/0378-3812(92)87069-Y.

[13] B. Lagourette, C. Boned, H. Saint-Guirons, P. Xans, and H. Zhou, 'Densimeter calibration method versus temperature and pressure', Meas. Sci. Technol., vol. 3, no. 8, pp. 699–703, Aug. 1992, doi: 10.1088/0957-0233/3/8/002.

[14] L. F. S. Souza, S. Herrig, R. Span, and J. P. M. Trusler, 'Experimental density and an improved Helmholtz-energy-explicit mixture model for ($CO_2$ + CO)', Applied Energy, vol. 251, p. 113398, Oct. 2019, doi: 10.1016/j.apenergy.2019.113398.

[15] E. C. Ihmels and J. Gmehling, 'Densities of Toluene, Carbon Dioxide, Carbonyl Sulfide, and Hydrogen Sulfide over a Wide Temperature and Pressure Range in the Sub- and Supercritical State', Ind. Eng. Chem. Res., vol. 40, no. 20, pp. 4470–4477, Oct. 2001, doi: 10.1021/ie0011356.

[16] M. Atilhan, S. Aparicio, F. Karadas, K. R. Hall, and R. Alcalde, 'Isothermal PρT measurements on Qatar's North Field type synthetic natural gas mixtures using a vibrating-tube densimeter', The Journal of Chemical Thermodynamics, vol. 53, pp. 1–8, Oct. 2012, doi: 10.1016/j.jct.2012.04.008.

[17] C. D. Holcomb and S. L. Outcalt, 'A theoretically-based calibration and evaluation

procedure for vibrating-tube densimeters', Fluid Phase Equilibria, vol. 150–151, pp. 815–827, Sep. 1998, doi: 10.1016/S0378-3812(98)00362-8.

[18] S. L. Outcalt and M. O. McLinden, 'Automated Densimeter for the Rapid Characterization of Industrial Fluids', Ind. Eng. Chem. Res., vol. 46, no. 24, pp. 8264–8269, Nov. 2007, doi: 10.1021/ie070791e.

[19] C. C. Sampson, X. Yang, J. Xu, and M. Richter, 'Measurement and correlation of the (p, ρ, T) behavior of liquid propylene glycol at temperatures from (272.7 to 393.0) K and pressures up to 91.4 MPa', The Journal of Chemical Thermodynamics, vol. 131, pp. 206–218, Apr. 2019, doi: 10.1016/j.jct.2018.10.016.

[20] X. Yang, C. C. Sampson, O. Frotscher, and M. Richter, 'Measurement and correlation of the (p, ρ, T) behaviour of liquid ethylene glycol at temperatures from (283.3 to 393.1) K and pressures up to 100.1 MPa', The Journal of Chemical Thermodynamics, vol. 144, p. 106054, May 2020, doi: 10.1016/j.jct.2020.106054.

[21] C. Bouchot and D. Richon, 'An enhanced method to calibrate vibrating tube densimeters', Fluid Phase Equilibria, vol. 191, no. 1–2, pp. 189–208, Nov. 2001, doi: 10.1016/S0378-3812(01)00627-6.

[22] M. A. Gomez-Osorio, R. A. Browne, M. Carvajal Diaz, K. R. Hall, and J. C. Holste, 'Density Measurements for Ethane, Carbon Dioxide, and Methane + Nitrogen Mixtures from 300 to 470 K up to 137 MPa Using a Vibrating Tube Densimeter', J. Chem. Eng. Data, vol. 61, no. 8, pp. 2791–2798, Aug. 2016, doi: 10.1021/acs.jced.6b00138.

[23] F. Jiao, S. Z. S. Al Ghafri, T. J. Hughes, and E. F. May, 'Extended calibration of a vibrating tube densimeter and new reference density data for a methane-propane mixture at temperatures from (203 to 423) K and pressures to 35 MPa', Journal of Molecular Liquids, vol. 310, p. 113219, Jul. 2020, doi: 10.1016/j.molliq.2020.113219.

[24] I. M. S. Lampreia and C. A. Nieto de Castro, 'A new and reliable calibration method for vibrating tube densimeters over wide ranges of temperature and pressure', The Journal of Chemical Thermodynamics, vol. 43, no. 4, pp. 537–545, Apr. 2011, doi: 10.1016/j.jct.2010.11.002.

[25] M. Mantovani, P. Chiesa, G. Valenti, M. Gatti, and S. Consonni, 'Supercritical pressure–density–temperature measurements on CO2–N2, CO2–O2 and CO2–Ar binary mixtures', The Journal of Supercritical Fluids, vol. 61, pp. 34–43, Jan. 2012, doi: 10.1016/j.supflu.2011.09.001.

[26] M. Nazeri, A. Chapoy, A. Valtz, C. Coquelet, and B. Tohidi, 'Densities and derived thermophysical properties of the 0.9505 CO2+ 0.0495 H2S mixture from 273 K to 353 K and pressures up to 41 MPa', Fluid Phase Equilibria, vol. 423, pp. 156–171, Sep. 2016, doi: 10.1016/j.fluid.2016.04.024.

[27] M. Nazeri, A. Chapoy, A. Valtz, C. Coquelet, and B. Tohidi, 'New experimental density data and derived thermophysical properties of carbon dioxide – Sulphur dioxide binary mixture ($CO_2$ - $SO_2$) in gas, liquid and supercritical phases from 273 K to 353 K and at pressures up to 42 MPa', Fluid Phase Equilibria, vol. 454, pp. 64–77, Dec. 2017, doi: 10.1016/j.fluid.2017.09.014.

[28] B. Gimeno, M. Artal, I. Velasco, J. Fernández, and S. T. Blanco, 'Influence of SO 2 on CO 2 Transport by Pipeline for Carbon Capture and Storage Technology: Evaluation of CO 2 /SO 2 Cocapture', Energy Fuels, vol. 32, no. 8, pp. 8641–8657, Aug. 2018, doi: 10.1021/acs.energyfuels.8b01666.

[29] M. Doninelli et al., 'Experimental investigation of the $CO_2$+$SiCl_4$ mixture as innovative working fluid for power cycles: Bubble points and liquid density measurements', Energy, vol. 299, p. 131197, Jul. 2024, doi: 10.1016/j.energy.2024.131197.

[30] R. Span and W. Wagner, 'A New Equation of State for Carbon Dioxide Covering the Fluid Region from the Triple-Point Temperature to 1100 K at Pressures up to 800 MPa', Journal of Physical and Chemical Reference Data, vol. 25, no. 6, pp. 1509–1596, Nov. 1996, doi: 10.1063/1.555991.

[31] O. Kunz and W. Wagner, 'The GERG-2008 Wide-Range Equation of State for Natural Gases and Other Mixtures: An Expansion of GERG-2004', J. Chem. Eng. Data, vol. 57, no. 11, pp. 3032–3091, Nov. 2012, doi: 10.1021/je300655b.

[32] S. T. Blanco, C. Rivas, J. Fernández, M. Artal, and I. Velasco, 'Influence of Methane in CO 2 Transport and Storage for CCS Technology', Environ. Sci. Technol., vol. 46, no. 23, pp. 13016–13023, Dec. 2012, doi: 10.1021/es3037737.

[33] J. W. Magee and J. F. Ely, 'Isochoric (p, v, T) measurements on $CO_2$ and (0.98 $CO_2$+0.02 $CH_4$) from 225 to 400 K and pressures to 35 MPa', Int J Thermophys, vol. 9, no. 4, pp. 547–557, Jul. 1988, doi: 10.1007/BF00503153.

[34] C. Rivas, S. T. Blanco, J. Fernández, M. Artal, and I. Velasco, 'Influence of methane and carbon monoxide in the volumetric behaviour of the anthropogenic $CO_2$: Experimental data and modelling in the critical region', International Journal of Greenhouse Gas Control, vol. 18, pp. 264–276, Oct. 2013, doi: 10.1016/j.ijggc.2013.07.019.

[35] Y. Arai, G.-I. Kaminishi, and S. Saito, 'THE EXPERIMENTAL DETERMINATION OF THE P-V-T-X RELATIONS FOR THE CARBON DIOXIDE-NITROGEN AND THE CARBON DIOXIDE-METHANE SYSTEMS', J. Chem. Eng. Japan / JCEJ, vol. 4, no. 2, pp. 113–122, 1971, doi: 10.1252/jcej.4.113.

[36] I. Al-Siyabi, 'Effect of impurities on $CO_2$ stream properties', Thesis, Heriot-Watt University, 2013. Accessed: Aug. 22, 2024. [Online]. Available: https://www.ros.

hw.ac.uk/handle/10399/2643

[37] R. Simon, C. J. Fesmire, R. M. Dicharry, and F. H. Vorhis, 'Compressibility Factors for CO2-Methane Mixtures', Journal of Petroleum Technology, vol. 29, no. 01, pp. 81–85, Jan. 1977, doi: 10.2118/5052-PA.

# Analysis of Solid-Solid Phase Change Materials for Solar Thermal Applications

**Pengyu Cheng[1], Sebastiano Tomassetti[1,#], Francesca Luzi[2], Pietro Forcellese[2], Tiziano Bellezze[2], Giovanni Di Nicola[1]**

1 *Department of Industrial Engineering and Mathematical Sciences, Marche Polytechnic University, Ancona, Italy*
2 *Department of Materials, Environmental Sciences and Urban Planning, Marche Polytechnic University, Ancona, Italy*

*# Corresponding Author:* s.tomassetti@univpm.it

Keywords: Differential scanning calorimetry, solid-solid PCM, thermal energy storage, solar heating

## Abstract

Phase change materials (PCMs) for thermal energy storage (TES) applications have attracted significant attention in recent years. Compared with traditional solid-liquid (S-L) PCMs, solid-solid (S-S) PCMs generally provide high energy density, negligible volume change during phase transition, and long cyclic life, which show giant potential in TES systems.
In this study, the mixture of pentaerythritol (PE) and pentaglycerine (PG), which are considered suitable for medium-temperature applications (from 80 °C to 150 °C), is investigated. This mixture is obtained by two methods and their phase transition, and thermal properties are analyzed by differential scanning calorimetry (DSC) and thermogravimetric analysis (TGA). A comparison among the results obtained for the studied samples is carried out to understand the most reliable method for producing this mixture. The applicability of the mixture in TES systems is also discussed. Although it has promising properties for TES applications, further research is necessary.

### *1. Introduction*

The application of phase change materials (PCMs) in thermal energy storage (TES) systems is considered as one of the most promising methods to store thermal energy within small temperature constraints [1]. PCMs are specific materials able to absorb and release thermal energy during the reversible phase transition at specific temperatures suitable for different applications [1], [2]. Compared with sensible thermal storage materials, PCMs are characterized by higher density in thermal energy storage. Thus, PCMs have been widely studied in various industrial applications, such as building textile and electronic applications [2], [3], [4], [5], [6], [7].

The typical transitions in PCMs include four kinds of phase change processes, solid to liquid (SL), solid to solid (SS), solid to gas (SG) and liquid to gas (LG). Because of the

large volume change during the transition, the phase change processes involving the gas phase are excluded in the TES systems. Among them, SL-PCMs are the most studied materials and have been extensively applied in different TES systems, such as solar energy management, industrial waste heat recovery and building temperature cooling [4]. However, SL-PCMs have some shortages, like liquid leakage and phase segregation. On the other hand, SS-PCMs have different advantages like long cycling life and negligible volume changes [1], [2], but they have not been widely investigated, especially for the low-medium temperatures (80-150) °C. The most well-known SS-PCMs include polymeric and polyalcohol materials with phase transition temperatures between (10 and 190)°C, ceramic-based materials with a phase transition temperature range of 30- 120°C and metal alloys with ultra-high phase transition temperature of 600- 1000 °C [1], [2].

The SS-PCMs can be classified into three categories: organic, inorganic, and hybrid PCMs. Among the organic SS-PCMs, polyalcohols are considered potential materials for medium temperature TES systems. In the phase transition in such materials, the structure transferred from a crystalline structure at low temperature to an amorphous phase at high temperature, while they keep the solid state. Their transition temperatures range from 40 to 187°C and the transition enthalpies are from 130.9 to 303.0 J/g [8], [9]. Common polyalcohols used as SS-PCMs are reported in Table 1, together with their physical properties [8], [9]. In addition, these polyalcohols can be mixed to obtain PCMs characterized by properties suitable for specific TES applications. In fact, such mixtures are characterized by variable transition temperatures tuned through the change of their composition. Despite the original studies on these materials dates back to many years ago, such as measurements of the fundamental properties of polyalcohol [10], [11], [12], the research about polyalcohol used as PCMs still remains at an early stage [13], [14], [15]. Therefore, for their application in TES systems, further research and measurement are necessary, such as cycling test, stability test and the measurements of additional thermophysical properties.

**Table 1.** Phase transition temperature ($T_{TR}$), transition enthalpy ($\Delta H_{TR}$), melting temperature ($T_M$) and melting enthalpy ($\Delta H_M$) of different polyalcohols used as SS-PCMs [8], [9].

| Compound | $T_{TR}$ (°C) | $\Delta H_{TR}$ (J/g) | $T_M$ (°C) | $\Delta H_M$ (J/g) |
|---|---|---|---|---|
| Pentaglycerine (PG) | 81 | 192.4 | 198 | 45.2 |
| Neopentylglycol (NPG) | 40 | 130.9 | 126 | 44.2 |
| Pentaerythritol (PE) | 188 | 303.0 | 260 | 36.9 |
| Tris(hydroxymethyl)aminomethane (TAM) | 134 | 284.8 | 172 | 28.1 |

In this study, the mixture containing the polyalcohols PE and PG was studied. Two methods to obtain the mixture were compared. The phase transition and physical properties were measured by TG and DSC. In addition, cycling tests of the mixture were carried out to analyze the application in TES systems.

## 2. Materials and methods

### 2.1 Materials

The samples of pentaerythritol (PE, CAS number 115-77-5) and pentaglycerine (PG, CAS number 77-85-0) were purchased from Thermo Fisher Scientific Inc. The purity of PE and PG samples are 98% and 97%, respectively. Details about their degree of health hazard are available in [16].

### 2.2 Preparation methods for mixture

Three PE/PG mixtures with mole fractions of PE (xPE) equal to 25%, 50% and 75% were obtained using the following method:

- Firstly, the raw materials in powder form were mixed at the desired molar ratio and the obtained powder was loaded into a sealed container. Silicon ring and Teflon tape were used to seal it.
- Then, the loaded container was put into an electric oven at 280°C for 1 h to guarantee the obtainment of melt mixture.
- After, the container was cooled down to room temperature to get the solid mixture for the analysis.

To make sure that there was no leakage during the heating of the container, its mass was weighted before and after the heating. Since differences between the two masses were in the range of hundredths of grams, it was verified that there was no mass loss during the mixture preparation.

Since the method based on the melting of the mixture allowed to prepare only few

grams in each cycle, another method based on the solid mixture dissolution was used and tested to obtain larger amounts. More specifically, dissolution method was used to prepare only the PE/PG mixture with xPE = 50% for preliminary investigations. The mixture was obtained by using the following procedure:

- Firstly, the raw powders of PE and PG at the desired molar ratio were dissolved in deionized water in a crystallizer.
- Then the solution was continuously stirred for 1 h to make it homogeneous.
- Afterwards, the crystallizer with the solution was put into the oven at 50 °C for 24 h until the water evaporated. The mass was also weighted in each step to check that there was no substance leakage or contamination.

### *2.3 Measurements*

Differential scanning calorimetry (DSC) measurements were performed to evaluate the transition temperature and the enthalpy of the solid-solid phase change in the PE/PG mixture and the pure components. The heat flow of the substance was recorded in heating and cooling scans as a function of temperature in the ranges 25 - 200°C. The measurements were done by means of a Seiko EXSTAR 6000 calorimeter at a scan rate of 10 °C $min^{-1}$, under a nitrogen flow rate of 50 mL min-1.

Thermogravimetric analysis (TGA) measurements were performed for PE, PG and PE/PG mixture. All the samples were heated to 800 °C at a heating rate of 10°C/min. The TGA data and their differential (DTG) were analyzed in this study.

The cycling tests were carried out to examine thermal cycling stability of the studied samples [17]. This analysis was performed by a customized methodology based on the method suggested by other authors [18]. To prevent the leakage of the sample at high temperature, the PCMs were loaded into sealed stainless-steel tubes with a thermal couple inside each tube. The containers were sealed by silicon resin. The heating program was set as follows. Firstly, an electric oven was heated to about 240 °C. Then, each tube was put into the oven and taken out until it was heated to 10 °C above its transition temperature. After each tube cooled down to room temperature by air, it was ready for the next cycle.

Before and after the cycling test, DSC tests were performed to evaluate if the phase transition properties changes after the cycling test.

## 3. Results and discussion

### 3.1 Phase transition properties

The transition temperatures and the enthalpies of the mixture samples are shown in Figure 1 and they are compared with the corresponding values related to pure samples that we reported before [16] in Table 2. The $T_{tr}$ of the mixture increases with x. However, the $\Delta H_{tr}$ of mixture with x=25% is decreased compared to pure PG.

In addition to the pure components, the phenomenon of supercooling can be also observed in PE/PG mixture. This phenomenon refers to the release of heat in cooling at a temperature lower than that where the phase transition occurs in heating. The values of $T_{tr}$ are listed in Table 2 ("h" and "c" in the subscripts stay for onset transition temperature during heating and cooling directions, respectively). It is evident that all the measured sampled showed supercooling, i.e., the material released the phase transition enthalpy during the cooling at a temperature lower than the transition temperature during the heating. Compared with pure PE or PG, the difference of $T_{tr}$ in cooling and heating increased in the mixture, indicating supercooling with higher intensity. However, the supercooling in PCMs is hard to be well explained by the theory. It is assumed that it is related to the high degree of directional disorder and mobility of the molecules in the high-temperature phase [19].

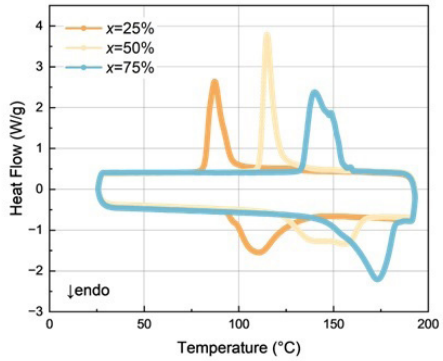


**Figure 1.** DSC curves of the PE/PG mixture with x=25%, 50% and 75%.

**Table 2.** Ttr in cooling and heating of PE/PG mixture

| $x_{PE}$ | $T_{tr,h}$ (°C) | $T_{tr,c}$ (°C) | $\Delta H_{tr,h}$ (J/g) | $\Delta H_{tr,c}$ (J/g) |
|---|---|---|---|---|
| 0 | 82 | 70 | 146 | -132 |
| 25 | 111.9 | 87.8 | 133 | -114 |
| 50 | 156.8 | 115.3 | 159 | -165 |
| 75 | 173.7 | 139.9 | 181 | -184 |
| 100 | 186 | 176 | 255 | -242 |

The transition properties of PE/PG mixture available in the literature were collected and compared with the measurements performed in this work. The values of $T_{tr}$ and ΔH are reported in Figure 2 and Figure 3, respectively. The measurements of mixture obtained from DSC were collected and the properties of pure PE and PG were taken from our previous study [16]. The solid symbols represent the onset transition temperature ($T_{tr,onset}$), and the hollow symbols are the ending transition temperature ($T_{tr,ending}$), taken in the heating direction. It can be observed that the value of $T_{tr,onset}$ of the mixtures in our research are generally in agreement with previous research [10]. But the enthalpies of phase transition are slightly lower than the data of previous research, which could be caused by the different experimental conditions in measurements.

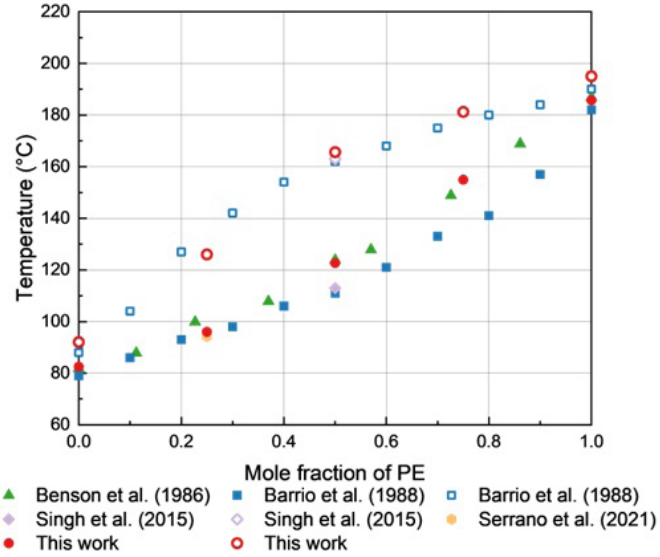


**Figure 2.** Phase transition temperatures of PE/PG mixture as function of the mole fraction. A part of data comes from the references [10], [11], [15], [19]. The solid symbols represent the $T_{tr,onset}$, and the hollow symbols are the $T_{tr,ending}$.

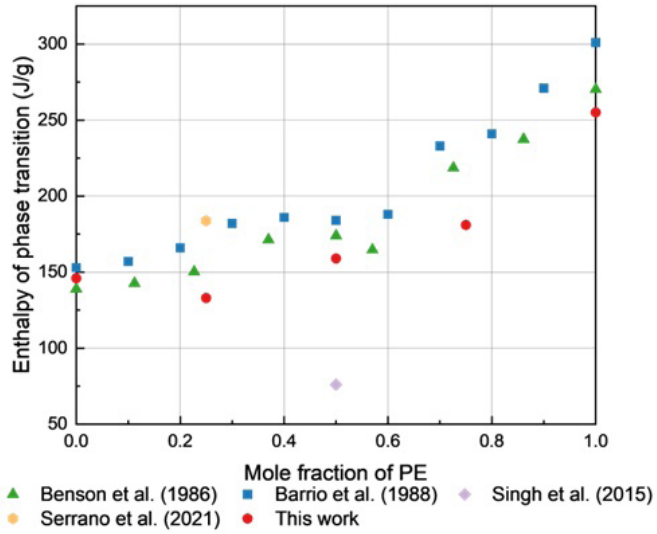


**Figure 3.** Enthalpy in phase transition of PE/PG mixture as function of the mole fraction. A part of data comes from the reference [10], [11], [15], [19].

### *3.2 Physical properties of the mixture*

The TGA and the DTG curves are illustrated in Figure 4. The unique peak in each DTG curve indicates the only one mass loss event in the heating of PCM mixtures. As the temperature continued to rise, the samples lost all the mass. Considering that the mass loss started at the temperature below their melting point, it could be inferred that it can be due to sublimation. The temperatures at different mass losses were determined and reported in Table 3. From this table, it can be noted that the mass loss of almost all the samples started at temperatures lower than their $T_{tr}$ probably due to sublimation, as mentioned before. Anyway, in TES applications, the sublimation of these PCMs should be prevented by packaging.

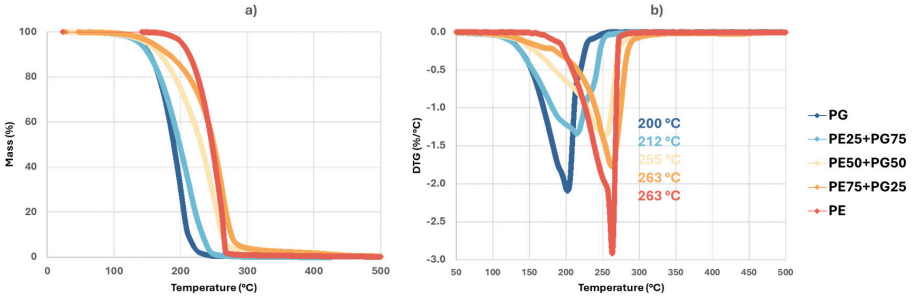


**Figure 4.** a) TGA and b) DTG curves of PE/PG mixtures

**Table 3.** Temperatures at different mass losses of PE/PG mixtures

| Mass | Temperature (°C) | | | | |
|---|---|---|---|---|---|
| | xPE = 0 % | xPE = 25 % | xPE = 50 % | xPE = 75 % | xPE = 100 % |
| 99% | 110.8 | 104.8 | 108.1 | 117.8 | 178.6 |
| 95% | 140.7 | 138.8 | 150.4 | 157.4 | 201.9 |
| 90% | 153.6 | 152.5 | 169.0 | 182.4 | 212.7 |

### *3.3 Cycling test*

With respect to PE/PG mixture, there is few research on the cycling test. In this section, to further confirm the thermal stability of the PE/PG mixture, thermal cycles are performed for PE, PG and the mixture with xPE = 50 % obtained by oven and solution method (named below Mix-Oven and Mix-Solution, respectively). The masses of the PCM systems are monitored after a certain number of cycles, and it is illustrated in Figure 5. The mass percentage of the PCM systems after 20 runs remained over 99% of the original value, which is acceptable. The mass loss of the PCM systems could be due to the aging of thermal couples and other parts of the system.

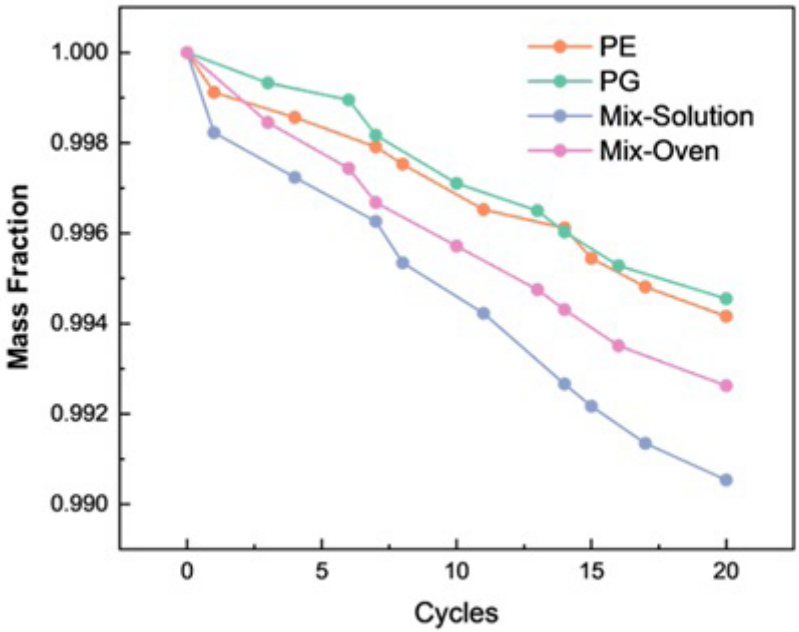


**Figure 5.** Mass fraction versus runs of cycling test curves in PCM systems. Mix-Oven and Mix-Solution are the mixture samples obtained by the oven and solution method, respectively.

The physical properties of the mixtures after 20 cycles were measured by DSC (Figure 6). The results of data elaboration are listed in Table 4. Concerning the Ttr in heating and cooling, 20 cycles have no great influence on the $T_{tr}$ of PE, PG and mixture obtained by using the oven. It could be observed that the supercooling in this mixture was reduced after the cycling test. On the contrary, the $T_{tr}$ of mixture by solution method is decreased. This result can be attributed to the separation of at least two phases, identified at the end of the mixture preparation as crystals of different shapes. Therefore, the solution method requires experimental improvements to obtain more homogeneous PE/PG mixtures with suitable phase stability.

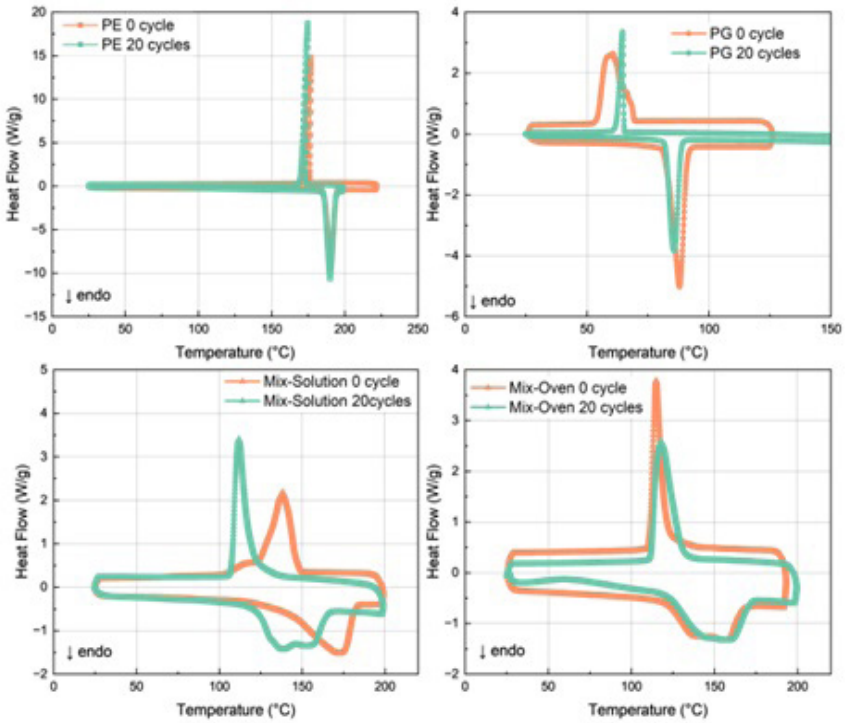


**Figure 6.** DSC curves of PE/PG mixtures before and after cycling test

**Table 4.** The physical properties of PE/PG mixtures before and after cycling test

| sample | cycle | $T_{tr,h}$ (cel) | $T_{tr,c}$ (cel) | $\Delta H_{tr,h}$ (J/g) | $\Delta H_{tr,c}$ (J/g) |
|---|---|---|---|---|---|
| PE | 0 | 186 | 176 | 255 | -242 |
| | 20 | 189.9 | 174.5 | 268 | -262 |
| PG | 0 | 82 | 70 | 146 | -132 |
| | 20 | 85.96 | 64.75 | 88.6 | -37.6 |
| Mix-Solution | 0 | 172.4 | 138.4 | 190 | -182 |
| | 20 | 138.4 | 112 | 176 | -173 |
| Mix-Oven | 0 | 156.8 | 115.3 | 159 | -165 |
| | 20 | 157.2 | 118.1 | 177 | -168 |

The heating curve temperatures of PCMs are shown in Figure 7. It is noted that the heating behaviors are with no significant change, and the phase transition occurs at the kink in heating curves. This temperature of most PCMs slightly decreased in a few circles at the start, while no change appears in mixture obtained from the oven. Especially in the last few cycles, the temperature of the kink keep constant, confirming the stability in multiple cycles of heating and cooling. However, further experiments with more cycles are essential to prove the promising stability in long terms.

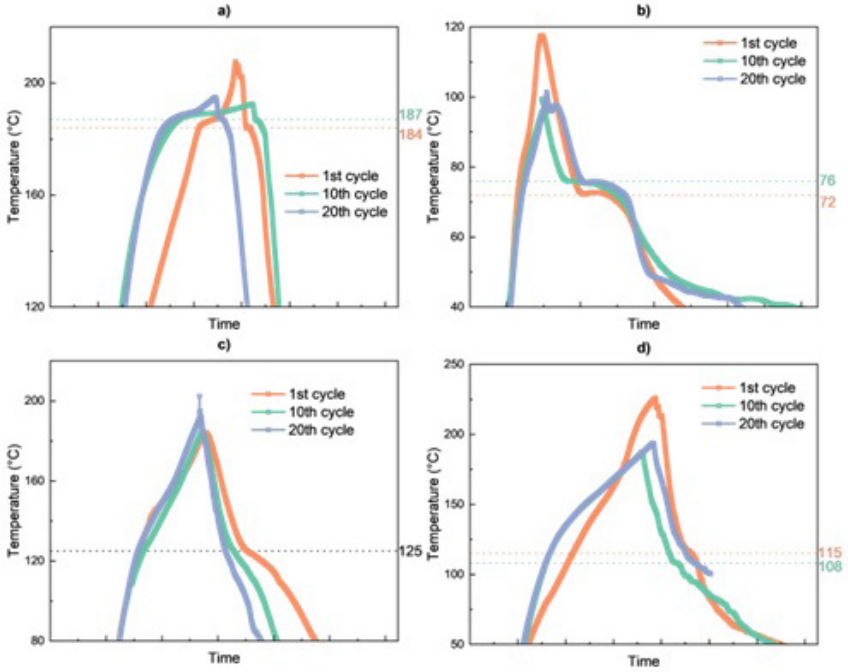


**Figure 7.** Heating curves of a) PE, b) PG, c) mixture obtained by oven and d) mixture by solution method in cycling test. The values in the right mark the temperature of the kink in 1st and 10th cycle with corresponding color.

### *4. Conclusion*

In this work, different compositions of the PE/PG mixture were successfully prepared and analyzed to study their potential use as PCMs applied in TES systems. Two different preparation methods were taken for further research on mass production. One method

is the traditional method by heating the mixed powder in the oven and another is the solution method to obtain the mixture by evaporating the well-mixed solution. The thermal properties were measured by DSC and TG tests. Finally, the cycling tests were performed to measure the stability of the PCMs in TES applications.

The data from the DSC measurements showed great agreement with the literature. Among the PE/PG mixtures, the mixture with xPE=50% shows promising results for TES applications, considering its Ttr is 156.8 °C and shows a good ΔH=159 J/g. From the TG test, it was observed mass losses below the melting point of PCMs, which was probably caused the sublimation. This could affect the application in TES systems and proves that the PE/PG mixture should be packaged. On the other hand, the supercooling in the mixtures is greater than the pure PE or PG compounds, and it requires improvements to suppress it.

Apart from Ttr, the thermal stability was confirmed by cycling test. After 20 thermal cycles in our self-build testing systems, the mass losses of all PCM systems were very limited. The DSC data before and after the cycling test showed that the mixture with xPE=50% obtained by oven kept the value of thermal properties near constant. This outcome confirmed that the PCM system with PE/PG mixture is stable after 20 cycles. However, the mixture obtained from the solution method showed a great change in thermal properties after the cycling test. This could relate to the phase separation in the preparation. Thus, the solution method remains to improve to overcome this problem.

In conclusion, the results proved that the PE/PG mixture obtained by oven seems more suitable to be used as a potential PCM in medium range TES system. However, the supercooling in the mixture has to be solved and more cycling tests should be performed in further research to confirm their applicability in TES systems.

## *NOMENCLATURE*

**Latin symbols**

| | |
|---|---|
| T | Temperature, °C |
| x | Mole fraction |

**Greek and composite symbols**

| | |
|---|---|
| ΔH | Enthalpy, J/g |

**Subscripts**

| | |
|---|---|
| tr | Phase transition |
| c | cooling |
| h | heating |
| m | melting |

**Acronyms**

| | |
|---|---|
| DSC | Differential scanning calorimetry |
| PCM | Phase change material |
| PE | Pentaerythritol |
| PG | Pentaglycerine |
| S-S | Solid-solid |
| TES | Thermal energy storage |
| TGA | Thermogravimetric analysis |
| DTG | Differential thermogravimetry |

### *References*


[1] A. Usman, F. Xiong, W. Aftab, M. Qin, and R. Zou, "Emerging Solid-to-Solid Phase-Change Materials for Thermal-Energy Harvesting, Storage, and Utilization," Adv. Mater., vol. 34, (no. 41), p. 2202457, 2022.

[2] A. Fallahi, G. Guldentops, M. Tao, S. Granados-Focil, and S. Van Dessel, "Review on solid-solid phase change materials for thermal energy storage: Molecular structure and thermal properties," Appl. Therm. Eng., vol. 127, pp. 1427–1441, 2017.

[3] C. R. Raj, S. Suresh, R. R. Bhavsar, and V. K. Singh, "Recent developments in thermo-physical property enhancement and applications of solid solid phase change materials: A review," J. Therm. Anal. Calorim., vol. 139, (no. 5), pp. 3023–3049, 2020.

[4] K. Du, J. Calautit, Z. Wang, Y. Wu, and H. Liu, "A review of the applications of phase change materials in cooling, heating and power generation in different temperature ranges," Appl. Energy, vol. 220, pp. 242–273, 2018.

[5] S. Rostami, M. Afrand, A. Shahsavar, M. Sheikholeslami, R. Kalbasi, S. Aghakhani, M. S. Shadloo, and H. F. Oztop, "A review of melting and freezing processes of PCM/nano-PCM and their application in energy storage," Energy, vol. 211, p. 118698, 2020.

[6] D. Zhou, C. Y. Zhao, and Y. Tian, "Review on thermal energy storage with phase change materials (PCMs) in building applications," Appl. Energy, vol. 92, pp. 593–605, 2012.

[7] C. Liu, D. Xu, J. Weng, S. Zhou, W. Li, Y. Wan, S. Jiang, D. Zhou, J. Wang, and Q. Huang, "Phase Change Materials Application in Battery Thermal Management System: A Review," Materials, vol. 13, (no. 20), Art. no. 20, 2020.

[8] A. Mishra, A. Talekar, D. Chandra, and W.-M. Chien, "Ternary phase diagram calculations of pentaerythritol–pentaglycerine–neopentylglycol system," Thermochim. Acta, vol. 535, pp. 17–26, 2012.

[9] R. Shi, D. Chandra, A. Mishra, A. Talekar, M. Tirumala, and D. J. Nelson, "Thermodynamic reassessment of the novel solid-state thermal energy storage materials: Ternary polyalcohol and amine system pentaglycerine-tris(hydroxymethyl)-amino-methane-neopentylglycol (PG-TRIS-NPG)," Calphad, vol. 59, pp. 61–75, 2017.

[10] D. K. Benson, R. W. Burrows, and J. D. Webb, "Solid state phase transitions in pentaerythritol and related polyhydric alcohols," Sol. Energy Mater., vol. 13, (no. 2), pp. 133–152, 1986.

[11] M. Barrio, J. Font, J. Muntasell, J. Navarro, and J. Ll. Tamarit, "Applicability for heat storage of binary systems of neopentylglycol, pentaglycerine and pentaerythritol: A comparative analysis," Sol. Energy Mater., vol. 18, (no. 1–2), pp. 109–115, 1988.

[12] J. Font, J. Muntasell, J. Navarro, and J. L. L. Tamarit, "Time and temperature dependence of the exchanged energy on solid-solid transitions of pentaglycerine/neopentylglycol mixtures," Sol. Energy Mater., vol. 15, (no. 5), pp. 403–412, 1987.

[13] A. Serrano, I. Garrido, S. Santos, M. Duran, J.-L. Dauvergne, M. Carmona, and E. Palomo Del Barrio, "Effect of processing on microstructure and mechanical properties of pentaglycerine based solid-solid phase change materials," J. Energy Storage, vol. 55, p. 105677, 2022.

[14] Z. Dai, X. She, C. Wang, Y. Ding, X. Zhang, and D. Zhao, "Thermodynamic Analysis on the Performance of Barocaloric Refrigeration Systems Using Neopentyl Glycol as the Refrigerant," J. Therm. Sci., vol. 32, (no. 3), pp. 1063–1073, 2023.

[15] H. Singh, A. Talekar, W.-M. Chien, R. Shi, D. Chandra, A. Mishra, M. Tirumala, and D. J. Nelson, "Continuous solid-state phase transitions in energy storage materials with orientational disorder – Computational and experimental approach," Energy, vol. 91, pp. 334–349, 2015.

[16] S. Tomassetti, F. Luzi, P. Cheng, P. Forcellese, A. Aquilanti, T. Bellezze, and G. Di Nicola, "Thermal Properties of Alternative Phase Change Materials for Solar Thermal Applications," Int. J. Heat Technol., vol. 41, (no. 3), pp. 481–488, 2023.

[17] C. Rathgeber, S. Hiebler, R. Bayón, L. F. Cabeza, G. Zsembinszki, G. Englmair, M. Dannemand, G. Diarce, O. Fellmann, R. Ravotti, D. Groulx, A. C. Kheirabadi,

S. Gschwander, S. Höhlein, A. König-Haagen, N. Beaupere, and L. Zalewski, "Experimental Devices to Investigate the Long-Term Stability of Phase Change Materials under Application Conditions," Appl. Sci., vol. 10, (no. 22), p. 7968, 2020.

[18] A. Shukla, D. Buddhi, and R. L. Sawhney, "Thermal cycling test of few selected inorganic and organic phase change materials," Renew. Energy, vol. 33, (no. 12), pp. 2606–2614, 2008.

[19] A. Serrano, M. Duran, J.-L. Dauvergne, S. Doppiu, and E. P. Del Barrio, "Tailored transition temperature plastic crystals with enhanced thermal energy storage capacity," Sol. Energy Mater. Sol. Cells, vol. 220, p. 110848, 2021.

# On Measuring Thermal Diffusivity of a Thin Foil: Photothermal Variations

**Paolo Bison[a,#], Giovanni Ferrarini[a], Stefano Rossi[a]**

*a Construction Technologies Institute, National Research Council (CNR), Padova, Italy*

*# Corresponding Author:* paolo-bison@cnr.it

## Abstract

Some analytical solutions of the heat conduction differential equation in 2D case are presented for the geometry of the *Thin Foil* with thickness so small that the temperature variation is negligible through it. The model is successively applied to some *Photothermal* experimental schemes to evaluate the thermal diffusivity of the material of the thin foil.

### *1. Modeling the pulse with gaussian distribution of energy*

The idea of an *instantaneous point source of heat*, that is, of a finite quantity of heat instantaneously liberated at a given point and time in an infinite solid, has proved most useful in the theory of conduction of heat [1].

The differential equation of heat conduction

$$\frac{\partial^2 T}{\partial x^2}+\frac{\partial^2 T}{\partial y^2}+\frac{\partial^2 T}{\partial z^2}-\alpha\frac{\partial T}{\partial t}=0 \qquad (1)$$

is satisfied by the fundamental instantaneous point source solution [2] which was systematically used for the first time by William Thomson (lord Kelvin)

$$T(x,y,z,t)=\frac{Q}{\rho c_p}\frac{1}{\pi^{3/2}}\frac{1}{(4\alpha t)^{3/2}}e^{-\frac{x^2+y^2+z^2}{4\alpha t}} \qquad (2)$$

where x,y,z [m] are the space variables, t [s] is time, T [K] is temperature, $\alpha = \lambda/\rho\, c_p$ [$m^2\, s^{-1}$] is the thermal diffusivity, $\lambda$ [$W\, m^{-1}\, K^{-1}$] the thermal conductivity, $\rho$ [$kg\, m^{-3}$] the density and $c_p$ [$J\, kg^{-1}\, K^{-1}$] the specific heat. Such solution tends to 0 as t -> 0 at all points except in x=0, y=0, z=0 where it becomes infinite.

Notwithstanding the usefulness of such basic solution, mainly as a genetic material to prepare other (more complex) solutions, primarily by convolution in space and time, it

is difficult to generate it within a solid and even more difficult to measure or visualize it. It is therefore interesting to reduce the number of space variable to x, y by making negligible the z. In this case it is easy to generate a point source (for example with a focused laser shot) and to visualize the temperature field (e.g. by an IR camera), without any perturbing contact with the system.

It is considered the solution of the heat conduction equation on the thin foil made of homogeneous and isotropic material. It lies on the z=0 plane, with thickness l [m] so small that the temperature variation over it is negligible. Being h [W $m^{-2}$ $K^{-1}$] the heat exchange coefficient between the foil and the environment, the PDE is [1]

$$\frac{\partial^2 T}{\partial x^2} + \frac{\partial^2 T}{\partial y^2} - \alpha \frac{\partial T}{\partial t} - \nu T = 0 \qquad (3)$$

and the solution [1] for the instantaneous release of a point source in O(0,0) is:

$$T_\delta(x, y, t) = \frac{Q}{4\pi\lambda l t} e^{-\alpha\nu t} e^{-\frac{x^2+y^2}{4\alpha t}} \qquad (4)$$

where $\nu = 2h/\lambda l$ [$m^{-2}$] is the parameter depending on the heat exchange with the ambient and Q [J] is the energy released by the pulse at the origin.

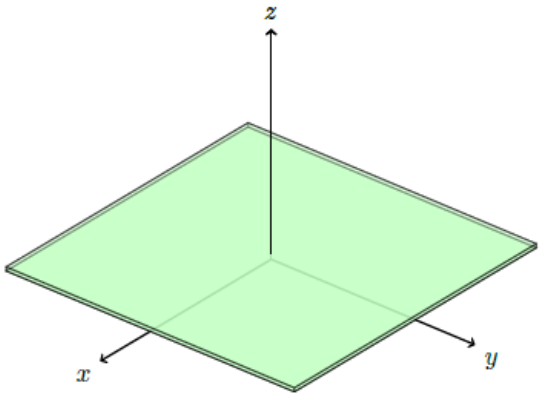


**Figure 1.** The thin foil

If the source is not a point but is distributed on the surface according to a prescribed function of the spatial coordinates, the solution can be obtained by spatial convolution

of Eq. 4 with the actual shape of the heating. The case of a laser beam with gaussian intensity profile [3], with diameter $D_0$ at 1/*e* is easily computed:

$$T_G(x,y,t) = \frac{Q}{4\,\pi\,\lambda\,l\,t} e^{-\alpha\nu t} \int_{-\infty}^{\infty} d\xi \int_{-\infty}^{\infty} d\eta \frac{1}{\pi} \frac{1}{D_0^2/2} e^{-\frac{\xi^2+\eta^2}{D_0^2/2}} e^{-\frac{(x-\xi)^2+(y-\eta)^2}{4\alpha t}}$$

$$= \frac{Q}{\rho\, c_p\, l}\; e^{-\alpha\,\nu\,t}\; \frac{1}{\pi} \frac{1}{D_0^2/2+4\alpha\,t}\; e^{-\frac{x^2+y^2}{D_0^2/2+4\,\alpha\,t}} \qquad (5)$$

where the red color highlights the spatial gaussian distribution released on the surface. The solution is separable and integrating along x, y gives a constant value, independently from time. In this case, because the gaussian function is normalized, it is:

$$\frac{1}{\pi} \frac{1}{(D_0^2/2+4\alpha t)} \int_{-\infty}^{\infty} \int_{-\infty}^{\infty} e^{-\frac{x^2+y^2}{D_0^2/2+4\alpha t}} dx\, dy = 1 \qquad (6)$$

for each value of time t.

Hence, by integrating in x and y the temperature field, one obtains a function that decreases exponentially in time, with the time constant 1/αν:

$$\int_{-\infty}^{\infty} \int_{-\infty}^{\infty} T_G(x,y,t) dx\, dy = const \cdot e^{-\alpha\nu t} \qquad (7)$$

that can be used to evaluate the average heat exchange coefficient between the foil and the ambient, once the thermal diffusivity α has been estimated by the in-plane analysis, as shown by Cernuschi et al. [3].

### *2. Experimental lay-out*

A foil of AISI T302, 500X150 mm, and 25 μm thickness is clamped on both 150 mm sides, by two aluminum bars, tightened with 4 bolts and nuts. The foil is suspended vertically by suitable handles. A pulsed laser source is used to heat one side of the foil. The energy released by the laser is ~ 1 J. The pulse duration is 1 ms. The beam has a diameter of 1" and it is focused by a lens on the back side of the foil. The diameter of the focused beam (assuming it being distributed as a gaussian function) is ~ 1 mm at 1/e. On the other side of the foil, the IR camera (FLIR X6981 SLS LW [7.5 – 12.0μm], 640 X 512 pixels, frame rate

1 kHz) collects a sequence of images, in correspondence of the laser shot. The camera is equipped with a microscope lens 1:1, that means the field of view of each pixel is equal to the pitch of the detector, i.e. 25X25 μm. The experimental lay-out is shown in Fig. 2.

## *3. Experiments*

### *3.1 The foil coated with graphite*

The foil was coated with graphite Graphit 33, on the heated side to increase the absorptivity coefficient, and, on the camera side, to increase the emissivity.

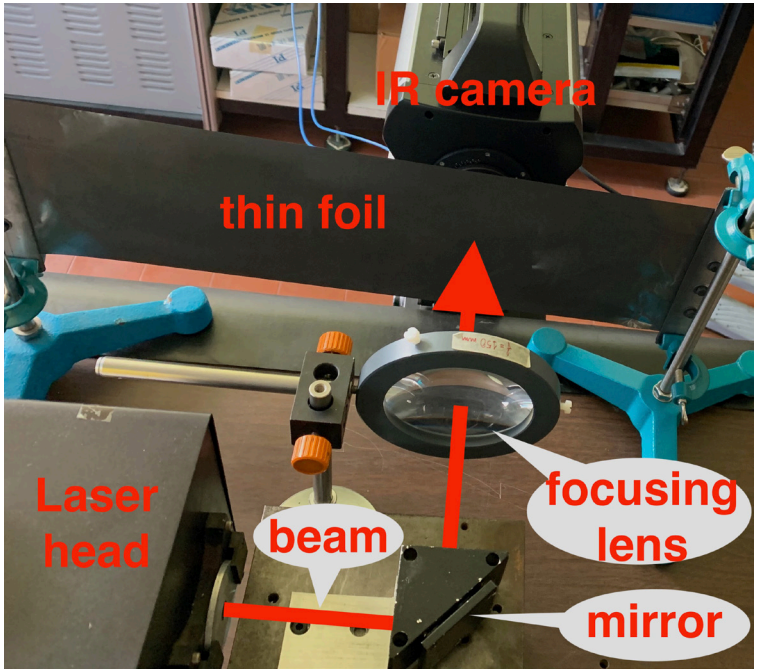


**Figure 2.** Experimental lay out

The laser shots one pulse and the camera collects 100 images (100 ms) before the shot and 500 images (500 ms) after the shot. The images before the shot are averaged and subtracted to the images during and after the shot. The temperature plot, measured on the camera side of the foil, in correspondence of the center of the gaussian heating and at 750 μm and 1250 μm far from the center, are shown in Fig. 3.

### *3.2 The foil without the graphite coating*

The graphite coating could false the correct measurement of the in-plane thermal diffusivity. Indeed, the layers of graphite, sprayed on both sides of the foil, even though very thin, could increase the overall thermal conduction of the foil. To verify if it could affect the final result, the graphite coating was eliminated from both sides of the foil. Evidently, the measurement is becoming more difficult. On one side (the laser side), the energy absorbed decreases due to the low absorptivity of the foil (it is by eyes almost a mirror). On the other side (the camera side), the emissivity is very low, and the apparent thermographic signal is poor. As a result, the signal to noise ratio (S/N) is unacceptable. The S/N could be improved by statistical analysis of many experiments carried on at the same conditions. The experiments can be successively averaged. The signal is expected to emerge from the noise that, if randomly distributed, should decrease as the square root of the number of the experiments. On this purpose, the laser system is configured to deliver periodically a shot with duration 1 ms and energy 1 J. The period between two successive shots is 1 s. In correspondence of each shot the laser system sends a trigger to the IR camera system that starts the acquisition of 50 images at a frame rate of 1 kHz, that is for 50 ms after each shot.

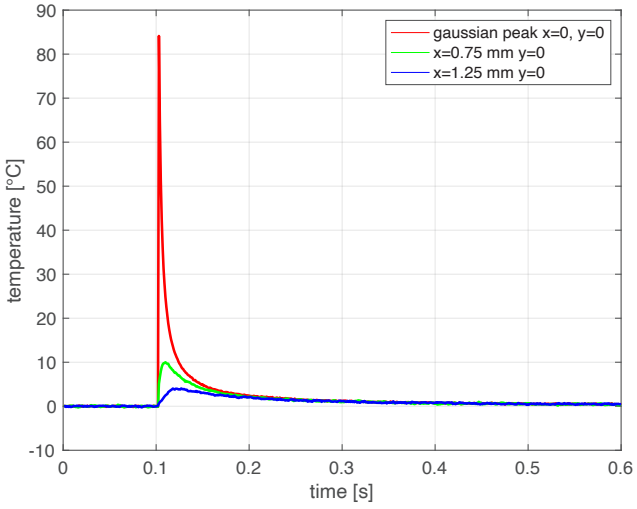


**Figure 3**. Temperature plot in correspondence of the center of the gaussian distribution of heat and far from the center at 0.75 mm and 1.25 mm respectively. Notice the maximum of temperature moving forward in time when spatially moving far from the center of the gaussian distribution.

An unexpected phenomenon appeared during the test without graphite coating. As expected, the temperatures in the image appear largely negative (see Fig. 4). This is due to the poor emissivity and consequently to the large reflectivity. Therefore, the temperature the camera collects is that of its cooled detector that is mirrored by the foil. It is known as the 'Narcissus' effect. The unexpected phenomenon is the apparent decrease of temperature, in phase with the laser shot, far from the supposed heated zone. Fig. 5 shows on the left a sequence of 20 shots at a frequency of 1 Hz. On the right a blow-up of three shots. It is apparent the decrease of the temperature in a zone not affected by the shot (3.3 mm far from the spot). The reason can be found considering the thermal expansion that is well known and exploited in the pump and probe photothermal/photoacoustics techniques [4]. The thermal expansion distorts the viewing angles of some parts of the foil. The highly directional reflectivity changes the apparent cold zones periodically, in phase with the shot. Due to this effect, that makes impossible a reliable fit of the temperature field, it was decided to paint with graphite the thin foil side facing the IR camera. The one facing the laser beam was left unpainted. Evidently, the thermal expansion is still present, but the apparent variation of temperature is cancelled, because the reflectivity becomes negligible and the graphite owns an emissivity that is not dependent from the angle of view (Lambertian emission).

### *4. Data reduction*

In the following sections the processing of data is described.

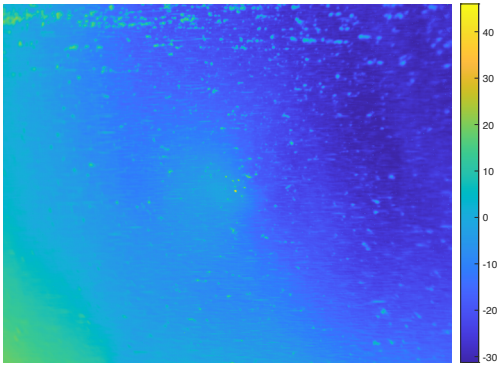


**Figure 4**. Without graphite coating, the surface reflects the temperature of the camera detector that is 67 K. For this reason, the temperature appears largely negative. This is known as the 'Narcissus' effect. In the center of the image, the laser spot barely appears.

### *4.1 With graphite coatings*

Each sequence is treated in the following way:

1. The 100 pre-trigger images are averaged pixel by pixel along time. The resulted image is subtracted, pixel by pixel to any other image in the post-trigger sequence. As a result, the signal of the post-trigger images starts from around zero. Moreover, the IR images appear less affected by localized non-uniformities due to the emissivity variations. See Fig. 6.
2. The post-trigger sequence is considered: the imprint of the gaussian shot emerges from the background immediately after the shot due to the negligible thickness of the foil. See Fig. 7
3. Each post-trigger image is fitted with a 2D gaussian function. Among the estimated parameters, the most important is the denominator of the argument of the exponential function, that is increasing in time, from its initial value $D_0^2/2$, with a 2 slope equal to $4\alpha$. See Fig. 8.

### *4.2 Results with graphite*

Total number of tests was 136. The results are reported in Fig. 9. Some outliers can be noticed that correspond to a poor laser shot. Indeed the lamp voltage is tuned to a very low value that is at the limit of laser ignition. Nonetheless a mean value of thermal diffusivity around $1.66 \cdot 10^{-5}$ is quite evident.

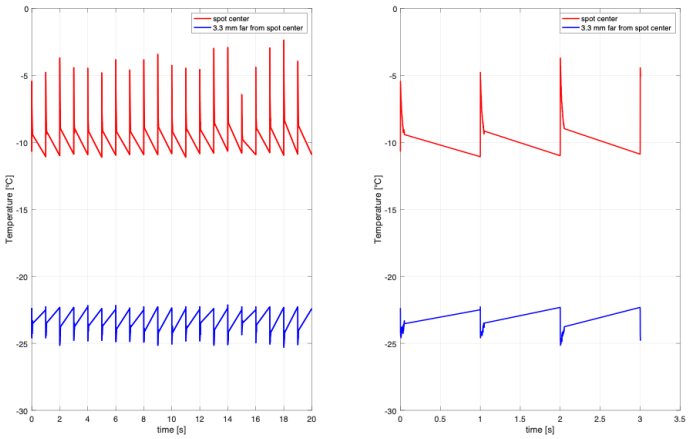


**Figure 5.** On the left a sequence of 20 shots. On the right the blow up of the plot that shows better the increase of temperature in correspondence of the shot (red curve) and the corresponding decrease of temperature far from the shot (blue curve). Data are collected for 50 ms after the trigger. The first image (datum) is at ambient temperature. The second image shows the shot. From 50 ms till the successive trigger (shot), 1 s later, no data are collected. This explains the straight line that connects the last datum of every periodic grabbing with the successive one.

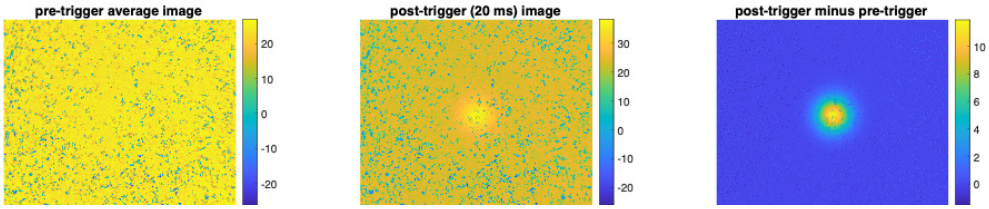


**Figure 6.** On the left the averaged image of the pre-trigger buffer. On the center the image taken 20 ms after the laser shot. On the right, the former minus the latter. The image on the right is an improved version of the center image, because the structural noise due to the emissivity variation was partially cancelled by the subtraction with the pre-trigger image.

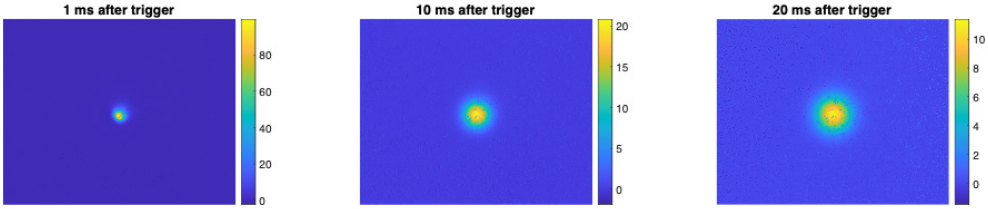


**Figure 7.** The temperature maps showing the gaussian distribution of heat are shown at the moment of the shot and at successive times. Notice the spreading of the distribution and the decrease of its maximum value (see the scale on the left of each image).

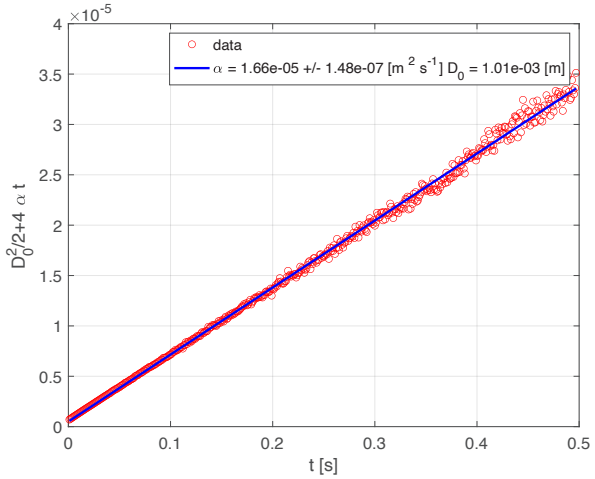


**Figure 8.** Plot of the diameter of the gaussian function that fit at best the temperature data. The fitting is applied to each image in the post-trigger sequence. The diameter is increasing in time as shown by the red dots. The slope of the straight line, fitting the red dots, gives the in-plane thermal diffusivity. In this case the pixel calibration is necessary to obtain the thermal diffusivity. Thanks to the 1:1 optics that is mounted on the IR camera, the pixel dimension is known to be the

pitch of the matrix detector, that is 25 µm. The diameter $D_o$ at t = 0 s is related to the intercept of the line with the y axis.

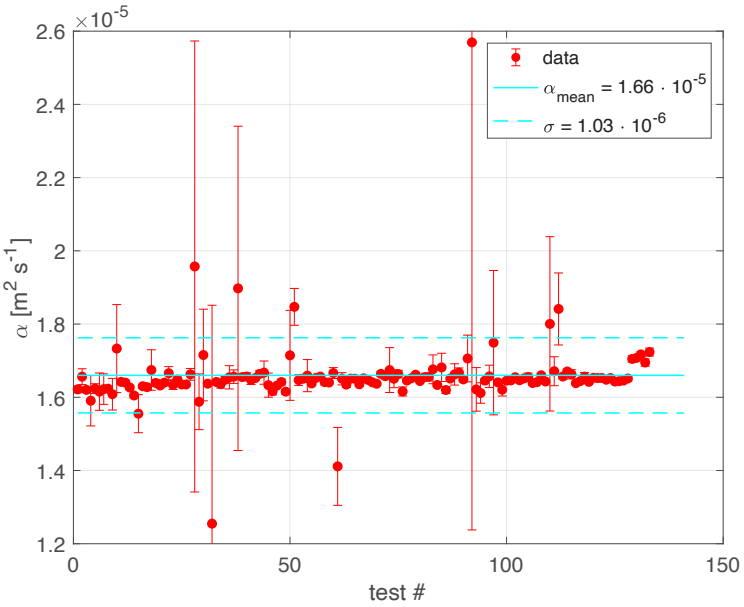


**Figure 9.** Plot of the results of 136 tests. The errorbar for the singular test is generally lower than the global errorbar that can be inferred by repeating the test. Evidently, the non-controlled parameters that affect the measurements (e.g. the energy of laser that is not stable) affect the results.

### *4.3 Without graphite coatings*

Each sequence is treated in the following way:

4. A first run is done without any laser shot. This needs to eliminate a small drift due the intermittent (periodic) working time of the camera that does not reach the steady state during the short 50 ms interval during which the images are collected. An equal number of triggers (20 in the specific case) and the successive 50 ms of data for each trigger, were taken.
5. The second run is done with the laser shot, that heat the foil every time the trigger is sent. Similarly to the first run, 20 shots and the successive 50 ms of data for each trigger, were taken.
6. The two runs are subtracted: the first to the second run. After that, each 50 ms interval of data is summed to the successive, for a total of 20 intervals. A sequence of 50 ms duration is finally obtained.

7. The sequence of IR images (50 images long) is submitted to the same data reduction described in the previous case.

### *4.4 Results without graphite coating on the laser side*

The result is reported in Fig. 10. The value of thermal diffusivity around $1.60 \cdot 10^{-5}$ very close to that obtained in the previous case.

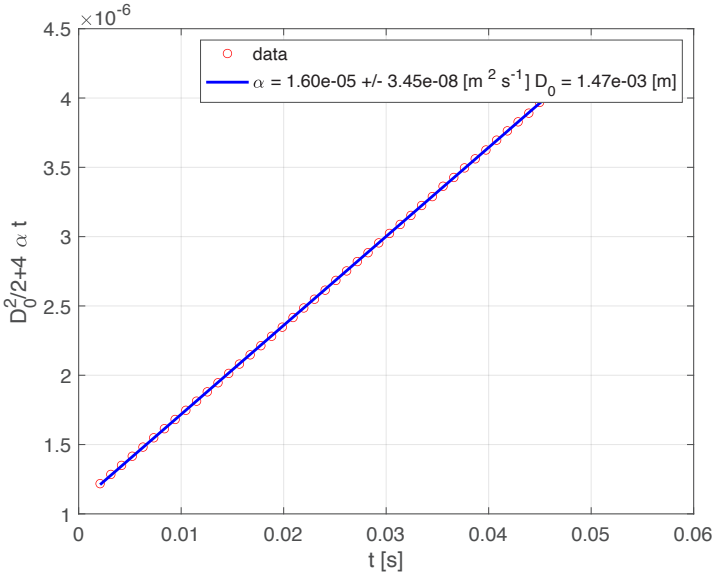


**Figure 10.** Plot of the diameter of the gaussian function that fit at best the temperature data. The fitting is applied to each image in sequence obtained after summing up 20 shots. The diameter Do at t = 0 s is related to the intercept of the line with the y axis.

## *5. Conclusion*

In this work the thermal diffusivity of the AISI T302 thin foil was measured. The results are reported together with the in-plane testing procedure that use a pulsed laser spot as heat source and a fast IR camera to collect the temperature field.

## *References*

[1] H. S. Carslaw and J. C. Jaeger. Conduction of Heat in Solids. Oxford University Press, second edition, 1959.

[2] Lord Kelvin William Thomson. Compendium of the Fourier mathematics for the conduction of heat in solids and the mathematically applied physical subjects of diffusion of fluids and transmission of electric signals through submarine cables. In Mathematical and Physical Papers, volume 2. Cambridge at the University press, 1884.

[3] F. Cernuschi, A. Russo, L. Lorenzoni, and A. Figari. In-plane thermal diffusivity evaluation by infrared thermography. Review of Scientific Instruments, 72(10):3988, 2001.

[4] C. Glorieux. Laser ultrasonics for material characterization and defect detection. https://www2.ung.si/~isschool/2018Erice/CG.pdf, 2018.

# Optimum Experimental Set-up for Thermal Conductivities Measurement of Composite Materials

**Giampaolo D'Alessandro#, Filippo de Monte, Stefano Sfarra**

*Department of Industrial and Information Engineering and Economics, University of L'Aquila, L'Aquila, Italy*

*# Corresponding Author: giampaolo.dalessandro@univaq.it*

## Abstract

The optimum set-up of a two-dimensional (2D) transient heat conduction experiment aimed at estimating simultaneously the out-of- and in-plane thermal conductivities, namely kx and ky, of composite materials is designed. The experimental apparatus here investigated consists of a thin electrical heater put in contact with two larger samples of the same material and thickness, so that the heat diffusion within the specimens is 2D. Moreover, temperature measurements useful for the estimation procedure are obtained only from the unheated surface of the sample which can be subject either to heat losses with the external environment or to heat losses with an insulating material.
A D-optimum criterion, known as Δ+ criterion, is applied to design the optimal experiment which is determined not only as the optimum heating and experiment times, but also in terms of the optimum sample aspect ratio and the optimum width of the heated region. One the one hand, this criterion ensures the minimization of the confidence region of the estimated parameters; on the other hand it allows the determinant of the Fisher matrix to be maximized.
From a mathematical point of view, the 2D heat conduction problem is modeled through a rectangular plate (i.e., the sample) partially heated at the front boundary through a surface heat flux, whereas the opposite boundary can be subject either to heat transfer by free convection with the surrounding air or to heat losses with an insulating material, through a heat transfer coefficient. All the other boundaries are always kept insulated. Once the orthotropic model is reduced to the common isotropic heat diffusion equation, the exact analytical temperature solution is obtained starting from a generalized solution available in the specialized literature. After that the superposition principle can also be applied to account for a finite heating period. Then, the so-called scaled sensitivity coefficients of temperature with respect to the parameters of interest are computed, and a sensitivity analysis is performed to establish whether correlation between them exists. Finally, the optimal experiment aimed at estimating simultaneously the in- and out-of-plane thermal conductivities as well as the heat transfer coefficient (which represent a disturbance of the thermal model) is designed applying the mentioned criterion.

# Adapted Laser-Flash Method for Estimating Thermal Diffusion Properties of a Porous Material Surrounded by Compact Layers

**Elena Campagnoli[a,#], Valter Giaretto[a]**

*a Dipartimento Energia, Politecnico di Torino, Torino, Italy*

*# Corresponding author:* elena.campagnoli@polito.it

## Abstract

Composite structures obtained by superimposing layers of different materials find application in various technological fields. The number of layers and the characteristics of the constituent materials are chosen based on different needs, e.g. for thermal protection of metal components or to preserve high mechanical strength by reducing the overall weight of the structure. For reasons related to production methods, some layers are not available separately from others and the study of their thermal properties cannot be achieved using methods conceived for homogeneous samples. For the evaluation of the properties of these non-free-standing layers, some modifications of the traditional laser-flash method are necessary, especially regarding measurements post-processing.
In the present work, the measurements on three-layer samples were carried out using the classic laser-flash technique, but the analysis of the thermal response of the sample was carried out with a significantly different approach compared to that proposed by Parker and for which the method introduced by Cowan allows heat losses to be considered. The non-normalized thermal response that is measured on the rear surface of the sample was analyzed with a 1D heat diffusion analytical solution, considering both the heat losses on the front and rear surfaces of the sample and the finite pulse effect.
The tested samples are three layers of the same material (Ti6Al4V) but with a different structure. In fact, the two external layers are compact, while the intermediate one is made up of sintered powder of various porosities, which is deposited through additive manufacturing. Since the thermal properties of the internal porous layer are of great interest (in particular its apparent thermal conductivity), the article describes the procedure adopted to estimate them and discusses their identifiability. Furthermore, using the thermal conductivity data available in the literature, a first validation of the adapted laser-flash method is also provided.

### *1. Introduction*

The laser flash method, since its invention about 60 years ago [1-3], has been widely used for the determination of thermal diffusivity.

There are several advantages that have made this technique very popular, to name just a few the speed with which measurements can be carried out, the very small size of the samples and the multiplicity of materials that can be measured.

The original method, as is well known, consists in sending a flash of energy, produced for

example by a laser, onto the base surface of a sample of cylindrical shape, recording on the opposite face the increase in temperature over time via a sensor (thermocouple or detector IR). In its original version, proposed by Parker [1], the thermal diffusivity can be calculated starting from the thermal transient recorded as:

$$\alpha = 1.38 \cdot \frac{L^2}{\pi^2 \cdot t_{1/2}} = 0.139 \cdot \frac{L^2}{t_{50\%}} \qquad (1)$$

where:

α is the thermal diffusivity [$m^2/s$]

L is the thickness of the sample [m]

$t_{1/2}=t_{50\%}$ is the time required to reach half the maximum temperature rise [s].

The method proposed by Parker allows the thermal diffusivity to be accurately determined only if the hypotheses underlying the model are respected when carrying out the measurement. Among these of special relevance are both the hypothesis that the thermal transient that follows the absorption of the energy released by the flash in a thin layer of the sample is adiabatic and the hypothesis that the pulsed energy is released instantaneously.

An adiabatic measurement, as assumed by Parker, cannot be obtained experimentally, even when operating in high vacuum conditions. The presence of radiative losses causes the experiment to deviate from this hypothesis more evidently the higher the measurement temperature and the thicker the sample.

For this reason, at the end of the transient, the maximum temperature reached is lower than that obtainable for the same energy pulse in the adiabatic case. Consequently, the $t_{50\%}$ term in Eq. (1) is underestimated and the thermal diffusivity overestimated. In addition, the thermogram does not present a stable plateau over time once the maximum increase in temperature has been reached, but the temperature decreases over time in a more marked manner the higher the temperature of the sample.

Under these conditions the previous Eq. (1) is no longer accurate and therefore to use the laser flash method in the years following its invention, various models have been developed to take radiation losses into account [4–10].

Regarding the effect of the finite time of the pulse, the “non-instantaneous" energy

release results in a slower temperature increase with a consequent increase in the $t_{50\%}$ term in Eq. (1) which leads to an underestimation of the thermal diffusivity value. This effect, which is particularly relevant with highly diffusive materials and very thin samples, has also been widely studied and corrective methods have been proposed in the literature [7, 11–13].

Aware of these problems, in the present work the measurements were performed using the laser-flash technique in its classic version, but the analysis of the thermal transient was carried out in significantly different way.

First of all, the thermal transient recorded on the rear surface of the sample was not normalized using the maximum recorded temperature whose value, as previously mentioned, is influenced by heat losses. The thermal response to the energy pulse, as described below, was then analyzed using a 1D heat diffusion analytical solution considering both heat losses from the front and rear surface of the sample and the effect of the finite time of the pulse.

The samples used to test the model are three-layer samples of Ti6Al4V in which the two external layers are massive while the intermediate one is made up of sintered powder deposited through additive manufacturing.

The thermal properties of the intermediate layer, which cannot be obtained as a free-standing sample, are of particular interest. The article describes the procedure adopted to estimate these properties and discusses their identifiability.

## *2. Methodology*

Over the course of several decades, the flash technique has consolidated itself as an important method for the estimation of thermal diffusion properties of metals and alloys. In this period, in addition to the improvements of the experimental apparatus consistent with the technical evolution of the hardware components, significant modifications of the methods for determining the thermal properties of interest have been proposed. In fact, compared to the Parker method mentioned in the previous section, in which only a few experimental data were used to determine the thermal diffusivity, nowadays, thanks to the greater capacity for in silico data reduction, more complex estimation algorithms, which typically involve the entire thermogram recorded, are gaining ground.

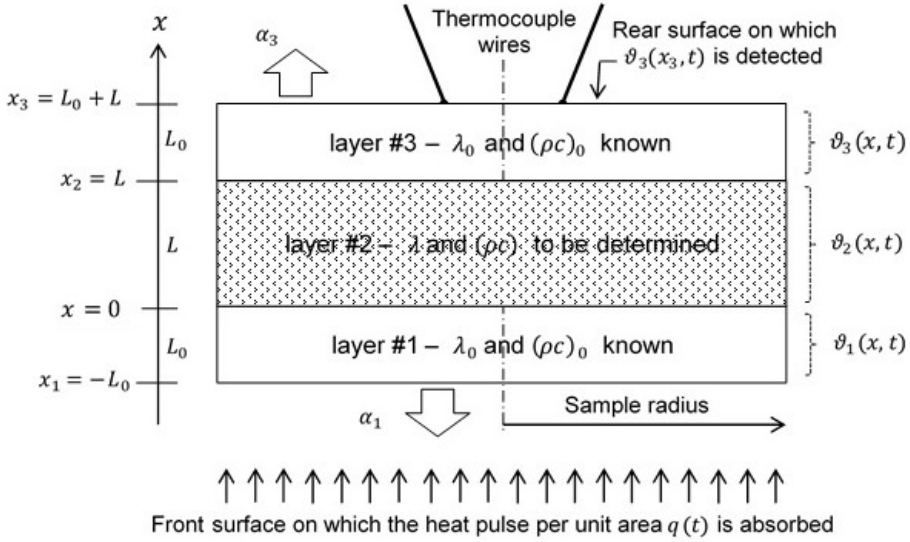


**Figure 1.** Geometric scheme of the sample and arrangement of the layers.

In the case studied, due to the configuration of the samples, the original Parker method cannot be used, and the estimation of the thermal diffusion properties necessarily requires a non-linear procedure. In fact, the material under test is made up of a porous intermediate layer characterized by a dispersed solid matrix (sintered powder), surrounded by two layers with the same chemical composition but with a compact structure.

The geometric scheme in Fig. 1 shows how the external layers have the same nominal thickness L_0, the extent of which can be compared with the thickness L of the porous layer.

The property estimation method that was used is based on two different models, which will be called direct and inverse in the following. Based on the assigned boundary conditions, the direct model provides, starting from the provisional values assigned to the properties to be estimated, the temperature distribution as a function of time within the sample volume. The inverse model is instead arranged on a recursive algorithm, based in our case on least squares, which proposes at each iteration a new set of values

of the thermal properties of the material under test. Once convergence is achieved, the property values obtained are those that minimize the difference between the measured temperature values and those calculated by the direct model for the entire observed transient.

From a general point of view, theoretical treatments and applications of the direct model are reported in the literature cited in the introduction, while the complete theory for the inverse model can be found, for example, in [14]. As regards the direct model, the 1D analytical solution for a three-layer sample is reported in [15, 16], and is obtained using the Laplace transform and its inverse, considering the heat losses by radiation, the contact thermal resistance between the layers and the finite duration of the thermal pulse.

Although this solution can be applied directly to the case in question, it is however possible to formulate some simplifying assumptions and hypotheses as follows:

- according to the 1D model, the heat losses are imposed only at the front and rear surfaces ($x=x_1$ and $x=x_3$ in Fig. 1). The radiative exchanges involving these surfaces were linearized [9] and calculated at the initial temperature T_0 of the sample (equivalent film coefficient), assuming the same emissivity $\varepsilon_0(T_0)$ for both surfaces:

$$\alpha_1 = \alpha_3 = \alpha(T_0) = 4\sigma\varepsilon_0(T_0)\,T_0^3 \qquad (2)$$

  where σ is the Stefan – Boltzmann constant,
- the contact resistances between the intermediate layer and the surrounding ones were not considered because the powder sintering process aims to create a porous structure mechanically connected to the interfaces with the compact layers ($x=0$ and $x=x_2$ in Fig. 1). The presence of defects on these interfaces (typically bubbles) could be considered in the model as thermal contact resistances, but the estimated values of the properties of the porous layer could not however be purified from this effect. Therefore, perfect thermal contact between the layers was assumed and therefore the temperature at the interface between two layers (Fig. 1) is the same:

$$\vartheta_1(0,t) = \vartheta_2(0,t),\ \ \vartheta_2(x_2,t) = \vartheta_3(x_2,t) \qquad (3)$$

- Regarding the finite duration of the heat pulse, its effect on the thermal response of the non-pulsed surface was determined a priori. The response versus time q(t) of the laser system used was approximated by the normalized distribution H(t) suggested by Larson and Koyama [11], such that:

$$q(t) = Q_0 H(t) = Q_0 \, (t/t_P^2) \exp(-t/t_p) \qquad (4)$$

where Q_0 represents all the energy per unit surface area uniformly absorbed in a very thin sublayer of the front surface of the sample and t_p is the instant of time at which the peak energy release occurs which for the laser device used (Nd:YAG laser) is close to 0.2 ms. By adopting the theoretical values available in the literature for the thermal properties of the sintered powder [17-19], some comparisons were carried out considering or neglecting the finite duration of the thermal pulse. Both due to the relatively high thickness of the specimen and the total energy release time, greater than 99.9% in 2 ms, the effect of the finite-pulse time was found to be negligible compared to the case in which the pulse is approximated by the Dirac function δ(0). Consequently, the finite duration of energy pulse was not considered ($t_p$ -->0), so

$$q(t) = Q_0 \delta(0) \qquad (5)$$

Based on these assumptions and considering both the set temperature $T_0$ of the vacuum chamber and the initial condition $\vartheta_j$ (x,t)=$T_j$ (x,t)-$T_0$=0 for each layer and assuming as boundary conditions

$$-\lambda_0(T_0) \frac{\partial \vartheta_1(x_1,t)}{\partial x} = Q_0 \delta(0) - \alpha_0(T_0) \vartheta_1(x_1, t) \qquad (6)$$

$$-\lambda_0(T_0) \frac{\partial \vartheta_3(x_3,t)}{\partial x} = \alpha_0(T_0) \vartheta_3(x_3, t) \qquad (7)$$

the increase in temperature on the non-pulsed rear surface reported in [16] can be written as

$$\vartheta_3(x_3, t) = 8 \frac{Q_0}{C_0 L_0} \sum_{k=1}^{\infty} D_k^{-1} \exp\left(-\mu_k^2 \frac{\lambda_0}{C_0 L_0^2} t\right) \qquad (8)$$

where $C_0=(\rho c)_0$ , $\lambda_0$, and $L_0$ are respectively the volumetric heat capacity, the thermal conductivity and the thickness of the surrounding layers, while the quantity $Q_0$ represents the energy absorbed per unit area of the pulsed surface. The dimensionless term $D_k$ in the sum of Eq. (8) can be expressed as

$$D_k = \psi_1\chi_1 cos(\psi_1\mu_k) + 2\psi_2\chi_2 cos(\psi_2\mu_k) + \psi_3\chi_3 cos(\psi_3\mu_k) + \\ +(2\beta_0^2/3)\{\ 2[\chi_1 sin(\psi_1\mu_k) - 2\chi_2 sin(\psi_2\mu_k) + \chi_3 sin(\psi_3\mu_k)] \\ - \mu_k[\psi_1\chi_1 cos(\psi_1\mu_k) + \psi_3\chi_3 cos(\psi_3\mu_k)]\ \} + \\ + 2(\beta_0/\mu_k^2)\{\chi_1[cos(\psi_1\mu_k) + \psi_1\mu_k sin(\psi_1\mu_k)] + \chi_3[cos(\psi_3\mu_k) + \\ + \psi_3\mu_k sin(\psi_3\mu_k)]\} \qquad (9)$$

in which

$$\beta_0 = \alpha(T_0)L_0/\lambda_0, \qquad (10)$$

$$\chi_1 = 2 + 1/\sqrt{\eta\,\kappa} + \sqrt{\eta\,\kappa},\ \ \chi_2 = \sqrt{\eta\,\kappa} - 1/\sqrt{\eta\,\kappa},\ \ \chi_3 = 2 - 1/\sqrt{\eta\,\kappa} - \sqrt{\eta\,\kappa} \qquad (11)$$

$$\psi_1 = 2 + \frac{L}{L_0}\sqrt{\kappa/\eta}, \qquad \psi_2 = \frac{L}{L_0}\sqrt{\kappa/\eta}, \qquad \psi_3 = 2 - \frac{L}{L_0}\sqrt{\kappa/\eta} \qquad (12)$$

where the quantities to be estimated $\kappa=\lambda/\lambda_0$ and $\eta=C/C_0=((\rho c))/(\rho c)_0$ represent the thermal conductivity and volumetric heat capacity of the sintered powder, both dimensionless using the similar properties of the adjacent layers.

The terms $\mu_k$ in the Eq. (9) are the k-th eigenvalue obtained from the solution of the following equation:

$$\chi_1 sin(\psi_1\mu_k) + 2\chi_2 sin(\psi_2\mu_k) + \chi_3 sin(\psi_3\mu_k) - \{2(\beta_0/\mu_k)[\chi_1 cos(\psi_1\mu_k) + \\ \chi_3 cos(\psi_3\mu_k)] + (\beta_0^2/\mu_k^2)[\chi_1 sin(\psi_1\mu_k) - sin(\psi_2\mu_k) + \chi_3 sin(\psi_3\mu_k)]\} = 0 \qquad (13)$$

The maximum temperature increase detectable on the rear surface corresponds to the asymptotic value $\vartheta_\infty$ achieved in the case of an adiabatic sample, defined as

$$\vartheta_\infty = \frac{Q_0}{2C_0L_0 + CL} = \frac{Q_0}{C_0L_0}\left(2 + \frac{L}{L_0}\eta\right)^{-1} \qquad (14)$$

Through this asymptotic value, the thermal response given by Eq. (8) can be normalized, becoming independent of the amount of the absorbed heat $Q_0$

$$\Theta_3(x_3,t) = \frac{\vartheta_3(x_3,t)}{\vartheta_\infty} = 8\left(2 + \frac{L}{L_0}\eta\right)\sum_{k=1}^{\infty} D_k^{-1}\exp\left(-\mu_k^2 \frac{\lambda_0}{c_0 L_0^2} t\right) \qquad (15)$$

Since the expected duration of the transient is well above one second, the sample cannot be assumed adiabatic and heat losses involving the surrounding layers make it arduous to experimentally determine $\vartheta_\infty$. In fact, compared to the asymptotic value of Eq. (14), the maximum temperature increase detectable on the non-pulsed surface is smaller the greater the heat losses. Moreover, the peculiar arrangement of the material under test inside the specimen makes it impossible to perform an a posteriori correction for the effect of thermal losses on the estimated properties [9-10].

For this reason, it was decided not to normalize the response recorded on the rear surface of the sample and among the quantities to be estimated, in addition to the dimensionless parameters κ and η previously introduced, the quantity of heat $Q_0$ absorbed on the pulsed surface of the sample was added. The estimate of this last quantity is not of particular interest but is necessary due to the configuration of the sample being studied.

As regards the inverse model, the theory for an equivalent case is detailed in [20], and therefore only some aspects concerning the identifiability of the parameters to be estimated are recalled here. Fundamental help is given by the so-called sensitivity coefficients, defined through first partial derivatives of the dependent variable with respect to the parameters to be estimated. In this case the dependent variable is the temperature increase given by Eq. (8) and its derivatives with respect to the parameters κ, η and $Q_0$ were calculated numerically at each time step and for each iteration.

The sensitivity coefficients provide important information in the estimation problem. The sensitivity coefficient matrix is composed of as many rows as the time intervals observed and in this case of three columns (as many as the parameters to be estimated) and allows us to highlight the possible linear dependence between the parameters to be estimated. In fact, for the simultaneous identification of the parameters the product between the sensitivity matrix and its transpose gives a square matrix whose determinant must always be different from zero, as happens in the proposed case. Furthermore, for the

parameters to be estimated, the magnitude of these coefficients allows their estimation uncertainty to be established, the higher the magnitude of the coefficient, the lower the estimation uncertainty.

### *3. First results and discussion*

The described method was applied to several samples with layers arranged according to the geometry shown in Fig. 1, but with different thicknesses of the sintered powder layer [20]. Since the method requires the estimation of the energy input that induces the thermal transient, some preliminary results are reported below to investigate this aspect. The samples tested are two, characterized by the same overall thickness and by some differences in the thickness of the layers, as reported in Tab. 1.

**Table 1.** Layer thicknesess

| Sample | Thickness $L_0$ of the surrounding layers (mm) | Thickness L of the sintered powder (mm) |
|---|---|---|
| #1 | 0.61 | 1.81 |
| #2 | 0.50 | 2.03 |

For the second sample, which has a greater thickness of sintered powder than the first, the tests were conducted by modifying the input energy assigned to the laser and increasing it by approximately 25%. The aim was both to verify that the estimated values of the properties of the sintered powder were independent of the flash energy and to verify that the estimated values for the absorbed energy $Q_0$ were consistent with the energy used for the pulse.

Both samples were studied from room temperature to 800 °C by taking measurements approximately every 200 °C within this range. In this temperature range the values of the thermal diffusion properties of the compact Ti6Al4V were taken from the literature [19] as well as those relating to the sintered powder with the same composition. In the literature the latter are only available starting from a temperature of 200 °C and are obtained based on the properties of the compact material assuming three-dimensional aggregation schemes for the sintered powder [17-18].

Regarding the radiative heat losses approximated by Eq. (2), the emissivity $\varepsilon_0 (T_0)$ of the compact Ti6Al4V surfaces (both the front and rear ones) was here assumed independent

of the temperature and considered equal to 0.3.

The estimated values of thermal conductivity and volumetric heat capacity of the sintered powder are shown in Figs. 3-4 using the rhomboid and circular markers respectively for samples #1 and #2. The error bars in the figure refer to the estimated standard deviation for the bilateral t-distribution for a confidence level of 95%. In both figures the solid lines represent the trend obtained considering the estimated values for both samples while the dashed lines refer to what was found in the literature for the sintered powder and the dotted lines to the properties of the compact material.

The comparison between the values obtained from the measurements and those available in the literature shows good agreement. It is also interesting to note that the properties of the compact material are as expected higher, by approximately seven times for thermal conductivity and two times for volumetric heat capacity in a temperature-independent manner.

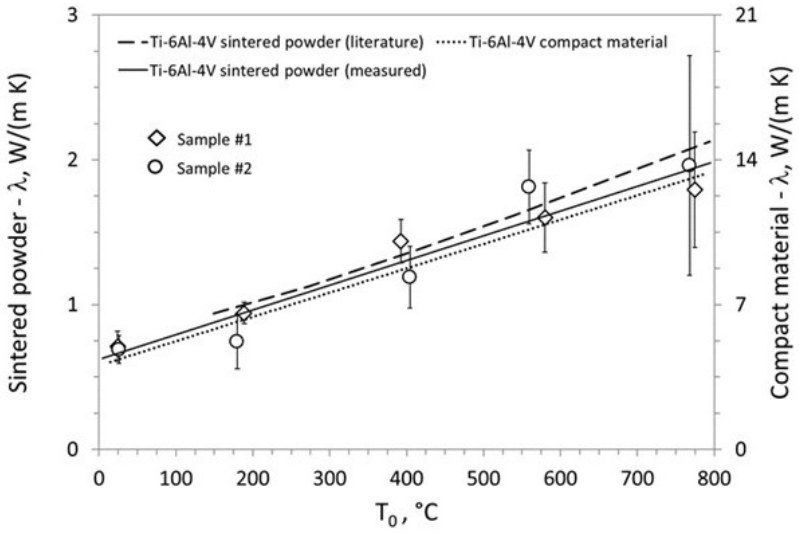


**Figure 2.** Trend of the estimated thermal conductivity as a function of temperature and comparison with literature data for the compact material and for the sintered powder.

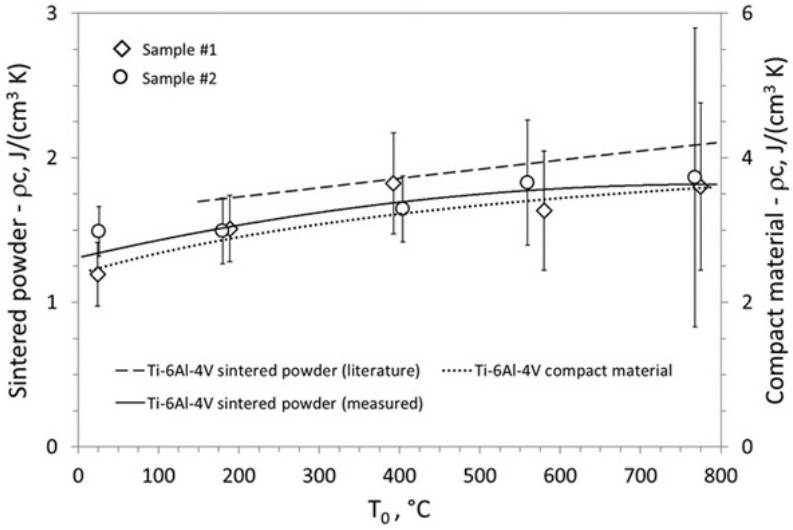


**Figure 3.** Estimated volumetric heat capacity versus test temperature for the sintered powder and comparison with literature data and compact material.

Figure 4 shows the estimated values of the energy Q_0 that is absorbed per unit surface area of the samples. Since for sample #2 the energy pulse used is higher, the trend of the estimated values of the absorbed energy in Fig. 4 seems to confirm the validity of the calculations. In fact, as can be seen in Fig. 4, the ratio between the estimated values of the energy Q_0 for the two samples is almost constant at all test temperatures T_0. Examining the results obtained it is possible to verify that the energy absorbed by sample #2 is approximately 15% higher compared to an increase in flash energy of approximately 25%. This difference can reasonably be explained by considering both the efficiency of the laser system and the fact that the flash energy value is not a measured quantity. What is considered most important here is that these ratios are approximately independent of the test temperature.

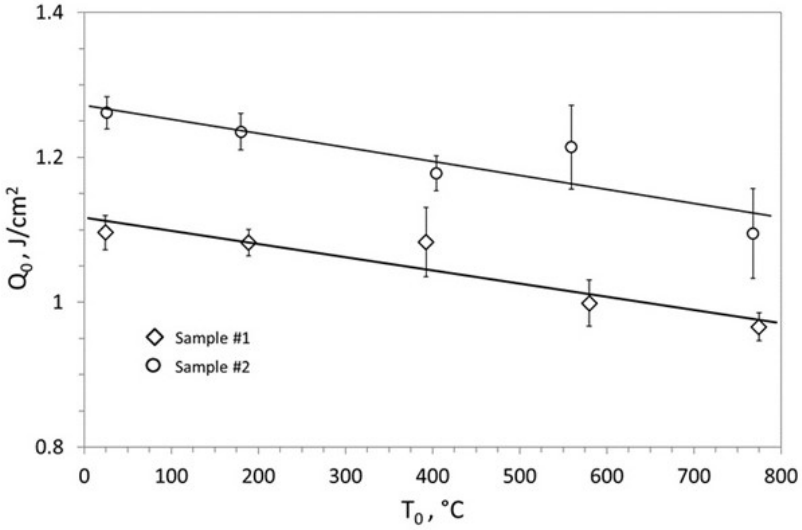


**Figure 4.** Estimation of the energy absorbed on the front surface of the samples as a function of the test temperature.

As regards the identifiability of this parameter, it is less simple to explain the trend as a function of temperature with a negative slope found in the two cases examined. Among the extreme temperature values investigated, the relative variation of Q_0 is about 15% for both samples. We can list three possible reasons: the inverse model, the assumptions about quantities influencing the heat losses, in particular the temperature-independent emissivity, and the behavior of the measuring equipment when the temperature varies. The good agreement between the expected and estimated values for the thermal properties of the sintered powder allows us to exclude at the moment the first two reasons listed as both would affect these results. As regards the apparatus, the optical path of the laser beam is mainly external to the measurement chamber. Lenses and mirrors are kept at room temperature, except for the optical window on the measuring chamber which allows the passage of the laser beam. The temperature dependence of the optical properties of this window could explain the reduction in laser beam intensity, but this has yet to be demonstrated.

### *References*


[1] W.J. Parker, R.J. Jenkins, C.P. Butler, G.L. Abbott, "Flash method of determining thermal diffusivity, heat capacity, and thermal conductivity", J Appl Phys, 32 (9) pp.1679–1684, 1961.

[2] F. Righini, A. Cezairliyan, "Pulse method of thermal diffusivity measurements (a review)", High Temperature-High Pressure, 5 pp. 481-501, 1973.

[3] K.D. Maglic, A. Cezairliyan, V.E. Peletsky, Compendium of Thermophysical Property Measurement Methods, 2, Plenum Press, 1992.

[4] R.D. Cowan, "Pulse method of measuring thermal diffusivity at high temperatures", J Appl Phys, 34 (4) pp.926–927, 1963.

[5] D.A. Watt, "Theory of thermal diffusivity by pulse technique", J Appl Phys, 46 (2) pp.714–719, 1975.

[6] L.M. Clark, R.E. Taylor, "Radiation loss in the flash method for thermal diffusivity", J Appl Phys, 17 (2) pp.231–240, 1966.

[7] R.C. Heckman, "Finite pulse-time and heat-loss effects in pulse thermal diffusivity measurements", J Appl Phys, 44 (4) pp.1455–1460, 1973.

[8] J.A. Cape, G.W. Lehman "Temperature and finite pulse time effects in the flash method for measuring thermal diffusivity", J Appl Phys, 34 (7) pp.1909–1913, 1963.

[9] L. Dusza, "Combined solution of the simultaneous heat loss and finite pulse corrections with the laser flash method", High Temperature-High Pressure, 27/28 (5) pp. 467-473, 1995.

[10] A.R. Mendelsohn, "The effect of heat loss on the flash method of determining thermal diffusivity", Appl Phys Lett, 2 (1) pp.19–21, 1963.

[11] K.B. Larson, K. Koyama, "Correction for finite-pulse-time effects in very thin samples using the flash method of measuring thermal diffusivity", J Appl Phys, 38 (2) pp.465–474, 1967.

[12] J. Xue, X. Liu, R. Taylor, "The effects of a finite pulse time in the flash thermal diffusivity method", Int J Thermophys, 14 (1) pp.123–133, 1993.

[13] T. Azumi, Y. Takahashi, "Novel finite pulse-width correction in flash thermal diffusivity measurement", Rev Sci Instrum, 52 (9) pp.1411–1413, 1981.

[14] J. V. Beck, K. J. Arnold, Parameter estimation in engineering and science, Wiley, New York, pp. 340-341, 1977.

[15] H.J. Lee, Thermal Diffusivity in Layered and Dispersed Composites, PhD thesis, Purdue University, Lafayette, IN, USA, 1975.

[16] J.N. Sweet, Data Analysis Methods for Flash Thermal Diffusivity Experiments, Sandia National Laboratories, Albuquerque, NM, USA, 1989. https://doi.org/10.2172/6312039

[17] N.K. Tolochko, M.K. Arshinov, A.V. Gusarov, V.I. Titov, T. Laoui, L. Froyen, "Mechanisms of selective laser sintering and heat transfer in Ti powder" Rapid Prototyp J, 9 (5) pp. 314–326, 2003.

[18] M. Shapiro, V. Dudko, V. Royzen, Y. Krichevets, S. Lekhtmakher, V. Grozubinsky, et al., "Characterization of Powder Beds by Thermal Conductivity: Effect of Gas Pressure on the Thermal Resistance of Particle Contact Points", Part. Part. Syst. Charact., 21 pp. 268–275, 2004.

[19] M. Boivineau, C. Cagran, D. Doytier, V. Eyraud, M.H. Nadal, B. Wilthan, et al., "Thermophysical properties of solid and liquid Ti6Al4V (TA6V) alloy", Int J Thermophys, 27 (2) pp. 507–529, 2006.

[20] M. Galati, E. Campagnoli, V. Giaretto, L. Iuliano, "Modelling the thermal behavior of Ti6Al4V sintered powder bed in electron beam powder bed fusion (EB-PBF)", Procedia CIRP, 118 pp. 664–669, 2023.

# Lo sviluppo del biofilm può influenzare la trasmissione del calore nei mezzi fratturati?

**Francesco Anaclerio*, Adriana Dammicco*, Nicola Pastore*, Concetta I. Gasi***

** Dipartimento di Ingegneria Civile, Ambientale, del Territorio, Edile e di Chimica, Politecnico di Bari, Italy*

*# Corresponding Author:* adriana.dammicco@poliba.it

**Keywords:** trasmissione di calore, biofilm, mezzi fratturati, modello fisico

## Abstract

La trasmissione del calore, tra mezzi fratturati nel sottosuolo e i fluidi che circolano al loro interno, è una tematica che presenta implicazioni significative in vari ambiti quali i processi industriali, la salvaguardia dell'ambiente e ovviamente quello dei sistemi geotermici. Sono molteplici i fattori che possono influenzare la trasmissione del calore. Negli ultimi anni, l'influenza dei fattori fisici e chimici sono stati parzialmente discussi da diversi autori, mentre gli effetti dei processi biologici sulla trasmissione del calore sono ancora poco conosciuti. In questo lavoro, viene presentato un setup sperimentale di laboratorio per studiare l'effetto della crescita del biofilm sulla trasmissione di calore tra le acque sotterranee e un blocco di calcare fratturato. Il setup sperimentale include un blocco di calcare fratturato di forma parallelepipeda di 0.08 m × 0.040 m × 0.060 m, interrotto da 14 fratture e saturato con acqua sotterranea proveniente dall'area industriale di Bari. Sono stati praticati diversi fori lungo le fratture per osservare la variazione di temperatura dell'acqua che scorre attraverso il network di fratture. Condizioni al contorno di temperatura costante e adiabatiche sono state imposte rispettivamente sulla superficie laterale e sulle superfici superiore e inferiore. Il blocco di calcare fratturato è collegato a un circuito idraulico mediante porte di ingresso e di uscita. L'acqua riscaldata scorre attraverso la rete di fratture secondo dei cicli termici imposti. Attraverso l'osservazione, in corrispondenza delle porte di ingresso e di uscita, delle variazioni di flusso, della pressione, del pH, del potenziale redox, della composizione del biofilm nonché l'osservazione della distribuzione della temperatura in diverse posizioni della rete di fratture, il setup sperimentale sviluppato può chiarire la dinamica della crescita del biofilm e il suo effetto sull'interazione della trasmissione del calore, inclusi i modelli di colonizzazione microbica, sviluppo strutturale e composizione del biofilm. La Comprensione di queste dinamiche è cruciale per ottimizzare la gestione dei serbatoi geotermici nei mezzi fratturati in formazioni carbonatiche. Inoltre, questo lavoro aiuta l'avanzamento della conoscenza delle dinamiche ecologiche e biogeochimiche negli acquiferi carbonatici fratturati e fornisce informazioni preziose per la gestione e la bonifica degli acquiferi contaminati e dei processi industriali che coinvolgono tali acquiferi. In particolare, questo lavoro ha indagato le variazioni delle proprietà termofisiche correlate alla crescita della patina di biofilm sulle fratture per comprendere se essa costituisca una riduzione dello scambio di calore tra il fluido e la roccia circostante.

### *1. Introduzione*

L'uso delle fonti rinnovabili è diventato un elemento cruciale per affrontare le sfide globali legate al cambiamento climatico, alla sicurezza energetica e alla sostenibilità ambientale. La crescente preoccupazione per i cambiamenti climatici e la necessità di ridurre le emissioni di gas serra hanno spinto le attività di ricerca e lo sviluppo per rendere l'utilizzo delle fonti energetiche rinnovabili economicamente ed ambientalmente sostenibile. Il sistema dei distretti energetici, data la loro elevata efficienza, rappresenta la soluzione energetica più efficace ed efficiente. Laddove i distretti utilizzano fonti di energia rinnovabile, possono ridurre significativamente le emissioni di gas serra e la dipendenza dai combustibili fossili, aumentando la resilienza e la sostenibilità delle aree urbane e industriali. In tale contesto i sistemi di immagazzinamento termico nel sottosuolo (UTS) rappresentano una tecnologia ampiamente validata e giocano un ruolo fondamentale, combinandosi e integrandosi con altre tecnologie rinnovabili in modi diversi al fine di soddisfare la domanda di riscaldamento e raffreddamento dei distretti residenziali e industriali. I sistemi UTS rappresentano un' importante tecnologia che permette di utilizzare il calore residuo proveniente ad esempio dai processi industriali (waste heat) o quello fluttuante per esempio derivante dagli impianti solari termici. L'energia disponibile in maniera discontinua tutto l'anno, può essere accumulata nel sottosuolo durante il suo picco di produzione. Successivamente sarà il sottosuolo a cedere calore alle utenze civili, agricole e industriali. I sistemi di immagazzinamento e recupero di energia termica negli acquiferi (*Aquifer Thermal Energy Storage* - ATES) rappresentano una soluzione efficiente e sostenibile per l'immagazzinamento e recupero di calore proveniente da altre fonti rinnovabili come il solare termico (Bloemendal et al., 2015; Bloemendal e Hartog, 2018; Omer, 2008).

Una delle maggiori problematiche che ostacola l'utilizzo sostenibile degli ATES è rappresentata dai processi di intasamento (*clogging*), responsabile della riduzione della efficienza fino alla compromissione del sistema (Burté et al., 2019; Gjengedal et al.,2020). Il clogging avviene su diversi livelli, ossia: sulle pareti filtranti sui pozzi di estrazione e re-immissione, all'interno degli scambiatori di calore dell'impianto, nonché sulle pareti dei grani, negli acquiferi porosi e sulle pareti delle fratture negli acquiferi fratturati. I fenomeni di clogging avvengono principalmente attraverso tre meccanismi (Baveye et al., 1998): fisico, causato della presenza di minerali a grana fine e/o frammenti di

roccia o bolle d'aria, chimico, tramite la precipitazione di composti chimici e biologico, per la formazione di biofilm (Gjengedal et al., 2020). Questi tre processi sono correlati e dipendenti dalle caratteristiche geochimiche dell'acqua della falda acquifera e dal tipo di formazione geologica che ospita l'acquifero. In letteratura, ci sono pochi studi sull'effetto della crescita del biofilm sulle proprietà idrauliche e termiche degli acquiferi e quindi sull'efficienza degli ATES (Beretta, 2017). Beretta (Beretta 2017) analizza i problemi connessi all'intasamento dei pozzi dovuto alla presenza di bolle d'aria, di solidi sospesi, alla crescita batterica, nonché alle razioni chimico-fisiche correlate. In particolare, l'autore ha messo in luce come la crescita batterica determini la formazione di *biofouling* ossia un film di microrganismi in corrispondenza dei filtri che ostacola il flusso idrico. L'entità e la velocità di tale crescita dipendono anche dalla presenza di nutrienti nelle acque reimmesse nell'acquifero. Castagner et al. 2006, discute della persistenza del biofilm all'interno degli acquiferi fratturati. A tale scopo gli autori hanno messo a punto un setup sperimentale per simulare e osservare la persistenza a lungo termine in un blocco di calcare fratturato. Si è osservato, a seguito di una fase di biostimolazione, un decremento della conducibilità idraulica, ovvero anche una instabilità della conducibilità idraulica a seguito di eventi successivi di occlusione e disostruzione. La mutazione della popolazione batterica in termini di cambiamento morfologico, invecchiamento del biofilm e rilascio di depositi minerali rappresenta il fattore principale di questa instabilità. Gjengedal et al. 2019, focalizza l'attenzione su strategie di monitoraggio in grado di rilevare e identificare lo sviluppo di processi di clogging senza dover necessariamente sospendere l'impianto. Gli autori mettono a punto un test che richiede un minimo di quattro sensori di temperatura e due sensori di pressione per descrivere le prestazioni del sistema. Il test viene eseguito sistematicamente durante il funzionamento e una prestazione alterata del sistema avverte circa eventuali problemi di intasamento o incrostazione in modo tale da poter pianificare una manutenzione costante evitando danni al sistema. Il biofilm è un aggregato strutturato di cellule microbiche che convivono in una matrice polimerica extracellulare autoprodotta e idratata di sostanze polimeriche extracellulari (Allison,2023). La stabilità di un biofilm può essere definita come la sua capacità di resistere al degrado e di mantenere la sua originale adesione superficiale e struttura coesiva (Flemming, 2002). Tale stabilità influisce sulla persistenza del biofilm a lungo termine, sul comportamento idrodinamico e termico (Zhang e Bishop, 2003;

Picoreanu et al.,2001; Ross e Bickerton, 2002).
L'obiettivo del presente studio è valutare, attraverso la realizzazione di un modello fisico di laboratorio rappresentativo delle dinamiche di flusso e trasporto che avvengono negli ATES, gli effetti della crescita del biofilm sull'efficienza dello scambio termico.

## *2. Setup sperimentale*

È stato messo a punto un modello fisico di laboratorio volto a rappresentare le dinamiche di flusso, trasporto di calore, nonché i processi di crescita del biofilm e le loro interazioni all'interno di un ambiente di geometria e caratteristiche idrauliche e termiche note, nonché sotto condizioni al contorno controllate. Il cuore del setup sperimentale è rappresentato da un blocco fratturato di calcare di Altamura di dimensioni 0.8 m x 0.4 m x 0.6 m. Tale blocco è stato utilizzato per precedenti studi sul flusso (Cherubini et al., 2012), trasporto di massa (Cherubini et al. 2013, 2014) e calore (Cherubini et al., 2017; Heinze and Pastore, 2023) nei mezzi fratturati.
Per convenienza si riporta una breve descrizione della preparazione del blocco utilizzata nei precedenti studi. È stata generata una rete di fratture mediante colpi di martello da 5 kg sul blocco di calcare. Le fratture che interessano il blocco sono 14, di cui le due principali corrono lungo la dimensione maggiore del blocco. Le fratture sono state ripulite dai detriti e le fessure sono state sigillate con del silicone. È stata applicata una resina epossidica con una conduttività termica di 0.502 W/mK su tutte le facce del blocco. Successivamente, è stato costruito un telaio di 0.085 m × 0.405 m × 0.605 m intorno al blocco ed è stato versato uno strato di resina epossidica tra la pietra calcarea e il telaio per ottenere su tutte le facce uno spessore di resina epossidica di 0.005 m. All'estremità del blocco sono stati praticati dei fori con un diametro di 0.01 m, chiusi con una boccola esagonale e sigillati con resina epossidica a rapido indurimento. Queste porte consentono l'ingresso e la fuoriuscita di fluido dal network di fratture. Tale blocco rappresenta l'ambiente all'interno del quale si intende investigare l'interazione tra le dinamiche di flusso e trasporto di calore e la crescita di biofilm. A tale scopo il blocco, dopo un revamping, è immerso in un ambiente controllato che permettere lo scambio di calore esclusivamente dalla superficie laterale dello stesso. All'interno del blocco circola acqua di falda prelevata dall'area Metropolitana di Bari le cui caratteristiche chimo-fisiche sono riportate in Tabella. 1

**Tabella 1.** Risultati analitici relativi alle acque di falda nella zona di Bari-Modugno.

| Parametri MICROBIOLOGICI | Unità di misura | Risultati |
|---|---|---|
| Coliformi fecali | UFC/100 ml | 107.89 |
| Coliformi Totali | UFC/100 ml | 939.24 |
| Ricerca e numerazione di Escherichia coli | UFC/100 ml | 25.68 |
| Streptococchi fecali | UFC/100 ml | 77.52 |
| Spore di clostridi solfito riduttori | UFC/100 ml | 10.97 |
| Colonie su agar a 22°C | UFC/1 ml | 2006.24 |
| Colonie su agar a 37°C | UFC/1 ml | 3292.44 |
| Staphylococcus aureus/ staffilococchi patogeni | UFC/250 ml | 9.38 |
| Pseudomonas aeruginosa | UFC/250 ml | 153.20 |
| Parametri CHIMICI | Unità di misura | Risultati |
| pH | pH | 8.08 |
| Conduttività | µs/cm | 2552.30 |
| Carbonio organico totale TOC | mg/l | 5.62 |
| Alcalinità | mg/l | 625.67 |
| Sodio | mg/l | 409.71 |
| Potassio | mg/l | 27.92 |
| Magnesio | mg/l | 71.50 |
| Calcio | mg/l | 118.94 |
| Azoto ammoniacale | mg/l | 0.48 |
| Nitrati | mg/l | 32.40 |
| Nitriti | µg/l | 97.61 |
| Fluoruri | µg/l | 436.12 |
| Cloruri | mg/l | 685.79 |
| Solfati | mg/l | 161.42 |

L'acqua circola all'interno del network di fratture dalla porta di immissione (inlet) alla porta di uscita (outlet). Tali porte sono situate lungo la dimensione maggiore del blocco. L'acqua di falda viene riscaldata ad una temperatura di immissione di circa 35°C attraverso un sistema di riscaldamento descritto in seguito.

Il revamping del blocco consiste nelle seguenti lavorazioni (Fig. 1). In primo luogo, per impostare una condizione al contorno di temperatura costante solo sulla superficie laterale del blocco, è stato asportato il rivestimento di resina epossidica sul contorno

superiore e inferiore della superficie laterale e sostituito con del materiale termicamente isolante ovvero un cordolo in polietilene da 0.01 m con conducibilità termica pari 0.035 W/mK. All'interno del blocco, in corrispondenza delle fratture sono stati eseguiti fori da 0.004 m dove sono state inserite 8 termoccoppie di tipo K per monitorare la temperatura all'interno del blocco e sigillate con boccole esagonali e resina epossidica a rapido indurimento. Inoltre, si sono posizionate 7 termocoppie in corrispondenza di tutte le porte all'estremità del blocco (1-7) per monitorare la temperatura all'estremità del network di fratture. Due sensori di pressione RS 828-507 (range: 0 -50 mbar) posti in corrispondenza delle porte di entrata e uscita monitorano la caduta di pressione all'interno del network di fratture. Un sensore di flusso meccatronico SBG232 (range 0,000005 - 0,00025 m3/sec) è installato a monte della porta di ingresso al fine di monitorare la portata in entrata al network di fratture. Tutti i sensori sono collegati a 3 data logger a 8 canali Picolog TC-08.

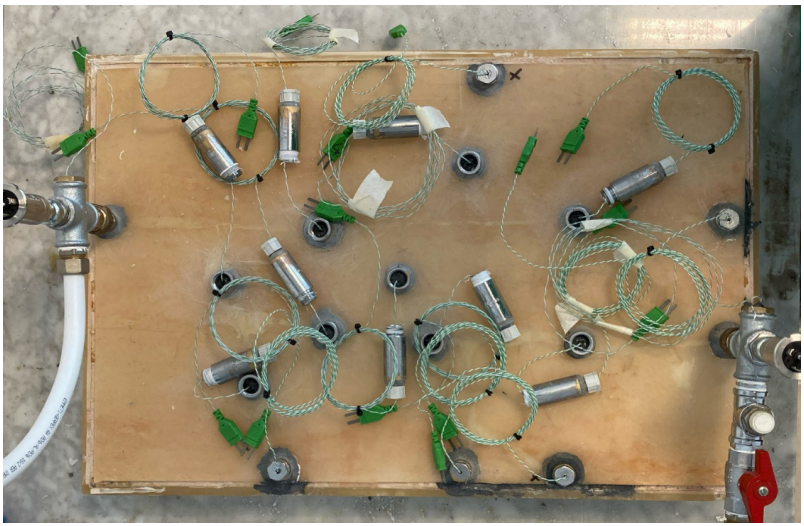

**Figura 1.** Vista frontale del blocco durante le operazioni di revamping.

Sulla superficie superiore e inferiore del blocco è stato posto un rivestimento costituito da pannelli di polistirene estruso dello spessore di 0.04 m al fine di isolare termicamente il blocco su tali superfici.

Il blocco così lavorato è stato inserito all'interno di un ambiente artificiale (Fig. 2),

costituito da una vasca in HDPE delle dimensioni di 0.61 m x 0.92 m x 0.55 m riempita in parte con sabbia silicea. Il blocco è posizionato al centro di tale vasca, dove in corrispondenza della superfice laterale del blocco è posizionata una serpentina costituita da un tubo in multistrato da 0.016 m collegata, mediante un circuito idraulico (circuito idraulico primario), ad un chiller che garantisce il raffreddamento del sistema. L'acqua di falda circola all'interno del blocco grazie alla presenza di un ulteriore circuito idraulico (circuito idraulico secondario) configurato per immettere l'acqua di falda all'interno del network di fratture. Tale circuito idraulico secondario è composto da un serbatoio posto ad un'altezza idraulica prefissata hc pari a ~ 0.50 m rispetto porta di ingresso del blocco, garantendo così che il carico idraulico a monte di quest'ultima sia costante. Il serbatoio è alimentato dall'acqua riscaldata proveniente da un tubo di acciaio di diametro pari a 0.13 m e altezza pari a 0.45 m. L'acqua viene prelevata dalla parte superiore del tubo, mediante una pompa sommersa, e reimmessa, dopo il passaggio all'interno del blocco, nella parte inferiore del tubo stesso. Tale tubo è sottoposto a condizioni termiche controllate grazie al fatto che è situato al centro di un serbatoio cilindrico in HDPE che presenta diametro e altezza pari a 0.45 m, isolato termicamente con lana di roccia. Il volume tra le pareti del serbatoio e il tubo metallico è riempito con ghiaia satura di acqua di fonte. In tale volume è immersa una serpentina collegata ad un boiler termostatato, con potenza di 2000 W e volume di 0.200 m³ che permette il mantenimento della temperatura dell'intero sistema.

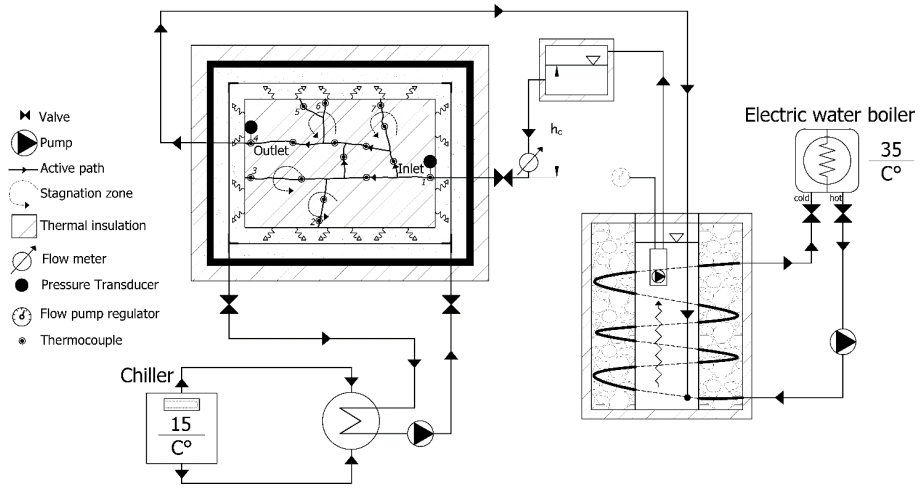


**Figura 2.** Sketch del setup sperimentale realizzato.

### *3. Risultati attesi e conclusioni*

A partire dalla necessità di monitorare le cause che generano incrostazioni e intasamenti nei sistemi circuito aperto come gli ATES, è necessario analizzare le prestazioni effettive del sistema e identificare se si è verificato un intasamento nei pozzi di produzione ed iniezione per pianificare le normali procedure di manutenzione (Gjengedal et al.,2019). Ad ogni modo, la misurazione in continuo, anche se permetterebbe di individuare criticità nel sistema, non giungerebbe ad identificare la tipologia e la causa dell'intasamento, che risultano collegate a dinamiche complesse che avvengono all'interno degli acquiferi. La presenza di biofilm e il conseguente intasamento dei vuoti nei mezzi geologici fratturati porterebbero ad una significativa riduzione della conducibilità idraulica. Tale riduzione deriva da più fattori tra cui la produzione e l'accumulo delle cellule batteriche, la ritenzione e precipitazione di sostanze organiche ed inorganiche, l'intrappolamento di gas (Baveye et al., 1998; Castegnier et al., 2006). L'intasamento riduce l'efficienza degli ATES ed è influenzato principalmente dalla reintroduzione di acqua nel sottosuolo, seppure derivante dallo stesso acquifero.

I microrganismi aderiscono al supporto poroso attraverso forze elettrostatiche, forze di idratazione ed interazioni idrofobiche e steriche. Alcuni batteri possono produrre gas che rimangono intrappolati nel biofilm o possono migrare ed occludere i pori nella matrice dell'acquifero. Il biofilm ha una massa sufficientemente grande da occupare una parte significativa dei vuoti del network di fratture e di conseguenza si verificherebbero fenomeni di ostruzione e/o occlusione dei pori con conseguente diminuzione della velocità nel network di fratture. La parte biologica può influire sulle reazioni chimico-fisiche in quanto la crescita di biofilm sulle pareti delle fratture potrebbe abbassare il pH e sottrarre $CO_2$ inducendo precipitazione di minerali.

Il setup sperimentale proposto permette di arricchire la comprensione delle dinamiche complesse che avvengo negli acquiferi, permettendo di valutare, in termini quantitativi e qualitativi, l'incidenza della crescita del biofilm sulla riduzione della quantità di calore accumulabile all'interno del blocco sottoposto a vari cicli termici di accumulo e recupero di calore. Attualmente le fasi sperimentali sono ancora in corso e si prevede che si protrarranno per un anno al termine del quale si procederà con la validazione dei dati sperimentali ottenuti.

***Bibliografia***


[1] M. Bloemendal, T. Olsthoorn, F. van de Ven, "Combining climatic and geo-hydrological preconditions as a method to determine world potential for aquifer thermal energy storage", Science of The Total Environment, pag. 621-633, 2015.

[2] Martin Bloemendal, Niels Hartog , "Analysis of the impact of storage conditions on the thermal recovery efficiency of low-temperature ATES systems", Geothermics vol. 71, pag 306-319, 2018.

[3] Omer, A.M. "Energy, Environment and Sustainable Development", Renewable and Sustainable Energy Reviews, vol.12, pag.2265-2300, 2008.

[4] Luc Burté*, Charles A. Cravotta III, Lorine Bethencourt, Julien Farasin, Mathieu Pédrot, Alexis Dufresne, Marie-Françoise Gérard, Catherine Baranger, Tanguy Le Borgne, and Luc Aquilina, "Kinetic Study on Clogging of a Geothermal Pumping Well Triggered by Mixing-Induced Biogeochemical Reactions", Environ Sci. Technol, pag.21-53, 2019.

[5] Gjengedal, Brøtan, Buset et al., "Fluid flow through 3D-printed particle beds: a new technique for understanding, validating, and improving predictability of permeability from empirical equations". Transp Porous Med 134, pag.1-40, 2020.

[6] Philippe Baveye, Philippe Vandevivere, Blythe L. Hoyle, Show all 5 authors, Diego Lozada, "Environmental Impact and Mechanisms of the Biological Clogging of Saturated Soils and Aquifer Materials", Critical Reviews In Environmental Science and Technology 28(2):123-191, 1998.

[7] Beretta, G. P. "Groundwater recharge through wells in open loop geothermal system: problems and solutions" - part 1. Acque Sotterranee - Italian Journal of Groundwater, 6(2), 2017.

[8] Castagnier, Nathalie Ross , Robert P. Chapuis , Louise Deschênes , Réjean Samson, "Long-term persistence of a nutrient-starved biofilm in a limestone fracture", Water Research, vol. 40, issue 5, pages 925-934, 2006.

[9] Sondre Gjengedal, Randi K. Ramstad, Bernt O. Hilmo, Bjørn S. Frengstad, "Fouling and clogging surveillance in open loop GSHP systems: A systematic procedure for fouling and clogging detection in the whole groundwater circuit", Bulletin of Engineering Geology and the Environment, 2019.

[10] Allison, D.G., "The biofilm matrix. Biofouling", The Journal of Bioadhesion and Biofilm Research vol.19 (2), pag.139–150, 2023.

[11] Flemming, H.-C., "Biofouling in Water Systems–Cases, Causes and Countermeasures". Applied Microbiology and Biotechnology, vol.59 (6), pag.629–640, 2002.

[12] Picioreanu, C., van Loosdrecht, M.C.M., Heijnen, J.J., "Twodimensional model of biofilm detachment caused by internal stress from liquid flow", Biotechnol. Bioeng. 72 (2), 205–218, 2001.

[13] Ross, N., Bickerton, G., "Application of biobarriers for groundwater containment at fractured bedrock sites", Remediation 12 (3), pag. 5-21, 2002.

[14] Zhang, X., Bishop, P.L., "Biodegradability of biofilm extracellular polymeric substances", Chemosphere vol.50 (1), pag.63–69, 2003.

[15] Cherubini, C., Giasi, CI, e Pastore N., " Bench scale laboratory test to analyze non-linear flow in fractured media", Hydrol. Earth Syst. Sci., vol.16, pag. 2511–2522.

[16] Cherubini, C., Giasi, CI, e Pastore N., "Evidence of non-Darcy flow and non-Fickian transport in fractured media at laboratory scale", Hydrol. Earth Syst. Sci., vol. 17, pag. 2599–2611, 2013.

[17] Cherubini, C., Giasi, CI, e Pastore N., "On the reliability of analytical models to predict solute transport in a fracture network", Hydrol. Earth Syst. Sci., vol. 18, pag. 2359–2374, 2014.

[18] Cherubini, C., Giasi, CI, e Pastore N., "Laboratory experimental investigation of heat transport in fractured media", Nonlin. Processes Geophys., vol. 24, pag.23–42, 2017.

[19] Cherubini, C., Giasi, CI, e Pastore N., "Velocity-dependent heat transfer controls temperature in fracture networks", Nature Communications, vol. 14(1), pag.362, 2023.

# Calculation of the thermodynamic properties of binary reactive mixture. An application to $N_2O_4$ = 2 $NO_2$

**Konstantin Samukov**[a], **Silvia Lasala**[a,#]

*a Université de Lorraine, CNRS, LRGP, Nancy, France*

*# Corresponding author:* silvia.lasala@univ-lorraine.fr

## Abstract

The implementation of reactive working fluids, instead of inert ones, in thermodynamic cycles may open new opportunities in the production of electricity and thermal energy. This investigation is the topic of the ERC project REACHER. In a recent work, we have presented a generalized methodology enabling the thermodynamic modelling of binary mixtures being the place of a reversible and fast dimerization reaction, as $N_2O_4 \rightleftarrows 2NO_2$. Such a system being mono-variant in vapour-liquid equilibrium conditions, it behaves similarly to a pure component: its phase envelope is characterized by a unique curve starting and ending on a unique triple and critical point, respectively. The methodology we proposed, based on the use of cubic equations of state, enables the prediction of the thermodynamic properties of these systems. Indeed, the critical point of the pure species forming the mixtures (N2O4 and NO2), necessary as input to the application of cubic equations of state, are not measurable because the reaction evolves in the vapour-liquid equilibrium domain according to chemical equilibrium and the pure species are not separable at their specific critical points. Such a methodology uses force field Monte-Carlo and Quantum Mechanics to calculate the input properties, respectively, critical coordinates and ideal gas properties. However, because of the relatively high uncertainty in the determination of these input properties, a perspective work to be performed was the further optimization of these properties on experimental data. This is the objective of the present work, where the optimization strategy is applied to $N_2O_4 \rightleftarrows 2NO_2$. The optimized properties were used to calculate thermodynamic properties of the system under investigation, and results of calculations were compared with available experimental data in order to validate the proposed methodology.

### *1. Introduction*

Thermal power cycles have a dominating role in the global electricity production. However, due to thermodynamic limitations of conventional power plants, only about one third of input thermal energy is converted into electricity and remaining energy is dissipated as heat into the environment. The average efficiency of the electricity system is indeed 35% [1]. The maximum efficiency that can be ideally reached by a power plant is the Carnot efficiency, which equals about 50-60% for coal and nuclear power plants; thus, improvement of currently existing power plants is still possible.

Nowadays, most of the thermal power plants use inert molecules as working fluids, i.e., air and flue gases, water, carbon dioxide. Differently, the project REACHER funded by the European Research Council [2] proposes the original use of reactive fluids, instead of inert ones. When it comes to reactive fluid, this refers to a fluid wherein a rapid reversible reaction (or reactions) takes place, whose evolution follows chemical equilibrium: its composition, thermodynamic and transport properties change along the thermodynamic cycle as a consequence of the modification of temperature and pressure along the different unit operations. As an example, we have previously demonstrated [3] that the reaction evolves in the exothermic (association) direction when it is expanded and evolves in the endothermic (dissociation) direction when it is compressed; it dissociates when it is heated up and associates when it is cooled down, as suggested by the Le Chatelier's principle.

Preliminary calculations, based on the generalized methodology for fictitious reactive fluids with a reaction of the form $A_{n(g)} \rightleftarrows (n/m)\ A_{m(g)}$ in Brayton power cycle, have shown very promising results: the implementation of reactive fluids as working bodies in thermodynamic cycles may lead to the improvement of the efficiency of power plants by more than 30% [3]. Moreover, in the past, a few real reactive fluids were considered: dinitrogen tetroxide $N_2O_4 \rightleftarrows 2NO_2 \rightleftarrows 2NO + O_2$, dialuminum hexachloride $Al_2Cl_6 \rightleftarrows 2AlCl_3$ and dialuminum hexabromide $Al_2Br_6 \rightleftarrows 2AlBr_3$ (further in the text for the sake of brevity reactive fluids will be referred as $N_2O_4$, $Al_2Cl_6$ and $Al_2Br_6$). Some of the properties of these fluids are presented in Table 1.

**Table 1.** Physico-chemical properties of reactive fluids $N_2O_4$, $Al_2Cl_6$ and $Al_2Br_6$ [4,5]

| *Property* | *Reactive fluid* | | |
|---|---|---|---|
| | $N_2O_4 \rightleftarrows 2NO_2 \rightleftarrows 2NO + O_2$ | $Al_2Cl_6 \rightleftarrows 2AlCl_3$ | $Al_2Br_6 \rightleftarrows 2AlBr_3$ |
| *M, kg/mol* | 0.09202 | 0.2667 | 0.53346 |
| $T_{(b,1bar)}$, *K* | 294.3 | 466.15 | 529.15 |
| $T_c$, *K* | 431.35 | 625.85 | 768.15 |
| $P_c$, *bar* | 101.3 | 26.3 | 28.0 |
| $\rho_c$, *kg/m3* | 557 | 529 | 887 |
| $\Delta_{vap} H_{298.15K}$, *kJ/kg* | 416.0 | 150.6 | 93.3 |
| $T_{tr}$, *K* | 261.85 | 465.75 | 370.15 |

| $\Delta_R H_{298.15K}$, kJ/mol | 57.3 / 113.8 | 121.0 | 125.5 |
|---|---|---|---|
| *Temperature range of reaction(s), K:* | | | |
| *1 bar* | 300-1120 | 470-1270 | 550-1470 |
| *100 bar* | 300-1470 | 570-1470 | 620-1970 |

$N_2O_4$ was considered to be implemented in simple cycles, $Al_2Cl_6$ and $Al_2Br_6$ – in binary cycles [4]. As a final result of the work of the Nuclear Power Institute of the Sciences of the Byelorussian SSR, two copies of mobile power station «Pamir-630D» that used mixture of N2O4 with ~1% of nitrogen monoxide NO as a working fluid were created (NO was added in order to reduce corrosion caused by nitric acid, product of the reaction of N2O4 with water vapor) [6]. At the moment, «Pamir-630D» is the only known example of successful implementation of reactive fluids in thermodynamic cycles.

In a previous work, we have proposed a multi-scale methodology to determine in a predictive way the thermodynamic properties of $N_2O_4 \rightleftarrows 2NO_2$ [7], by the use of a cubic equation of state (EoS), Monte Carlo (MC) simulations and Quantum Mechanics (QM) calculations. Indeed, this system being at chemical equilibrium at each subcritical temperature, the critical properties of pure $N_2O_4$ and $NO_2$ -necessary input to cubic EoS- are not measurable but only assessable by Monte Carlo simulations. As a second and final step of the methodology, this paper aims to present the further optimization of these input properties over VLE data and the validation of the model on available liquid and supercritical properties.

## 2. *Scientific approach*

### *2.1. Reactive fluid*

Thermodynamic calculations are performed in this work for $N_2O_4$ which is the most explored reactive fluid which has been already successfully implemented in thermodynamic cycles. At its melting point, $N_2O_4$ is a colorless substance, but with increase of temperature, it transforms rapidly into a brown gas due to the presence of nitrogen dioxide $NO_2$, as dictated by the chemical reaction $N_2O_4 \rightleftarrows 2NO_2$.

The dissociation of $N_2O_4$ into $NO_2$ and the reverse reaction are indeed considered as fast with respect to the resident time of the fluid in the unit operations of a power plant: the relaxation time in a gas phase at pressures above 1 bar does not exceed 10-4 seconds [8];

experimental data have revealed that the reaction is likewise rapid in a liquid phase [9]. At higher temperatures $NO_2$ decomposes with formation of nitrogen monoxide NO and oxygen according to the equation $2NO_2 \rightleftarrows 2NO + O_2$ [10]; a liquid phase consists mostly of $N_2O_4$ [11], and the presence of the second reaction in liquid phase may be neglected. The modeling of the reactive system has been begun taking into account only the first reaction $N_2O_4 \rightleftarrows 2NO_2$ which will be also demonstrated to be a good assumption.

### 2.2. Thermodynamic modelling

System $N_2O_4 \rightleftarrows 2NO_2$, as well as any other binary reactive system $A_n \rightleftarrows (n/m)\ A_m$, is characterized by a special thermodynamic behavior. This fact can be shown by a consideration of Gibbs phase rule:

$$v = c + 2 - \varphi - r \qquad (1)$$

This system has two species (c=2) and one chemical reaction (r=1). For a single-phase system (φ=1) and a system at two-phase equilibrium (φ=2) we have:

$$\begin{matrix} v = 2, if\ \varphi = 1 \\ v = 1, if\ \varphi = 2 \end{matrix} \qquad (2)$$

Therefore, the reactive system $N_2O_4 \rightleftarrows 2NO_2$ has the same number of degrees of freedom as a pure component (c=1 and r=0). Consideration of Gibbs phase rule allowed to explain some of the experimental features detected in the behaviour of the system: single triple and critical point, single saturation curve (as shown in Figure 1).

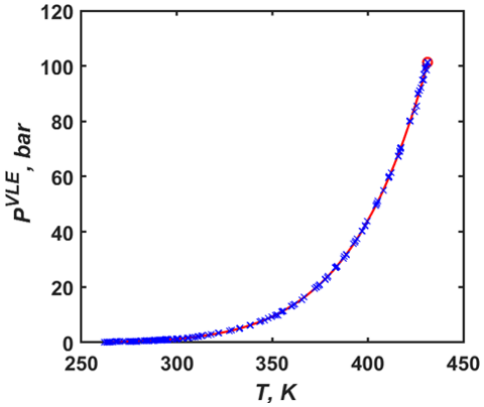


**Figure 1.** VLE pressure as a function of temperature for the reactive binary system $N_2O_4 \rightleftarrows 2NO_2$. Blue crosses are experimental data, red line and its end critical point (circle) are taken from DIPPR [12].

The modified version of the Peng-Robinson equation of state (EoS) [13], introduced by Lasala et al. [14], was chosen to describe the thermodynamic properties of the system:

$$P(T,v,\boldsymbol{z}) = \frac{RT}{v-b_m} - \frac{a_m}{v(v+b_m)+b(v-b_m)},$$
$$b_m = \sum_{i=1}^{N_{comp}} z_i b_i, \frac{a_m}{b_m} = \sum_{i=1}^{N_{comp}} z_i \frac{a_i}{b_i} + \frac{a_{res}^{E,\gamma}}{\Lambda_{EoS}} \quad (3)$$

where z is vector of the molar composition, T is the temperature, R is the universal gas constant, v is the molar volume, $a_m$ and $b_m$ are the attractive and co-volume parameters of the mixture.

The EoS parameters are calculated in this work using advanced mixing rules. In Eq. (3), $\boldsymbol{a_{res}^{E,\gamma}}$ is the residual part of excess Helmholtz energy calculated from an activity coefficient model, $\Lambda_{EoS}$ is a numerical parameter being a function of the considered EoS; in this work, it is assumed that the non-reacting system $N_2O_4$ / $NO_2$ is athermal (both molecules are assumed to generate similar interactions) and therefore, $\boldsymbol{a_{res}^{E,\gamma}}$ was considered to be zero. The parameters of pure compounds $a_i$ and $b_i$ are calculated by Eq. (3):

$$\begin{cases} b_i = \Omega_b \frac{RT_{c,i}}{P_{c,i}}, \Omega_b \approx 0.0777960739 \\ a_i(T) = a_{c,i}\left[1 + m_i\left(1 - \sqrt{\frac{T}{T_{c,i}}}\right)\right]^2, a_i = \Omega_a \frac{R^2 T_{c,i}^2}{P_{c,i}}, \Omega_b \approx 0.457235529 \\ \omega_i \le 0.491:\ m_i = 0.37464 + 1.54226\omega_i - 0.26992\omega_i^2 \\ \omega_i > 0.491:\ m_i = 0.379642 + 1.48503\omega_i - 0.164423\omega_i^2 + 0.01666\omega_i^3 \end{cases} \quad (4)$$

Critical properties and acentric factors of individual species $T_{(c,i)}$, $P_{(c,i)}$ and $\omega_i$ are required to calculate parameters of pure components $a_i$ and $b_i$. However, as it has been shown before, it is not possible to separate the species in a binary reactive fluid and to measure experimentally the properties of individual species. In order to model such a system, $T_c$, $P_c$ and ω of each pure component should thus be estimated. In this work, these parameters have calculated from Monte-Carlo simulations [7]; the values of the parameters are presented in Table 2.

In order to perform chemical equilibrium calculations, it is necessary to have an expression for the calculation of the equilibrium constant. This requires the knowledge

of the standard molar enthalpies of formation, standard molar absolute entropies and standard molar isobaric heat capacities of pure species. In this work, the standard state is chosen as an ideal gas.

$$\ln K(T) \equiv -\frac{\Delta_R G^{\circ}(T)}{RT}, \Delta_R G^{\circ}(T) = \Delta_R H^{\circ}(T) - T\Delta_R S^{\circ}(T) \quad (5)$$

$$\Delta_R H^{\circ}(T) = \sum_{i=1,2} \nu_i \Delta_f H^{\circ}_{i,298.15K} + \int_{298.15K}^{T} \left(\nu_i c^{\circ}_{P,i}(T)\right) dT \quad (6)$$

$$\Delta_R S^{\circ}(T) = \sum_{i=1,2} \nu_i S^{\circ}_{i,298.15K} + \int_{298.15K}^{T} \left(\nu_i \frac{c^{\circ}_{P,i}(T)}{T}\right) dT \quad (7)$$

In Eq. (5)-(7), K(T) is the equilibrium constant; $\Delta_R$ G° (T), $\Delta_R$ H° (T) and $\Delta_R$ S° (T) are the standard Gibbs energy, enthalpy and entropy of the reaction, respectively; $\nu_i$, $\Delta_f H^{\circ}_{i,298.15K}$, $S^{\circ}_{i,298.15K}$, $c^{\circ}_{P,i}(T)$ are the stoichiometric coefficient, standard molar enthalpy of formation at 298.15 K, standard molar entropy at 298.15 K and standard molar isobaric heat capacity of the species i, respectively. In this work, the ideal-gas properties of pure $N_2O_4$ and $NO_2$ were calculated from quantum mechanics (QM) simulation [7] (see Table 2). Isobaric heat capacities data of pure $N_2O_4$ and $NO_2$ were also generated by QM and correlated with the DIPPR correlation #107 (coefficients of this correlation were fitted to QM data).

**Table 2.** Critical properties and acentric factors of pure N2O4 and NO2 obtained from the results of Monte-Carlo simulations and ideal gas standard molar enthalpy of formation and standard molar entropy of $N_2O_4$ and $NO_2$ at 298.15 K obtained from Quantum Mechanics calculations [7].

| Compound | $T_c$, K | $P_c$, bar | $\omega$ | $\Delta_f H^{\circ}_{i,298.15K}$, kJ/mol | $S^{\circ}_{i,298.15K}$, J/mol/K |
|---|---|---|---|---|---|
| $N_2O_4$ | 484.2 | 55.9 | 0.3212 | 9.99 | 297.65 |
| $NO_2$ | 282.2 | 68.2 | 0.0565 | 34.2 | 240.03 |

### *2.3. Equilibrium calculations*

A review of the algorithms performing chemical equilibrium calculations, with both fluid phase and reactional equilibrium, for specified temperature, pressure and global

composition of the system is given in two main papers [15,16].

In this work, the modified RAND method [17], a recent version of the nonstoichiometric approach, was chosen. The advantages of the modified RAND method are its quadratic convergency and the satisfaction of the material balance constraints at every iteration. Slower initialization procedures coupled with a robust and efficient RAND algorithm allow to perform calculations without any incidents of divergence or failure for the considered systems.

When applying the RAND method, the input variables are the temperature T, the pressure P and the initial global composition of the fluid. The RAND method can thus be applied to systems having T and P as independent variables. For the single-phase $N_2O_4 \rightleftarrows 2NO_2$ system, temperature and pressure are independent (two degrees of freedom in such a system) but are not independent when the system is in VLE (one degree of freedom). In this latter case, in order to perform simultaneous phase and chemical equilibrium calculations, the RAND method can not be used and it is necessary to solve a specific system:

$$\begin{cases} \mu_{N_2O_4}^{liq} = \mu_{N_2O_4}^{vap} \\ \mu_{NO_2}^{liq} = \mu_{NO_2}^{vap} \\ \Delta_R G = 0 \end{cases} \qquad (8)$$

Implementing an equation of state to perform calculations, we obtain following set of five equations:

$$\begin{cases} \hat{f}_{N_2O_4}^{liq}\left(T, v^{liq}, \boldsymbol{x}\right) = \hat{f}_{N_2O_4}^{vap}\left(T, v^{vap}, \boldsymbol{y}\right) \\ \hat{f}_{NO_2}^{liq}\left(T, v^{liq}, \boldsymbol{x}\right) = \hat{f}_{NO_2}^{vap}\left(T, v^{vap}, \boldsymbol{y}\right) \\ K(T) = \prod_{i=1,2}\left(\frac{\hat{f}_i^{vap}\left(T, v^{vap}, \boldsymbol{y}\right)}{P^{\circ}}\right)^{\nu_i}\left[= \prod_{i=1,2}\left(\frac{\hat{f}_i^{vap}\left(T, v^{vap}, \boldsymbol{y}\right)}{P^{\circ}}\right)^{\nu_i}\right] \\ P - P_{EoS}\left(T, v^{liq}, \boldsymbol{x}\right) = 0 \\ P - P_{EoS}\left(T, v^{vap}, \boldsymbol{y}\right) = 0 \end{cases} \qquad (9)$$

In Eq. (9), vectors with molar composition of the liquid and vapor phase are denoted as

$$\boldsymbol{x} = \{x_{NO_2}, x_{N_2O_4}\} = \{x_{NO_2}, 1 - x_{NO_2}\} \text{ and } \boldsymbol{y} = \{y_{NO_2}, y_{N_2O_4}\} = \{y_{NO_2}, 1 - y_{NO_2}\},$$

respectively. The system has five equations and six variables $(T, P, v^{liq}, v^{vap}, x_{NO_2}, y_{NO_2})$.

Since the number of degrees of freedom is equal to one, it is possible to fix one intensive variable and to solve the system for the left unknowns. In this work, at specified temperature, system (9) is solved for $(P, v^{liq}, v^{vap}, x_{NO_2}, y_{NO_2})$. In order to calculate the entire VLE curve, calculations may be performed from the triple point temperature to the critical temperature of the system with a specified value of temperature step. For each temperature, the system of 5 equations was solved numerically by the Newton-Raphson method and the convergence was considered to be reached if the maximum value of the residual vector was lower than 10-8. The results of calculations were presented by the P-T and T-ρ curves. The critical line of the non-reactive system $N_2O_4$-$NO_2$ was calculated using the method proposed by Cismondi and Michelsen [18] for binary non-reactive systems. The critical point of the reactive system $N_2O_4 \rightleftarrows 2NO_2$ was determined as a point on the critical line where the condition of chemical equilibrium is reached.

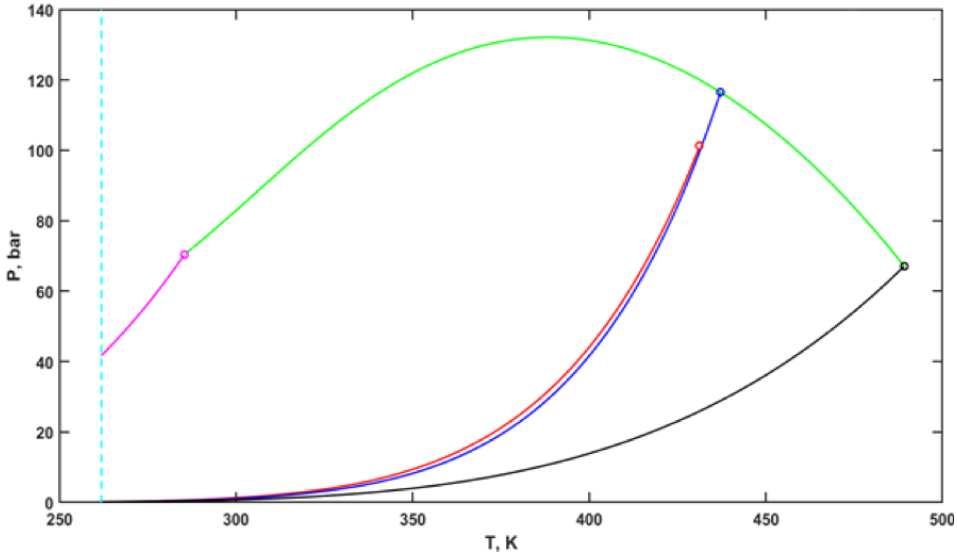


**Figure 2.** Results of P^VLE calculations of the $N_2O_4 \rightleftarrows 2NO_2$ system: blue curve – results of calculations; red curve – correlation from DIPPR database [12]; pink and black curve correspond to saturation curves of pure $NO_2$ and $N_2O_4$, respectively; green curve – critical line of non-reactive mixture $N_2O_4$–$NO_2$; cyan line corresponds to triple point temperature of the reactive mixture.

Furthermore, calculated values of molar volumes and molar compositions of the liquid and vapor allowed to calculate saturated densities of phases. This is shown in Figure 3.

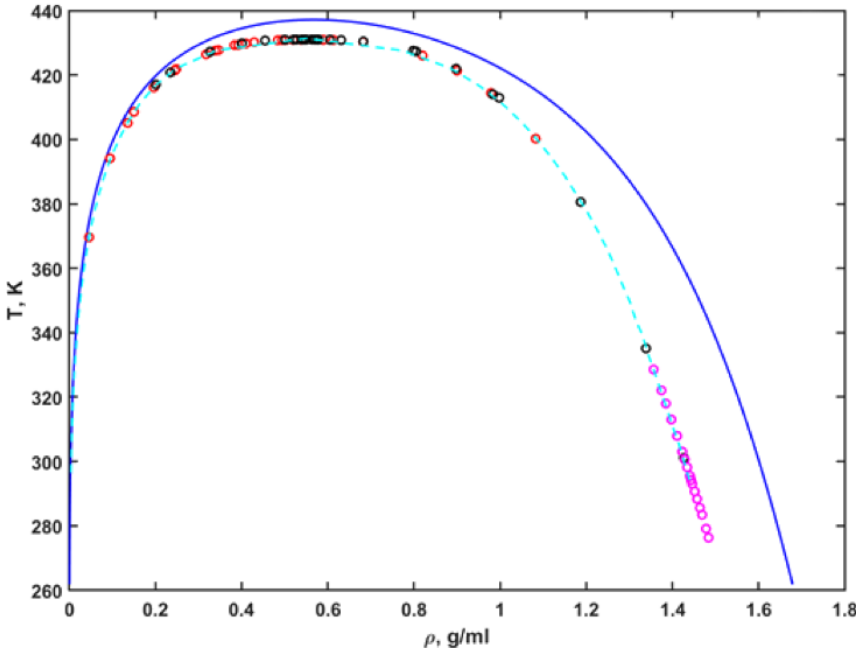


**Figure 3.** Results of calculations of densities at VLE of the $N_2O_4 \rightleftarrows 2NO_2$ system: blue curve – results of calculations; cyan line, pink, red and black points – experimental data [19–22].

It can be seen that the combination of the EoS with its input parameters predicted from QM and molecular simulation tools do not allow to describe the properties of the system satisfactorily. Considering that the input parameters of the model used here ($T_c$, $P_c$, ω of pure species and thermochemistry data for characterizing the chemical equilibrium) were determined with predictive tools, it was decided to reasonably modify their values in order to better reproduce the experimental data of the reactive system.

### *2.4. Optimization of input properties required by the cubic EoS*

The eight key input properties used to model the reacting system considered are:

- The critical temperatures, critical pressures and acentric factors of $N_2O_4$ and $NO_2$ (6 properties)
- The standard molar enthalpy and entropy of the reaction $N_2O_4 \rightleftarrows 2NO_2$ at 298.15 K (2 properties)

In order to define which, among these properties, should be optimized, it has been

necessary to perform a sensitivity analysis. Then, most sensitive input properties has been fitted to the experimental data of the reacting system. The sensitivity analysis has shown that the four properties $T_c$ ($N_2O_4$), $P_c$ ($N_2O_4$), $\Delta_R H^\circ_{298.15K}$ and $\Delta_R S^\circ_{298.15K}$ have the highest influence on the results of calculations, so it was decided to fit these parameters to the experimental data of the reacting system. The following objective function, to be minimized, was considered:

$$F = \sum_{properties\ X} \left[ \frac{1}{n_X^{exp}} \sum_{i=1}^{n_X^{exp}} \left( \frac{X_i^{calc} - X_i^{exp}}{X_i^{exp}} \right)^2 \right] \qquad (10)$$

The properties considered for the minimization are VLE data (phase boundary pressure, densities of liquid and vapor at VLE, mixture critical temperature, mixture critical pressure). The indices "calc" and "exp" refer to calculated and experimental values, respectively. The quasi-Newton BFGS (Broyden-Fletcher-Goldfarb-Shanno) algorithm was chosen as an optimization method. In order to verify the reliability of the optimization procedure, each optimization was performed 10 times for different initializations. Success of the optimization was determined by the low number of points out of model (points that showed a discrepancy between the calculated and experimental phase type) and low values of MAPE (mean average percentage error).

The lowest value of objective function was reached for $\Delta_R H^\circ_{298.15K}$ = 57.4 kJ/mol, $T_c$ ($N_2O_4$) = 473.87 K, $P_c$ ($N_2O_4$) = 60.25 bar, and $\Delta_R S^\circ_{298.15K}$ = 175.26 J/mol/K. The results of calculations were compared with experimental data and pseudo-experimental results of Monte-Carlo simulations, all results are in a good agreement between each other (see Figures 4-5 and Table 3).

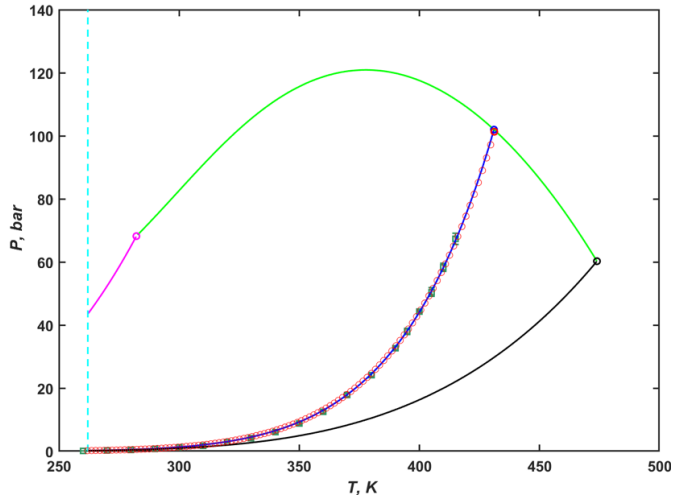


**Figure 4.** Phase diagram of the reactive $N_2O_4 \rightleftarrows 2NO_2$ system; calculations were performed with optimized parameters. Red points were generated from DIPPR correlation [12], green squares correspond to results obtained from Monte-Carlo simulations [7]; description of the other data sets coincide with the ones given in Figure 2.

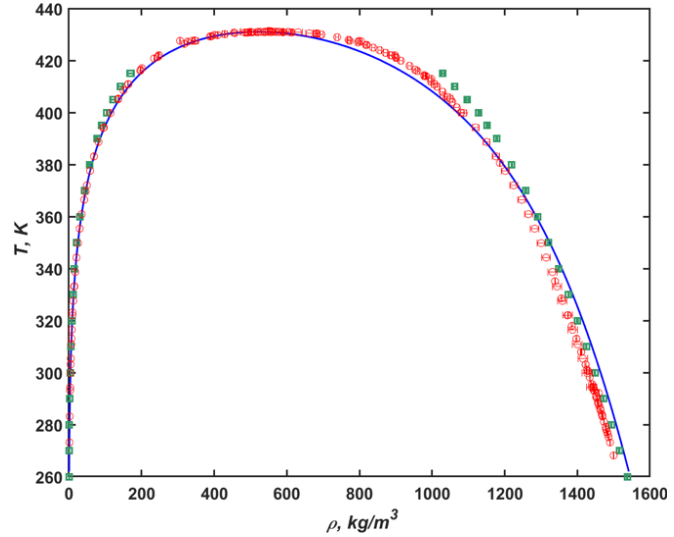


**Figure 5.** Densities of coexisting phases in the reactive $N_2O_4 \rightleftarrows 2NO_2$ system; calculations were performed with optimized parameters. Red points correspond to available experimental data, green squares correspond to results obtained from Monte-Carlo simulations [7].

Optimization of the parameters allowed to improve significantly the model. Model deviations are characterized by the values of MAPE (Mean Average Percent Errors) presented in Table 3.

**Table 3.** MAPE for calculations of equilibrium thermodynamic properties in cases of non-optimized and optimized input parameters.

| Property | MAPE before optimization, % | MAPE after optimization, % |
|---|---|---|
| Equilibrium vapor pressure | 11.3 | 0.81 |
| Density of liquid at VLE | 8.0 | 3.8 |
| Density of vapor at VLE | 9.3 | 2.8 |
| Critical temperature | 0.051 | 0.045 |
| Critical pressure | 7.2 | 0.66 |
| Critical density | 9.3 | 6.0 |

### *2.5. Validation of the model*

Other than saturation pressure and densities, various data were found in the literature for the properties of $N_2O_4$ in the liquid phase and supercritical region. Their main features are reported in Table 4. These data have been used to validate the model.

**Table 4.** Experimental data on the properties of the fluid $N_2O_4$.

| Property | Number of points | Temperature range, K | Pressure range, bar |
|---|---|---|---|
| Density | 213 | 263-511 | 1-596 |
| Isobaric heat capacity | 307 | 262-441 | 1-180 |
| Enthalpy increment | 213 | 283-482 | 49-294 |
| Speed of sound | 499 | 282-452 | 1-196 |

With the knowledge of the equilibrium compositions, the calculation of thermodynamic properties of the reactive fluids may be performed. Molar enthalpy and entropy of the reactive system are calculated in the same manner as in the case of inert systems:

$$h(T,v,\boldsymbol{z}) = \sum_i z_i \left( \Delta_f H^{\circ}_{i,298.15K} + \int_{298.15K}^{T} c^{\circ}_{P,i}(T)\, dT \right) + h^{res}(T,v,\boldsymbol{z}), \tag{11}$$

$$s(T,v,\boldsymbol{z}) = \sum_i z_i \left( S^{\circ}_{i,298.15K} + \int_{298.15K}^{T} \frac{c^{\circ}_{P,i}(T)}{T} dT \right) + R \ln \frac{RT}{P^{\circ} v} - R \sum_i z_i \ln z_i + s^{res}(T,v,\boldsymbol{z}), \tag{12}$$

where $h^{res}$ (T,v,z) and $s^{res}$ (T,v,z) are residual enthalpy and residual entropy calculated from the equation of state [23].

Heat capacity of reactive fluid may significantly exceed heat capacity of inert fluid because of the contribution of the heat of reaction. Isobaric heat capacity is typically defined as a derivative of the enthalpy of the system with respect to the temperature at constant pressure and composition of the system, as recalled in eq. (13).

$$c_P \equiv \left( \frac{\partial h}{\partial T} \right)_{P,\boldsymbol{n}} \tag{13}$$

This definition is not applicable to reactive fluids which follow chemical equilibrium, since the composition of the system is a function of temperature and pressure. Therefore, for such reactive fluids, isobaric heat capacity is defined along the chemical equilibrium path and corresponds to what would be measured using a calorimetric device:

$$c_{P,\Delta_R G=0} \equiv \left( \frac{\partial h}{\partial T} \right)_{P,\Delta_R G=0} \tag{14}$$

In this work, the isobaric heat capacity of reactive fluid was calculated numerically using the direct definition of the property for input temperatures, pressures and global composition of the system.

The density of the reactive liquid mixture (experimental versus calculated one) is shown in Figure 6.

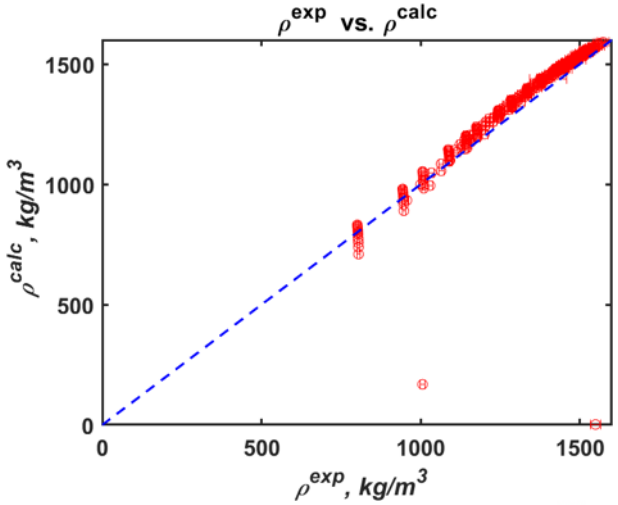


**Figure 6.** Parity plot comparing calculated values of liquid density of $N_2O_4 \rightleftarrows 2NO_2$ with results of measurements.

Two points that show high deviation correspond to the points situated in the vicinity of the VLE line, where the resolution of the equation of state chooses vapor as a stable phase of the system while the real phase is liquid; for other points, liquid is the stable phase. Average relative deviation of calculated densities from experimental ones is equal to 3.5 %.

Furthermore, caloric properties have been calculated. Figure 7 shows the results of calculations of isobaric heat capacity for certain isobars and compares them with experimental data.

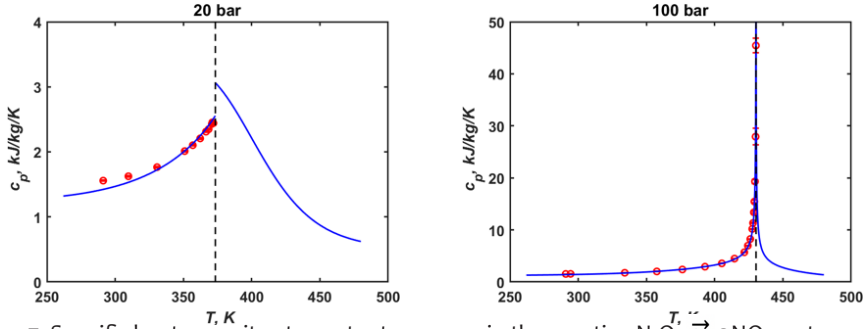


**Figure 7.** Specific heat capacity at constant pressure in the reactive $N_2O_4 \rightleftarrows 2NO_2$ system: red points – experimental data, blue lines – calculations.

In general, heat capacities predicted by the cubic EoS are not always in a good agreement with the experimental data [24]. However, for the considered system, it was possible to obtain quite accurate description of the property even in the vicinity of the critical point. The corresponding MAPE is equal to 4.9 %, the largest average deviation is equal to 11.0 % and was found for isobar 140 bar. The calculations have also been performed for a such caloric property as enthalpy increment. An enthalpy increment corresponds to the difference in the enthalpy of the system between two points at the same pressure $\Delta h=h(T,P)-h(T_0,P)$. As in the case of heat capacity, the model associated with optimized parameters allowed to describe well the existing experimental data on enthalpy increment. The corresponding MAPE is equal to 4.0 %; several points showing the highest deviations lay in the vicinity of critical point (Figure 8).

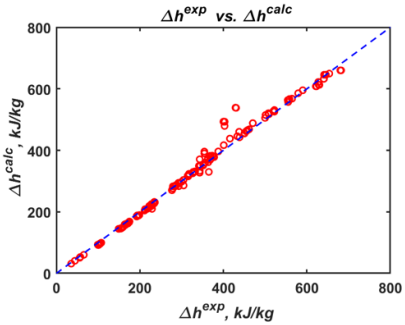


**Figure 8.** Parity plot comparing computational values of enthalpy increment in the reactive $N_2O_4 \rightleftarrows 2NO_2$ system with results of experimental measurements.

## *Conclusions*

This paper presents a methodology enabling to model the thermodynamic properties of reactive systems being characterised by one reversible reaction at chemical equilibrium, for example $N_2O_4 \rightleftarrows 2NO_2$. Systems of this type exhibit a unique behaviour: since the chemical reaction taking place in the system constantly evolves due to change of the system's temperature and pressure, it is never possible to obtain the pure N2O4 and the pure NO2 and thus, measure their individual properties; system always exists only as a mixture of two compounds having a single triple point, critical point and saturation curve.

In order to calculate thermodynamic properties, the Peng-Robinson equation of state

associated to advanced mixing rules EoS+ $a_{res}^{E,\gamma}$ with a zero- $a_{res}^{E,\gamma}$ is applied. Individual properties of pure $N_2O_4$ and $NO_2$ were evaluated by Monte-Carlo simulations and Quantum Mechanics. Since results of calculations show relatively high deviation from the experimental data, some of these properties have been optimised on the properties of the system at vapor-liquid equilibrium: the critical temperature and pressure of $N_2O_4$, and the standard molar enthalpy and entropy of the reaction $N_2O_4 \rightleftarrows 2NO_2$ at 298.15 K.
The optimal value of these properties has been validated on thermodynamic properties of the system in the liquid and supercritical phase. The validation has shown that those values allow to describe existing data with very high accuracy.
The considered methodology has proven to be able to greatly upgrade the description of thermodynamic properties of the $N_2O_4 \rightleftarrows 2NO_2$ system and is thus proposed to preliminarily predict the thermodynamic properties of other similar real reactive systems for which experimental data exist in the literature.


### *Acknowledgments*

This work has received funding from the European Research Council (ERC) under the European Union's Horizon Europe research and innovation program (grant agreement No. 101040994).


### *References*


[1] G.V.P. Varma, T. Srinivas, Power generation from low temperature heat recovery, Renewable and Sustainable Energy Reviews 75 (2017) 402–414. https://doi.org/10.1016/j.rser.2016.11.005.

[2] Web-site of the REACHER project., (n.d.). https://www.univ-lorraine.fr/erc-reacher/.

[3] S. Lasala, R. Privat, O. Herbinet, P. Arpentinier, D. Bonalumi, J.-N. Jaubert, Thermochemical engines: Unexploited high-potential energy converters, Energy Convers. Manag. 229 (2021) 113685. https://doi.org/10.1016/j.enconman.2020.113685.

[4] Dissociating gases as coolants and working substances in power plants (Proceedings of All-Union Conference), Nauka i Tehnika, Minsk, 1970.

[5] Thermodynamic and transport properties of chemically reacting gaseous systems, Part I., Nauka i Tekhnika, Minsk, 1967.

[6] A.Zh. Greben'kov, A.A. Mikhalevich, G.A. Sharovarov, O.I. Yaroshevich, To the history of the creation of a mobile nuclear power plant "Pamir-630" in Belarus, p. 121-153, in:

History of nuclear energy in the Soviet Union and Russia. I. 5. History of small-scale nuclear power, IzdAT, Moscow, 2004: p. 167. https://elib.biblioatom.ru/text/istoriya-atomnoy-energetiki_v5_2004/.

[7] S. Lasala, K. Samukov, H. Mert Polat, V. Lachet, O. Herbinet, R. Privat, J.-N. Jaubert, O. Moultos, K. de Ras, T. J. H. Vlugt, Application of thermodynamics at different scales to describe the behaviour of fast reacting binary mixtures in vapour-liquid equilibrium, J. Chem. Eng. 483 (2024) 148961. https://doi.org/10.1016/j.cej.2024.148961.

[8] S.H. Bauer, Historiography of a Very Fast Gas Reaction: A Case History That Spanned about 12 Decades, Chem. Rev. 102 (2002) 3893–3904. https://doi.org/10.1021/cr0204045.

[9] H.-J. von Bauer, M. Arlt, H. Hoffmann, Schallabsorption in flüssigem N2O4 infolge Relaxation des Dissoziationsgleichgewichts, Acta Acust. 17 (1966) 98–101.

[10] M. Bodenstein, Bildung und Zersetzung der höheren Stickoxyde, Zeitschrift für Physikalische Chemie 100U (1922) 68–123. https://doi.org/10.1515/zpch-1922-10007.

[11] A.J. Vosper, The dissociation of dinitrogen tetroxide in the liquid phase, J. Chem. Soc. A (1970) 2191. https://doi.org/10.1039/j19700002191.

[12] DIPPR® Project 801 Database, [Online]: https://www.aiche.org/dippr, (n.d.).

[13] D.-Y. Peng, D.B. Robinson, The characterization of the heptanes and heavier fractions for the GPA Peng-Robinson programs, Gas Processors Association, 1978.

[14] S. Lasala, P. Chiesa, R. Privat, J.-N. Jaubert, VLE properties of CO2 – Based binary systems containing N2, O2 and Ar: Experimental measurements and modelling results with advanced cubic equations of state, Fluid Phase Equilibria 428 (2016) 18–31. https://doi.org/10.1016/j.fluid.2016.05.015.

[15] W.R. Smith, R.W. Missen, Chemical Reaction Equilibrium Analysis: Theory and Algorithms, John Wiley & Sons, Inc., New York, 1982.

[16] F. van Zeggeren, S.H. Storey, The computation of chemical equilibria, Cambridge University Press, Cambridge, 1970.

[17] C. Tsanas, E.H. Stenby, W. Yan, Calculation of Multiphase Chemical Equilibrium by the Modified RAND Method, Ind. Eng. Chem. Res. 56 (2017) 11983–11995. https://doi.org/10.1021/acs.iecr.7b02714.

[18] M. Cismondi, M.L. Michelsen, Global phase equilibrium calculations: Critical lines, critical end points and liquid–liquid–vapour equilibrium in binary mixtures, The Journal of Supercritical Fluids 39 (2007) 287–295. https://doi.org/10.1016/j.supflu.2006.03.011.

[19] H.H. Reamer, B.H. Sage, Volumetric Behavior of Nitrogen Dioxide in the Liquid Phase, Ind. Eng. Chem. 44 (1952) 185–187. https://doi.org/10.1021/ie50505a052.

[20] A. Mittasch, E. Kuss, H. Schlueter, Dichten und Dampfdrucke von wäßrigen Ammoniaklösungen und von flüssigem Stickstofftetroxyd für das Temperaturgebiet 0° bis 60°, Z. Anorg. Allg. Chem. 159 (1927) 1–36. https://doi.org/10.1002/zaac.19261590102.

[21] A.B. Verzhinskaya, V.P. Tsurbelev, P.M. Klepatskiy, Impact of nitrogen monooxide on shape of the coexistence curve of N2O4 and vicinity of the critical point liquid-vapor, in: 5th All-Union School "Application of mathematical methods for description and studying of the phisico-chemical equilibria" (extended abstracts of reports), Part II, Novosibirsk, 1985: pp. 120–123.

[22] N.G. Polikhronidi, R.G. Batyrova, I.M. Abdulagatov, Isochoric heat capacity measurements of nitrogen tetroxide system at temperatures between 410 and 484 K and pressures up to 35 MPa, Fluid Ph. Equilib. 175 (2000) 153–174. https://doi.org/10.1016/S0378-3812(00)00457-X.

[23] J.-N. Jaubert, R. Privat, Thermodynamic Models for Chemical Processes: Design, Develop, Analyse and Optimize, ISTE Press Ltd - Elsevier Inc, 2021.

[24] A. Diedrichs, J. Rarey, J. Gmehling, Prediction of liquid heat capacities by the group contribution equation of state VTPR, Fluid Phase Equilib. 248 (2006) 56–69. https://doi.org/10.1016/j.fluid.2006.07.009.

# Combining Thermochemical and Phase Change Materials for Thermal Energy Storage: the Echo Project

**Laura Vallese[a,b,#], Giulia Lombardo[a,b], Davide Menegazzo[a], Giovanni Ferrarini[a], Mauro Scattolini[a], Sergio Bobbo[a], Laura Fedele[a]**

[a] *Construction Technologies Institute, National Research Council (CNR), Padova, Italy*
[b] *Department of Industrial Engineering, University of Padova, Padova, Italy*

[#]*Corresponding Author:* laura.vallese@phd.unipd.it

## Abstract

Buildings are responsible for 40% of the total energy consumption in Europe, making this sector crucial to achieve the decarbonization goals set by the European Green Deal. Against this background, thermal energy storage (TES) plays a pivotal role in reducing the mismatch between energy supply and demand, along with favoring the integration of renewable energy sources. While sensible heat storage is a well-established technology, research is focusing on latent heat and thermochemical systems, which are characterized by higher energy density.
In this context, the Horizon Europe project ECHO is going to combine innovative phase change materials (PCMs) with a composite vermiculite-$CaCl_2$ thermochemical material (TCM), with the aim to develop an efficient, compact, and modular TES system. A heat pump will charge a closed TCM reactor at 80 °C, thus coupling the electricity and heating sector by converting the excess photovoltaic power to stored heat. The reactor will be insulated through polyurethane PCM foams. A paraffin-based PCM storage will be used as a buffer during periods of high heating demand and as a source for humidification of the air during the discharging phase. Additionally, a cold storage system exploiting a eutectic PCM solution of $Na_2CO_3$ is planned for high cooling loads. Three test cases are going to be installed in Italy, Serbia, and Belgium, to assess the performance of the systems in different conditions, demonstrating its flexibility and adaptability to both stand-alone and grid-connected buildings.

## *1. introduction*

### *1.1. Thermal energy storage*

The objectives of the European Green Deal require to achieve net zero greenhouse gas (GHG) emissions by 2050 [1]. Renewable energy sources (RES) are the most promising alternatives to fossil fuels, in the perspective of mitigating climate change and reaching the set goals. However, their intrinsic intermittency requires adopting energy storage solutions [2]. Among the different categories, thermal energy storage (TES) is the most suitable for application in buildings, which in Europe account for 40 % of the final energy consumption. Decarbonizing this sector is of great importance, considering that

fossil fuels supply two thirds of the energy for space heating and cooling [3]. The main advantages of TES systems include the reduction of the mismatch between energy demand and supply [4] any improvements in thermal energy management practices can significantly benefit the society. One key function in thermal energy management is thermal energy storage (TES, and the opportunity to integrate RES through sector coupling, decarbonizing both the heating and electricity sector [5].

TES systems can be classified according to the application, the temperature range or, most commonly, the technology. Sensible heat storage is the simplest and most mature TES technology, involving the increase or decrease of temperature of the storage medium, usually water [6]. Latent heat storage is based on the phase transition of specific materials, offering high energy density with a reduced operating temperature range [7]. Thermochemical energy storage takes advantage of reversible chemical reactions, usually consisting of sorption. During charging, the two components involved in the reaction are separated by exploiting an external heat source. They can be stored until when heat is discharged through an exothermic reaction. This technology can achieve values of energy storage density 5-10 times higher than sensible and latent heat storage systems [8].

## *2. The echo project*

### *2.1. Description and aim*

The Horizon EU project ECHO (Efficient Compact Modular Thermal Energy Storage) contributes to research on thermal energy storage by designing and developing an innovative system, intended for application in buildings [10]. The proposed TES configuration integrates both PCMs and a TCM for supplying heating, cooling and domestic hot water to the user. The final aim is to store thermal energy in an efficient way, allowing the integration of RES and providing load shifting. The project is well described and synthesized through the following five objectives:

1. Definition of the fundamental parameters for the design of the system, thus considering different energy scenarios, energy demands and possibilities of connection to the electricity grid.
2. Selection of the most suitable materials, which are the core of the system and include a TCM and two different kinds of PCMs.
3. Construction of the complete plug&play system, whose main strengths are

modularity, flexibility and digital control.

4. Demonstration of the benefits of innovative TES systems, which represent an important opportunity to the transition towards more efficient, sustainable and adaptive heating, ventilation, and air conditioning (HVAC) systems.
5. Raise awareness on affordability, supply security and grid stability of adopting innovative TES solutions for buildings.

The core of the system is the TCM reactor, which is directly charged by a heat pump specifically designed for this application (Figure 1). This allows to integrate RES and to provide load shifting, by converting the excess photovoltaic power to stored heat. During the charging phase, air at around 80 °C flows through the reactor containing a composite of vermiculite and $CaCl_2$, arranged in drawers. On the other hand, discharging of the stored thermal energy involves the hydration of the composite TCM through humid air. For this purpose, an ultrasonic humidifier will be employed. To meet high cooling requirements in summer, an additional unit consisting of a cold PCM storage is added to the system. PCMs are also going to be used for insulation of the TCM reactor and to fill a buffer tank functioning as energy source for water evaporation.

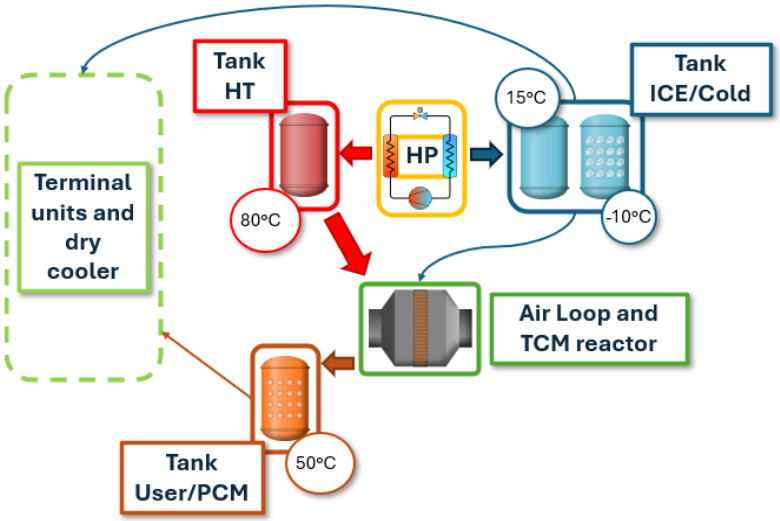


**Figure 1.** Schematic overview of the TES system.

### 2.2. Work packages

ECHO involves seventeen partners from Italy, Spain, Turkey, UK, Serbia, Belgium and Romania, and is organized in eight work packages (WPs).

Project management and coordination are addressed by WP1, whose main purposes are to monitor and supervise the progression in time of the project, to take care of the administrative and financial activities and to manage the data related to the project and the achieved results.

WP2 focusses on the conceptualization and design of the TES system, aiming to assess its impact through agent-based simulations, called ECHOTSS (ECHO transaction simulation system). Scenarios involving different climates and energy demands will be simulated. The work is set in the European context through a comprehensive analysis of the state of the art on TES systems, the creation of a database including the available technologies and a SWOT analysis. The WP is also in charge for the definition of design and control indicators and for assessing the risks related to the three demo sites.

The selection of the materials and the related design of the system is carried out in WP3. A significant effort is dedicated to the characterization and fabrication of a suitable TCM, necessary for properly designing the reactor at the heart of the TES system. Proper PCMs are selected to fulfil the buffer and the cold storage requirements, respectively. Potential risks, such as corrosion, are analyzed and suitable solutions to contrast them are found.

The main objective of WP4 is the construction of a lab-scale prototype of the system. This is preceded by a preliminary design and the creation of a numerical model to support the control of the system. The prototype will be monitored in different conditions, assessing its energy performance and optimizing it.

The control system is being developed in WP5, including the design and manufacturing of the hardware, the creation of the control algorithm and the application of the control system to the demo sites.

The demonstration of three test cases is on charge of WP6. The ECHO TES system will be monitored in different locations and conditions, considering the performance, adaptability and reliability. Moreover, tests for the implementation of ECHOTSS will be conducted.

WP7 focusses on the evaluation of the potential reduction of the environmental impact

and of the peak load minimizing costs through the life cycle assessment (LCA) and LCCA respectively. Environmental and risk assessment will be carried out, together with the definition of actions to favor market exploitation and planning.
Finally, WP8 involves dissemination, communication, and networking and training activities.

## *3. Materials for thermal energy storageE*

### *3.1. Thermochemical materials*

Thermochemical materials are the most promising mediums for energy storage, thanks to their high theoretical energy density. These materials undergo a reversible chemical reaction. The charging phase consists of the decomposition or desorption of the material, which are endothermic processes, while the discharging process is exothermic [11]. The main features sought for storage applications are a large porous surface area, good mechanical properties and low charging temperature [12]. Among the available options, salt hydrates are particularly suitable for providing space heating and DHW in buildings, thanks to their low operating temperature and relatively low cost [13]. However, they are usually incorporated in composite materials to improve their stability and heat and mass transfer. The materials functioning as matrixes are chosen among adsorbents, like zeolite or silica gel, or for their porosity, like natural rocks, or for their high thermal conductivity, such as expanded graphite [14].
In the context of the ECHO project, the partners involved in WP3 have selected a composite of $CaCl_2$ and vermiculite. $CaCl_2$ is a non-toxic hygroscopic salt which can adsorb up to six water molecules. Its main advantages include a high sorption rate, chemical stability and low corrosiveness. Vermiculite is interesting as host matrix thanks to its low cost, high porosity, durability and low weight [15]. According to Zhang et al., vacuum impregnation is the most promising method for synthesizing this composite TCM. The benefits compared to other methods include higher salt infiltration and higher volumetric energy density (2.05 GJ $m^{-3}$) [16]. The composite TCM was characterized through the scanning electron microscope (SEM) analysis, to evaluate its morphology and microstructure. The content of salt was evaluated through an inductively coupled plasma optical emission spectrometer (ICP-OES), and an energy storage density analysis was carried out. Further experimentation on the cyclability of the material is foreseen,

as well as a more detailed characterization in the context of the prototype and of the demo sites.

### *3.2. Phase change materials*

Phase change materials can store large amounts of heat during phase change, at approximately constant temperature. When choosing a PCM, the melting point is one of the most important features to take into account, and it should be compatible with the operating range [17]. Other required properties are high latent heat and thermal conductivity, minimum subcooling during melting and chemical stability [18] but also within architects and engineers. Many publications have appeared, and several books, but the information is disseminated and not very much organised. This paper shows a review of the latest publications on the use of phase change materials (PCM. PCMs can be classified according to their operating temperature or the type of phase transition. Solid-liquid PCMs are the most widespread and are further divided into inorganic and organic substances [7]. The advantages of organic PCMs include high stability, non-corrosiveness and high latent heat of fusion. On the other hand, inorganic compounds are characterized by high phase change enthalpy and thermal conductivity. Eutectic PCMs combine two or more organic or inorganic materials, which change phase at the same moment [17].

For the ECHO project, two different PCMs have been selected so far.

A paraffin-based PCM (Table 1) was proven to be the best option for the buffer storage, to be operated between 27 and 35 °C.

**Table 1** Properties of the selected paraffin-based PCM A32, according to the manufacturer [19].

| | **Phase change T (°C)** | **Density (kg /m³)** | **Latent Heat Capacity (kJ/kg)** | **Volumetric Heat capacity (MJ/m³)** | **Specific Heat capacity (kJ/KgK)** | **Thermal conductivity (W/mK)** | **Maximum operating temperature (°C)** |
|---|---|---|---|---|---|---|---|
| **A32 PCM** | 32 | 845 | 120 | 101 | 2.2 | 0.121 | 200 |

The choice was made after comparing it to a salt hydrate based on sodium sulphate, which during experimental tests showed stability issues and subcooling around 27 °C. Furthermore, the salt hydrate is subject to the risk of decomposition at temperatures

higher than 60 °C, not compatible with temperatures that can be reached in the system. The average latent heat and subcooling of the two PCMs were characterized through differential scanning calorimetry (DSC).

For the cold storage application, the phase change temperature is required to be below 0 °C. The selection of the most suitable PCM was based on the analysis of its thermophysical properties, including the phase change temperature, the specific heat capacity and the latent heat. The last two properties were measured through DSC at the Construction Technologies Institute of the National Research Council of Italy (ITC-CNR). The eutectic mixture identified as most suitable candidate for this application is sodium carbonate and water ($Na_2CO_3 + H_2O$), being characterized by a higher latent heat compared to another water-salt solution.

Along with the characterization of the composite TCM, also the thermophysical properties of these PCMs will be evaluated more in depth during the operation of the prototype and of the demo sites.

### *4. Conclusions*

TES is a key technology to reach the ambitious goals set by the European Green Deal. In this framework, the Horizon EU ECHO project advances research in TES by developing an innovative system integrating PCMs and a TCM to support buildings' heating, cooling, and domestic hot water needs. The project's objectives emphasize designing a modular, flexible, and digitally controlled system, which can demonstrate the advantages of TES in improving the efficiency, sustainability, and adaptability of HVAC systems.

Materials selection is crucial when implementing new TES technologies. In the ECHO project, the chosen materials include a composite of $CaCl_2$ and vermiculite for the TCM reactor, a paraffin-based PCM for the buffer storage, and a eutectic mixture of $Na_2CO_3$ and $H_2O$ for the cold accumulator. The chosen materials exhibit favorable properties such as high energy density, stability, and compatibility with the operating conditions.

This project's innovations highlight the potential of TES systems to contribute significantly to the energy transition, favoring the spread of RES and increasing efficiency in buildings.

### *Acknowledgments*

This research was funded by the European Union's Horizon Europe research and innovation program within the ECHO project, under grant agreement No. 101096368.

### *References*


[1] «COMMUNICATION FROM THE COMMISSION TO THE EUROPEAN PARLIAMENT, THE EUROPEAN COUNCIL, THE COUNCIL, THE EUROPEAN ECONOMIC AND SOCIAL COMMITTEE AND THE COMMITTEE OF THE REGIONS,The European Green Deal», Brussels, dic. 2019.

[2] E. Sayed et al., «Renewable Energy and Energy Storage Systems», Energies, vol. 16, fasc. 3, p. 1415, feb. 2023, doi: 10.3390/en16031415.

[3] «Directive (EU) 2024/1275 of the European Parliament and of the Council of 24 April 2024 on the energy performance of buildings (recast) (Text with EEA relevance)».

[4] G. Alva, Y. Lin, e G. Fang, «An overview of thermal energy storage systems», Energy, vol. 144, pp. 341–378, feb. 2018, doi: 10.1016/j.energy.2017.12.037.

[5] P. Royo et al., «Experimental analysis of a power-to-heat storage with high-temperature phase change materials to increase flexibility and sector coupling», Appl. Therm. Eng., vol. 236, p. 121889, gen. 2024, doi: 10.1016/j.applthermaleng.2023.121889.

[6] I. Sarbu e C. Sebarchievici, «A Comprehensive Review of Thermal Energy Storage», Sustainability, vol. 10, fasc. 1, p. 191, gen. 2018, doi: 10.3390/su10010191.

[7] K. Pielichowska e K. Pielichowski, «Phase change materials for thermal energy storage», Prog. Mater. Sci., vol. 65, pp. 67–123, ago. 2014, doi: 10.1016/j.pmatsci.2014.03.005.

[8] G. Airò Farulla, M. Cellura, F. Guarino, e M. Ferraro, «A Review of Thermochemical Energy Storage Systems for Power Grid Support», Appl. Sci., vol. 10, fasc. 9, p. 3142, apr. 2020, doi: 10.3390/app10093142.

[9] A. H. Abedin, «A Critical Review of Thermochemical Energy Storage Systems», Open Renew. Energy J., vol. 4, fasc. 1, pp. 42–46, ago. 2011, doi: 10.2174/1876387101004010042.

[10] «ECHO Project | Efficient Compact Modular Thermal Energy Storage System», ECHO Project. Consultato: 13 agosto 2024. [Online]. Disponibile su: https://echo-euproject.eu/

[11] Y. Ding e S. B. Riffat, «Thermochemical energy storage technologies for building applications: a state-of-the-art review», Int. J. Low-Carbon Technol., vol. 8, fasc. 2, pp. 106–116, giu. 2013, doi: 10.1093/ijlct/cts004.

[12] H. Jarimi et al., «Materials characterization of innovative composite materials for solar-driven thermochemical heat storage (THS) suitable for building application», Int. J. Low-Carbon Technol., vol. 14, fasc. 3, pp. 313–325, set. 2019, doi: 10.1093/ijlct/ctx017.

[13] J. Lin, Q. Zhao, H. Huang, H. Mao, Y. Liu, e Y. Xiao, «Applications of low-temperature thermochemical energy storage systems for salt hydrates based on material classification: A review», Sol. Energy, vol. 214, pp. 149–178, gen. 2021, doi: 10.1016/j.solener.2020.11.055.

[14] Q. Zhao, J. Lin, H. Huang, Q. Wu, Y. Shen, e Y. Xiao, «Optimization of thermochemical energy storage systems based on hydrated salts: A review», Energy Build., vol. 244, p. 111035, ago. 2021, doi: 10.1016/j.enbuild.2021.111035.

[15] Z. Chen, Y. Zhang, Y. Zhang, Y. Su, e S. Riffat, «A study on vermiculite-based salt mixture composite materials for low-grade thermochemical adsorption heat storage», Energy, vol. 278, p. 127986, set. 2023, doi: 10.1016/j.energy.2023.127986.

[16] Y. Zhang, Z. Chen, Y. Zhang, Y. Su, e S. Riffat, «Parameter control in synthesis of Vermiculite-CaCl2 composite materials for thermochemical adsorption heat storage», Energy, vol. 291, p. 130478, mar. 2024, doi: 10.1016/j.energy.2024.130478.

[17] H. Jouhara, A. Żabnieńska-Góra, N. Khordehgah, D. Ahmad, e T. Lipinski, «Latent thermal energy storage technologies and applications: A review», Int. J. Thermofluids, vol. 5–6, p. 100039, ago. 2020, doi: 10.1016/j.ijft.2020.100039.

[18] L. F. Cabeza, A. Castell, C. Barreneche, A. De Gracia, e A. I. Fernández, «Materials used as PCM in thermal energy storage in buildings: A review», Renew. Sustain. Energy Rev., vol. 15, fasc. 3, pp. 1675–1695, apr. 2011, doi: 10.1016/j.rser.2010.11.018.

[19] «PCM products». Consultato: 28 agosto 2024. [Online]. Disponibile su: https://www.pcmproducts.net/

# Pla/Croconaine Blended Composite Materials as High Nir Absorbers for Pcm Latent Heat Storage

**Maria Montrone[a,b], Umberto Berardi[a], Maria Annunziata M. Capozzi[b], Antonio Cardone[c]**

[a]*Politecnico di Bari, Bari, Italy*
[b]*Universita' di Bari, Bari, Italy*
[c]*CNR-ICCOM di Bari, Bari, Italy*

[#]*Corresponding Author: m.montrone3@phd.poliba.it*

## Abstract

Latent Heat Thermal Energy Storage (LHTES) systems are gaining significant attention for their ability to efficiently store and release energy, particularly in renewable energy applications. These systems utilize Phase Change Materials (PCM), which absorb or release large amounts of latent heat during phase transitions. Despite their high energy storage density, the widespread application of PCMs is hindered by their low thermal conductivity, which limits heat transfer rates, reducing the efficiency of the storage and retrieval process. To address this challenge, recent research has focused on the incorporation of organic materials to improve the thermal conductivity of PCMs without compromising their latent heat storage capabilities. These organic materials not only enhance thermal conductivity but also provide advantages like chemical compatibility, flexibility, and sustainability. This paper discusses the integration of organic-based materials in PCM-enhanced LHTES systems, giving an intriguing idea to improve thermal performance of PCMs using a benzo-indolenine based croconine (CR-BI) as photothermal organic material and Polylactic acid (PLA) as base polymer for the preparation of a photothermal layer.

### *1. Introduction*

Latent Heat Thermal Energy Storage (LHTES) is a technology that stores thermal energy using phase change materials (PCMs), which absorb or release heat during phase transitions, typically between solid and liquid states. This technology has numerous benefits in various applications, such as energy management, renewable energy integration, and building systems. For this reason, it is considered an interesting solution to be used for eliminating the mismatch between energy provide and demand. The main benefits of LHTES are high energy density, temperature stability, energy efficiency, cost saving, sustainability and environmental benefits, extended system lifespan and flexibility in applications. Those benefits are assigned to phase change material use. PCMs store large amounts of energy in a small volume due to the latent heat of phase change. This makes LHTES more energy-dense compared to sensible heat storage systems, which

store heat by increasing the temperature of the material. In addition, PCMs typically have long life cycles, with the ability to undergo numerous phase transitions without significant degradation, resulting in longer-lasting storage systems. However, those materials possess low thermal conductivity that degrades their thermal performance in latent heat thermal energy storage systems. Thermal performance of PCMs could be improved using organic materials with photothermal properties. These organic materials not only enhance their thermal conductivity but also provide advantages like chemical compatibility, flexibility, and sustainability.

Organic photothermal materials are a class of compounds that have the unique ability to convert absorbed light into heat. Lots of organic materials such as conjugated polymers, supramolecular complexes, organic cocrystal and organic small molecules have been designed to perform good photothermal conversion in various applications such as energy redistribution, solar harvesting, water purification and catalysis. When incorporated into biological systems, these materials can be exploited for photothermal therapy, which destroys cells using localized heating from focused light irradiation [1-6]. These materials are increasingly gaining attention due to their tunable properties, biocompatibility and environmental friendliness compared to their inorganic counterparts. They function through the non-radiative relaxation of excited states (Fig. 1), where absorbed photons are efficiently converted into thermal energy. Their development leverages the advantages of organic chemistry, including the ability to fine-tune molecular structures for desired optical properties, stability, and compatibility with different environments. As research in this field advances, organic photothermal materials are poised to play a critical role in next-generation technologies that require efficient light-to-heat conversion.

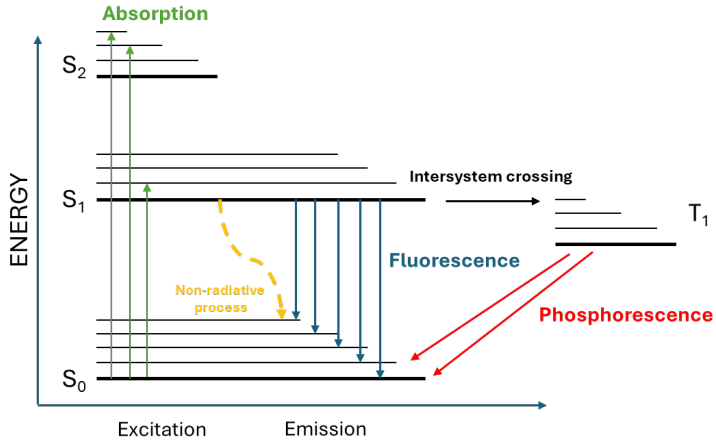


**Figure 1.** Non-radiative relaxation (yellow) in Jablonski Diagram.

Among several active organic photothermal materials, the croconic acid-based compounds are of particular interest thanks to their outstanding properties for high performance photothermal heating [7]. Cronconic acid-based compounds, often simply named Croconaines (CRs) has been widely used in solar-thermal devices [8], welding applications [9-10] and as mesogenic calamitous materials [11]. Fluorescent CRs were also exploited as phototherapeutic agents for applications in synergistic photothermal/ photodynamic therapy of cancer guided by NIR fluorescence imaging [12]. Generally, CRs are a class of small organic molecules consisting of 2 donor moieties connected to 1 and 3 positions of the central 5-member croconate ring, with a donor-acceptor-donor (D-A-D) structure, as shown in Fig. 2. By an accurate choice of donor units, it is possible to modulate the HOMO and LUMO energy levels and then the band gap, addressing electrical and optical properties for specific applications. The D-A-D structure ensures an extended π-conjugation which gives these materials semiconductor properties with a high absorption capacity spanning from the visible to the NIR region, and peculiar characteristics such as, high molar extinction coefficient, solubility tuneable in organic or aqueous solvents, easy processability from solution, intrinsic bio-compatibility and eco-compatibility.

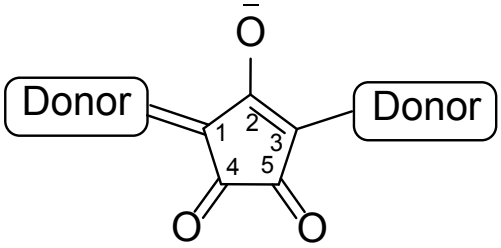


**Figure 2.** Croconaine: 1,3-disubstituted-croconic acid.

Some numerical data of laser-induced photothermal heating of CRs were given by Sun et al. [8] and Pang et al. [12] as value of photothermal conversion efficiency (PCE) (Tab. 1).

**Table 1.** The PCE of different CR dyes.

| *Dye Structure* | *Excitation Wavelength (nm)* | *PCE %* | *Ref.* |
|---|---|---|---|
| 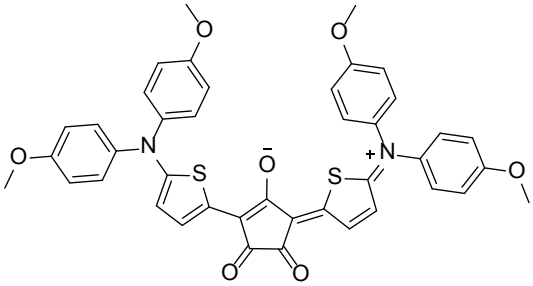 CR1 | 808 | 79.5 | [8] |
| 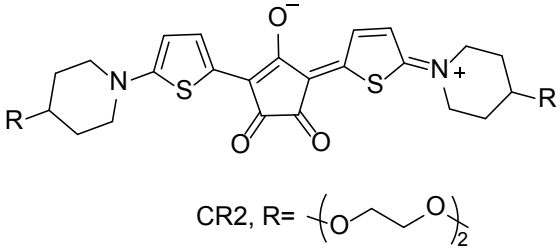 CR2, R= | 735 | 77 | [12] |

Sun et al. exploited the light harvesting ability and high photothermal conversion efficiency of a CR dye (CR1, Tab.1), to fabricate a self-healing flexible film with

poly(dimethylsiloxane). Using CR dyes to convert light into thermal energy has several inherent advantages, i.e. simple chemical structure, easy synthetic access, easy tunability of structural and chemico-physical properties.

In our work, we propose a photothermal layer made by dispersing a CR dye (**CR-BI**) into a polymeric matrix (polylactic acid **PLA**). The layer was prepared by dissolving **CR-BI** and **PLA** in chloroform and then casting the resulting solution onto a proper support. The resulting film **CR-BI/PLA** was submitted to investigation aimed to determine properties such as photothermal conversion, thermal conductivity, thermal resistivity and thermal absorptivity. Following, this photothermal layer **CR-IB/PLA** was tested as interlayer between two PCM layers for LHTES applications.

## *2. Methodology*

### *2.1. CR-BI/PLA layer preparation*

Polylactic acid (PLA, Mw = 64700 [Da], Mn = 32100 [Da], PDI [Mw/Mn] = 2,10) (commercial source). The synthesis of **CR-BI** (Fig. 3) was performed following the procedure reported by Capozzi at al. [13]. A solution of CR-BI ($1x10^{-6}$ M) and PLA (0.2 mg/ml) in chloroform was prepared. Finally, the solution was deposited by casting on glass and dried at room temperature for 3 days. A light brown film was obtained.

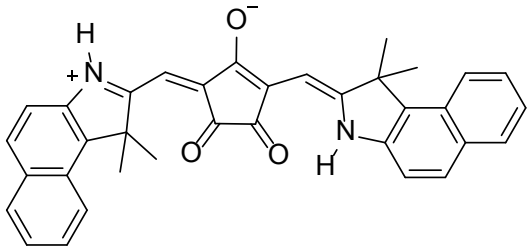


**Figure 3.** Chemical structure of CR-BI, used for the CR-BI/PLA layer

## *3. Results*

**CR-BI** (1,1-Dimethyl-1,3-dihydro-2H-benzo[e]indol-2-ylidene)methyl)-5- ((1,1-dimethyl-1H-benzo[e]indol-3-ium-2-yl)methylene)-3,4-dioxocyclopent-1-en-1-olate) is a benzo-indolenine based CR with thermal stability, good photostability and strong absorption

capacity in the NIR light region (around 800 nm) [14-15] (Fig. 4).

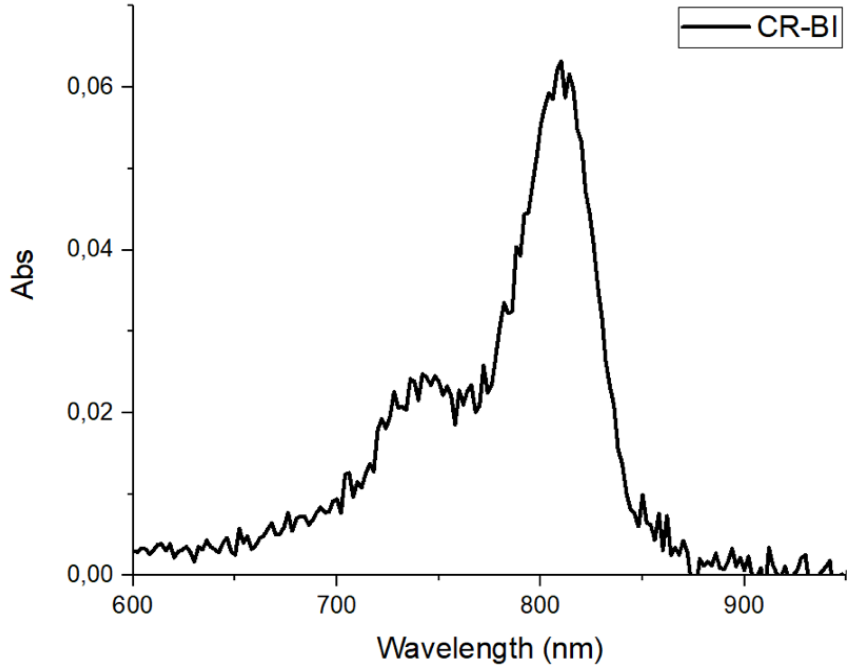


**Figure 4.** UV-Vis-Absorption spectra of **CR-BI** in chloroform ($1*10^{-6}$ M).

As a matrix for the manufacture of **CR-BI/PLA** layers, we used the PLA, an interesting eco-friendly polymer that can be obtained from bio-refinery (from agro-industrial waste), with good transparence in the visible and NIR region and easily processable from solution. **CR-BI** shows a good affinity with the PLA, making a homogeneous film when casted on glass surfaces. In Fig. 5 are reported the absorbance spectra of pure **CR-BI** (in $CHCl_3$), **CR-BI/PLA** (in $CHCl_3$) and **CR-BI-/PLA** film. As evident, the PLA matrix doesn't modify the absorbance of **CR-BI**, both in solution and thin film.

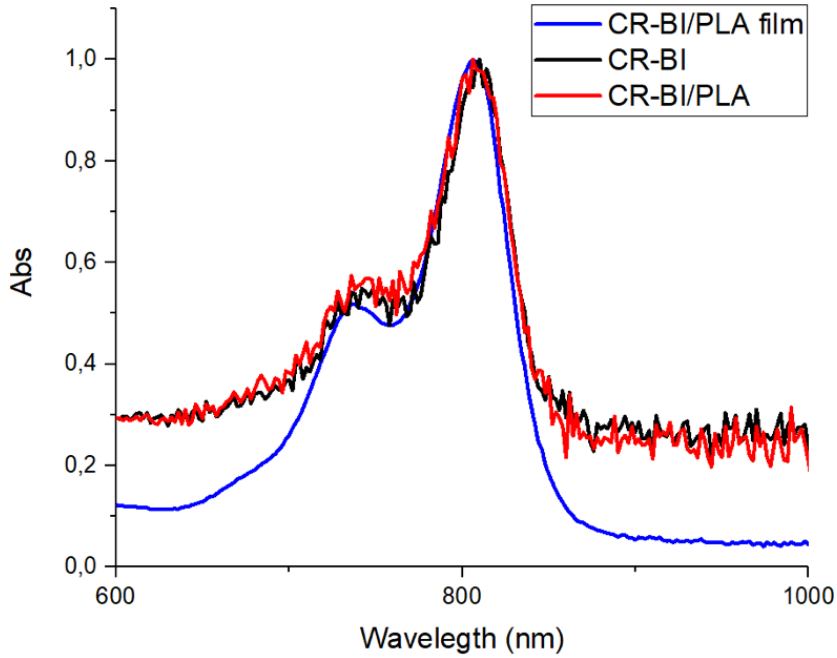


**Figure 5.** Absorption spectra of **CR-BI, CR-BI/PLA** and **CR-BI/PLA film** (in $CHCl_3$)

### *4. Conclusions*

This paper has discussed the integration of organic-based materials in PCM-enhanced LHTES systems, giving an intriguing idea to improve thermal performance of PCMs using a benzo-indolenine based croconine (CR-BI) as photothermal organic material and Polylactic acid (PLA) as base polymer for the preparation of a photothermal layer. Future steps will include the thermal characterization of the materials.

### *Acknowledgments*

The Italian Ministero dell'Istruzione, dell'Università e della Ricerca (MIUR) is gratefully acknowledged for the support. This work has been developed under the projects "Fibre e tessuti intelligenti ed ECOsostenibili per l'abbigliamento TECnico e l'alta moda (ECOTEC)" and "Processi di EstRazione di bioprodotti da sCartiagroIndustriali e

VALorizzazione in cascata PON ARS01_00869 PERCIVAL- Programma di ricerca n. 03.231- CUP: B95F21001900005".

### *5. References*

[1] Tang, B., Li, W. L., Chang, Y., Yuan, B., Wu, Y., Zhang, M. T., Xu, J.F., Li, J., Zhang, X. "A supramolecular radical dimer: high-efficiency NIR-II photothermal conversion and therapy", Angewandte Chemie International Edition, vol. 58.43, pp.15526-15531, 2019.

[2] Wang, Y., Zhu, W., Du, W., Liu, X., Zhang, X., Dong, H., Hu, W.,"Cocrystals Strategy towards Materials for Near-Infrared Photothermal Conversion and Imaging." Angewandte Chemie, vol. 130.15, pp. 4027-4031, 2018.

[3] Zhang, M. M., Chen, S. L., Bao, A. R., Chen, Y., Liang, H., Ji, S., Chen, J., Ye, B.,Yang, Q., Liu, Y., Li, Y., Chen, W., Huang, X., Ni, S., Dang, L., Li, M. D. "Anion-Counterion Strategy toward Organic Cocrystal Engineering for Near-Infrared Photothermal Conversion and Solar-Driven Water Evaporation." Angewandte Chemie, vol. 136.10, e202318628, 2024.

[4] Chen, Y. T., Wen, X., He, J., Li, Z., Zhu, S., Chen, W., Yu, L., Guo, Y., Ni, S., Chen, S., Dang, L., Li, M. D. "Boosting near-infrared photothermal conversion by intermolecular interactions in isomeric cocrystals." ACS Applied Materials & Interfaces, vol. 14.25, pp. 28781-28791, 2022.

[5] Huang, Q., Ye, X., Chen, W., Song, X., Chen, Y. T., Wen, X., Zhang, M., Wang, Y., Chen, S.L., Li, M. D. "Boosting Photo-thermo-electric Conversion via a Donor–Acceptor Organic Cocrystal Strategy." ACS Energy Letters. Vol. 8.10, pp. 4179-4185, 2023.

[6] Neumann, O., Urban, A. S., Day, J., Lal, S., Nordlander, P., & Halas, N. J. "Solar vapor generation enabled by nanoparticles". ACS nano, vol. 7.1, pp. 42-49, 2013.

[7] G. T. Spence, V. H. Gregory, B. D. Smith, "Activated photothermal heating Using croconaine dyes", Chemical Science, vol. 4.11, pp. 4240-4244, 2013.

[8] J. Sun, E. Zhao, J. Liang, H. Li, S. Zhao, G. Wang, X. Gu, B. Z. Tang, "Diradical- Featured Organic Small-Molecule Photothermal Material with High-Spin State in Dimers for Ultra-Broadband Solar Energy Harvesting",Advanced Materials, vol. 34(9), pp. 2108048, 2022.

[9] T. Brock-Nannestad, M. Pittelkow, H. Ø. Bak, A method for laser welding of Mplastic materials, WO 2014/166506 A1, 2014.

[10] A. Jeppesen, B. E. Nielsen, T., Brock-Nannestad, M. Pittelkow, Thermally Stable NIR Dyes For Laser Welding Of Plastic Materials, WO 154974, 2019.

[11] L. X. Guo, M. H. Liu, S. M. Sayed, B. P. Lin, P. Keller, X. Q. Zhang, Y. Sun, H. Yang, "A calamitic mesogenic near-infra-red absorbing croconaine Dye/liquid crystalline elastomer composite", Chemical Science, vol. 7(7) 4400–4406, 2016.

[12] E. Pang, R. Huang, S. Zhao, K. Yang, B. Li, Q. Tan, S. Tan, M. Lan, B. Wang, X. Song, "Water-soluble thiophene-croconaine dye with high molar extinction coefficient for NIR fluorescence imaging-guided synergistic photothermal/photodynamic therapy of cancer", J. Mater. Chem. B., vol. 10, pp. 9848-9854, 2022.

[13] N. Zappimbulso, M. A. M. Capozzi, A. Porcheddu, G. M. Farinola, A. Punzi, "Solvent-free reactions for the synthesis of indolenine-based squaraines and croconaines: Comparison of thermal heating, mechanochemical milling, and IR Irradiation", ChemSusChem, vol. 14(5), pp.1363-1369, 2021.

[14] A. Punzi, M. A. M. Capozzi, V. Fino, C. Carlucci, M. Suriano, E. Mesto, E. Schingaro, E. Orgiu, S. Bonacchi, T. Leydecker, P. Samorì, R. Musio, G. M. Farinola, "Croconaines as molecular materials for organic electronics: synthesis, solid state structure and use in transistor devices", Journal of Materials Chemistry C, vol. 4(15), pp. 3138-3142,2016.

[15] M. A. M. Capozzi, A. Punzi, F. Babudri, R. Musio, G.M. Farinola, "Synthesis and Computational Study of Semicroconaines and Nonsymmetric Croconaines", J. Org. Chem, vol. 83.23, pp.14396–14405, 2018.

# Impact of Wood Bio-Aggregate Content on the Thermo-Physical and Mechanical Properties of Bio-Based Composites

**Amanda Aguiar[a,#], Antonio Caggiano[b], Romildo Toledo Filho[a]**

*a Federal University of Rio de Janeiro, Rio de Janeiro, Brazil*
*b Università degli studi di Genova, Genova, Italy*

*# Corresponding author:* amanda.aguiar@coc.ufrj.br

Keywords: wood bio-based composite, thermo-physical properties; thermal insulation.

## ABSTRACT

Wood bio-based composite (WBBC) is a promising eco-friendly alternative construction material offering enhanced thermal insulation and reduced environmental impact. This study investigates the influence of wood bio-aggregate content on the thermo-physical and mechanical properties of WBBC. The mixtures were prepared using varying wood shaving contents (i.e., 40%, 50%, and 60% by volume) and a cementitious matrix comprised of a cement-fly ash-metakaolin blend. Thermal conductivity, bulk density, and scanning electron microscopy (SEM) tests were performed on samples at 28 days of age. In addition, uniaxial compressive strength tests were performed to characterize the composites mechanically. Results indicate that thermal conductivity decreased with increasing biomass content. WBBC60 exhibited a thermal conductivity value approximately 40% lower than WBBC40. Density and compressive strengths followed a similar trend, with lower values observed for higher bio-aggregate contents. SEM analysis revealed the detailed porosity of wood aggregates and the cementitious matrix, along with the interfacial interactions between them. These findings demonstrate the potential of WBBC as an effective thermal insulator, particularly with higher bio-aggregate content.

### *1. Introduction*

The rapid rise of global industrialization and urbanization has led to substantial consumption of non-renewable energy and a significant release of greenhouse gases, resulting in a rise in global temperature and causing numerous environmental degradation issues [1]. The building sector is responsible for the consumption of large amounts of energy and resources. Concrete is the second most consumed resource by mankind after water [2], and 5% to 8% of global anthropogenic $CO_2$ emissions is caused by the production of cement alone [3]. The growing emphasis on sustainable construction is driving the search for renewable alternatives to conventional materials like concrete aggregates, which are increasingly scarce due to overexploitation [4]. Several studies [5–8] have demonstrated the potential use of plant origin particles (hemp, rapeseed, rice

husk, wheat straw, sunflower pith, bamboo, wood, etc.) as total or partial replacement of the aggregates in cementitious materials and other mineral matrices. The use of bio-aggregates, primarily derived from waste materials, is gaining attention as a method to reduce $CO_2$ emissions. These materials effectively store biogenic carbon that was absorbed by trees during their growth [9].

Wood industries produce substantial amounts of waste globally. For every 1,000 board feet of lumber produced, sawmills generate approximately 1 ton of by-products, including sawdust, shavings, slabs, and edgings; approximately 75% of this useless material is wood content, and 25% is bark [10]. Wood waste can be repurposed for various non-energy applications, including the production of composite boards, surfacing materials, compost, and cement board [11].

The incorporation of wood waste as bio-aggregates in cement composites has been a growing area of research in recent years. Dias et al. [12] developed lightweight cement composites incorporating up to 15% wood particles and found that while the addition of wood particles significantly reduces the mechanical performance of the hardened material, these composites remain suitable for applications with low structural demands. Da Gloria et al. [13] developed a method for designing bio-based, low-carbon building materials utilizing wood waste and cementitious pastes. By incorporating bio-aggregate volume fractions of 40% to 50% and employing a low-cement matrix—where 70% of the cement was replaced by fly ash and metakaolin—the authors produced lightweight bio-concretes with densities ranging from 715 to 1,207 kg/m$^3$. These materials exhibited compressive strengths between 0.64 and 12.27 MPa and negative greenhouse gas emissions.

Compared to conventional building materials, bio-based building materials offer several advantages, including lower density, good acoustic properties [14,15], excellent moisture buffering capacity [16,17], and effective thermal insulation [15,16]. From a thermal perspective, these materials improve building energy efficiency due to their lower thermal conductivity, which is lower than that of conventional materials [18].

The excellent thermal insulation properties of bio-based materials have made their thermos-physical characteristics a primary research focus. Sellami et al. [4] investigated the thermal properties of bio-composites reinforced with diss fibers for insulation applications. Composites containing 20, 25, and 30% diss fibers by cement mass exhibited

densities ranging from 965 to 1440 kg/m³. Thermal conductivity decreased with increasing fiber content: 0.26 W/m·K (20%), 0.17 W/m·K (25%), and 0.14 W/m·K (30%) [4]. Moisture content and the method of composite densification significantly affect thermal conductivity. Dry hempcrete exhibits a thermal conductivity of 0.11 W/m·K, while this value increases to 0.32 W/m·K at 100% relative humidity and, for non-compacted hemp shiv, it ranges from 0.05 to 0.1 W/m·K [19]. Corinaldesi et al. [16] demonstrated a 25% reduction in the thermal conductivity of mortars by incorporating just 5% wood waste, decreasing the value from 0.815 W/m·K to 0.625 W/m·K. This highlights the significant potential of bio-aggregates to enhance the thermal insulation of composites, even at low concentrations.

In this context, the objective of this research is to investigate the thermo-physical and mechanical performance of workable WBBCs composed of 40, 50, and 60% biomass. The effects of wood bio-aggregate content on density, thermal conductivity, thermal effusivity, and compressive strength were evaluated.

## 2. *Materials and methods*

### *2.1. Raw materials*

The composite cement matrix consists of high-early-strength Portland cement (Brazilian type CPV-ARI, produced by Lafarge Holcim), metakaolin (Metacaulim do Brasil Company, Brazil), and fly ash (Pozofly Company, Brazil). Supplementary cementitious materials were introduced to achieve a more sustainable concrete mix by reducing cement consumption. Table 1 details the chemical composition, analyzed by X-ray fluorescence (XRF), and the density, measured using a helium gas pycnometer, of these materials.

**Table 1.** Chemical composition and specific density of cementitious materials.

| Oxides | Cement | Metakaolin | Fly ash |
|---|---|---|---|
| CaO | 71.96 % | - | 2.27% |
| $SiO_2$ | 13.10 % | 41.46% | 50.46% |
| $Al_2O_3$ | 4.86 % | 48.14% | 33.86% |
| $Fe_2O_3$ | 3.84% | 5.84% | 5.28% |
| $SO_3$ | 3.32 % | 1.25% | 1.58% |
| $K_2O$ | 1.07 % | 0.58% | 3.49% |

| | | | |
|---|---|---|---|
| SrO | 0.48 % | - | 0.02% |
| $TiO_2$ | 0.30% | 1.01% | 1.23% |
| MnO | 0.15% | 0.11% | 0.05% |
| BaO | - | 0.40% | 0.59% |
| $ZrO_2$ | - | 0.19% | 0.11% |
| LOI | 0.94% | 0.96% | 0.99% |
| Specific density | 3.09 g/cm³ | 2.51 g/cm³ | 1.89 g/cm³ |

Wood bio-aggregates (WBA) for this study were sourced from the state of Rio de Janeiro, Brazil. They comprised a random mixture of four species: Hymenolobium petraeum, Cedrela fissilis, Erisma uncinatum warm, and Manilkara salzmanni.

To achieve properties suitable for bio-based composite production, the wood bio-aggregates underwent a specific processing regimen in one batch. The material was initially subjected to mechanical sieving, retaining only the fraction exceeding a nominal diameter of 1.18 mm [20]. Subsequently, the wood particles were immersed in a calcium hydroxide solution (Ca(OH)2 0.73 %) for two hours to facilitate the removal of extractives and enhance the interfacial bonding between the bio-aggregate and the cement matrix [21]. Finally, the material was air-dried and homogenized. Wood shavings are shown in Fig. 1. The bulk density, water absorption, and moisture content of the WBA were 580 kg/m³, 80%, and 12.5%, respectively.

**Figure 1.** Wood bio-aggregates.

### 2.2. Wood bio-based composite

Wood bio-based composites (WBBC) were formulated with three varying volumetric fractions of wood bio-aggregates: 40%, 50%, and 60% (values by weight in Tab. 2). The cementitious matrix consisted of (by weight): 40% Portland cement (PC), 30% metakaolin (MK), and 30% fly ash (FA). A water-binder ratio of 0.35 was set for all mixtures. To achieve good workability, the water content was adjusted to account for both cement hydration (Wh) and water absorption by the wood bio-aggregates (Wa). Calcium chloride (CC) was incorporated as setting accelerator at a dosage of 3% by mass of the cementitious components. The proportions of supplementary cementitious materials and wood bio-aggregates were adopted based on Caldas et al. [22] with the goal of reducing cement consumption and the environmental impact while maintaining workable WBBC.

**Table 2.** Mixture composition (kg/m³).

| WBBC | WBA | PC | MK | FA | CC | Wh | Wa |
|---|---|---|---|---|---|---|---|
| WBBC40 | 232.0 | 282.5 | 211.9 | 211.9 | 26.7 | 247.2 | 185.6 |
| WBBC50 | 290.0 | 235.4 | 176.6 | 176.6 | 22.3 | 206.0 | 232.0 |
| WBBC60 | 348.0 | 188.3 | 141.3 | 141.3 | 17.8 | 164.8 | 278.4 |

The WBBC production process followed adapted guidelines from ABNT NBR 16697 [23]. The cementitious materials were initially combined with wood bio-aggregates and mixed for a duration of one minute. Subsequently, water containing calcium chloride was progressively incorporated into the mixture over a one-minute period. A homogeneous composite was produced after a total mixing time of four minutes.

Bio-based composites were cast in three layers, each subjected to 10 seconds of mechanical vibration (68 Hz). After 24 hours, samples were demolded and cured for 28 days at 22 ± 3 °C and 55 ± 5 % relative humidity.

### 2.3. Thermo-physical properties

Bulk density of WBBC was determined for each 28-day-old mixture using five 50 mm diameter x 100 mm height cylindrical specimens according to NBR 9778 [24].

Thermal conductivity and thermal effusivity of WBBC (16% moisture content) were determined using TCi C-Therm equipment (Fig. 2a). For each biomass content, three 100 x 100 x 25 mm specimens were tested, with four readings taken at three points (two ends,

one center) using thermal paste (Fig. 2b). The equipment determines thermal properties by applying heat to the sample via a reflectance sensor. The resulting temperature increase at the sensor-sample interface induces a voltage change, which is correlated to the material's thermal properties. The software outputs thermal conductivity and thermal effusivity for each reading.

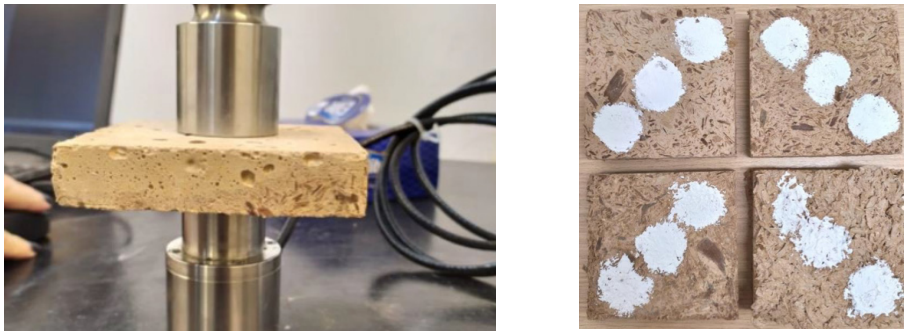

(a) (b)

**Figure 2.** Thermal conductivity test: (a) set-up, (b) WBBC samples.

Based on the experimental data, the specific heat capacity (Cp) was calculated using the following equation:

$$C_p = \frac{e^2}{\rho \cdot k} \quad (1)$$

being e the thermal effusivity [$Ws^{1/2}/(m^2K)$], ρ the density [$kg/m^3$] and k the thermal conductivity of the samples [W/mK].

### *2.4. Compressive strength*

Uniaxial compression tests were performed on five cylindrical WBBC specimens (50 mm diameter × 100 mm height) to determine their compressive strength and elastic modulus. The testing procedure adhered to the guidelines outlined in Brazilian standards NBR 5739 [25] and NBR 8522 [26]. A servo-controlled press with a 1000 kN load capacity was used to apply a constant displacement rate of 0.3 mm/min. Longitudinal deformation was monitored using a pair of linear variable differential transformers (LVDTs).

### *2.5. Scanning electron microscopy (SEM)*

Microstructural analysis was conducted to investigate the wood shavings-cementitious matrix interface and assess the composite's porosity. The test was performed using backscattered electron imaging in a Hitachi TM 3000 scanning electron microscope (SEM).

## *3. Results and discussion*

### *3.1. Thermo-physical properties*

A linear correlation between bulk density and bio-aggregate content was observed in WBBC composites (Fig. 3). Density values ranged from 1109 to 663 kg/m³, classifying the produced WBBC as lightweight materials based on RILEM functional classification. Compared to WBBC40, the density decreased by 23% and 43% for WBBC50 and WBBC60, respectively.

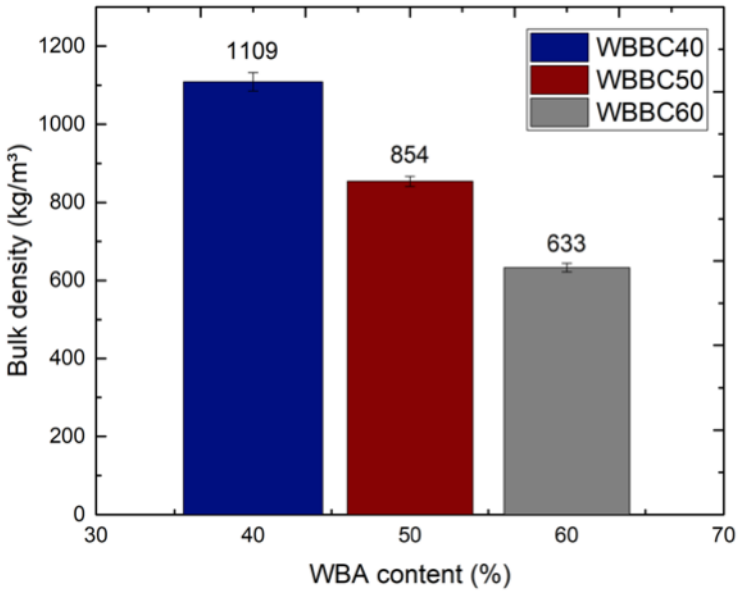


**Figure 3.** Bulk density of wood bio-based composites.

Density values in bio-concrete research exhibit variability influenced by factors such as bio-aggregate type and species, pozzolan incorporation, water-to-cement ratio, and

mixing/consolidation processes. Da Gloria et al. [20] reported bulk density values ranging from 715 to 1207 kg/m³ for wood bio-concretes containing 40-50% bio-aggregate and water-to-binder ratios varying from 0.35 to 0.45. Andreola et al. [27] produced bamboo bio-concretes with bulk densities ranging from 693 to 786 kg/m³ for mixtures containing 45-50% bio-aggregate and water-to-binder ratios of 0.40-0.50. Therefore, the density values determined in this study are consistent with those reported in the literature for similar bio-concrete compositions.

The average thermal conductivity and thermal effusivity values of the wood bio-based composites are presented in Fig. 4. Both thermal conductivity and thermal effusivity decreased with decreasing composite density.

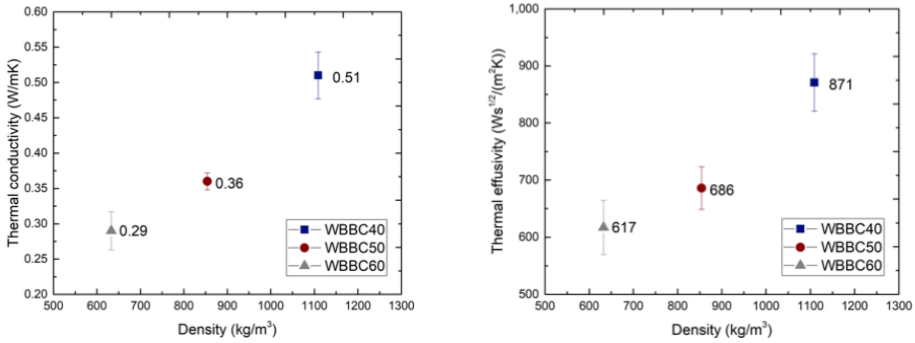


**Figure 4.** Thermal properties of WBBC: (a) thermal conductivity, (b) thermal effusivity.

Biomass content significantly influenced the thermal properties of the wood bio-based composite. Based on Fig. 5a, the thermal conductivity ranged from 0.51 to 0.29 W/mK, which represents a reduction of up to 43% from WBBC40 to WBBC60. The porosity of these materials is related to their heat conduction properties. A porous structure, with air trapped within, creates a lightweight material with enhanced thermal insulation. Generally, increased porosity results in lower bulk density and thermal conductivity, improving the material's insulating performance [18]. According to NBR 15220-2 [28], which establishes thermal conductivity recommendations for construction materials, all wood bio-based composites in this study qualify as insulating materials with conductivity values below 0.6 W/mK.

Andreola et al. [27] reported thermal conductivity values of 0.32 to 0.52 W/mK for bamboo bio-concretes with bio-aggregate contents similar to this study (45-50%). Da Gloria et al. [20] obtained comparable results (0.46-0.54 W/mK) for wood-based bio-concretes with equivalent bio-aggregate proportions.

Thermal effusivity is a crucial property for thermal insulation materials, characterizing their ability to absorb and release heat at the surface, thereby influencing interior climate regulation [4]. Figure 5b shows a variation in thermal effusivity values from 871 to 617 $Ws^{1/2}/(m^2K)$. Compared to WBBC40, thermal effusivity decreased by 21% for WBBC50 and 29% for WBBC60. This is a significant finding in thermal insulation, as effective insulation materials require not only low thermal conductivity but also the ability to delay heat transfer [29].

Sellami et al. [4] emphasize that the combined effect of low bio-aggregate thermal conductivity and high composite porosity results in relatively lower thermal effusivity values compared to traditional masonry materials, such as solid bricks (1000 $J/m^2Ks^{1/2}$) and common concrete (2035 $J/m^2Ks^{1/2}$).

The calculated specific heat capacity values for WBBC40, WBBC50, and WBBC60 were determined to be 1.34 J/gK, 1.53 J/gK, and 2.07 J/gK, respectively. These results confirm that a higher wood content correlates with improved thermal energy storage capacity.

### *3.2. Compressive strength*

Table 3 summarizes the compressive strength (σ) and Young's modulus (E) values obtained for the WBBC. All values represent the average of five test specimens per mixture, with corresponding coefficient of variation values shown in parentheses. The results indicate a strong correlation between WBA content and compressive strength. A reduction of approximately 70% in compressive strength was observed from WBBC40 to WBBC50, while a decrease of approximately 94% occurred from WBBC40 to WBBC60. The Young's modulus values followed the same pattern as compressive strength, with reductions of 50% and 90% recorded for WBBC50 and WBBC60, respectively, when compared to WBBC40. Da Gloria and Toledo Filho [20] demonstrated that increased bio-aggregate content diminishes bio-concrete strength and stiffness due to enhanced porosity. The results presented align with their findings, showing a positive correlation between compressive strength and first crack toughness, primarily attributed to the cementitious matrix.

**Table 3.** Compressive strength and Young´s modulus (coefficient of variation in %).

| | WBBC40 | WBBC50 | WBBC60 |
|---|---|---|---|
| σ (MPa) | 8.18 (9.1) | 2.48 (6.2) | 0.53 (7.6) |
| E (GPa) | 1.66 (6.8) | 0.84 (10.7) | 0.16 (10.1) |

Figure 5 illustrates the stress-strain behavior obtained from uniaxial compression tests conducted on the composites. The curves display an initial linear elastic response, subsequently transitioning to a nonlinear region characterized by increasing stress until reaching a maximum load-bearing capacity. Post-peak behavior indicates the material's capacity for energy absorption, consistent across all bio-aggregate contents, even under minor tension variation. WBBC50 and WBBC60 curves exhibit post-peak plateaus, demonstrating increased energy absorption capacity with higher bio-aggregate content.

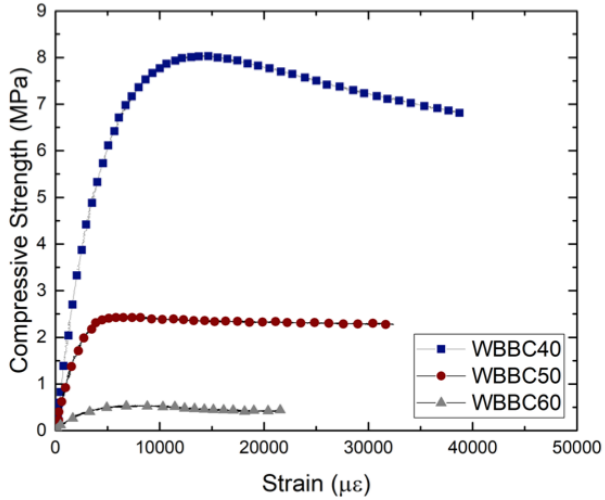


**Figure 5.** Stress-strain curves of WBBC samples.

### *3.3. Scanning electron microscopy (SEM)*

The scanning electron microscopy observations show the porous microstructure of the wood bio-aggregate (Fig. 6a). Calcium hydroxide deposits, resulting from the biomass treatment, are evident as white points within the wood structure (Fig. 6a). Figures 6b-d illustrate the microstructure of the bio-based composites. While WBBC40 (Fig. 6b) and

WBBC50 (Fig. 6c) exhibit stronger adhesion between the bio-aggregate and cement paste, WBBC60 displays pronounced microcracking surrounding the bio-aggregate, correlating with its reduced mechanical performance. Additionally, the presence of entrapped air and pores, which increases with higher biomass content, contributes to the reduced thermal conductivity of all composites.

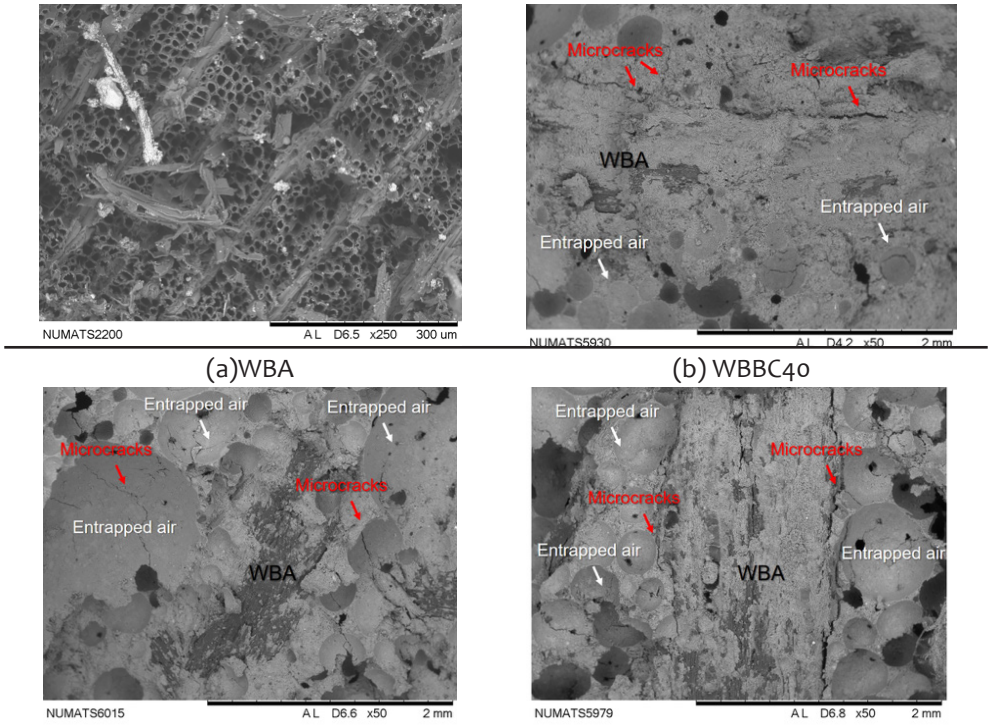


**Figure 6.** SEM photographs: (a) Wood bio-aggregate, (b) WBBC40, (c) WBBC50, (d) WBBC60.

### *4. Conclusions*

This study investigated the thermo-physical properties and mechanical performance of wood bio-based composites (WBBC) with varying bio-aggregate contents.

The following conclusions can be drawn from the results:

- Increasing bio-aggregate content significantly reduced density, thermal

conductivity, and thermal effusivity due to higher porosity and entrapped air, making WBBC effective thermal insulators for energy-efficient building materials.

- Compressive strength and Young's modulus exhibited a substantial decrease with increasing bio-aggregate content, attributed to weaker bonding with the cement matrix and increased porosity. However, composites with higher bio-aggregate content showed better energy absorption capacity.

These results highlight the trade-offs between thermal performance and structural integrity, suggesting that future research should focus on optimizing bio-aggregate content to balance mechanical performance and functionality.


### *Acknowledgments*

The authors gratefully acknowledge the financial support of the Brazilian institutions: CAPES (Coordenação de Aperfeiçoamento de Pessoal de Nível Superior) – Finance Code 001, and CNPq (Conselho Nacional de Desenvolvimento Científico e Tecnológico). We sincerely thank the European Commission for its support and funding through the Marie Skłodowska-Curie Actions scheme under grant agreement 101086440, specifically for the BEST (Bio-based Energy-efficient Materials and Structures for Tomorrow) project. For more details, please visit: https://cordis.europa.eu/project/id/101086440/es.


### *References*


[1] L. Chen, · Goodluck Msigwa, M. Yang, A.I. Osman, · Samer Fawzy, · David, W. Rooney, P.-S. Yap, "Strategies to achieve a carbon neutral society: a review", Environ Chem Lett 20, 2277–2310, 2022.

[2] E. Fehling, M. Schmidt, J. Walraven, T. Leutbecher, S. Fröhlich, "Ultra-High Performance Concrete UHPC: Fundamentals, Design, Examples", 1–188, 2015.

[3] J. Farfan, M. Fasihi, C. Breyer, "Trends in the global cement industry and opportunities for long-term sustainable CCU potential for Power-to-X", J Clean Prod 217, 821–835, 2019.

[4] A. Sellami, D. Bouayad, A. Benazzouk, S. Amziane, M. Merzoud, "Study of toughness and thermal properties of bio-composite reinforced with diss fibers for use as an insulating material", Energy Build 276, 112527, 2022.

[5] C. Niyigena, S. Amziane, A. Chateauneuf, "Multicriteria analysis demonstrating the impact of shiv on the properties of hemp concrete", Constr Build Mater 160, 211–222, 2018.

[6] J. Sheridan, M. Sonebi, S. Taylor, S. Amziane, "The effect of long term weathering on hemp and rapeseed concrete", Cem Concr Res 131, 106014, 2020.

[7] T. Lopes, S. Labeni, R. Sonnier, L. Ferry, A. Regazzi, P. Uwizeyimana, L. Aprin, P. Delot, A.H. de Menibus, M. Potin, "Ignition of biobased concretes", Constr Build Mater 440, 137423, 2024.

[8] M.Y.R. da Gloria, V.M. Andreola, D.O.J. dos Santos, M. Pepe, R.D. Toledo Filho, "A comprehensive approach for designing workable bio-based cementitious composites", Journal of Building Engineering 34, 101696, 2021.

[9] L. Rosse Caldas, A. Bernstad Saraiva, V.M. Andreola, R. Dias Toledo Filho, "Bamboo bio-concrete as an alternative for buildings' climate change mitigation and adaptation", Constr Build Mater 263, 120652, 2020.

[10] U. Saal, H. Weimar, U. Mantau, "Wood Processing Residues", Adv Biochem Eng Biotechnol 166, 27–41, 2017.

[11] J. A. Murphy, P. M. Smith, J. Wiedenbeck. "Wood residue utilization in Pennsylvania: 1988 vs. 2003." Forest products journal 57.4, 2007.

[12] S. Dias, J. Almeida, B. Santos, P. Humbert, A. Tadeu, J. António, J. de Brito, P. Pinhão, "Lightweight cement composites containing end-of-life treated wood – Leaching, hydration and mechanical tests", Constr Build Mater 317, 125931, 2022.

[13] M.Y.R. da Gloria, L.R. Caldas, J.A.O. Barros, R.D. Toledo Filho, "A Comprehensive Approach for Designing Low Carbon Wood Bio-Concretes", Materials 17, 2024.

[14] O. Kinnane, A. Reilly, J. Grimes, S. Pavia, R. Walker, "Acoustic absorption of hemp-lime construction", Constr Build Mater 122, 674–682, 2016.

[15] Y.X. Chen, F. Wu, Q. Yu, H.J.H. Brouwers, "Bio-based ultra-lightweight concrete applying miscanthus fibers: Acoustic absorption and thermal insulation", Cem Concr Compos 114, 103829, 2020.

[16] V. Corinaldesi, A. Mazzoli, R. Siddique, "Characterization of lightweight mortars containing wood processing by-products waste", Constr Build Mater 123, 281–289, 2016.

[17] F. Fedorik, J. Zach, M. Lehto, H.R. Kymäläinen, R. Kuisma, M. Jallinoja, K. Illikainen, S. Alitalo, "Hygrothermal properties of advanced bio-based insulation materials", Energy Build 253, 111528, 2021.

[18] A. Bakkour, S.E. Ouldboukhitine, P. Biwole, S. Amziane, "A review of multi-scale hygrothermal characteristics of plant-based building materials", Constr Build Mater 412, 134850, 2024.

[19] S. Amziane, F. Collet, eds. Bio-aggregates based building materials: state-of-the-art report of the RILEM Technical Committee 236-BBM. Vol. 23. Springer, 2017.

[20] M.Y.R. da Gloria, R.D. Toledo Filho, "Innovative sandwich panels made of wood bio-concrete and sisal fiber reinforced cement composites", Constr Build Mater 272, 121636, 2021.

[21] A.L.D. Aguiar, C.G. Bezerra, L.R. Caldas, A.S. Bernstad, R.D. Toledo Filho, "Environmental Performance of Wood Bioconcretes with Different Wood Shavings Treatments", Bio-Based Building Materials, Trans Tech Publications Ltd, pp. 69–76, 2022.

[22] L.R. Caldas, M.Y.R. Da Gloria, F. Pittau, V.M. Andreola, G. Habert, R.D. Toledo Filho, "Environmental impact assessment of wood bio-concretes: Evaluation of the influence of different supplementary cementitious materials", Constr Build Mater 268, 121146, 2021.

[23] ABNT, NBR. 16697. "Cimento Portland-Requisitos.", 2018.

[24] ABNT, NBR. 9778. "Argamassa e Concreto Endurecidos—Determinação da Absorção de Água, Índice de Vazios e Massa Específica", 2005.

[25] ABNT, NBR. 5739. "Concreto-Ensaio de Compressão de Corpos de Prova Cilíndricos", 2018.

[26] ABNT, NBR. 8522. "Concreto-Determinação do módulo estático de elasticidade à compressão", 2008.

[27] V.M. Andreola, M.Y.R. da Gloria, M. Pepe, R.D. Toledo Filho, "A Comprehensive Experimental Study on the Physical Performance and Durability of Bamboo Bio-Concrete", Sustainability (Switzerland) 16, 2024.

[28] ABNT, NBR. 15220-2. "Desempenho térmico de edificações-Parte 2: Métodos de cálculo da transmitância térmica, da capacidade térmica, do atraso térmico e do fator solar de elementos e componentes de edificações.", 2005.

[29] A. Djoudi, M.M. Khenfer, A. Bali, T. Bouziani, "Effect of the addition of date palm fibers on thermal properties of plaster concrete: experimental study and modeling", J Adhes Sci Technol 28, 2100–2111, 2014.

edizioni
Consiglio Nazionale delle Ricerche